Cilt 5 Sayı 2 Aralık 2024
Volume 5 Number 2 December 2024

ISSN: 2717-8811(Online)

JOURNAL

Materials and Mechatronics:A

2024

JOURNAL

Materials

and

Mechatronics: A

e-ISSN: 2717-8811

Cilt: 5 Sayı: 2 Aralık 2024

Volume:5 Number: 2 December 2024

2024

JOURNAL of
MATERIALS and MECHATRONICS:A

Editör Kurulu / *Editorial Board*		
Yusuf KAYALI (Editor-in-Chief)	ykayali@aku.edu.tr	Afyon Kocatepe University, TURKEY
Malzeme Mühendisliği / Materials Engineering		
Ali GÜNEN (Section Editor)	ali.gunen@iste.edu.tr	İskenderun Technical University, TURKEY
Reza BAKHTIARI (Section Editor)	reza. bakhtiari@uwaterloo. ca	Waterloo University, CANADA
Gökhan GÖRHAN (Section Editor)	ggorhan@aku.edu.tr	Afyon Kocatepe University, TURKEY
Ali ERÇETİN (Section Editor)	aercetin@bandırma.edu.tr	Bandırma Onyedi Eylül University, TURKEY
Fayaz HUSSAİN (Section Editor)	fhussain@neduet.edu.pk	Ned University, PAKİSTAN
Shkelzen SHABANI (Section Editor)	shkelzen.shabani@uni-pr.edu	Prishtina University, KOSOVA
Mekatronik Mühendisliği / Mechatronics Engineering		
İsmail YABANOVA (Section Editor)	iyabanova@aku.edu.tr	Celal Bayar University, TURKEY
Güray SONUGÜR (Section Editor)	gsonugur@aku.edu.tr	Afyon Kocatepe University, TURKEY
Elektrik ve Elektronik Mühendisliği / Electrical and Electronics Engineering		
Said Mahmut ÇINAR (Section Editor)	smcinar@aku.edu.tr	Afyon Kocatepe University, TURKEY
Douniazad MEZDOUR (Section Editor)	d_mezdour@univ-jijel. dz	Mohamed Seddik Benyahia University, ALGERIA
Enerji Sistemleri Mühendisliği / Energy Systems Engineering		
Ali KECEBAŞ (Section Editor)	alikecebas@mu.edu.tr	Muğla Sıtkı Koçman University, TURKEY
Ömer Faruk GÜLER (Section Editor)	afguler@aku.edu.tr	Afyon Kocatepe University, TURKEY
Bilgisayar ve Yazılım Mühendisliği / Computer and Software Engineering		
Gür Emre GÜRAKSIN (Section Editor)	emreguraksin@aku.edu.tr	Afyon Kocatepe University, TURKEY
Makine Mühendisliği / Mechanical Engineering		
Mehmet Erdi KORKMAZ (Section Editor)	merdikorkmaz@karabuk.edu.tr	Karabük University, TURKEY
İsmail Doğan KÜLCÜ (Section Editor)	ismaildogan.kulcu@ikc.edu.tr	İzmir Katip Celebi University, TURKEY
Faruk Emre AYSAL (Section Editor)	faruk.aysal@giresun.edu.tr	Giresun University, TURKEY
Manjunath PATEL G.C. (Section Editor)	manjunath. mech@pestrust edu.in	Pes Institute of Technology and Management, INDIA
Avinash LAKSHMIKANTHAN (Section Editor)	dravinash.laks01@gmail.com	Nitte Meenakshi Institute of Technology, INDIA

JOURNAL of
MATERIALS and MECHATRONICS:A

Otomotiv Mühendisliği / Automotive Engineering		
Fatih AKSOY (Section Editor)	faksoy@aku.edu.tr	Afyon Kocatepe University, TURKEY
Hicri YAVUZ (Section Editor)	hyavuz@aku.edu.tr	Afyon Kocatepe University, TURKEY
Halil DEMOLLİ (Section Editor)	halil.demolli@uni-pr.deu	Prishtina University, KOSOVA
Kimya-Kimya Mühendisliği / Chemical-Chemical Engineering		
Aysel BUYUKSAĞİŞ (Section Editor)	absagis@aku.edu.tr	Afyon Kocatepe University, TURKEY
Biyomedikal Mühendisliği / Biomedical Engineering		
Mehmet Lütfi YOLA (Section Editor)	mlutfi.yola@hku.edu.tr	Hasan Kalyoncu University, TURKEY
Yiğit Ali ÜNCÜ (Section Editor)	yuncu@akdeniz.edu.tr	Akdeniz University, TURKEY
Fizik-Fizik Mühendisliği / Physics-Physics Engineering		
Mehmet ÖZKAN (Section Editor)	mozkan@aku.edu.tr	Afyon Kocatepe University, TURKEY
Dil Editörleri / Language Editors		
Şükrü TALAŞ (Language Editor)	stalas@aku.edu.tr	Afyon Kocatepe University, TURKEY
Aytekin HİTİT (Language Editor)	hitit@aku.edu.tr	Afyon Kocatepe University, TURKEY

Danışma Kurulu / *Advisory Board*	
Dr. Adnan MAQBOOL	University of Engineering and Technology, PAKISTAN
Dr. Anas Al ATTIEH	German University of Jordan, JORDAN
Dr. Aytaç Uğur YERDEN	Gedik University, TURKEY
Dr. Dursun ÖZYÜREK	Karabük University, TURKEY
Dr. Erdoğan KANCA	İskenderun Technical University, TURKEY
Dr. Fatih Onur HOCAOĞLU	Afyon Kocatepe University, TURKEY
Dr. Ivan Enrique Campos SİLVA	Instituto Politécnico Nacional, MEXİCO
Dr. Kubilay ASLANTAŞ	Afyon Kocatepe University, TURKEY
Dr. Metin ÖZGÜL	Afyon Kocatepe University, TURKEY
Dr. Mourad KEDDAM	University of Science and Technology Houari Boumediene, ALGERIA
Dr. Mst.Alpona AKHTAR	University of North Texas, USA
Dr. M. Serhat BAŞPINAR	Afyon Kocatepe University, TURKEY
Dr. Oğuz ARSLAN	Bilecik Seyh Edebali University, TURKEY
Dr. Özkan GÖKÇEKAYA	Osaka University, JAPAN
Dr. Ramazan KAÇAR	Karabük University, TURKEY
Dr. Peter JURčİ	Slovak University of Technology in Bratislava, SLOVAKYA
Dr. Selçuk AKTÜRK	Muğla University, TURKEY
Dr. Shabana SHEIK	University of Pune, INDIA
Dr. Süleyman GÜNDÜZ	Karabük University, TURKEY
Dr. Uğur ÇALIGÜLÜ	Fırat University, ELAZIG
Dr. Undrakh MISHIGDORZHIYN	East Siberia State University, RUSSIA
Dr. Yılmaz YALÇIN	Afyon Kocatepe University, TURKEY

JOURNAL of
MATERIALS and MECHATRONICS:A

Yayımcı / Publisher	
Yusuf KAYALI	ykayali@aku.edu.tr

Mizanpaj Editörü / Layout Editor	
Mahmud Cemaleddin YALÇIN	mcyalcin@aku.edu.tr
Fatih ÇOLAK	fatihcolak@usak.edu.tr

Temel İletişim / Primer Contact	
Journal of Materials and Mechatronics: A	editorjournalmm@gmail.com iletisimjournalmm@gmail.com

Sekreter / Secretary	
Yavuz Bahadır KOCA	ybkoca@aku.edu.tr, journalmmsekreter@gmail.com

JOURNAL of
MATERIALS and MECHATRONICS:A

JOURNAL of
MATERIALS and MECHATRONICS:A

JOURNAL of
MATERIALS and MECHATRONICS:A

JOURNAL of
MATERIALS and MECHATRONICS:A

e-ISSN 2717-8811
JournalMM, 2024, 5(2), 214-227
https://doi.org/10.55546/jmm.1453536

Araştırma Makalesi / Research Article

Coating of the Surface of 316L Stainless Steel with Hydroxyapatite Produced from Eggshell Using the Sol-Gel Method

Levent ÖZCAN[1*], Adile ŞAHİN[2], Betül KARABULUT[3], Nagehan SÜRÜK[4]

[1*] Afyon Kocatepe University, Faculty of Engineering, Department of Biomedical Engineering, Afyonkarahisar, Türkiye, ORCID ID: https://orcid.org/0000-0003-4504-4237, leventozcan@aku.edu.tr
[2] Afyon Kocatepe University, Faculty of Engineering, Department of Biomedical Engineering, Afyonkarahisar, Türkiye, ORCID ID: https://orcid.org/0009-0006-4446-1214, adilesahhin@gmail.com
[3] Afyon Kocatepe University, Faculty of Engineering, Department of Biomedical Engineering, Afyonkarahisar, Türkiye, ORCID ID: https://orcid.org/0009-0006-1858-7294, betulkrblt3@gmail.com
[4] Afyon Kocatepe University, Faculty of Engineering, Department of Biomedical Engineering, Afyonkarahisar, Türkiye, ORCID ID: https://orcid.org/0009-0005-0646-3668, nagehansrk@gmail.com

Geliş/ Received: 15.03.2024; **Revize/Revised:** 28.06.2024 **Kabul / Accepted:** 01.07.2024

ABSTRACT: In this study, the production of high-yield and purity calcium nitrate from eggshell, a biological waste, and the usability of the obtained calcium nitrate in the production of hydroxyapatite (HAP) by the sol-gel method were investigated. In addition, the obtained HAP was used to coat 316L steel using the dip coating method. For this purpose, calcium nitrate, which will be used as a precursor in HAP production, was produced from chicken eggshells with high calcium carbonate content. The surface of 316L stainless steel discs was coated with sol-gel obtained from a mixture of calcium nitrate and triethyl phosphite by dip-coating method. Then, the 316L discs were dried and heat treated at 500 °C to form HAP on their surfaces. XRD and SEM techniques were used for the characterization of the obtained HAP structure. Unlike previous studies, it has been shown that chicken eggshell, a biological waste, can be used to produce HAP, a biocompatible material, and the surface of 316L stainless steel can be coated with the produced HAP.

Keywords: Hydroxyapatite, Eggshell, 316L stainless steel, Sol-gel method

---

*Sorumlu yazar / Corresponding author: leventozcan@aku.edu.tr

Bu makaleye atıf yapmak için /To cite this article

Özcan, L., Şahin, A., Karabulut, B., Sürük., N. (2024). Coating of the Surface of 316L Stainless Steel with Hydroxyapatite Produced from Eggshell Using the Sol-Gel Method. Journal of Materials and Mechatronics: A (JournalMM), 5(2), 214-227.

Yumurta Kabuğundan Üretilmiş Hidroksiapatit ile 316L Paslanmaz Çelik Yüzeyinin Sol-Jel Yöntemi Kullanılarak Kaplanması

ÖZET: Bu çalışmada biyolojik bir atık olan yumurta kabuğundan yüksek verim ve saflıkta kalsiyum nitrat eldesi ve elde edilen kalsiyum nitratın sol-jel yöntemiyle hidroksiapatit (HAP) üretiminde kullanılabilirliği araştırılmıştır. Ayrıca elde edilen HAP daldırıp-çıkarma (dip-coating) yöntemi kullanılarak 316L çeliğinin kaplanmasında kullanılmıştır. Bu amaçla, HAP üretiminde öncül olarak kullanılacak kalsiyum nitrat, kalsiyum karbonat içeriği yüksek tavuk yumurtası kabuklarından üretildi. 316L paslanmaz çelik disklerin yüzeyi, kalsiyum nitrat ve trietil fosfit karışımından elde edilen sol-jel ile daldırıp-çıkarma (dip-coating) yöntemiyle kaplandı. Sonra, 316L diskler kurutuldu ve yüzeylerinde HAP oluşturmak için 500 °C'de ısıl işleme tabi tutuldu. Elde edilen yapıların karakterizasyonunda XRD ve SEM tekniklerinden faydalanılmıştır. Daha önce yapılan çalışmalardan farklı olarak, biyolojik bir atık olan tavuk yumurtası kabuğunun biyouyumlu bir malzeme olan HAP üretiminde kullanılabileceği ve üretilen HAP ile 316L paslanmaz çeliğin yüzeyinin kaplanabileceği gösterilmiştir.

Anahtar Kelimeler: Hidroksiapatit, Yumurta kabuğu, 316L paslanmaz çelik, Sol-jel yöntemi

1. INTRODUCTION

Mechanical properties, corrosion resistance, and moderate biocompatibility of metallic implants such as Ti, Co-Cr, Mg alloys, and stainless steel are the properties that lead to the use of these materials as implants (Narushima et al., 2013; Rezaei et al., 2020; Mohandesnezhad et al., 2022). Among metallic implants, 316L stainless steel is of interest to be used in artificial knee and hip joints, orthopedics, orthodontics, and heart valve parts due to its availability, low cost, and simple manufacturing procedure (Sanchez-Hernandez et al., 2014; Sutha et al., 2013). However, the lack of bioactivity and biocompatibility at the desired level is a problem that must be overcome in the successful use of this material in implant manufacturing. 316L stainless steel is mainly composed of Cr, Ni, V, and Mo elements, and problems may be encountered due to the release of these elements into the body in the corrosive environment of body fluid (Gurappa 2002; Navarro et al., 2008; Yazıcı et al., 2015). To overcome such difficulties encountered in the in vivo application of metallic implants, coating with a biocompatible and bioactive material is a viable, efficient, and cost-effective strategy. Calcium phosphate coatings especially hydroxyapatite (HAP) have suitable biocompatibility and are used for this purpose. In particular, HAP with a Ca/P ratio of 1.67 has higher biocompatibility, bioactivity, and stability in physiological environments compared to other members of the calcium phosphate family (Habibovic et al., 2002; Yazdani et al., 2018; Ahmed and Rehman 2020; Awasthi et al., 2021; Zhou et al., 2020).

Many studies have been carried out on the application of HAP in the structure of $Ca_{10}(PO_4)_6(OH)_2$ to the surface of metallic materials. The driving force behind these studies is that HAP is similar to human bone and teeth in terms of chemical and mineralogical composition and crystallographic structure (Asri et al., 2016). It is also preferred in the coating of metallic implants to support new bone growth due to its strong chemical bonds (Song et al., 2008). The coating of biomaterials with HAP creates a layer that prevents ionic dissolution of metals, increases their resistance to corrosion, and increases their bonding capacity to bone (Zhong et al., 2015).

Techniques such as sol-gel (Ballarre et al., 2010), electrochemical deposition (Coşkun et al., 2014), electrophoretic deposition (Rojaee et al., 2013; Prabakaran et al. 2005), plasma sputtering (Chu et al., 2002), and biomimetic deposition (Bigi et al., 2005) have been developed to coat HAPs on metallic implants. The sol-gel process used in conjunction with the dip-coating technique has been widely used for coating metallic biomaterials to improve adhesion (Zhang et al., 2011).

Sol-gel method generally uses sol-gel, which is obtained by adding suitable chemicals that act as a source of calcium and phosphorus to a water-ethanol solution. Phosphorus pentoxide or triethyl phosphite is mostly used as a source of phosphorus, and calcium nitrate is used as a source of calcium. As shown in Fig. 1, the first step of the sol-gel process is to obtain a homogeneous solution of CaP precursors in a water-miscible organic solvent. It should be noted that the organic solvent to be used should be miscible with the reagents to be used in the next steps. In the second stage, the sol structure undergoes polycondensation and becomes a "gel" structure. Afterward, the sol-gel is aged, dried, and calcined, respectively (Asri et al., 2016).

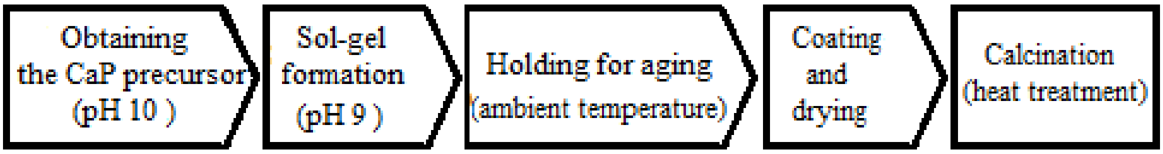

Figure 1. Process steps applied in obtaining and coating HAP by sol-gel method.

Eggshell is an important biowaste, and in previous studies, hydroxyapatite was obtained from the reaction of CaO and phosphoric acid obtained by calcining the eggshell at high temperatures (Curkovic et al. 2017). Powder hydroxyapatite can be obtained by this method, known as the chemical precipitation method. However, the sol-gel method is widely used to coat metallic surfaces with a thin HAP film. This situation was taken into consideration in our study and the use of calcium nitrate from chicken egg shells as a source of Ca in HAP production and its use in coating 316L stainless steel surfaces with the sol-gel method were studied. Although the study of coating the 316L surface with HAP with the sol-gel method was carried out previously, commercially available calcium nitrate was used as a source of Ca in the preparation of the sol-gel in previous studies (Azem and Çakır, 2009). The difference of this study is to show the usability of calcium nitrate obtained from eggshells, which is a waste biological resource, in the production of HAP and in coating the surface of metallic biomaterials.

2. MATERIALS AND METHODS

2.1 Materials and Devices

The nitric acid, triethyl phosphite, ethanol, acetone, and ammonia used are of analytical purity. 316L stainless steel was obtained from Birçelik Company (1.0 cm diameter) and its chemical composition is given in Table 1.

Table 1. Chemical Composition of 316L (Ugitech) Stainless Steel.

C	Mn	Cr	Si	Mo	P	S	N	Ni
0.030	2.0	16.5-18.0	1.0	2.0-2.5	0.045	0.03	0.10	10.0-13.0

The pure water used was obtained from the TKA Smart 2 Pure brand ultrapure water device. Protherm brand "PLF-110/10" model laboratory furnace with temperature adjustment was used for heat treatment in HAP production. Memmert brand incubator was used for drying processes. Ekopol 200 Polisher sanding device was utilized for sanding 316L stainless steel discs. Bandelin brand

Sonorex Model ultrasonicator was used in ultrasonic cleaning processes. The pH of the solutions was adjusted using the Thermo-Fisher brand Orion model pH meter. Before pH measurements, the pH meter was calibrated with standard buffer solutions.

CaO, $Ca(NO_3)_2$ ve HAP formations were confirmed by X-ray diffractometry (Bruker D8 Advance) using CuKα (λ = 1.544 A°) radiation. Surface imaging and EDX measurements were performed with a NanoSEM 650 model (FEI Company) scanning electron microscope.

2.2 Obtaining Calcium Nitrate from Egg Shell

The chicken egg shells used in the study were obtained by choosing the white ones from the cafeteria in the dormitories of the students who carried out this study within the scope of the undergraduate thesis. After the egg shells were boiled, their inner membranes were separated by hand and the shells were left at room temperature for 24 hours to dry. After the dry egg shells were ground into powder by grinding with a grinder (Empero), they were placed in the laboratory furnace and heated at this temperature for 1 hour after the temperature reached 900 °C. This way, the eggshell of 98% $CaCO_3$ (Kılınç 2016) was transformed into CaO. It has been reported in the literature that CaO obtained by calcining eggshells at 900 °C for 1 hour has a high purity of 99.06% by mass (Tangboriboon et al. 2012). Additionally, Nath et al. (2021) reported higher purity conversion of $CaCO_3$ to CaO in the calcination of eggshells at 900 °C compared to that at 800 and 700 °C. For this reason, 900 C was preferred for the calcination temperature. The resulting powder was reacted with 65% nitric acid in a fume hood to contain more than the stoichiometric ratio of CaO. The reaction medium was stirred continuously using a magnetic stirrer. It waited for 1 day for the insoluble particles in the mixture obtained as a result of this process to settle to the bottom, and the insoluble particles were completely removed by filtration under a vacuum. For the water in the solution to evaporate sufficiently, the filtered part was heated and then kept in an oven at 190°C for 24 hours to obtain anhydrous calcium nitrate. The obtained calcium nitrate was kept in a closed glass jar so that it did not absorb moisture. Photographs of the relevant production processes are shown in Fig. 2. The production yield of $Ca(NO_3)_2$ from eggshell was calculated as 95%.

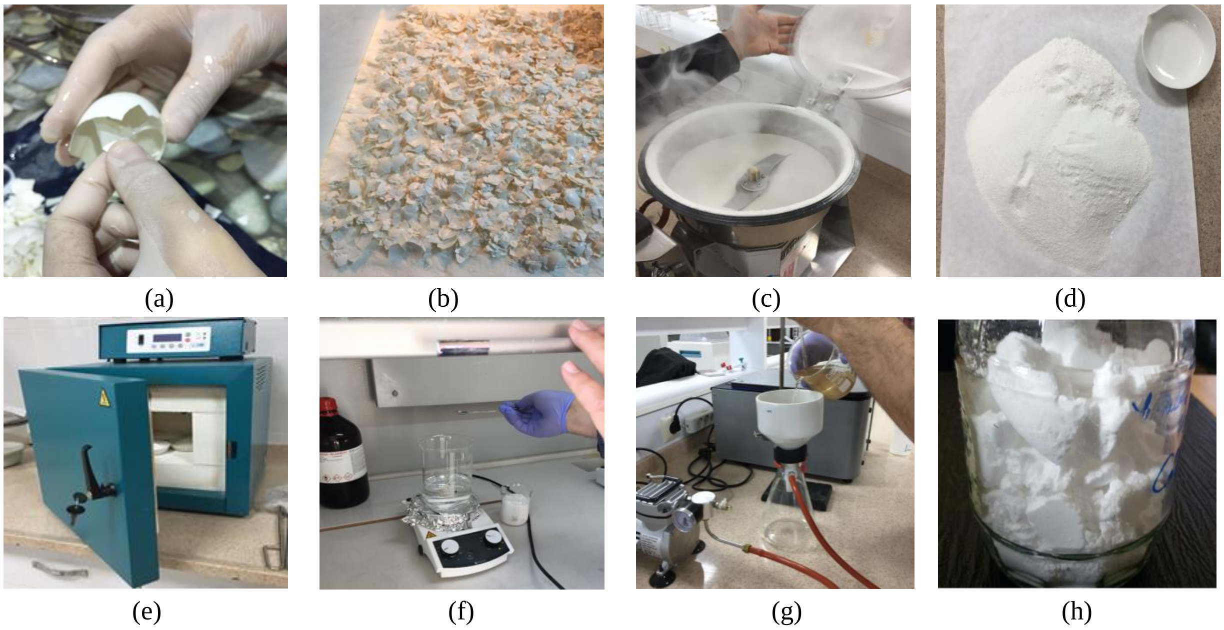

(a) (b) (c) (d)

(e) (f) (g) (h)

Figure 2. (a) Separation of membranes from boiled eggshell (b) Dried egg shells (c) Pulverizing egg shells using a grinder (d) Powdered eggshells (e) Conversion of powdered eggshells to CaO by baking (f) Reaction of CaO with HNO_3 (g) Separation of insoluble particles by vacuum filtration (h) Anhydrous calcium nitrate stored in a sealed jar.

2.2 Processes Applied to 316L Stainless Steel Before Coating

The supplied 316L stainless steel bars 1.0 cm in diameter and 1 m in length were cut with a lathe into 1.5 cm long pieces. Then, it was sanded using sandpaper with 60, 80, 120, 220, 320, 600, 800, 1000, and 1200 grit grades using a sanding device (Ekopol 200 polisher). In each step of the sanding process, the discs were re-sanded by turning them 90° according to the direction of the first sanding operation. The sanded discs were ultrasonically cleaned for ten minutes in distilled water, ethanol, acetone, and again in pure water, respectively. SEM images taken at different magnifications of 316L stainless steel, which has undergone these processes, are given in Fig. 3.

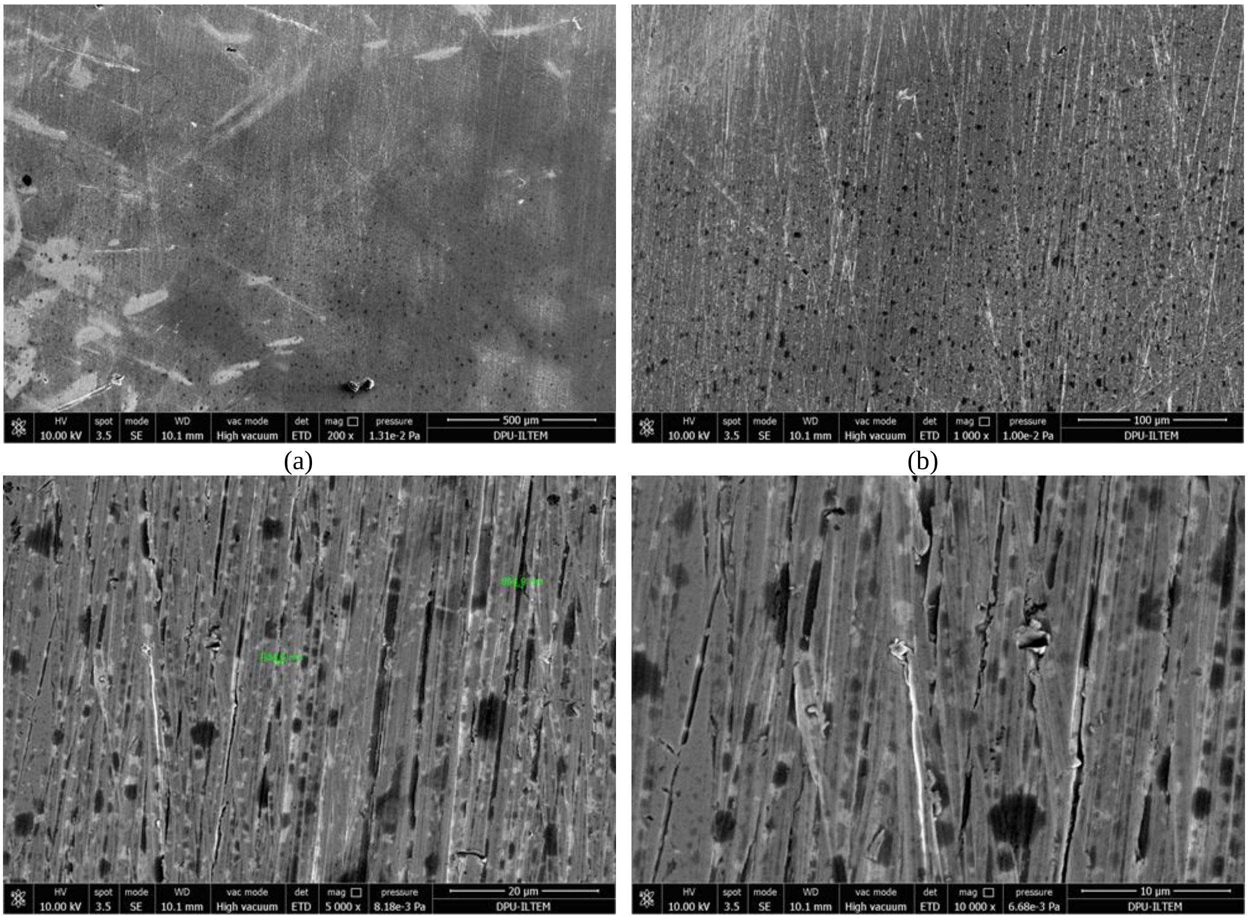

(a) (b)

(c) (d)

Figure 3. SEM images of sanded and cleaned 316L stainless steel (a) 200 (b) 1000 (c) 5000 (d) 10000 times magnification.

2.3 Preparation of Sol-gel used for HAP Coating

In the sol-gel preparation, $Ca(NO_3)_2$ obtained from egg shells was used as a calcium source, and triethyl phosphite was used as a phosphorus source. The reason for choosing triethyl phosphite as a phosphorus source is that its hydrolysis activity is reported to be high (Kılınç, 2016). The mixture consisting of 20.6 mL of triethyl phosphite and 30.0 mL of distilled water was stirred at 500 rpm for 24 hours to hydrolyze. 32.8 g of calcium nitrate was dissolved in a solution containing 20% water and 80% ethanol by volume. This solution was added dropwise from a burette to the triethyl phosphite solution, which was left to hydrolyze for 24 hours. This process was carried out while stirring the solution containing triethyl phosphite at 300 rpm. To improve the gelation of the prepared mixture, 3.5 mL of ammonia solution (% 28 NH_3) was added as a basic catalyst and left for 24 hours before coating (Azem and Çakır 2008). The pH value of the sol-gel, which was left for 24 hours, was determined to be 1.23 with a pH meter (Thermo-Fisher, Orion). The photographs of the relevant process steps are given in Fig. 4.

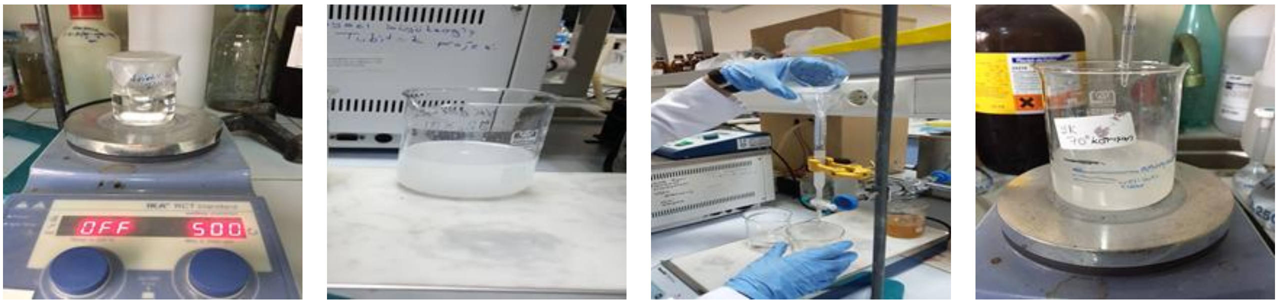
(a) (b) (c) (d)

Figure 4. (a) Preparation of triethyl phosphite solution (b) Dissolving calcium nitrate in ethanol (c) Addition of calcium nitrate solution dropwise to triethyl phosphite solution (d) Sol-gel obtained after the respective procedures.

2.4 HAP Coating of 316L Stainless Steel Discs

The steel discs were slowly immersed in the sol-gel in a beaker and left for 2 minutes, then slowly removed and left at room temperature until the solvents evaporated. Once this process was performed, it was observed that the coating efficiency on the 316L stainless steel disc surface was not sufficient, there were some uncoated areas on the surface and it had an irregular surface morphology. Therefore, this process was repeated twice. After the discs were coated with sol-gel and dried at room temperature, they were dried at 80 °C for 1 hour. Then, the heat treatment was applied by keeping it in a laboratory furnace at 500 °C (temperature increase rate: 2 °C/min) for 1 hour. Images of these process steps are given in Fig. 5. Azem and Çakır (2009) reported that when the calcination temperature of the sol-gel coating on the 316L stainless steel substrate is reached by applying a low-temperature increase rate (eg. 2 °C/min), the removal of organic impurities from the sol-gel structure is more controlled and a more dense HAP coating can be obtained. For this reason, this temperature increase rate (2 °C/min) was preferred in this study.

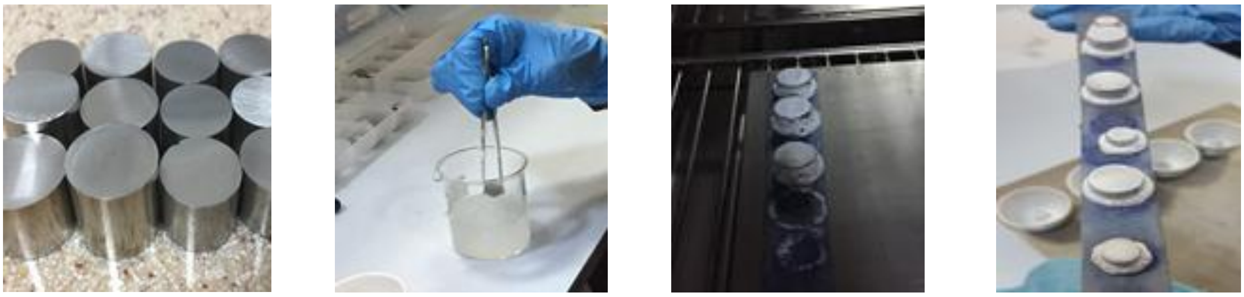
(a) (b) (c) (d)

Figure 5. a) Sanded and cleaned discs b) Immersion of discs in sol-gel c) Images of the discs coated with sol-gel after drying in an incubator at 80 °C d) Images of sol-gel coated discs after calcination at 500 °C.

3. RESULTS AND DISCUSSION

3.1 Characterization of CaO and $Ca(NO_3)_2$ Structures by XRD

The XRD diffractogram for CaO obtained from eggshells is given in Fig. 6. When Fig. 6 is examined, peaks compatible with the values of 18.1°, 32.3°, 37.4°, 53.9°, 64.2°, 67.4°, and 88.6° obtained for the CaO phase at the 2θ angle were obtained in the literature (Chen et al. 2014; Lani et al. 2019; Madhu et al. 2021). The very low intensity of the peaks of $Ca(OH)_2$, which correspond to values around 34.0°, 48.0°, 51.0° and 62.0°, can be associated with the formation of very small amounts of $Ca(OH)_2$, which occurs as a result of contact with the air in the atmosphere (Tan et al. 2015).

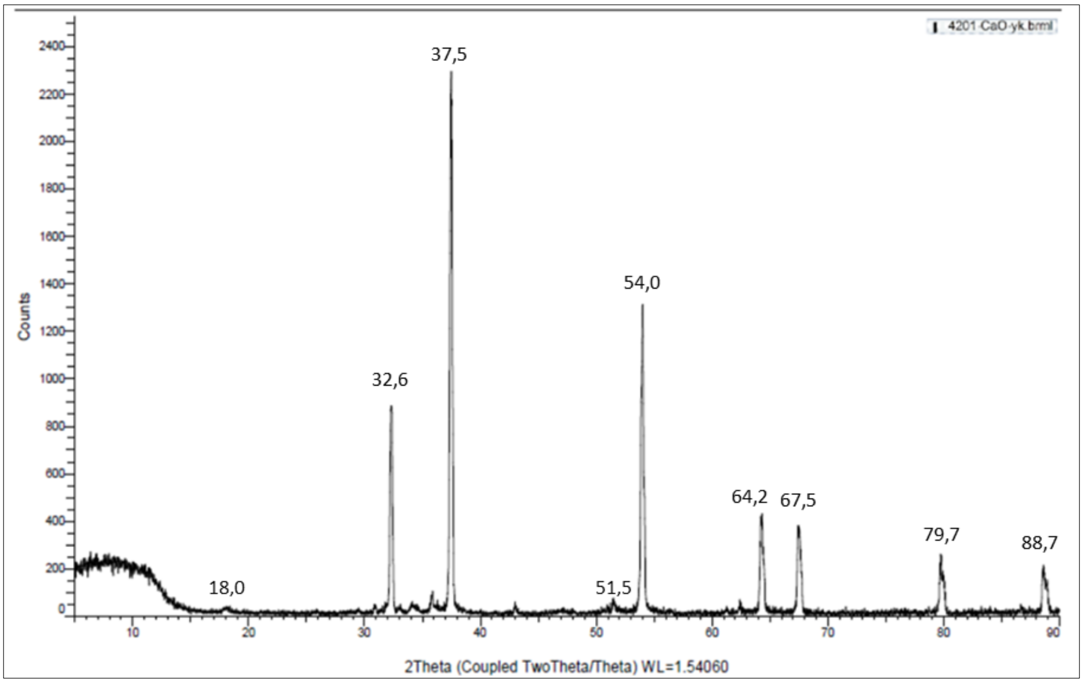

Figure 6. XRD diffractogram of CaO from the eggshell.

The XRD diffractogram of $Ca(NO_3)_2$ obtained from the reaction of CaO obtained from eggshell with nitric acid is given in Fig. 7.

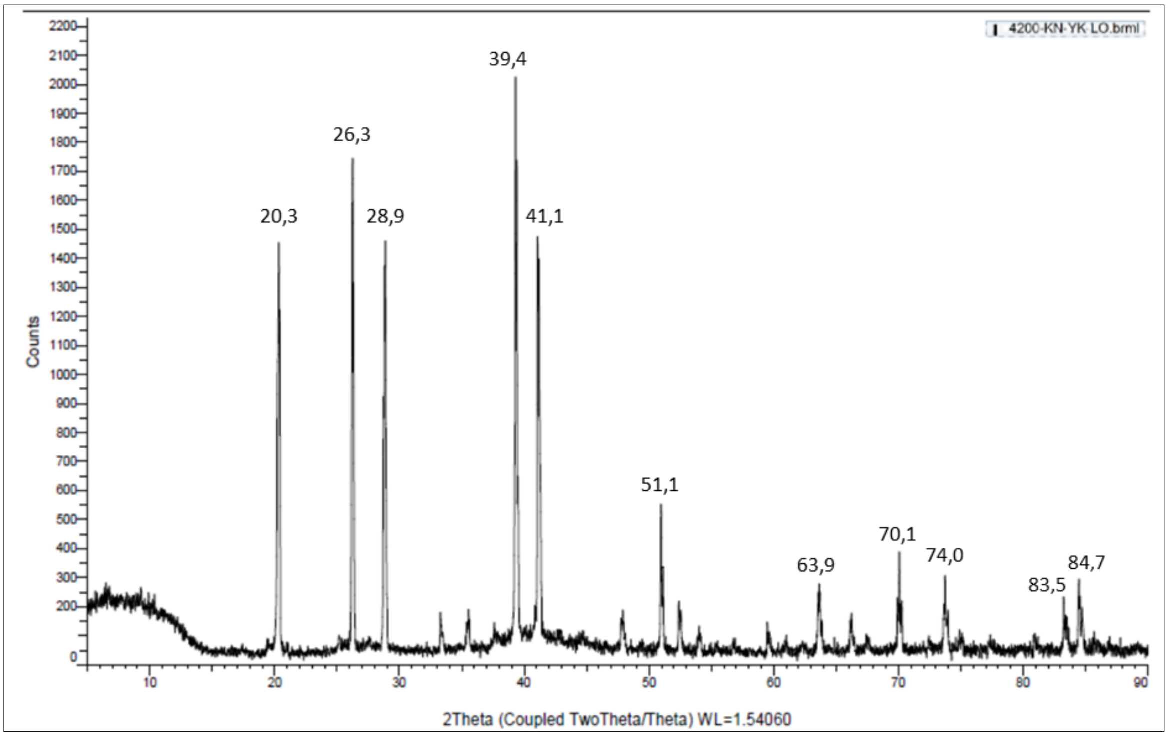

Figure 7. XRD diffractogram of $Ca(NO_3)_2$ obtained from eggshell.

3.2 Characterization of HAP Structure by XRD and SEM

To determine whether there would be differences in the HAP structures obtained by using commercially obtained calcium nitrate and eggshell calcium nitrate as a calcium source, the sol-gels in the porcelain crucible prepared according to section 2.3 were first dried at 80 ºC. These dried sol-gels were then calcined in the oven at 500 ºC for one hour. According to this procedure, the XRD diffractogram of the HAP structure obtained using commercial calcium nitrate is shown in Fig. 8, and the XRD diffractogram of the HAP structure obtained using calcium nitrate obtained from eggshell is seen in Fig. 9. XRD data of both structures show that the structures obtained are very similar and there is no serious difference in obtaining HAP. The peaks in Figures 8 and 9 match the peak values stated for HAP in the literature (Liu et al. 2002; Mišković-Stanković et al. 2015; Mokhtari et al. 2019). High intensity HAP peaks at 2θ = 26.0°, 31.8°, 32.2°, and 32.9° (Standard PDF card No. 01-86-1199) is crystalline plane of (002), (211), (112), and (300), respectively (Mišković-Stanković et al. 2015).

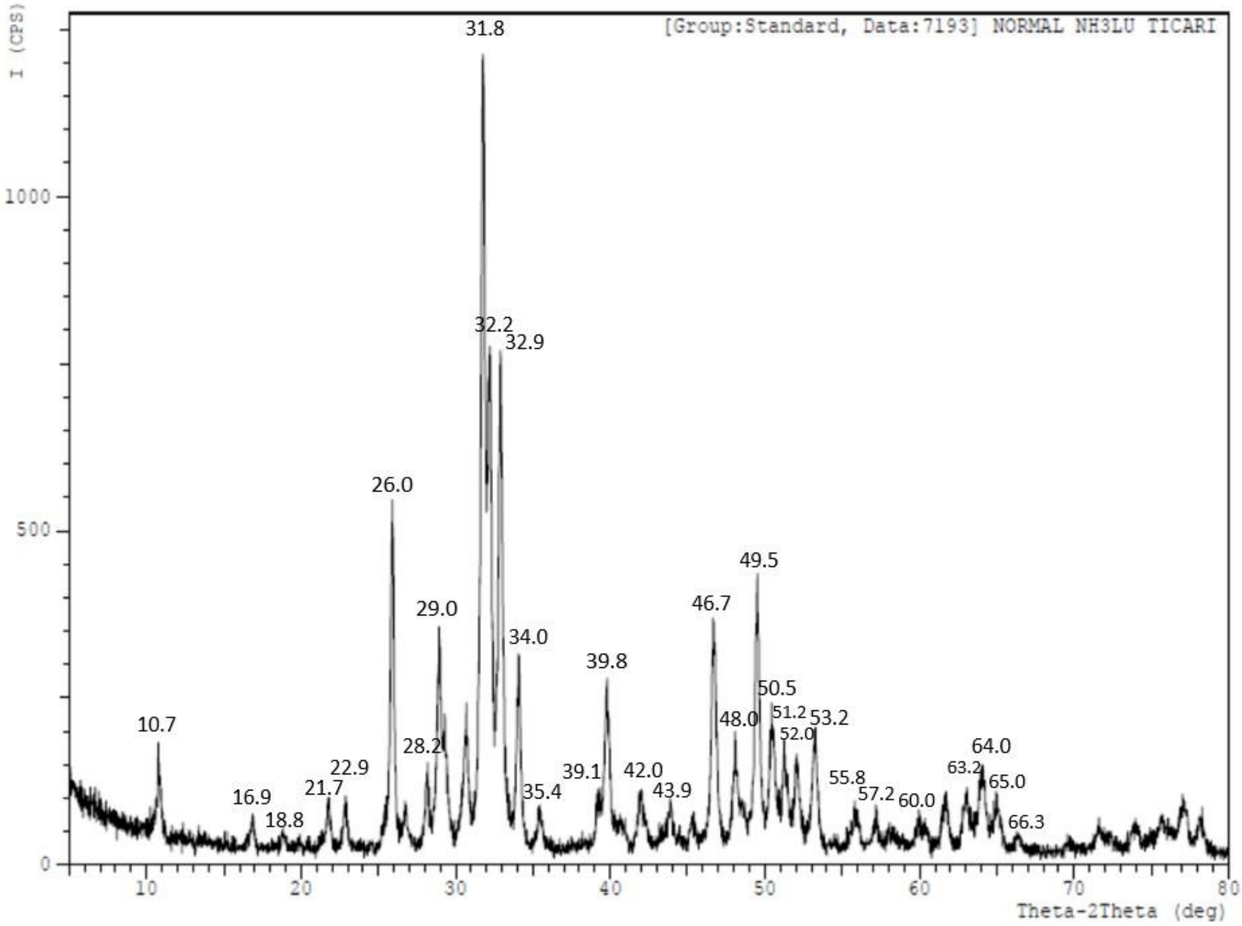

Figure 8. XRD diffractogram of the HAP structure obtained using commercial calcium nitrate.

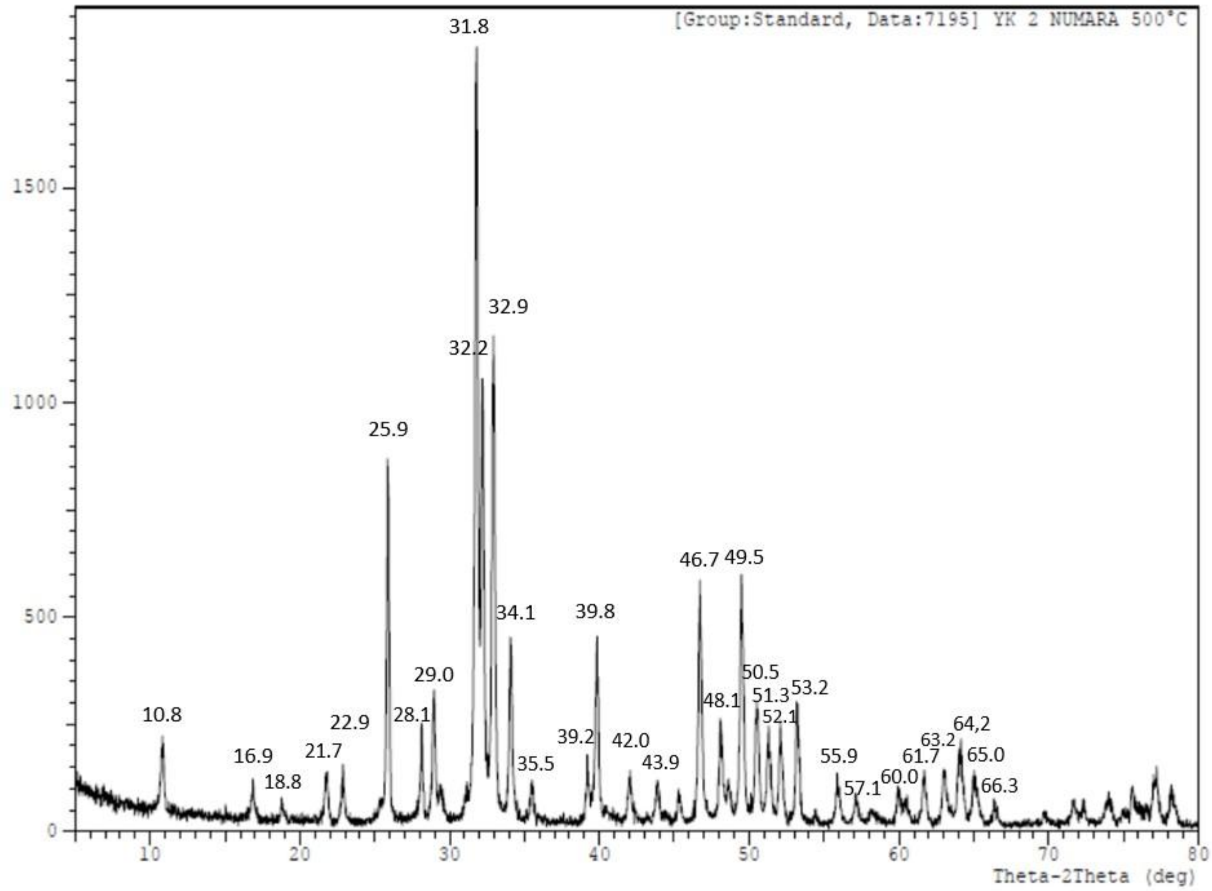

Figure 9. XRD diffractogram of the HAP structure obtained using calcium nitrate from the eggshell.

When the SEM images of the HAP structure coated on the 316L stainless steel surface in Fig. 10 are examined, it is seen that a spongy structure with open pores is formed (Fig. 10a and 10b). Additionally, when Fig. 10-b is examined at a higher magnification, a structure with more cracks and separation from the HAP coating below is noted in the upper part. This may be because the process of dipping and removing the stainless steel discs was done manually, without using a device. By using the sol-gel dip coating technique, a thin layer coating can be applied at low annealing temperatures without excessive cracking. However, serious cracks in the coating layer are frequently encountered due to rapid fluctuations in temperature and solidification of the coating (Kim et al. 2004). In addition, shrinkage of the gel structure is also a common occurrence during the drying process (Toygun et al. 2013). Fig. 10c and d at much higher magnifications show that the structure has a very homogeneous appearance in the parts where there are no cracks. EDX analysis in Fig. 10e show the presence of Ca, O, and P elements in the HAP structure of the coating, as well as Fe, Cr, and Ni elements in the stainless steel structure.

Azem and Çakır (2009) reported in their study that cracking and flake-shaped lifting defects occurred in some places due to heat treatment. Wei et al. (2005) explained this situation with the difference in thermal expansion coefficients between the materials. Sandblasting the substrate on which the HAP coating is applied, in addition to sanding, can also reduce crack formation. Kılınç (2016), in his study where he coated the Ti6Al4V alloy with HAP using the sol-gel method, performed the sandblasting process and stated that fewer cracks were observed in the HAP structure coated on the Ti6Al4V surface.

Additionally, it was observed that some parts of the HAP structure coated on the surface were separated from the surface when mechanical stress was applied. This observation shows that some additional processes are needed to increase the mechanical strength of the HAP coating on the 316L stainless steel surface and to ensure a stronger adhesion to the surface using the sol-gel method.

Although additional studies are required for a more effective HAP coating on the surface, it is advantageous that the HAP structure obtained by the sol gel method can be coated as a thin film by spin or dip deposition method. Additionally, sol-gel coating is a preferred method to provide uniform coating on large-sized surfaces with complex geometry. Thanks to this technique, the formation of protective and bioactive coatings in the form of pure, homogeneous films can be easily achieved at low temperatures (Kaur et al. 2019).

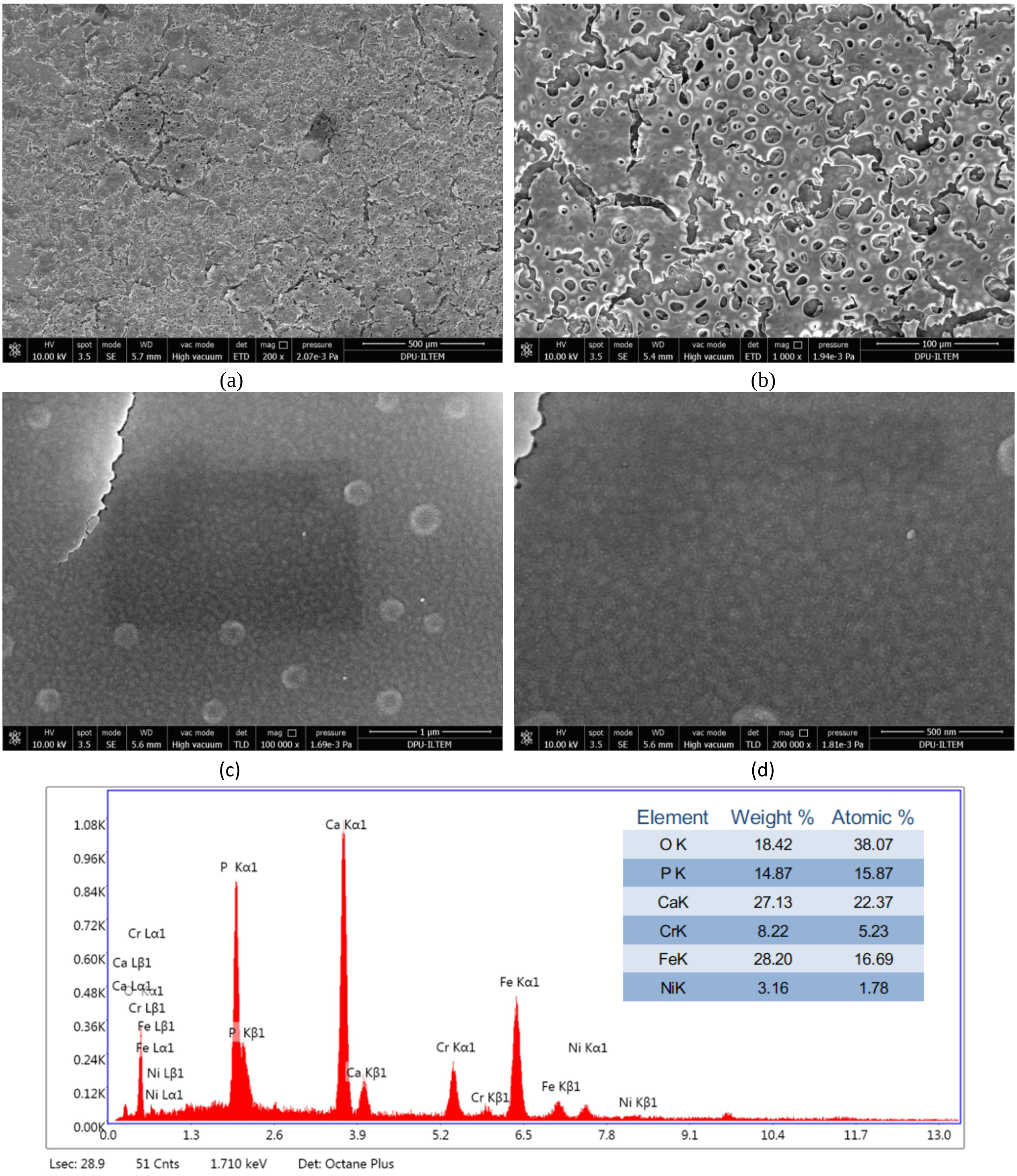

(a) (b) (c) (d)

Element	Weight %	Atomic %
O K	18.42	38.07
P K	14.87	15.87
CaK	27.13	22.37
CrK	8.22	5.23
FeK	28.20	16.69
NiK	3.16	1.78

(e)

Figure 10. SEM images and EDX analysis of the HAP structure coated on the surface of 316L stainless steel.

4. CONCLUSION

Calcium nitrate was obtained with 95% efficiency by reacting the powder obtained from eggshell with nitric acid. It was determined that the same quality HAP was obtained by heat treatment of the sol-gel formed by calcium nitrate obtained from eggshell and commercially available calcium nitrate with triethylphosphite at 500 °C. It has been proven by XRD measurements that the structures obtained are in the HAP structure. 316L stainless steel discs were dip-coated into the sol-gel structure created using calcium nitrate and triethyl phosphite obtained from egg shells, and HAP was formed on their surfaces by calcining at 500 °C. The surface morphology of the created HAP structure was examined by SEM.

Although HAP coating 316L was successfully performed, cracks were observed in the HAP structures coated on the disc surfaces, as seen in previous studies using the sol-gel method. Different approaches must be used to prevent these cracks, which the difference in thermal expansion of 316L stainless steel and HAP materials may cause. In this context, to ensure that 316L stainless steel and HAP materials adhere more firmly to the surface, it is noticed that the alloy must be subjected to preliminary surface treatments and different methods other than sol-gel may need to be used.

Despite this disadvantage, calcium nitrate obtained from eggshell is used for HAP synthesis by different methods in the literature. However, this study has brought a different perspective to the coating of HAPs obtained from eggshells onto 316L using the sol-gel method.

5. CONFLICT OF INTEREST

Author(s) approve that to the best of their knowledge, there is not any conflict of interest or common interest with an institution/organization or a person that may affect the review process of the paper

6. AUTHOR CONTRIBUTION

Determining the research/research method and analyzing of results: Levent Özcan, Adile Şahin, Betül Karabulut, Nagehan Sürük. Conducting experiments and collection of data: Adile Şahin, Betül Karabulut, Nagehan Sürük. Supervision and writing: Levent Özcan.

7. REFERENCES

Ahmed, Y., Rehman, M.A.U., Improvement in the surface properties of stainless steel via zein/hydroxyapatite composite coatings for biomedical applications. Surfaces and Interfaces 20, 100589, 2020.

Asri R.I.M., Harun W.S.W., Hassan M.A., Ghani S.A.C., Buyong Z., A Review of hydroxyapatite-based coating techniques: sol-gel and electrochemical depositions on biocompatible metals. Journal of the Mechanical Behavior of Biomedical Materials 57, 95-108, 2016.

Awasthi S. Pandey S.K., Arunan E., Srivastava C., A review on hydroxyapatite coatings for the biomedical applications: experimental and theoretical perspectives. Journal of Materials Chemistry B 9, 228-249, 2021.

Azem F.A. ve Çakır A., 316L paslanmaz çelik altlıkların üzerine sol-jel tekniği ile amonyak takviyeli çözelti kullanarak hidroksiapatit (HAP) kaplanması. Bilim-Teknoloji 26, 136-143, 2008.

Azem F.A. ve Çakır A., Sol-Jel Yöntemi ile İmplant Kalite 316L Paslanmaz Çelik Üzerine Üretilen Hidroksiapatit Kaplamaların Morfolojisi Üzerine Isıl İşlem Rejiminin Etkisi. Anadolu Üniversitesi Bilim ve Teknoloji Dergisi 10(1), 291-298, 2009.

Ballarre J., Manjubala I., Schreiner W.H., Orellano J.C. Fratzl P., Cere S., Improving the osteointegration and bone-implant interface by incorporation of bioactive particles in sol-gel coatings of stainless steel implants. Acta Biomaterialia 6, 1601-1609, 2010.

Bigi A., Boanini E., Bracci B., Facchini A., Panzavolta S., Segatti F., et al, Nanocrystalline hydroxyapatite coating on titanium: a new fast biomimetic method. Biomaterials 26, 4085-4089, 2005.

Chen GY, Shan R, Shi JF, Yan B.B., Ultrasonic-assisted production of biodiesel from transesterification of palm oil over ostrich eggshell-derived CaO catalysts. Bioresource Technology 171, 428–32 2014.

Chu P.K., Chen J., Wang L., Huang N., Plasma-surface modification of biomaterials. Materials Science Engineering: R: Reports 36, 143-206, 2002.

Ćurković L., Žmak I., Kurajica S., Tonković M. E., Šokčević Z., Renjo, M.M., From eggshells biowaste to hydroxyapatite biomaterial: Von Eierschalen als Bioabfall bis zum Hydroxylapatit-Biomaterial. Materialwissenschaft und Werkstofftechnik 48(8), 797-802, 2017.

Coşkun M., Karahan İ.H., Yücel Y., Optimized Electrode-position concentrations for hydroxyapatite coating on CoCrMo biomedical alloys by computational techniques. Electrochimica Acta 150, 46-54, 2014.

Gurappa, I., Development of appropriate thickness ceramic coatings on 316L stainless steel for biomedical applications. Surface and Coatings Technology 161, 70–78, 2002.

Habibovic P., Barrere F., Van Blitterswijk C.A., de Groot K., Layrolle P., Biomimetic hydroxyapatite coating on metal implants. Journal of the American Ceramic Society 85, 517–522, 2002.

Kaur S., Bala N. and Khoslac C., Characterization of hydroxyapatite coating on 316L stainless steel by sol–gel technique. Surface Engineering and Applied Electrochemistry 55(3), 357–366, 2019.

Kılınç, A. Ç., Ti6Al4V Metal Altlığının Yumurta Kabuğundan Türetilmiş Hidroksiapatit ile Sol-Jel Yöntemi Kullanılarak Kaplanması ve Karakterizasyonu, Dokuz Eylül Üniversitesi Fen Bilimleri Enstitüsü, Yüksek Lisans Tezi, İzmir, 2016.

Kim, H.-W., Kong, Y.-M., Bae, C.-J., Noh, Y.-J., Kim, H.-E., Sol–gel derived fluor-hydroxyapatite biocoatings on zirconia substrate. Biomaterials 25, 2919-2926, 2004.

Lani N.S., Ngadi N., Jusoh M., Mohamad Z., Zakaria Z.Y., Outstanding performance of waste chicken eggshell derived CaO as a green catalyst in biodiesel production: Optimization of calcination conditions. Journal of Physics: Conference Series 1349, 012051, 2019.

Liu D.-M., Yang Q., Troczynski T., Sol-gel hydroxyapatite coatings on stainless steel substrates. Biomaterials 23(3), 691–698, 2002.

Madhu B.J., Bhagyalakshmi H., Shruthi B., Veerabhadraswamy M., Structural, AC conductivity, dielectric and catalytic behavior of calcium oxide nanoparticles derived from waste eggshells. SN Applied Sciences 3, 637, 2021.

Mišković-Stanković V., Eraković S., Janković A., Vukašinović-Sekulić M., Mitrić M, Chan Jung Y., Park S.J., Rhee K.Y., Electrochemical synthesis of nanosized hydroxyapatite/graphene composite powder. Carbon Letters 16(4), 233-240, 2015.

Mohandesnezhad S., Etminanfar M., Mahdavi S., Safavi M.S., Enhanced bioactivity of 316L stainless steel with deposition of polypyrrole/hydroxyapatite layered hybrid coating: Orthopedic applications. Surfaces and Interfaces 28, 101604, 2022.

Mokhtari, A., Belhouchet, H., Guermat, A., In situ high-temperature X-ray diffraction, FT-IR and thermal analysis studies of the reaction between natural hydroxyapatite and aluminum powder. Journal of Thermal Analysis and Calorimetry 136, 1515-1526, 2019.

Narushima, T., Mineta, S., Kurihara, Y., Ueda, K., Precipitates in biomedical Co-Cr alloys. The Journal of the Minerals, Metals & Materials Society (TMS) 65, 489–504, 2013.

Nath D., Jangid K., Susaniya A., Kumar R., Vaish R., Eggshell derived CaO-Portland cement antibacterial composites. Composites Part C: Open Access 5, 100123, 2021.

Navarro, M., Michiardi, A., Castano, O., Planell, J.A., Biomaterials in orthopedics. J. R. Soc. Interface 5, 1137–1158, 2008.

Prabakaran K., Vijayalakshmi U., Rajeswari S., Fabrication, development and characterisation of calcium phosphate based bioceramic coatings on 316L stainless steel for biomedical applications. Surface Engineering 21, 225-228, 2005.

Rezaei, A., Golenji, R.B., Alipour, F., Hadavi, M.M., Mobasherpour, I., Hydroxyapatite/hydroxyapatite-magnesium double-layer coatings as potential candidates for surface modification of 316 LVM stainless steel implants. Ceramic International 46, 25374-25381, 2020.

Rojaee R, Fathi M., Raessi K., Electrophoretic deposition of nanostructured hydroxyapatite coating on AZ91 magnesium alloy implants with different surface treatments. Applied Surface Sciences 285 664-673, 2013.

Sanchez-Hernandez, Z.E., Dominguez-Crespo, M.A., Torres-Huerta, A.M., Onofre-Bustamante, E., Adame, J.A., Dorantes-Rosales, H., Improvement of adhesion and barrier properties of biomedical stainless steel by deposition of YSZ coatings using RF magnetron sputtering. Materials Characterization 91, 50–57, 2014.

Song Y.W., Shan D.Y., Han E.H., Electrodeposition of Hydroxyapatite Coating on AZ91D magnesium alloy for biomaterial application. Material Letters 62, 3276-3279, 2008.

Sutha, S., Kavitha, K., Karunakaran, G., Rajendran, V., In-vitro bioactivity, biocorrosion and antibacterial activity of silicon integrated hydroxyapatite/chitosan composite coating on 316L stainless steel implants. Materials Science and Engineering C 33, 4046–4054, 2013.

Tan Y.H., Abdullah M.O., Nolasco-Hipolito C., Taufiq-Yap Y.H., Waste ostrich- and chicken-eggshells as heterogeneous base catalyst for biodiesel production from used cooking oil: Catalyst characterization and biodiesel yield performance. Applied Energy 160 58–70, 2015.

Tangboriboon, N., Kunanuruksapong, R., Sirivat, A., Kunanuruksapong, R., Sirivat A., Preparation and properties of calcium oxide from eggshells via calcination. Materials Science. Poland 30 313–322, 2012.

Toygun Ş., Köneçoğlu G., Kalpaklı Y. General principles of sol-gel. Sigma Journal of Engineering and Natural Sciences 31, 456-476. 2013.

Wei M., Ruys A.J., Swain M.V., Milthorpe B.K., Sorrell C.C., Hydroxyapatite-coated metals: Interfacial reaction during sintering. Journal of Materials Science: Materials in Medicine 16, 101-106, 2005.

Yazdani, J., Ahmadian, E., Sharifi, S., Shahi, S., Dizaj, S.M., A short view on nanohydroxyapatite as coating of dental implants. Biomedicine & Pharmacotherapy 105, 553-557, 2018.

Yazıcı, M., Çomaklı, O., Yetim, T., Yetim, A.F., Çelik, A., The effect of plasma nitriding temperature on the electrochemical and semiconducting properties of thin passive films formed on 316L stainless steel implant material in SBF solution. Surface and Coatings Technology 261, 181–188, 2015.

Zhang J.X., Guan R.F., Zhang X.P., Synthesis and characterization of sol-gel hydroxyapatite coating deposited on porous NiTi Alloys. Journal of Alloys and Compounds 509, 4643-4648, 2011.

Zhong Z., Qin J., Ma J., Cellulose acetate/hydroxyapatite/chitosan coatings for improved corrosion resistance and bioactivity. Materials Science and Engineering: C 49, 251-255, 2015.

Zhou Z., Zheng B., Gu Y., Shen C., Wen J., Meng Z., Chen S., Ou J., Qin A., New approach for improving anticorrosion and biocompatibility of magnesium alloys via polydopamine intermediate layer-induced hydroxyapatite coating. Surfaces and Interfaces 19, 100501, 2020.

JOURNAL of
MATERIALS and MECHATRONICS:A

e-ISSN 2717-8811
JournalMM, 2024, 5(2), 228-249
https://doi.org/10.55546/jmm.1496963

Araştırma Makalesi / Research Article

Development and Application of A Wearable Technology Product That Detects and Informs The Presence of Electrical Energy

Burak BOĞAZKESENLİ[1], Aytaç Uğur YERDEN[2*]

[1] İstanbul Gedik Üniversitesi, Lisansüstü Eğitim Enstitüsü, İş Sağlığı ve Güvenliği Ana Bilim Dalı, Tezli Yüksek Lisans Öğrencisi, İstanbul, Türkiye,
ORCID ID: https://orcid.org/0009-0000-6143-1080, bb.burak@hotmail.com
[2*] İstanbul Gedik Üniversitesi, Mühendislik Fakültesi, Endüstri Mühendisliği Bölümü, İstanbul, Türkiye,
ORCID ID: https://orcid.org/0000-0002-3886-802X, aytac.yerden@gedik.edu.tr

Geliş/ Received: 06.06.2024; **Revize/Revised:** 21.08.2024 **Kabul / Accepted:** 26.08.2024

ABSTRACT: Electrical energy has both positive and negative effects nowadays, with the potential to cause property and human loss. Technical professionals working at electrical energy generation, distribution, and utilization points may die due to carelessness or neglect. Although there are protection elements (fuses, residual current protection relays, etc.) in electrical panels that interrupt the flow of electrical energy in the event of a shock, there may be working areas where energy cannot be cut off due to incorrect electrical connections caused by unauthorized people interacting with the panel. Existing protective components may be insufficient. The experiments include both wired protection elements and wireless detection elements. However, they need to be enhanced because they have limited detection distances. Furthermore, using an ergonomic design can improve operability. New protection and warning features must be designed using developing technology. To prevent employees from being shocked by being exposed to electrical energy in the workplace, AC voltage can be detected without contact using this study, which includes the design and test results of a wearable technology product that warns when electricity is present. An electrical circuit that technical staff can wear on their finger detects voltage without contact and displays the existence of energy with a red LED. It was discovered that the test circuit detects 230V AC electrical energy up to 8 cm away and warns with light.

Keywords: Non-Contact voltage detection, Wearable technology, Voltage detector, Non-Contact Voltage Detector.

---

*Sorumlu yazar / Corresponding author: aytac.yerden@gedik.edu.tr

Bu makaleye atıf yapmak için /To cite this article

Boğazkesenli, B., Yerden, A. U. (2024). Development and Application of A Wearable Technology Product That Detects and Informs The Presence of Electrical Energy. Journal of Materials and Mechatronics: A (JournalMM), 5(2), 228-249.

1. INTRODUCTION

Technologies for producing and distributing energy have advanced quickly since the discovery of electrical energy. The areas of use of electrical energy have expanded and become indispensable for life. Some of the main reasons for this development are the easy production and distribution of electrical energy and the proliferation of devices that use this energy over the years. Electrical energy is a type of energy that can be produced quickly, transmitted quickly, and used stably. Today, many energy sources can be converted into electrical energy. Thanks to these features, it is the most popular and widely used type of energy. However, it is not without its dangers. It even has effects that can be fatal if not taken care of. Of course, the critical point here is "if not careful". In the study (Ceylan, 2012), it is stated that approximately 7% of the personnel working at TEIAŞ are regularly trained in Occupational Health and Safety (OHS) every year, and it is thought-provoking that approximately 69% of the employees are exposed to accidents had received OHS training before. No matter how trained the technical personnel are, carelessness and similar reasons can always cause accidents with negative consequences. There is a threat at every point where electrical energy is generated, distributed, and converted into work and used with various devices. Electrical energy, an energy source that can cause loss of life and property as a result of poor workmanship and carelessness, is a resource that needs to be used with care and caution and be efficient and valuable.

Electrical science tells us to follow "Occupational Health and Safety" regulations despite all these dangerous features. For this reason, we must produce, distribute, and use this indispensable energy source by the established rules. Every person must comply with these rules at every point where electrical energy exists so that the measures taken will work. However, there may be direct exposure to electrical energy due to ignorance, poor workmanship, and carelessness. There can be a wide variety of reasons here. For example, in cases such as an employee working in the electrical panel where he works as a result of fatigue without cutting the energy or the energy of the panel is turned on by another employee without the knowledge of the technician working in the electrical panel, life and property damages and even loss of life may occur. In such cases, although there are protection elements in the panels and devices, there may be situations where they cannot prevent loss of life and property. Among these protection elements, the "Residual Current Protection Relay", which protects living beings, may not be used in many facilities, production sites, offices or residential units even today, when technology is developing. Alternatively, with the view that it will take a very short time, an electrical fault can be eliminated by working under energy.

Protection elements directly connected to the system with the cable are widely used worldwide to protect against the harmful effects of electrical energy. These systems include elements that open the line in case of shock, short circuit, etc. However, this form of protection may not be able to protect against damages that may occur due to non-standard equipment installations by unauthorized persons other than the elements connected to the electrical system by cable. Wireless remote monitoring systems are used in electricity generation and distribution points today. Instant data of the entire system can be obtained from the control center. However, there is no monitoring in places such as factories, homes, and schools where the end user is located. This situation brings many non-standard electricity usages. Centralized remote monitoring of the end user's electricity system is also costly. Therefore, there is a need for new protection equipment that can prevent the harmful effects of electrical energy from harming living things in many cases.

The main reason for this study is that employees are not exposed to working under electricity for various reasons (troubleshooting, etc.); if there is electrical energy in the area where they work (for example, an electrical distribution panel) and they are not aware of it, it is to make an efficient design for a wearable technology product that instantly notifies the employee of the presence of this electricity. The most efficient electronic circuit design and ergonomics were analyzed for the design to make it a wearable technology product.

2. LITERATURE REVIEW

The Tosun (2022) states that the causes of electrical accidents can be listed as accidents caused by insulation defects, accidents caused by electrical leakage and electrical charging of the metal parts of the devices, accidents that may occur as a result of contact with energy transmission channels, accidents occurring on or near power poles, accidents caused by work performed near live areas, hazards caused by explosions and accidents caused by short circuits in power lines. It is also stated that the source of this problem for our country is generally due to insulation failure and irregular controls (Tosun, 2022). According to the study (Mutlu & Cabuk, 2021), although there are many different causes of occupational accidents, 80% of them are caused by the defects of the employees. (Ates et al., 2019) stated that the most important method of protection from occupational accidents caused by electrical energy is to prevent them before they occur. Karadeniz (2012) reported that occupational health and safety inspections and legislation are inadequate in Asian countries, especially China and India (Karadeniz, 2012). The most common cause of accidents is electrical leakage in machinery and devices. Accidents caused by insulation faults follow this. In the electricity distribution sectors in Turkey, the most common accidents caused by electricity are people's exposure to active electric currents, falls from heights, cave-ins during underground cable work, and fires and arc explosions. For such reasons, new protection elements or measures are implemented with the developing technology. The rapid development of technology is becoming one of the most essential tools of sustainability (Karabiyik Yerden, 2023). Every measure or technology put into practice gains functionality with employees' awareness. However, if technological, occupational health, safety measures, and employee awareness are used together, this highly efficient energy source can be used healthily.

The ergonomic functionality of a wireless technology that senses and reports the presence of electrical energy is as necessary as its construction. Today, there is a wide range of research on wearable technologies. Pamuk and Yildiz (2021) reported that electrically conductive textile products are used in fields such as industry, space, military, protection, defense, and health (Pamuk & Yildiz, 2021). Wearable tissue technology products placed on and under the skin and their use, especially in health-related areas, were mentioned (Turkcan, 2021).

With the development of technology, there have been new studies on wireless voltage sensing. For example, a control pen can wirelessly indicate the presence of electrical energy in a conductor or metal surface over short distances. However, there are also disadvantages, such as short distances and ergonomic non-functionality. Since it only provides control when the device is operated, it has no continuity. It cannot perform instant monitoring.

Wireless voltage-sensing wearable technology products can also perform instantaneous monitoring. For example, the design shown below is designed as a wristband, making it ergonomically functional. In the study conducted at the University of Miami, detection was made using capacitive principles. It is designed for 120V voltage detection. There is a certain detection distance. The study states that it can make erroneous detection.

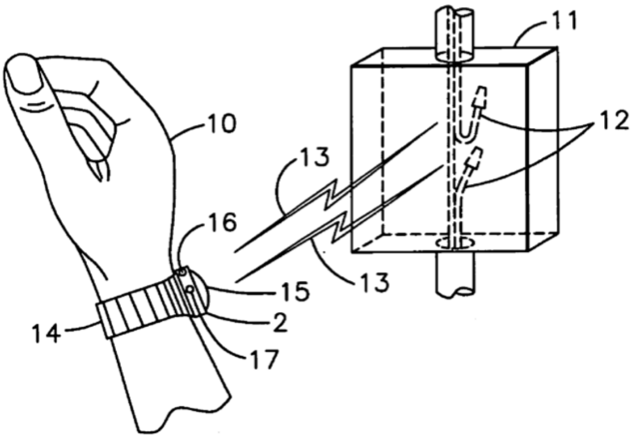

Figure 1. Patent for a wrist-wearable voltage detector (Crockett)

Some studies can perform remote wireless voltage sensing in high-voltage systems. The block diagram of a design designed with micromechanical systems (MEMS) technology that can detect the presence of energy in the conductor at a distance of 2 meters is given below. The wireless analog signal received from the sensor is converted into a digital signal and processed. It can be monitored with the alarm circuit and communication module.

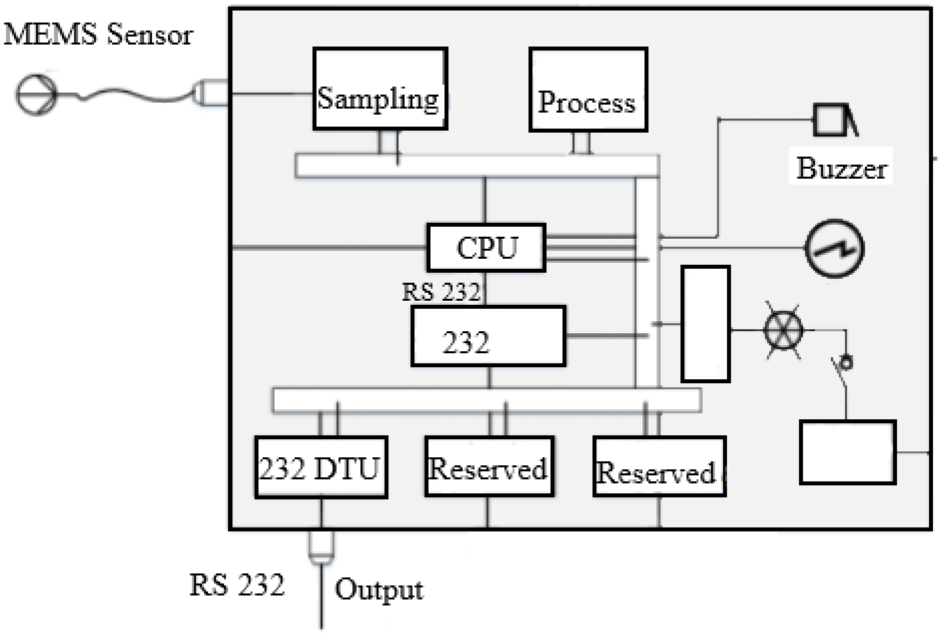

Figure 2. Block diagram of a contactless voltage detector (Zhu et al., 2018)

Some designs wirelessly report the presence and level of voltage. The image below shows a design that can wirelessly measure the amplitude of the voltage on transmission lines and works with electric field sensing.

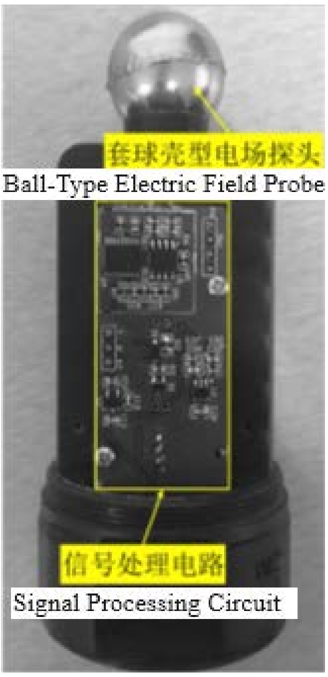

Figure 3. Electrical tester prototype (Yang et al., 2021)

Similar studies are also available. However, few studies are ergonomically available to technical personnel.

Wearable smart devices defined as; "Wearable technology", "wearable device" and "wearables" are all electronic or computer technologies that represent accessories and clothing that can be worn comfortably on the body" (Sagbas et al., 2016). As we can understand from the definition of wearable technologies, we can consider the essential design elements for these electronic-based devices under three main headings.

- Energy source
- Electronic-based functionality
- Comfort in the body (Ergonomics)

The battery is one of this work's most critical design parts and must be produced in small sizes. If a non-ergonomic battery is used for the design, it becomes cumbersome and defeats its purpose. The battery is one of the most essential parts necessary for the design to work by providing the appropriate voltage for the circuit. There are many battery technologies from the past to the present. These battery technologies mainly work on generating electrical energy from chemical reactions. However, some systems generate electrical energy using different energy sources. In order to produce electrical energy generated by the movement of electrons in the atomic structures of objects, a wide variety of methods are used to provide this movement. There are many ways to store energy (Kozak & Kozak, 2012). Electrical energy storage is one of them. The most efficient energy storage system is electrical energy storage with superconducting magnetic energy storage with an efficiency of 0.97. However, this method does not seem suitable for battery technology, which is also essential for its economic use in daily life. Rechargeable batteries under the following headings examined: Lead Acid Batteries, Nickel Cadmium Batteries, Nickel Zinc Batteries, Nickel-Metal Hydride Batteries, Lithium Ion Batteries, Lithium-Sulfur Batteries, Sodium-Ion Batteries, and Metal-Air Batteries. These batteries can be charged for continuous use. They are based on chemical reactions. Lithium-ion batteries seem the most promising for future development (Sezer et al., 2022). However, aside from the extensive use of chemical-based batteries in the market, there is a wide range of renewable and promising battery and power generation technologies based on various principles. They are both miniaturizable and renewable energy, which may mean we will soon use them widely instead of chemical-based batteries.

Thermoelectric generators (TEJ) generate electricity from body heat. This technology uses the temperature difference between skin heat and air to generate energy. It is a technology that can be used in this study as it is sustainable and can be produced in small sizes. Thermoelectric modules work with the Seebeck effect (Mamur, 2013). According to the 2nd Law of Thermodynamics, heat moves from the hot surface to the cold surface. In this way, DC voltage will occur at the TEJ terminals.

One of the studies carried out in recent years is to generate electrical energy using moisture in the air. Since moisture is everywhere, this method can be used for many systems without the problem of finding resources. Electrical energy can be generated with moisture in the air using protein nanoconductors (Liu et al., 2023). This system was named Air-Gen. This battery technology can be used in this study due to its small size and sustainability. The figure below shows the use of protein nanoconductors.

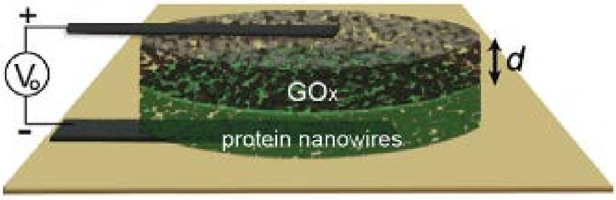

Figure 4. The use of protein nanoconductors as the basis of Air-Gen technology (Liu et al.,2023)

From a different perspective, supercapacitors are also shown as an energy source that can be used for wearable technology products. Li from the University of South Carolina produced a T-shirt that works like a supercapacitor (Korkmaz, 2018). He stated that a T-shirt from the store was immersed in fluoride solution and then produced at a high temperature in an oxygen-free environment. The surfaces of the clothing fibers turned into activated carbon, exhibiting supercapacitive behavior. He obtained a highly efficient solar cell with the paint he applied on flexible fabric (Eker, 2019). Such studies open the horizon for making flexible, ergonomic, and efficient energy sources for wearable technologies. One of the critical points in wearable technology products, such as the power supply, is the need for comfortable use on the body. Here, we come across the concept of ergonomics. Ergonomics is adapting the physical environment to human beings (Ertan & Eldem, 2022). Ergonomics can be created by working together with more than one discipline. At the beginning of these disciplines: engineering, physiology, anatomy, sociology, psychology, and architecture. In this study, the design was made as a ring to provide this feature. Today, athletes use wearable technologies with ring designs. Smart rings are designed to suit daily life with a sports-oriented perspective (Turgut et al., 2021). In this respect, we can conclude that the ring design is also suitable for this study. Because those who work with electrical energy, such as those who do sports activities, want to use their hands comfortably. In order to realize a design that is ergonomically small in size, the electronic circuit must also be small. While the size of a typical transistor was between 130 and 250 nanometers at the turn of the century, in 2016, a team of researchers at Lawrence Berkeley National Laboratory succeeded in making a 1-nanometer transistor using "carbon nanotubes" and "molybdenum disulfide (MoS2)" and that this transistor was the smallest transistor ever made (Ersoz et al., 2018). Such studies play an essential role in realizing ergonomically favorable and small-sized designs as they reduce the size of electronic circuits.

3. MATERIALS AND METHODS

The progress of the work was as follows: First, the characteristics of the environment in which the non-contact voltage would be detected were examined. Then, a detection circuit was designed and tested based on these characteristics. The results of the prototyped work were shared according to the test results.

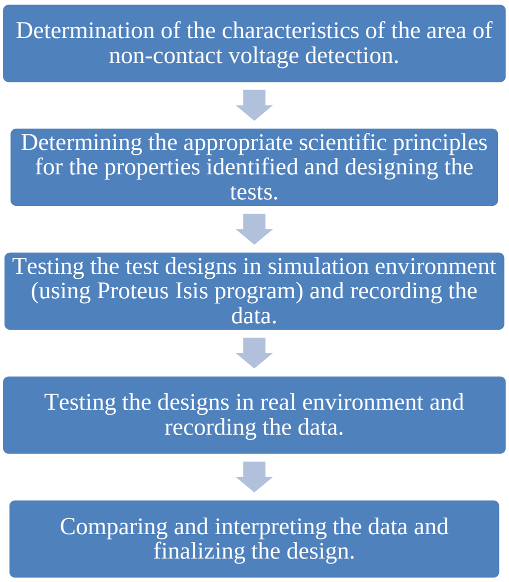

Figure 5. Progress of the study

When we look at the power line standards used in the world to reveal the characteristics of the environment to be measured for non-contact voltage sensor design, we see that various voltage and frequency values are adopted as standards in the networks in countries. In our country, the mains voltage is 230V, and the mains frequency is 50Hz. The voltage level varies to increase energy production and distribution efficiency. High voltage levels of 66kV, 154kV, 380kV, and medium voltage levels of 6.3kV, 15kV, and 33kV are used in the distribution of electrical energy. In end-user distribution panels, 400V and 230V are used. Since technical workers mainly encounter 220V and 380V in distribution panels, these will be the measurement values on which we will base our design. In addition, our primary frequency of 50 Hz is the other variable we will base on. The scientific calculations used in the study are essential for selecting electronic circuit elements for circuit design. Ambient AC voltage for operation: Since the frequency is 50 Hz, it should be designed to be sensitive to this frequency. However, since the operation will perform contactless detection, the circuit will receive this signal with the help of an antenna. At this point, it is necessary to design an antenna. Among omnidirectional antennas, the monopole antenna can be used for energy detection because the direction of the signal to be detected may not be the only one. This antenna design can detect omnidirectional signals. However, when the antenna length is calculated for the frequency under study,

$$\lambda = \frac{c}{f} = \frac{300\,000}{50} = 6\,000\,mt \quad (1)$$

$$\lambda \times 0.95 = 5\,700\,mt \quad (2)$$

$$\text{Antenna length} = 5\,700 \,/\, 4 = 1\,425 \text{ meters} \quad (3)$$

f : Transporter frequency

c : Speed of light ≈ 3× 〖10〗 ^8 m/s

λ : Carrier wavelength (carrier wavelength: λ=c/f)

This is unlikely for a small wearable technology product. Therefore, the antenna input signal will be calculated according to the capacitive effect in the antenna design. For the capacitive effect, the point with electrical energy can be considered as the capacitor conductor plate, the antenna of the testing circuit as the other plate, and the air in between as the insulator material. When the antenna of the non-contact voltage detector approaches the conductor, a capacitance is formed between them, and we can find the amplitude of the current in the antenna using the following calculation.

One turn around the coil;

$$\mathrm{a} = 2\pi\mathrm{r} = 2 \text{ x } \pi \text{ x } 0.05 = 0.0314 \quad (4)$$

Surface area;

$$\mathrm{A} = \text{Number of coil rounds x a} = 15 \text{ x } 0.0314 = 0.471 \text{ m}^2 \quad (5)$$

Capacity calculation (for a distance of 4 cm);

$$\mathrm{C} = \frac{\mathrm{A} \text{ x } \varepsilon_0}{\mathrm{d}} = \frac{0.471 \text{ x } 8.85 \text{ x } 10^{-12}}{0.04} = 0.1042 \text{ nF} \quad (6)$$

Capacitive reactance;

$$\mathrm{Xc} = \frac{1}{2\pi \mathrm{fC}} = \frac{1}{2\pi \text{ x } 50 \text{ x } 0.1042 \text{ x } 10^{-9}} = 30.5479 \text{ x } 10^6\ \Omega \quad (7)$$

Current to be generated in the coil (for 230V);

$$\mathrm{Ic} = \frac{\mathrm{V}}{\mathrm{Xc}} = \frac{230}{30.5479 \text{ x } 10^6} = 7.5291\ \mu\mathrm{A} \quad (8)$$

This calculated current value is the current value that will occur when the antenna with 15 turns and 1 cm diameter is 3 cm close to a 230V conductor. Also, for this current value to occur, the magnetic field strength in the conductor;

$$\mathrm{B} = \mu 0 \frac{\mathrm{N} \text{ x } \mathrm{I}}{\mathrm{L}} = \frac{4\pi \text{ x } 10^{-7} \text{ x } 7.5291 \text{ x } 10^6}{0.02} = 7.09601 \text{ x } 10^{-9} \text{ T} \quad (9)$$

a = Perimeter area of a single turn

A = Surface area

C = Capacity
E0 = Electric constant
d = Distance between plates
Xc = Capacitive reactance
f = Frequency
V = Voltage
I = Current
µ0 = Magnetic constant
N = Number of turns (Number of rounds)
L = Length of the coil (antenna)

If this calculated current value is applied to similar network voltage values in our country, the values in the table below are calculated.

Table 1. Current and required magnetic field values calculated according to voltage level

Voltage (V) AC	Current (µA)	Magnetic Field (T)
230	7.5291	7.09601x 10^{-9}
400	13.09	1.2337x 10^{-8}
480	15.71	1.48063x 10^{-8}
600	19.64	1.85103x 10^{-8}

The antenna shape to be used will be in the form of a solenoid coil. A spiral shape will also be used to increase the current in the antenna. The small current value generated in the antenna will be amplified in the transistors connected to the Darlington. It will be large enough to feed the warning elements such as LED, Buzzer. Circuits with two and three transistors were tested. In the circuit, several different transistor models were tested to increase the current in the antenna, and the efficient model was preferred. The block diagram of the designed circuit is as follows (Figure 6). As can be seen from the schematic, the signal from the antenna stage is amplified at the Darlington transistor stage and transmitted to the output stage. The LED at the output stage illuminates with sufficient antenna input signal to indicate the presence of electrical energy.

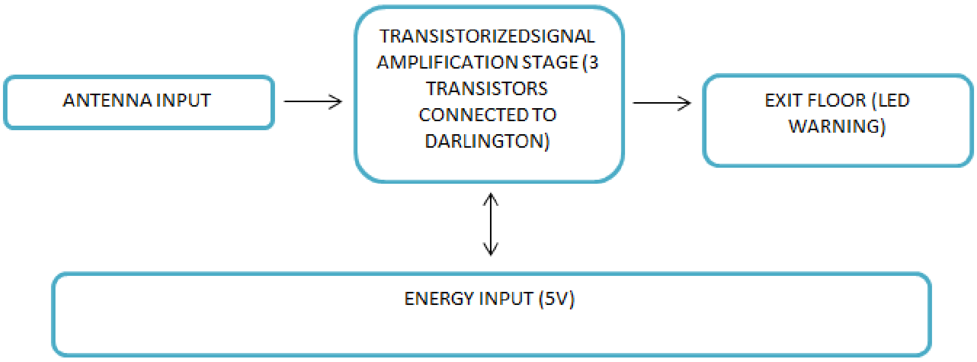

Figure 6. Block diagram of the circuit

When the transistors are connected in Darlington, the total current gain can be written as the product of the current gains of the individual transistors. For two transistors, when the transistor models used are the same beta kare, and for three transistors, β^3 can be written as.

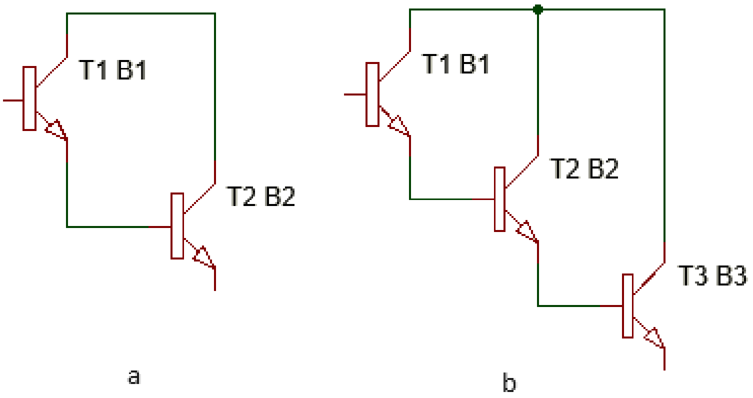

Figure 7. a) Two transistor darlington connection β^2, b) Three transistor darlington connection β^3

In the test circuit where two transistors are connected to Darlington, a detection test will be performed at the point where 220V voltage is present using "2N3004" and "BC547" transistors and a 15-turn wound antenna. The detection range will be found by changing the distance of the antenna to the conductor. The first test circuit is given in Figure 8.

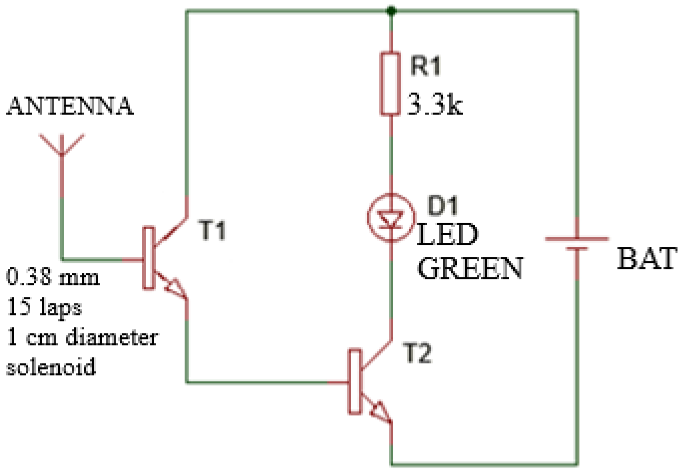

Figure 8. Test circuit for two transistor darlington connection (test circuit 1)

The second test circuit uses "2N3904" and "BC547" transistors with three transistor Darlington connections. The tests will be performed with the conductor carrying energy at a 230V voltage level. A 15-turn wound solenoid coil is used as an antenna. The second test circuit is given in Figure 9.

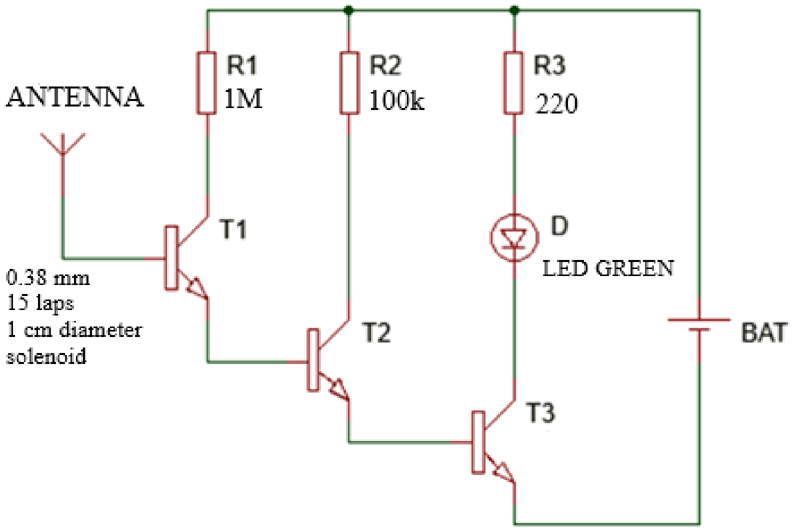

Figure 9. Test circuit for three transistor darlington connection (test circuit 2)

In both test circuits, the flattened antenna and the solenoid coil antenna will be tested. The characteristics of the selected transistors are close to each other. When we look at the information page of both transistors, β current gains according to the "Base" current calculated above is given as 100 on average. According to this, the total average current gain in a two-transistor Darlington connection;

β^2 = 100 x 100 = 10000

And the total average current gain in a three-transistor Darlington connection;

β^3 = 100 x 100 x 100 x 100 = 1000000.

The operation of the test circuits is shown in the flowchart in Figure 10.

According to the detection results of the test circuits in the simulation environment, the efficient circuit design will be used in the real environment test. The data obtained from the simulation are given in Table 2 and Table 3.

The designed circuits were tested in the simulation environment (Proteus Isis) at the calculated antenna current level and upper and lower values, and the output currents were measured. The LEDs connected to the output transistors were observed, and the data was recorded in Tables 2 and 3.

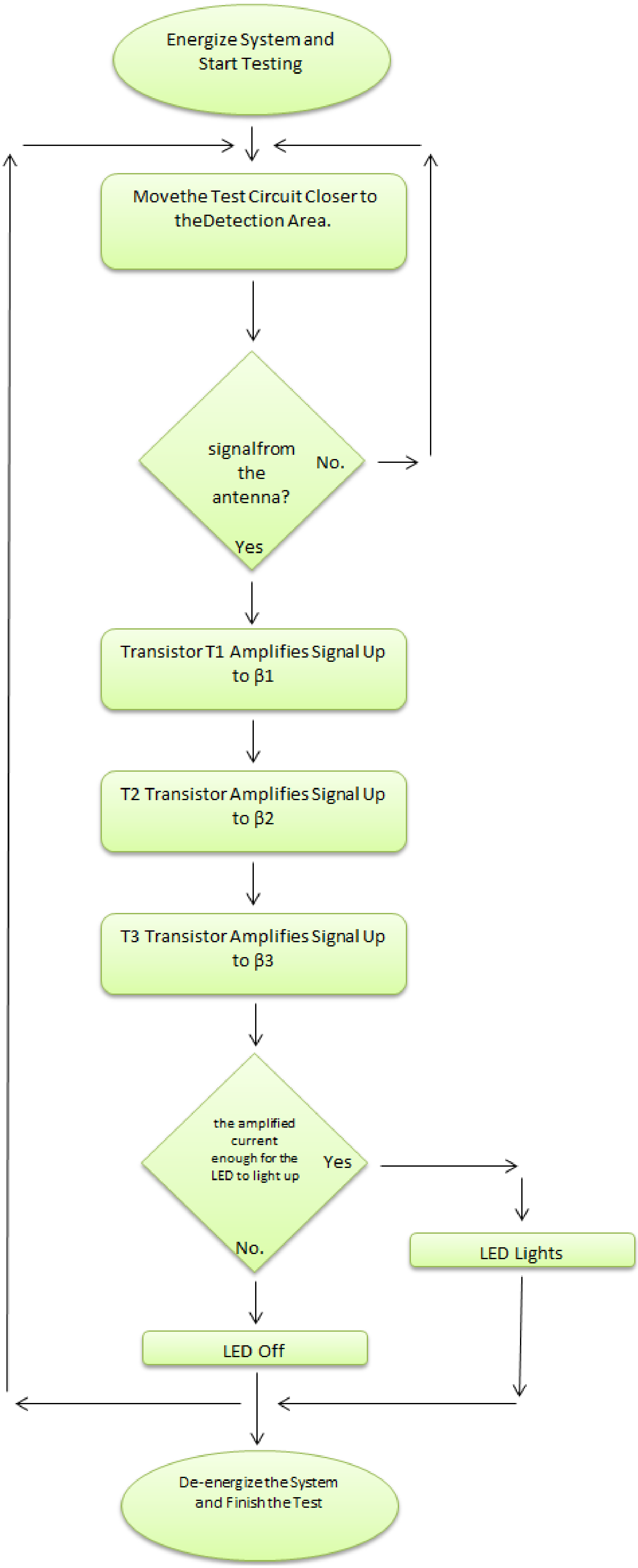

Figure 10. Flow diagram of the test circuit operation algorithm

Table 2. Measurements with test circuit 1

Test Circuit 1				
Supply Voltage 5V	2N3904		BC547	
	Output Current (mA)	LED Status	Output Current (mA)	LED Status
Ib1 Antenna Current (5µA)	0.84	FIRE ON FIRE	0.84	FIRE ON FIRE
Ib1 Antenna Current (7.5291µA)	0.85	FIRE ON FIRE	0.85	FIRE ON FIRE
Ib1 Antenna Current (10µA)	0.85	FIRE ON FIRE	0.85	FIRE ON FIRE
Ib1 Antenna Current (15µA)	0.85	FIRE ON FIRE	0.85	FIRE ON FIRE
Ib1 Antenna Current (20µA)	0.85	FIRE ON FIRE	0.85	FIRE ON FIRE

According to the measurements made in the simulation environment, the second test circuit with three Darlington-connected transistors has a higher current gain than the Darlington-connected circuit with two transistors. Therefore, the LED connected to the "Collector" end of the transistor T3 lights up more strongly. This shows us that test circuit 2 works more efficiently. Real-earth experiments will proceed through this circuit.

Since the transistor models are close to each other, they gave similar results. Of the two transistors, 2N3904 was chosen for the test.

Test circuit 2 will be used for a real-world test. For the test, the test circuit will be brought closer to the conductor line energized at a 230V voltage level at certain distances, and the detection limits of the circuit will be determined. In addition, the operating efficiency of the circuit will be measured in terms of the distance between a solenoid antenna and a spiral antenna.

Table 3. Measurements with test circuit 2

Test Circuit 2				
Supply Voltage 5V	2N3904		BC547	
	Output Current (mA)	LED Status	Output Current (mA)	LED Status
Ib1 Antenna Current (5µA)	10.2	BURNED	10.2	BURNED
Ib1 Antenna Current (7.5291µA)	10.3	BURNED	10.3	BURNED
Ib1 Antenna Current (10µA)	10.4	BURNED	10.4	BURNED
Ib1 Antenna Current (15µA)	10.5	BURNED	10.5	BURNED
Ib1 Antenna Current (20µA)	10.5	BURNED	10.5	BURNED

The test circuit was installed on a breadboard, and 15 turns of wound solenoid coil were used as an antenna.

The flow diagram of the sequence to be applied for the test is as follows.

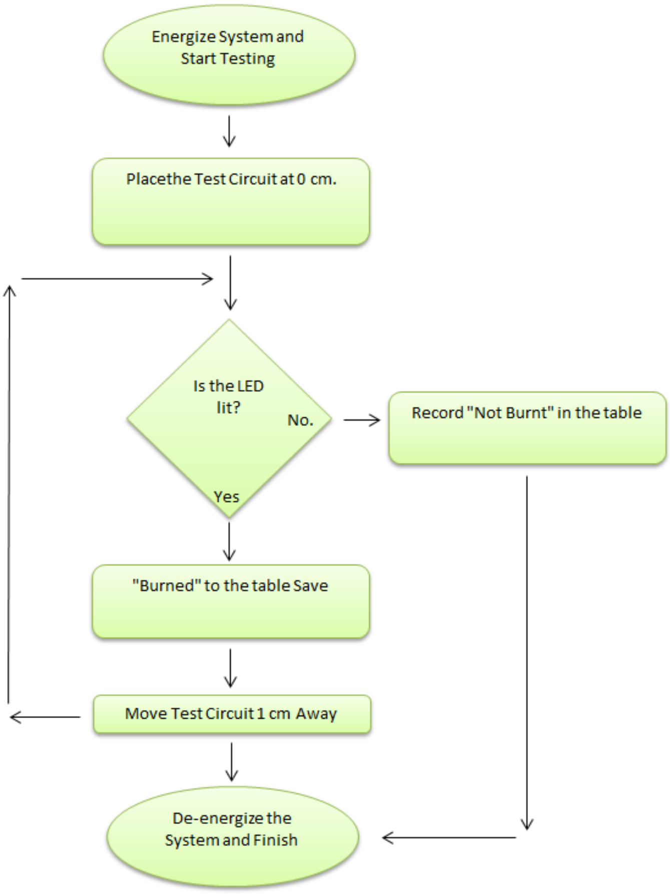

Figure 11. Flow diagram to be applied for testing

According to the flow diagram, the test circuit, which will be removed from the conductor passing electrical energy with a precision of 1 cm, will be tested with LED until it does not react. The results are shared in Table 4. During the test, the stable operation of the circuit will also be observed and recorded in the table.

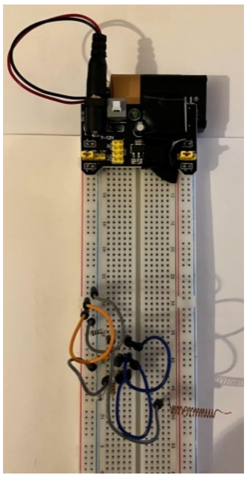

Figure 12. Test circuit (solenoid antenna)

Figure 12 shows the test circuit installed on the breadboard. The circuit made using "2N3904," selected as a transistor, is at the bottom of the breadboard. On the top side, a source is connected to energize the circuit.

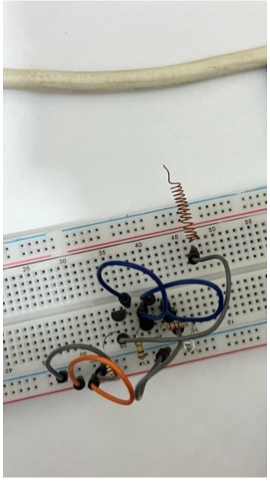

Figure 13. Test setup

Figure 13 shows the circuit's test setup. A meter measures the distance of the antenna to the conductor passing electrical energy.

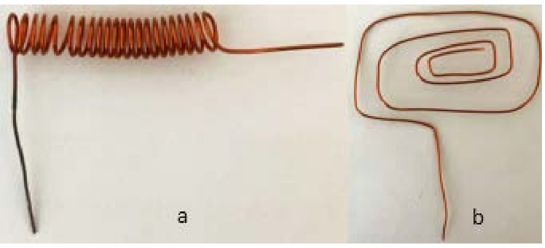

Figure 14. a) Solenoid antenna, b) Spiral antenna

Figure 14 shows the antennas used during the test.

The test circuit was tested by positioning the solenoid coil antenna at specific distances from the conductor with 230V AC electrical energy with the help of a meter. The power was cut and checked to see whether it was affected by a source other than the current on the conductor. It was also tested using a spiral antenna. The test circuit was brought closer to the conductor, passing 230V AC energy at certain distances. The LED's burning and non-lighting status was observed, and the range in which it can be measured was determined. The data obtained are presented in Table 4. According to the measurement results of the test circuit, the tests with the solenoid coil antenna were more successful than the tests with the spiral antenna. It was able to detect the presence of voltage at a longer distance. According to the circuit test with a solenoid coil antenna, stable operation up to 8 cm was achieved.

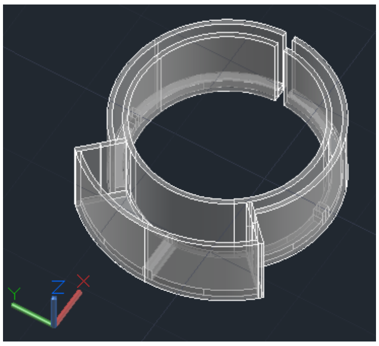

Figure 15. Ring-shaped wireless voltage sensing circuit design (Representative AutoCAD drawing)

Figure 15 shows a computer drawing of the design of this study. The drawing was drawn in the size of an average human finger. Thanks to the space left at the bottom of the ring shape, it has a design that can easily fit different finger sizes. The designed circuit will be placed in the ring shape printed from PLA material.

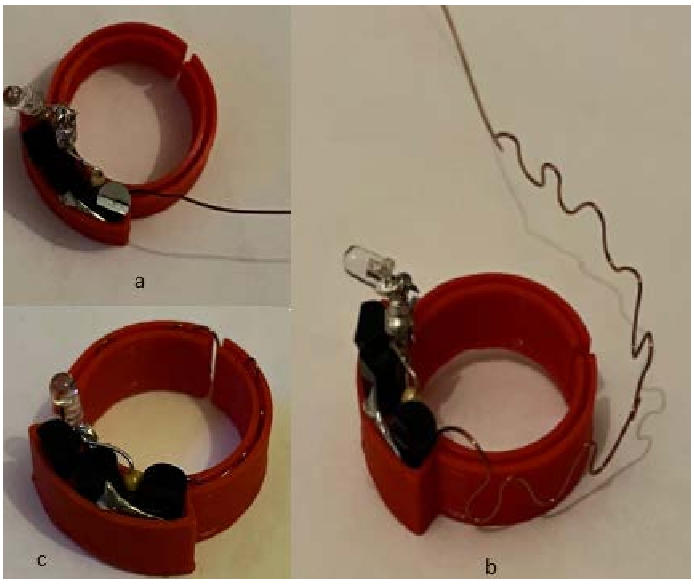

Figure 16. a) Placement of the sensing circuit in the design, b) Shaping the circuit antenna, c) Placement of the circuit antenna in the ring

As can be seen in the images given in Figure 16, the circuit that senses energy wirelessly was printed on a 3D printer in the shape of a ring. The area where the circuit is placed is at the top of the ring shape. The antenna for sensing was placed on the ring parts surrounding the finger.

Figure 17. Use of the design on the finger

Figure 17 shows a visual of the design in human hand. It shows that it is an ergonomic design thanks to its shape and dimensions that will not restrict hand and finger movements.

4. RESULTS AND DISCUSSION

The detection status of the test circuit according to the distance is given in Table 4.

Table 4. Physical environment test results

-Test Voltage AC 230V **-Test Circuit Supply DC 5V**		
	Solenoid Antenna	Spiral Antenna
Distance to Conductor (cm)	Detection Status of the Circuit According to the Lighting of the LED (Stable, Unstable, Very Unstable)	
1	Stable Operation	Stable Operation
2	Stable Operation	Stable Operation
3	Stable Operation	Worked Undecided
4	Stable Operation	X-No Detection
5	Stable Operation	X-No Detection
6	Stable Operation	X-No Detection
7	Stable Operation	X-No Detection
8	Stable Operation	X-No Detection
9	Stable - Unstable	X-No Detection
10	Stable - Unstable	X-No Detection
11	Worked Undecided	X-No Detection
12	Worked Undecided	X-No Detection

13	Worked Undecided	X-No Detection
14	Worked Undecided	X-No Detection
15	Worked Undecided	X-No Detection
16	Worked Undecided	X-No Detection
17	Worked Undecided	X-No Detection
18	X-No Detection	X-No Detection

As a result of the test, the solenoid coil antenna successfully detected up to 8 cm. At 9 and 10 cm, it was stable in some trials and unstable in others. In the spiral antenna design, stable measurements could be made up to 2 cm. According to these results, the use of solenoid antenna gave positive results. According to the test results, the 2nd test circuit and the solenoid antenna will be evaluated.

The SWOT analysis based on the test results is as follows.

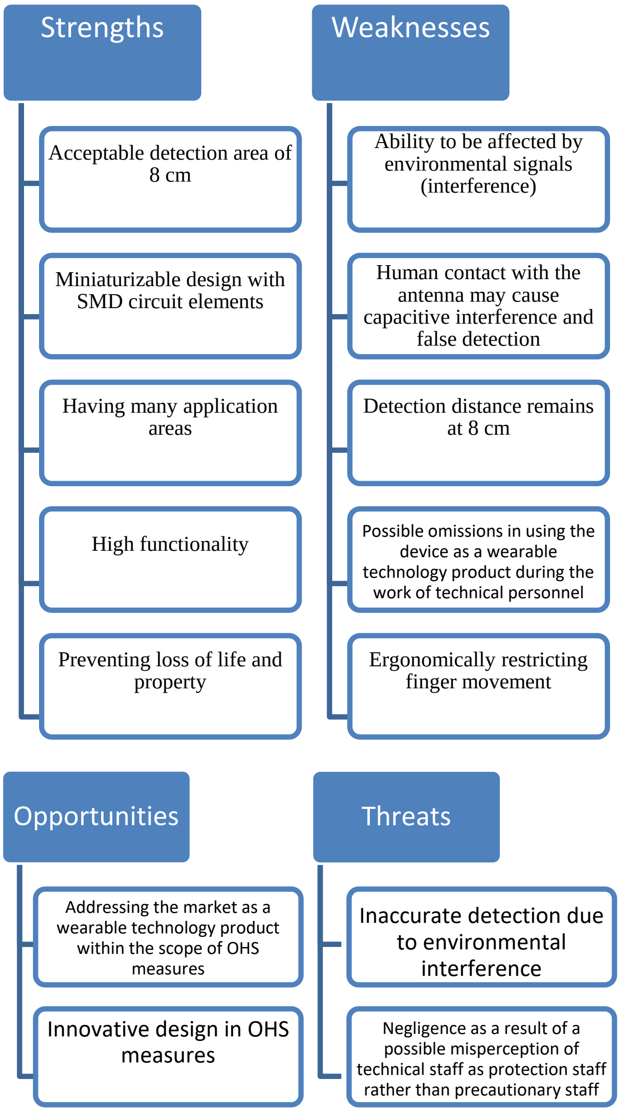

Figure 18. SWOT analysis of the study

As can be seen from the analysis, the design has the potential to be used in the form of an ergonomically appropriate ring.

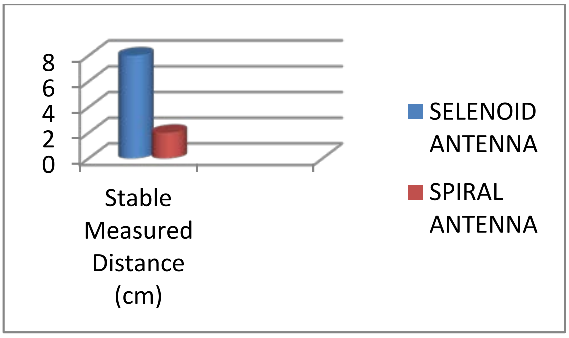

Figure 19. Antenna-detection distance comparison of three transistor darlington connected circuit

As can be seen in Figure 19, the design was tested with two different antennas and the solenoid antenna was able to achieve stable detection up to 8 cm. However, the spiral antenna was stable up to 2 cm.

SWOT analysis and circuit test results show that it works at acceptable distances. However, it needs to be reduced in size and ergonomically designed for the finger so as not to hinder hand movement. It can be reduced to small dimensions with a circuit to be designed using SMD models of circuit elements.

Since it is designed in the shape of a ring and will be reduced to small dimensions, a suitable battery is required. A 1 cell (3.7 V) battery can be used for performance and small size. The energy obtained by using human body heat can also be used to feed the circuit.

If we summarize the existing studies, there are glove, wristband (watch), pen and box shapes for higher voltage levels. When we compare them with technology and fulfillment of their function, we can say that they are designs that work at acceptable levels. The circuit design of this study also detects at acceptable distances. When we examine ergonomically, the studies are large in size. The ring design of this study is smaller in size. Therefore, it is expected to be more comfortable to use. Comparisons were made with the ring design through the designs given in Figure-1, Figure-2 and Figure-3. The design given in Figure-2 is in the form of a box. The design of this study is in the form of a ring (Figure 15).

5. CONCLUSION

In this study, we focus on wireless detection of the presence of electrical energy. In the study, it was observed that the three-transistor Darlington-coupled circuit design works more efficiently in detecting electrical energy than the two-transistor Darlington-coupled circuit design. Since the β current gain of the three-transistor circuit is higher than the two-transistor circuit, it increased the current generated in the antenna much more, allowing the LED to light up from longer distances. It was observed that the design works, but it is a fact that it needs to be reduced in size. Considering it as a wearable technology product, its small size is important as it will not restrict ergonomic mobility. The adoption of the ring shape in the design phase is ergonomically more suitable in terms of size than previous studies. The biggest reason for this is that it is a smaller design than, for example, a glove-shaped design. As a result, the study can be used as a wearable technology product that can be used by technical personnel during work if it is reduced to small sizes, free from environmental interference and ergonomically designed to fit the body. The design is reduced to small dimensions in the form of a ring. In this way, it provided ergonomic working comfort.

6. ACKNOWLEDGEMENTS

This research is part of the researcher's master's thesis at Istanbul Gedik University.

7. CONFLICT OF INTEREST

There is no conflict of interest or common interest with any institution/organization or person.

8. AUTHOR CONTRIBUTION

Burak BOĞAZKESENLİ was responsible for determining and managing the concept and/or design process of the research, data collection, data analysis, and interpretation of the results. He also prepared the manuscript and provided final approval, assuming full responsibility for the work. Aytaç Uğur YERDEN contributed to managing the concept and/or design process of the research, critically analyzing the intellectual content, and provided final approval, taking full responsibility for the work.

9. REFERENCES

Aslan I., Çelik Y., Occupational Health and Safety Investigation of Employees in the Electricity Distribution Sector: Mus, Bitlis and Van Provinces Application. Journal of Labor Relations 1, 130-145, 2022. Retrieved from https://dergipark. org.tr/en/pub/cider/issue/71068/1083460

Ates F. M., Teber A., Güngör O., A Study on Basic Precautions Against Electrical Accidents and First Aid. Bayburt University Journal of Science and Technology 2(2), 336-347, 2019.

Ceylan H., Analysis of Occupational Accidents Occurring in Electricity Transmission Facilities in Turkey. Ejovoc (Electronic Journal of Vocational Colleges) 2 (1), 98-109, 2012. Retrieved from https://dergipark.org.tr/tr/pub/ejovoc/issue/5394/73163

Crockett C., Gulley J. R., Smith R., Smith C., The Design of a Wearable Non-Contact Voltage Detector.

Eker H., Solar cell on cotton denim fabric, (Master's thesis, Institute of Science and Technology), 2019.

Ersoz M., Isıtan A., Balaban M., Nanotechnology 1. BilalOfest Basim-Yayin & Matbaacilik, 2018

Ertan K., Eldem C., A Study of A Representative Wearable Outer Skelette with Ergonomic Analysis Methods. Ergonomics 5(1), 18-25, 2022. https://doi.org/10.33439/ergonomi.1058235

Karabiyik Yerden N., Sustainability, European Green Deal, Marketing and a Research on Automotive Industry. Istanbul Journal of Social Sciences 38, 2023.

Karadeniz O., Work Accidents and Occupational Diseases and Inadequacy of Social Protection in the World and Turkey. Labor And Society, 3(34), 15-73, 2012.

Korkmaz S., GO/ceramic based supercapacitor fabrication and characterization, 2018.

Kozak M., Kozak S., Energy storage methods. International Journal of Technological Sciences 4(2), 17-29, 2012.

Liu X., Gao H., Sun L., Yao J., Generic Air-Gen Effect in Nanoporous Materials for Sustainable Energy Harvesting from Air Humidity. Advanced Materials 2300748, 2023.

Mamur H., Realization of a computerized data acquisition and test system for the investigation of electrical, thermoelectric and thermal parameters of thermoelectric generator, 2013

Mutlu M., Cabuk A., Root Cause Analysis in Electrical Accidents in Turkey. OHS Academic 3 (1), 15-24, 2021. Retrieved from https://dergipark. org.tr/en/pub/isgakademik/ issue/60198/849432

Pamuk O., Yildiz E. Z., Application of Electronic Circuits on Ready-to-Wear Clothing with Embroidery Process. Dokuz Eylul University Engineering Faculty Science and Engineering Journal 23(67), 319-325, 2021. https://doi.org/10.21205/deufmd.2021236728

Yang P., Wen X., Ni X., Peng C., A Novel Non-contact AC Voltage Detector Based on Concentric Double-layer Spherical Shell Structure. Journal of Electronics & Information Technology 43(6), 1637-1643, 2021. doi: 10.11999/JEIT200286

Tosun S., An Evaluation on Occupational Health and Safety in Electrical Work. Journal of Sustainable Engineering Applications and Technological Developments 5(2), 232-246, 2022. https://doi.org/10.51764/smutgd.1082589

Turgut Z. N., Danişan T., Tamer E., Evaluation and selection of wearable technologies in the world of sports and fashion with CRM methods. Journal of Sport and Recreation for Everyone 3(1), 1-11, 2021.

Turkcan C., Wearable Tissue Electronics. Beykent University Journal of Science and Engineering Sciences, 14(1), 27-34, 2021. https://doi.org/10.20854/bujse.931291

Sagbaş E. A., Balli S., Yildiz T., Wearable smart devices: past, present and future. Academic Informatics Conference 30, 749-756, 2016.

Sezer K. C., Basmaci G., An Overview of Rechargeable Batteries. Journal of Engineering Sciences and Design 10(1), 297-309, 2022.

Zhu J., Lei X., Su Z., Liu T., Liu K., Yu G., Zhu L., Study of Non-contact voltage detector of 1000kV UHV AC based on MEMS electric field sensor. In MATEC Web of Conferences, EDP Sciences 160, 02001, 2018.

Rojaee R., Fathi M., Raessi K., Electrophoretic deposition of nanostructured hydroxyapatite coating on AZ91 magnesium alloy implants with different surface treatments. Applied Surface Sciences 285, 664-673, 2013.

Sanchez-Hernandez Z. E., Dominguez-Cresp M. A., Torres-Huerta A. M., Onofre-Bustamante E., Adame J. A., Dorantes-Rosales H., Improvement of adhesion and barrier properties of biomedical stainless steel by deposition of YSZ coatings using RF magnetron sputtering. Materials Characterization 91, 50-57, 2014.

Song Y. W., Shan D. Y., Han E. H., Electrodeposition of Hydroxyapatite Coating on AZ91D magnesium alloy for biomaterial application. Material Letters 62, 3276-3279, 2008.

Sutha S., Kavitha K., Karunakaran G., Rajendran V., In-vitro bioactivity, biocorrosion and antibacterial activity of silicon integrated hydroxyapatite/chitosan composite coating on 316L stainless steel implants. Materials Science and Engineering C 33, 4046-4054, 2013.

Tan Y. H., Abdullah M. O., Nolasco-Hipolito C., Taufiq-Yap Y. H., Waste ostrich- and chicken-eggshells as heterogeneous base catalyst for biodiesel production from used cooking oil: Catalyst characterization and biodiesel yield performance. Applied Energy 160, 58-70, 2015.

Tangboriboon N., Kunanuruksapong R., Sirivat A., Kunanuruksapong R., Sirivat A., Preparation and properties of calcium oxide from eggshells via calcination. Materials Science Poland 30, 313-322, 2012.

Toygun Ş., Köneçoğlu G., Kalpaklı Y., General principles of sol-gel. Sigma Journal of Engineering and Natural Sciences, 31, 456-476. 2013.

Wei M., Ruys A. J., Swain M. V., Milthorpe B. K., Sorrell C. C., Hydroxyapatite-coated metals: Interfacial reaction during sintering. Journal of Materials Science: Materials in Medicine 16, 101-106, 2005.

Yazdani J., Ahmadian E., Sharifi S., Shahi S., Dizaj S. M., A short view on nanohydroxyapatite as coating of dental implants. Biomedicine & Pharmacotherapy 105, 553-557, 2018.

Yazıcı M., Çomaklı O., Yetim T., Yetim A. F., Çelik A., The effect of plasma nitriding temperature on the electrochemical and semiconducting properties of thin passive films formed on 316L stainless steel implant material in SBF solution. Surface and Coatings Technology 261, 181-188, 2015.

Zhang J. X., Guan R. F., Zhang X. P., Synthesis and characterization of sol-gel hydroxyapatite coating deposited on porous NiTi Alloys. Journal of Alloys and Compounds 509, 4643-4648, 2011.

Zhong Z., Qin J., Ma J., Cellulose acetate/hydroxyapatite/chitosan coatings for improved corrosion resistance and bioactivity. Materials Science and Engineering: C 49, 251-255, 2015.

Zhou Z., Zheng B., Gu Y., Shen C., Wen J., Meng Z., Chen S., Ou J., Qin A., New approach for improving anticorrosion and biocompatibility of magnesium alloys via polydopamine intermediate layer-induced hydroxyapatite coating. Surfaces and Interfaces 19, 100501, 2020.

JOURNAL of
MATERIALS and MECHATRONICS:A

e-ISSN 2717-8811
JournalMM, 2024, 5(2), 250-262
https://doi.org/10.55546/jmm.1541043

Araştırma Makalesi / Research Article

Development of Battery-Independent Illumination Drones Integrated into Tethered UAVs for Extended Operations

Tarık ÜNLER [1*]

[1*] Necmettin Erbakan Üniversitesi, Havacılık ve Uzay Bilimleri Fakültesi, Havacılık Elektrik ve Elektroniği Bölümü, Konya, Türkiye,
ORCID ID: https://orcid.org/0000-0002-2658-1902, tunler@erbakan.edu.tr

Geliş/ Received: 30.08.2024; **Revize/Revised:** 02.11.2024 **Kabul / Accepted:** 05.11.2024

ABSTRACT: This study presents the design of an unmanned aerial vehicle (UAV) specifically developed for extended illumination in surveillance, search and rescue (SAR) operations, security enforcement, border surveillance, and other applications requiring lighting, particularly in disaster areas. Traditional battery-powered UAVs have limited operational time; therefore, a tethered drone design was implemented in this study to overcome flight duration constraints. The direct current (DC) energy required for the tethered drone is supplied by a Gold Series switch-mode power supply (SMPS) mounted on the drone. The alternating current (AC) energy needed for the SMPS is transmitted through a cable. Additionally, the light-emitting diode (LED) projector, operating on AC 220 volts, is powered by the same cable that supplies the drone, eliminating the need for an additional DC converter. This design choice reduces weight and ensures an optimized configuration. The projector is mounted on servos with dual-axis capability, allowing both horizontal and vertical movement to precisely illuminate the target area. Although studies on tethered and illumination drones exist in the literature, this work combines two distinct drone systems to create a more efficient UAV design. In the design process, considerations were made for various environmental conditions, particularly wind. Consequently, the thrust-to-weight (T/W) ratio was determined to be 1.54. For cable cross section, a 1.5% voltage drop was accounted for, yielding a required cross section of 1.16mm². However, to ensure safety and reliability, a cable with a cross section of 1.5mm² was selected. This proposed model, distinct from other studies in the literature, offers a practical design for field applications, particularly for night SAR operations in disaster zones such as earthquake sites, due to its point-focus illumination capability and extended flight duration.

Keywords: Illumination drone, Tethered drone, SAR drone, Embedded system, Electronic control

---

*Sorumlu yazar / Corresponding author: tunler@erbakan.edu.tr

Bu makaleye atıf yapmak için /To cite this article

Ünler, T. (2024). Development of Battery-Independent Illumination Drones Integrated into Tethered UAVs for Extended Operations. Journal of Materials and Mechatronics: A (JournalMM), 5(2), 250-262.

1. INTRODUCTION

Tethered drones, also known as tethered Unmanned Aerial Vehicles (UAVs), have become prominent in nighttime surveillance, search and rescue (SAR) operations, and security applications due to their unique operational benefits. Their tethered design ensures continuous power supply and stable data transmission through a cable connected to a ground station. This feature is especially advantageous for operations requiring extended flight times and stable performance under varying conditions. A primary benefit of tethered UAVs is their ability to deliver uninterrupted power, enabling continuous operations far beyond the limits of traditional drones reliant on onboard batteries. This feature makes them ideal for surveillance tasks such as securing large-scale events or monitoring critical infrastructure. Moreover, the tether provides high-bandwidth data transmission, facilitating real-time video streaming from onboard sensors, which is essential for effective surveillance (Kishk et al., 2020). Nighttime illumination capabilities are further enhanced by integrating advanced imaging technologies. For instance, UAVs equipped with thermal infrared cameras excel at detecting heat signatures, which is vital for identifying potential threats in complete darkness (Kays et al., 2018). SAR missions also benefit from this technology, as thermal cameras can detect temperature variations, helping rescue teams locate individuals in challenging conditions (Banuls et al., 2015). In urban areas, where artificial lighting and shadows complicate surveillance, the stability of tethered UAVs ensures high-quality imagery (Semsch et al., 2009). The tether stabilizes flight by enabling the drone to hover at fixed altitudes, which is essential for precise imaging tasks, such as monitoring large areas for security breaches or conducting SAR operations (Lemaire et al., 2019; Lai et al., 2023). This stability also minimizes video jitter, improving the clarity of the collected data (Lemaire et al., 2019). Furthermore, tethered UAVs can integrate with other unmanned systems, such as ground vehicles, to create comprehensive surveillance networks adaptable to various operational needs (Bushnaq et al., 2021). Beyond surveillance, tethered UAVs have seen increasing use in environmental monitoring and disaster management. They provide real-time data for assessing forest fires or post-disaster damage, aiding emergency responders (Tao et al., 2022). The integration of artificial intelligence (AI) and machine learning further enhances these systems, enabling automated tracking and object identification—particularly valuable in dynamic environments (Cherif et al., 2023). The configuration of tethered UAVs significantly impacts their stability and maneuverability, both of which are essential for effective surveillance. Optimizing tether dynamics allows UAVs to withstand environmental challenges such as wind and turbulence while maintaining stable flight paths (Tang, 2024). Their versatility makes them suitable for deployment in urban settings where obstacles or limited visibility hinder traditional surveillance methods (Semsch et al., 2009). Tethered UAVs have also demonstrated considerable potential in SAR operations. Integrating Visible Light Communication (VLC) and advanced sensors enhances their utility in rescue missions. VLC technology allows LEDs to function as both illumination sources and data transmitters, offering low energy consumption and high-bandwidth communication crucial for real-time data sharing during SAR operations (Ibraiwish et al., 2024). Furthermore, advanced sensors, such as radar and sound localization systems, improve the UAV’s ability to detect vital signs and locate victims in distress (Islam, 2021; Hoshiba et al., 2017). UAV swarms, which autonomously coordinate to cover larger areas, further enhance search efficiency and operational flexibility (Khalil et al., 2022). Compared to traditional rescue methods, UAVs offer faster deployment in disaster zones, reducing response times and costs, thus improving rescue outcomes (Hashim and Tamizi, 2018). Additionally, they can establish temporary communication networks in disaster-stricken areas, facilitating coordination and decision-making (Mayor et al., 2019). Their deployment in maritime environments highlights their adaptability across diverse terrains (Alqurashi et al., 2023). In a study conducted with the Tello drone, rapid and flexible illumination was achieved. The study involved a small battery-powered drone autonomously navigating target areas to perform brief illumination operations (Ma et al., 2024). Additionally, another study developed drones with various lighting features to attract tourists' attention on the beach (Shirbhate and Das, 2019). In research focusing on drones that perform both illumination and communication functions, both features were integrated into a battery-powered drone. This UAV provides aerial lighting for emergency situations while also enabling communication (Huang et al., 2023; Yang et al., 2019). Furthermore, the drones are equipped with LEDs of different colors, allowing for visual shows. These drones can move in coordination, creating various visual displays in the air (Huang et al., 2023). In environments with low ambient light, such as outdoor shoots, drones equipped with lighting systems have been used to illuminate subjects. This offers a portable lighting solution for moving objects (Krátký et al., 2021).

Tethered UAVs integrated with advanced technologies represent a significant advancement in illumination night surveillance and SAR operations. Their ability to provide continuous power, deliver high-quality imaging, and adapt to various environments makes them indispensable tools in modern surveillance and emergency response efforts. This innovative study suggests that by adding an LED luminaire powered through the same tether, the effectiveness of these systems, particularly in areas like SAR and border security, will be enhanced. As a result, their applications will expand across a broad range of fields, from SAR to security and environmental monitoring.

2. MATERIALS AND METHODS

In this study, a tethered drone application was developed, with the necessary energy for the drone supplied using a cable. The AC power provided was used to feed an SMPS, which in turn delivered the required DC energy for the UAV. Additionally, an LED luminaire directly powered by AC was employed for illumination, eliminating the need for an extra DC converter. This approach optimized the weight of vehicle, resulting in a more user-friendly and practical design structure.

2.1 UAV Design

The most critical parameters in drone design are the weight of the UAV and the thrust force generated by the motors. In drone design, thrust (T) represents the motor's thrust force, while weight (W) denotes the total weight of the UAV. The ratio of these two values, T/W, must be greater than 1 for multicopter designs to achieve a lift-off. However, considering adverse factors such as wind resistance, maintaining this ratio above 1.5 is essential for optimal UAV performance. This ratio also directly affects the speed of maneuvers, making it generally recommended to select a T/W ratio between 1.5 and 2.0 for multicopter designs. Table 1 presents the materials used in the UAV and their corresponding weights.

Table 1. Component used in the drone, their weights, and total weight

Component	Quantity	Weight (grams)	Total Weight (grams)
Frame	1	380	380
Landing Gear	1	210	210
Brushless Motor	4	60	240
ESC (Speed Controller)	4	25	100
Autopilot	1	89	89
GPS	1	50	50

RF Transceiver	1	20	20
RF Telemetry	1	15	15
Power Module	1	15	15
Carbon Propeller	4	12	48
Cable for Tethered Power	20	16	320
LED Projector	1	142	142
100A SMPS	1	1650	1650
Servo 2 DOF Platform	1	30	30
		TOTAL	**3309 grams**

The aircraft was designed to operate at an altitude of 20 meters. For this purpose, a 2x1.5mm^2 pure copper cable was chosen. When calculating the weight, the scenario of the cable being fully extended was considered, resulting in the total weight of the 20-meter cable. The total weight of the aircraft was calculated to be 3309grams. The brand and the model of motors used are SunnySky 2814 900KV motors, paired with 10.5x5.5 carbon propellers, each providing a thrust of 1278 grams. With a total of 4 motors used, the total thrust ($Total_{Thrust}$) can be calculated using Equation 1.

$$Total_{Thrust} = Motor_{Thrust} \times 4 \tag{1}$$

When calculating using Equation 1, the total thrust is found to be 5112 grams. Accordingly, the thrust-to-weight ratio (T/W) is calculated to be 1.54. Each motor generates 1278 grams of thrust and draws 22.27A of current. For a total of 4 motors, the total motor current (I_{TM}) is calculated to be 89.08A using Equation 2.

$$I_{TM} = I_{Motor} \times 4 \tag{2}$$

For avionic components excluding the motor, the total current consumption (I_{TCO}) was measured to be approximately 0.45 A for other components such as the autopilot, telemetry, GPS, transceiver, and 2 DOF servo. Consequently, the overall current consumption (I_{TC}) was calculated as 89.53 A using Equation 3.

$$I_{TC} = I_{TM} + I_{TCO} \tag{3}$$

For DC conversion, a Gold 80 Series AC/DC converter was selected. Low-quality SMPS units may not provide the advertised power ratings under increased current demands, particularly with inductive loads such as motors, making them unsuitable for such applications. However, an 80 Plus Gold-rated SMPS meets these requirements and will not pose any issues when used in this type of aircraft (Joung et al., 2012). The specifications of the SMPS used in the UAV are presented in Table 2 below.

Table 2. The specifications of the SMPS used for the drone

Supply Voltage	Output Current	Output Voltage	Total Power
220V/AC	100A	12V/DC	1200W

The LED projector employed in this study is a 100W unit featuring a total of 128 LEDs and is designed to operate on an input voltage of 220V. Its compact dimensions of 173mm x 101mm were carefully selected to ensure unobstructed movement within the drone’s chassis. The on/off operations of the projector are controlled via a relay system, enabling the user to activate the device as needed. The auxiliary (AUX) outputs from the autopilot system have been utilized for this control mechanism. These output pins are specifically configured for On/Off operation and are assigned to a dedicated button on the transmitter. Figure 1 illustrates the relay circuit along with the transistor connection schematic, which is utilized for controlling the projector at 220V.

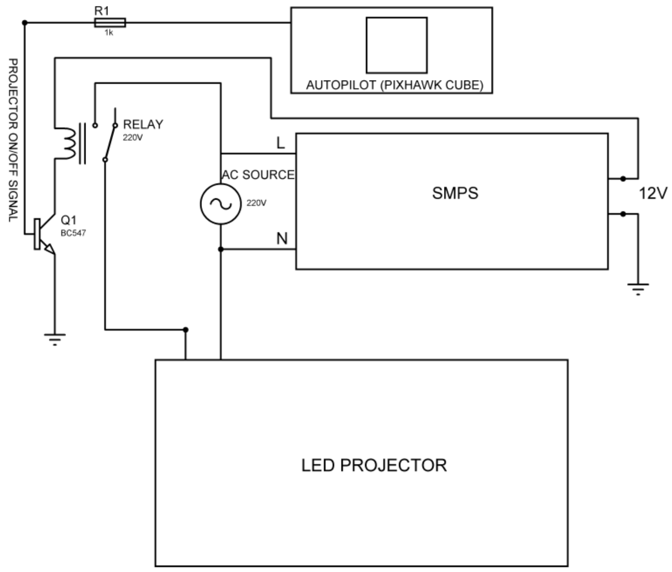

Figure 1. The schematic diagram used for controlling the projector's on/off function

A single NPN type BC547 BJT transistor was used to control the projector's on/off function via an On/Off signal. This transistor drives a relay which is activated to power the 220V projector when required.

Figure 2. Servo 2 DOF platform

For the pan-tilt control of the LED projector, a single 2 DOF servo platform, as shown in Figure 2, is utilized to achieve its orientation. Two of the AUX outputs from the autopilot are configured as servo drivers, and the servos were mounted accordingly.

2.2 Optimal Cable Cross-Section Selection

One of the most critical parameters for ensuring system safety and long-term operation in the design is cable cross-section selection. When choosing the cable, factors such as total power (T_{Power}), number of phases (Phase), cable length (L), desired voltage drop (e%), operating voltage (U), and the conductivity coefficient (K) of the conductor are of paramount importance for determining the cross-sectional area of the conductor. The parameter values used in the system are provided in Table 3.

Table 3. Cable cross-section calculation parameters used in the system

T_{Power} **(Watt)**	**Phase**	**L (meter)**	**e (%)**	**U(Volt)**	**K** $(\frac{S.m}{mm^2})$
1175W	1	20	1.5	220	56

The total power (P_T) is determined by aggregating the power consumption of the entire UAV with that of the LED projector, referred to as P_L. This calculation is expressed in Equation 4, yielding a total power consumption of 1175 W.

$$P_T = I_{TM} \times 12 + P_L \tag{4}$$

Using Equation 5, (Özkaya and Tüfekçi, 2011) it was calculated that the cable cross-sectional area (S) should be 1.16mm² for a 1.5% voltage drop.

$$S = \frac{200 \times L \times N}{K \times U^2 \times e} \tag{5}$$

With a 25% safety margin, the closest higher cable cross-sectional area to this value is 1.5mm², ensuring that the voltage drop remains within a maximum of 1.5% for these system parameters.

2.3 Experimental Setup

In the study, a Pixhawk autopilot was used to ensure stable and autonomous flight of the UAV. This autopilot was selected due to its open-source software, which allows for configuration through external AUX and MAIN ports to accommodate various options. Additional AUX pins were utilized for controlling the projector's power functions as well as the pan-tilt adjustments. Figure 3 illustrates the system's connection diagram.

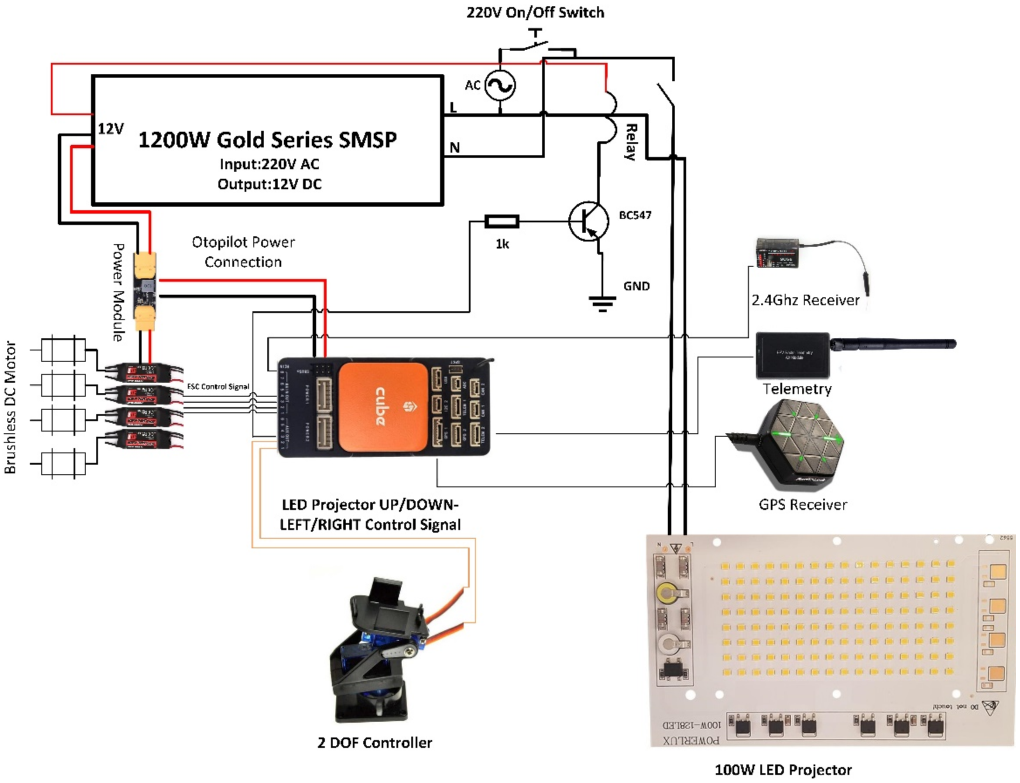

Figure 3. Tethered lighting drone system architecture

As shown in the Figure 3, the system includes essential avionics components required for a drone. The autopilot is connected to a GPS ground station for communication and to facilitate configuration loading, along with a telemetry module and a nine-channel 2.4 GHz receiver. The receiver operates in PPM mode using the RC-IN pin on the autopilot, freeing up the AUX pins for pan-tilt and on-off configurations. Additionally, a power module is included for power monitoring and to supply the autopilot. The motor control system comprises four ESCs and four brushless DC motors. The 2 DOF servos are connected to MAIN pins 5 and 6, and configurations are managed through the ArduPilot software. AUX pin 5 is configured as a relay on/off to control the LED projector's operation. Two gray adjustable inputs on the transmitter are assigned to channels 5 and 6 for pan-tilt control, with logical connections made via ArduPilot and telemetry. Figure 4 shows the UAV's projector on/off switch and main power switch.

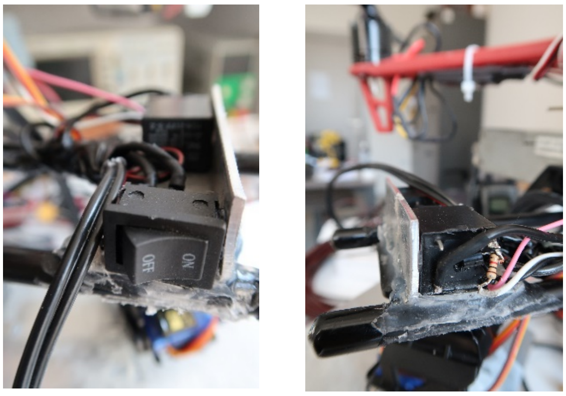
(a) (b)

Figure 4. (a) On/Off switch and (b) relay transistor control circuit assembly

The switch depicted in the diagram controls the power to the system, allowing it to be turned on or off. In case of an emergency, the entire system can be powered down using this switch. The circuit shown in Figure 3 illustrates the relay transistor resistor connection required for the activation and deactivation of the lighting. This circuit has been mounted underneath the relay. The white wire is connected to AUX pin number 5, which has been configured for relay on/off control by the autopilot. The pink wire is connected to the 12V output of the SMPS, providing power to the relay coil. The black wire is connected to the common GND of the system's DC side.

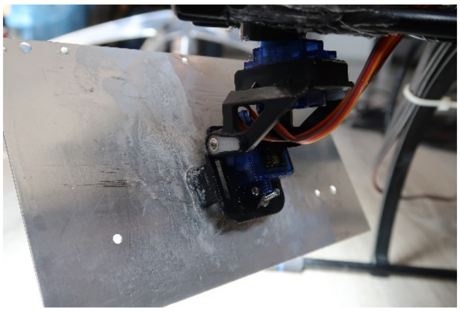

Figure 5. Pan-Tilt mechanism and projector assembly

Figure 5 illustrates the pan-tilt mechanism, which includes two servos and servo mounts. The LED projector is mounted onto the mechanism to enable directional adjustments. The servos are connected and powered through yellow, red, and brown wires. These connections are made to the MAIN outputs on the autopilot, specifically pins 5 and 6, ensuring both control and power supply for the servos.

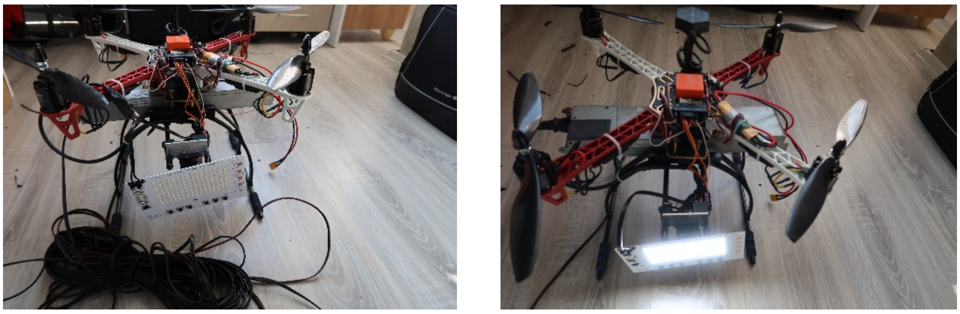

(a) (b)

Figure 6. (a) System configuration with mounted AC cables (b) Operational system with active projector

Figure 6(a) shows the system with mounted cables, SMPS, and LED projector, including a 20-meter cable connected to a 220V outlet connector. Additionally, an XT60 connector has been installed on the 12V output of the SMPS to facilitate easy connection and disconnection of the power module. Figure 6(b) depicts the system energized with the projector turned on.

3. RESULTS AND DISCUSSION

It has been observed that the 80 Plus Gold Series SMPS continues to operate at high performance levels under full power. The circuit designed for the system's power on/off function has been seen to perform its switching operations reliably. In the configuration, when the button on the remote control is activated, the relay triggers, powering the projector with 220V.

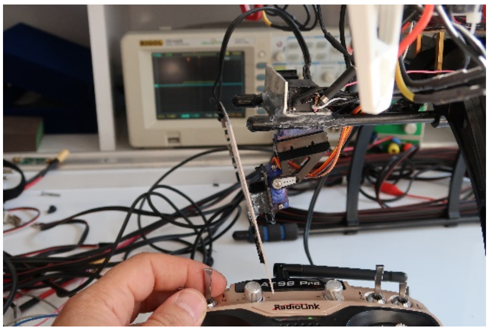

Figure 7. Measurement configuration for trigger signal generated by the on/off switch on the remote control

Figure 7 shows the experimental setup used to measure the trigger signal generated at the AUX 5 pin of the autopilot when switching occurs. For the measurement, one channel of the oscilloscope is connected to the resistor at the base of the transistor. During this process, the on/off operation is performed via the remote control, and the trigger signal is measured using the oscilloscope.

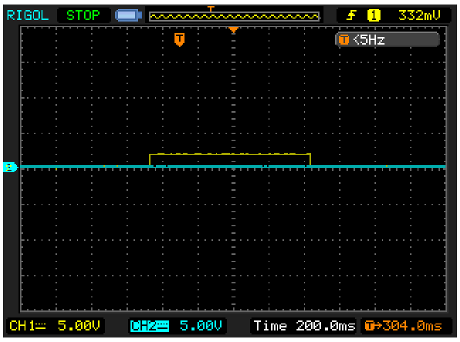

Figure 8. Trigger signal display on the oscilloscope screen

In Figure 8, the oscilloscope screenshot of the trigger signal is shown. As seen on the oscilloscope screen, when the on/off signal is sent from the remote control, a logic 1 signal appears on AUX pin 5, and it returns to 0 when turned off. The peak value of the logic 1 signal is measured at 3.3V. Thus, this signal triggers the transistor to drive the relay, which safely controls the 220V supply to the projector.

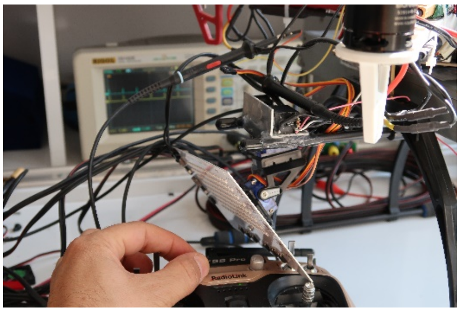

Figure 9. The test setup for measuring the channels while adjusting the pan-tilt controls on the transmitter

The test setup for measuring PWM signals from the MAIN 5-6 channels, connected to the outputs, as observed through the oscilloscope, is shown in Figure 9.

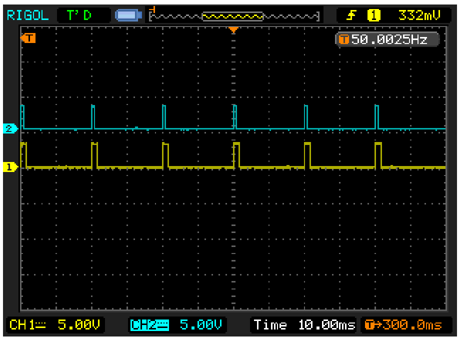

Figure 10. When adjusting pan-tilt controls on the controller, the PWM signal waveforms of the channels on the oscilloscope screen

In Figure 10, it is observed that the PWM signals are successfully generated while controlling the channels from the remote. Additionally, when the signal transmission from the remote is stopped, the last position PWM values continue to be output, resulting in the projector remaining fixed in its last position. Tests have shown that the designed system operates without issues, and the drone is capable of flying smoothly. The calculated T/W ratio of 1.54 clearly demonstrates that the aircraft remains stable even in windy conditions. Furthermore, the pan-tilt mechanism was tested for extended periods. The projector's on-off operations were carried out smoothly, and the system was observed to perform its tasks without problems. Although the projector was noted to heat up during prolonged ground tests, it was observed to cool down due to the airflow generated by the two front propellers during flight. Therefore, no additional cooling unit was installed to avoid increasing the aircraft's weight, as it would not overheat during operation.

A review of the literature reveals that various studies on lighting drones present distinct advantages and disadvantages. In Table 4, the proposed tethered lighting drone from this study is compared with other lighting drone designs found in the literature.

Table 4. A Summary of illumination works

Reference	Wide-area Illumination	Suitability for Disaster Zones	Long Operation Time	Flexibility	Continuous Operation	Adjustable Lighting Direction	Operation at High Altitudes
Huang et al.	×	√	×	√	×	×	√
Ma et al.	×	×	×	√	×	×	√
Shr. and Das	×	×	×	√	×	×	√
Krátký et al.	×	×	×	√	×	×	√
Yang et al	×	√	×	√	×	×	√
This paper	√	√	√	×	√	√	×

Since illuminating large areas requires a powerful LED or lighting fixture, the LED projector used in this study is larger than those in comparable works, allowing for significantly broader area coverage. Considering the requirements for disaster zones, the need for long-term illumination of extensive areas becomes evident. The use of small, battery-powered drones in other studies limits their applicability for SAR operations in disaster areas. When examining other designs, it is evident that the proposed drone is powered by a cable from the ground. This configuration enables the drone to remain airborne for extended periods, ensuring continuous illumination of the designated area. The designed drone has limited mobility due to its tethered configuration; however, it can operate freely within the range of the cable length. If required, the cable length can be increased with a modified design to expand the operational range. Since the drone in this study is powered through a tethered system, it provides uninterrupted illumination compared to other battery-powered drones. In contrast, battery-powered drones need to land for battery replacement once depleted, preventing continuous illumination. The proposed tethered drone is equipped with a servo-controlled LED projector system, enabling precise illumination of the desired area. In comparison, other drones need to maintain a specific angle to achieve targeted lighting, which can negatively impact their flight duration. Drones that operate independently of cables can ascend to higher altitudes; however, as altitude increases, illumination intensity decreases, necessitating operation at an optimal height. Exceeding a certain altitude creates disadvantages for effective lighting, making the 20-meter cable length sufficient for the optimal height in this tethered design. From this perspective, the height limitation is not a significant disadvantage for the lighting drone.

When considering potential applications, such as in disaster zones, area surveillance, or border security operations, the advantages of the tethered lighting drone demonstrate that it is more suitable than wireless designs for these use cases.

4. CONCLUSION

In the conducted study, the wired illumination drone was successfully operated, completing its application. The system's T/W ratio of 1.54 ensured that it continued to perform effectively even in adverse weather conditions, as demonstrated by the tests. Additionally, the drone's power supply through the cable enabled it to operate for extended periods. Despite the total DC power requirement of 1075W, the design included a high-performance SMPS and a 1200W operating mode (at 220V) with a 20% tolerance, allowing for long hours of operation without overheating. The cable cross-section, calculated for a 1.5% voltage drop, was found to be 1.16 mm², but considering the tolerance factor, a 1.5 mm² cross-section was chosen. This choice ensures high system performance and prevents overheating issues.

Moreover, system configurations were made for the on-off functionality of the LED projector via the controller. The integration of the pan-tilt mechanism for focusing the projector on the desired area in flight was completed, enabling successful point illumination control through the remote. The projector was mounted underneath the front propellers to facilitate cooling, thereby maintaining high performance and operational stability without increasing the T/W ratio. Unlike previous studies, this work combined the powerful features of tethered drones with the capabilities of illumination drones, resulting in an innovative aerial vehicle. This design provides a flexible and innovative solution for long-term illumination in nighttime disaster response, SAR operations, border security, and specialized area lighting.

In future studies, a reflective-type LED projector with higher luminous power can be utilized to illuminate larger areas, particularly during disaster scenarios, ensuring broader coverage.

5. ACKNOWLEDGEMENTS

This study did not benefit from any support.

6. CONFLICT OF INTEREST

Author approve that to the best of their knowledge, there is not any conflict of interest or common interest with an institution/organization or a person that may affect the review process of the paper

7. AUTHOR CONTRIBUTION

Tarık ÜNLER has the full responsibility of the paper about determining the concept of the research, data collection, data analysis and interpretation of the results, preparation of the manuscript and critical analysis of the intellectual content with the final approval.

8. REFERENCES

Alqurashi F., Trichili A., Saeed N., Ooi B., Alouini M., Maritime communications: a survey on enabling technologies, opportunities, and challenges. IEEE Internet of Things Journal 10(4), 3525-3547, 2023.

Banuls A., Mandow A., Vázquez-Martín R., Morales J., García-Cerezo A., Object detection from thermal infrared and visible light cameras in search and rescue scenes, In 2020 IEEE International Symposium on Safety, Security, and Rescue Robotics (SSRR), November, 2020, pp: 380-386.

Bushnaq O., Kishk M., Çelik A., Alouini M., Al-Naffouri T., Optimal deployment of tethered drones for maximum cellular coverage in user clusters, IEEE Transactions on Wireless Communications 20(3), 2092-2108, 2021.

Cherif N., Jaafar W., Vinogradov E., Yanıkömeroğlu H., Pollin S., Yongaçoğlu A., ITUAVs: intermittently tethered UAVs for future wireless networks. IEEE Wireless Communications, 30(4), 124-130, 2023.

Hashim A., Tamizi M., Development of drone for search and rescue operation in Malaysia flood disaster. International Journal of Engineering & Technology 7(3.7), 9-12, 2018.

Hoshiba K., Washizaki K., Wakabayashi M., Ishiki T., Kumon M., Bando Y., Okuno H., Design of UAV-embedded microphone array system for sound source localization in outdoor environments. Sensors 17(11), 2535, 2017.

Huang J., Tian G., Zhang J., Chen Y., On unmanned aerial vehicles light show systems: Algorithms, software and hardware. Applied Sciences 11(16), 7687, 2021.

Huang Q., Wen W., Liu M., Du P., Chen C., Energy-Efficient Unmanned Aerial Vehicle-Aided Visible Light Communication with an Angle Diversity Transmitter for Joint Emergency Illumination and Communication. Sensors 23(18), 7886, 2023.

Ibraiwish H., Eltokhey M. W., Alouini M. S., UAV-Assisted VLC Using LED-Based Grow Lights in Precision Agriculture Systems. IEEE Internet of Things Magazine 7(3), 100-105, 2024.

Islam S. M., Oba L., Lubecke V. M., Empirical Mode Decomposition (EMD) for platform motion compensation in remote life sensing radar, In 2022 IEEE Radio and Wireless Symposium (RWS), 2022, pp: 41-44.

Joung M., Kim H., Baek J., Dynamic analysis and optimal design of high efficiency full bridge LLC resonant converter for server power system, Twenty-Seventh Annual IEEE Applied Power Electronics Conference and Exposition (APEC), Orlando, FL, USA, 2012, pp: 1292-1297.

Kays R., Sheppard J., McLean K., Welch C., Paunescu C., Wang V., Crofoot M., Hot monkey, cold reality: surveying rainforest canopy mammals using drone-mounted thermal infrared sensors. International Journal of Remote Sensing, 40(2), 407-419, 2018.

Khalil H., Rahman S., Ullah I., Khan I., Alghadhban A., Al-Adhaileh M., ElAffendi M., A UAV-swarm-communication model using a machine-learning approach for search-and-rescue applications. Drones 6(12), 372, 2022.

Kishk M., Bader A., Alouini M., Aerial base station deployment in 6G cellular networks using tethered drones: the mobility and endurance tradeoff. IEEE Vehicular Technology Magazine 15(4), 103-111, 2020.

Krátký V., Alcántara A., Capitán J., Štěpán P., Saska M., Ollero A., Autonomous aerial filming with distributed lighting by a team of unmanned aerial vehicles. IEEE Robotics and Automation Letters 6(4), 7580-7587, 2021.

Lai Y. L., Lai Y. K., Yang K. H., Huang J. C., Zheng C. Y., Cheng Y. C., Chiang Y. W., An unmanned aerial vehicle for search and rescue applications. In Journal of Physics: Conference Series, IOP Publishing, November 2023, Vol. 2631, No. 1, p. 012007.

Lemaire P., Crispim-Junior C., Robinault L., Tougne L., Jitter-free registration for unmanned aerial vehicle videos. In Advances in Visual Computing: 15th International Symposium on Visual Computing, 2019, pp: 529-539.

Ma B., Pan Y., Xu Y., Zhang Z., Chen C., Li C., ILLUMINE: Illumination UAVs deployment optimization based on consumer drone. Ad Hoc Networks, 163, 103587, 2024.

Mayor V., Estepa R., Estepa A., Madinabeitia G., Communication drone technology for disaster management in rural and remote areas. IEEE Access 7, 76286-76295, 2019.

Özkaya M., Tüfekçi T., Aydınlatma Tekniği, Birsen Yayınevi, İstanbul, pp. 423-447, 2011.

Semsch J., Weller J., Janning B., UAV systems for urban surveillance: operational challenges and performance evaluation. Journal of Unmanned Vehicle Systems 7(2), 56-67, 2009.

Shirbhate A., Das S., Static and Dynamic Beach Lighting Using Cloud based UAV. In 2019 IEEE Pune Section International Conference (PuneCon) December 2019, pp: 1-4.

Tang X., Optimal design and analysis of tethered UAV systems for stable aerial operations. Aerospace Science and Technology 133, 106493, 2024.

Tao Y., Xie Z., Zhang S., Zhai Y., A novel UAV-based forest fire detection and monitoring system. International Journal of Remote Sensing 43(24), 8321-8344, 2022.

Yang Y., Chen M., Guo C., Feng C., Saad W., Power efficient visible light communication with unmanned aerial vehicles. IEEE Communications Letters 23(7), 1272-1275, 2019.

JOURNAL of
MATERIALS and MECHATRONICS:A

e-ISSN 2717-8811
JournalMM, 2024, 5(2), 263-285
https://doi.org/10.55546/jmm.1512549

Araştırma Makalesi / Research Article

Deep Learning Application and Analysis In Detection of Metal Plate Surface Defects

Can TUNCER[1*], Cemil KÖZKURT[2], Serhat KILIÇARSLAN[3]

[1*] GESBEY R&D Center, Balıkesir, Türkiye,
ORCID ID: https://orcid.org/0000-0003-0539-1381, can.tuncer@gri.com.es
[2] Bandırma Onyedi Eylül University, Faculty of Engineering and Natural Sciences, Department of Computer Engineering, Bandırma, Balıkesir, Türkiye,
ORCID ID: https://orcid.org/0000-0003-1407-9867, ckozkurt@bandirma.edu.tr
[3] Bandırma Onyedi Eylül University, Faculty of Engineering and Natural Sciences, Department of Software Engineering, Bandırma, Balıkesir, Türkiye,
ORCID ID: https://orcid.org/0000-0001-9483-4425, skilicarslan@bandirma.edu.tr

Geliş/ Received: 09.07.2024; **Revize/Revised:** 26.09.2024 **Kabul / Accepted:** 18.11.2024

ABSTRACT: In industrial manufacturing processes, detection of defects on the surfaces of metal plates supplied from iron and steel main industry manufacturers to be processed by machining and non-machining methods has an important place in estimating the values of the relevant plate such as safety and maintenance cost. With the developing technology and computer vision and deep learning applications finding a place in the industry, it has become possible to detect and classify metal plate surface defects more quickly and effectively with a lower error rate at an advanced technological level. Within the scope of this study, a deep learning model was created by using the TensorFlow library in the Python environment with using NEU Metal Surface Defects Dataset to detect metal plate surface defects. Then as an industrial application, a device prototype developed using Nvidia Jetson Nano and USB Camera, in order to test this model under real conditions.

Keywords: Metal plate, Surface defect, Deep learning, Computer vision, Artificial intelligence, Machine learning

---

*Sorumlu yazar / Corresponding author: can.tuncer@gri.com.es

Bu makaleye atıf yapmak için /To cite this article

Tuncer, C., Közkurt, C., Kılıçarslan S. (2024). Deep Learning Application and Analysis in Detection of Metal Plate Surface Defects. Journal of Materials and Mechatronics: A (JournalMM), 5(2), 263-285.

1. INTRODUCTION

Metal plates are one of the materials used as the main construction material in sectors such as machinery, automotive, shipbuilding, energy, and home electronics. Metal plates are shaped by various machining or chipless manufacturing methods such as cutting, bending, welded joining and used in structures within the framework of certain design and engineering decisions. There are many standards like EN ISO 8501-1:2007, EN 10130, ASTM A480/A480M, ASTM E45 that must be followed for the metal plates used to meet sufficient quality criterias. Compliance with the standards in which the basic physical and chemical properties of the material, surface roughness and quantity, effect and acceptance values of surface defects are defined emerge as the basic quality requirement of the enterprises.

One of the main problems seen in metal plates is the surface defects that have occurred on the plate surface. These defects may be caused by variables determined in various processes during the manufacturing phase of metal plates, as well as by different external factors such as environmental conditions, transportation, stacking. In this context, one of the quality control processes applied in enterprises is the inspection of surface defects of metal plates, and the rapid and accurate detection of these defects stands out as a critical condition for providing the necessary strength conditions in industrial production and increasing product quality. Within the scope of the control process, it can be decided to repair the metal plate or to discard it as a result of evaluations such as determining the presence of surface defects and their location on the plate, classifying them, determining their quantity, measuring the depth or height differences caused by the defect with various devices, determining the presence rate of the defects in the entire area and determining whether they are within tolerance. These defects have been described in the literature and generally classified in 6 main groups as crazing, inclusion, patches, pitted, rolled, scratches (Fu et al., 2019).

Different methods can be preferred to detect surface defects. The most basic, simple, fast and easy-to-apply method is visual control. Although visual controls are carried out by experienced operators, it is obvious that it is a method that is quite open to subjective errors related to humans. In this method, it is possible to experience negativities such as overlooking, neglecting, and misclassification of critical defects. Overlooked intolerance surface defects can cause negativities that may threaten human life, such as thinning of the wall, notch effect or the risk of corrosion formation.

Another method used for the detection of metal plate surface defects is the applications developed by using computer vision and deep learning models, which are among the sub-branches of artificial intelligence studies that are developing and becoming widespread today. This method can provide the detection of surface defects with much higher reliability and practicality than traditional methods. In this study, it was aimed to develop a deep learning model based on Convolutional Neural Network (CNN) for the detection of metal plate surface defects by deep learning. Convolutional Neural Networks are a subclass of deep learning models designed specifically to work on visual data. CNN’s are highly effective in areas such as image processing, video analysis, and medical imaging, and are often used successfully in tasks such as object recognition, facial recognition, automated vehicle driving systems (Mo et al., 2018). It will be ensured that the model to be developed with the study will be tested by using a large number of classified image data of metal surface defects in a data set. It is aimed to run the resulting model file on a mobile minicomputer and to detect and classify metal plate surface defects by detecting live images under real conditions with the camera connected to the computer.

In the "Introduction" section, the reasons for the initiation of the study are presented, and in the "material, method" section, the methods applied during the execution of the study are discussed in detail. The fundamentals of artificial intelligence and deep learning have been examined, and concepts such as libraries, layers, activation functions, optimizers, which are the sub-elements necessary for the construction of deep learning architecture using artificial neural networks, have been clarified in detail. In the "experimental studies" section, the details of how the deep learning model architecture is created, the training process of the model and the industrial application stages are revealed. In the "results and discussion" section, results and the value of the findings obtained was discussed and future studies were mentioned. Finally in the “conclusions” section, a summary of the results of the study is shared.

2. MATERIALS AND METHODS

A common feature of the case studies discussed to shape the methodology of the study in the preliminary research process is that they are based on the creation of a certain data set or its use by providing it ready-made. Since data collection specific to metal plate surface defects will require a long period of time on a yearly basis in order to encounter a sufficient number of defects to allow a healthy deep learning process to be carried out under the types of defects that occur, it was decided to bypass the data collection process, and instead of it, the open access NEU Metal Plate Surface Defects dataset (Song and Yan, 2019) is decided to be used.

The necessary codes to work on the Visual Studio Code application were created and run in the Python programming language for processing the data in this dataset, setting up the deep learning model, carrying out the training process, obtaining the performance values and to test the results practically. This program consists of 6 main parts: preparation, data preprocessing, model creation and training, evaluation of training performance, testing of the model and finally exporting the model.

To use the necessary libraries and activation functions during the preparation phase, it is ensured that they are called to the program and the locations of the training, test and verification clusters are specified. In the data pre-processing phase, data augmentation methods were applied by subjecting the image data in the data set to operations such as rotation, scrolling, mirroring, scaling, resizing, categorical classification. In the model creation and training phase, definitions were made about the use of the TensorFlow / Keras library, layer parameters were determined, the metrics to be used were selected, and the training process of the CNN model, which was developed by determining the number of cycles and iterations, was carried out.

After the completion of the training, the necessary code pieces were added to create the accuracy and loss functions to reveal how successful the training process was. The model is exported from the compiler so that it can run on a computer-independent device. In this way, it has become possible to test the developed deep learning model in real industrial conditions using a minicomputer with a camera integrated with high image processing capacity.

2.1 Artificial Intelligence

Artificial intelligence is a branch of science and engineering that aims to enable computer systems to gain human-like capabilities. It is the set of abilities that computers gain by using algorithms, data, and computational power to enable them to perform tasks associated with human intelligence, such as visual perception, speech recognition, learning, decision-making, language understanding and problem solving. Artificial intelligence applications, which are divided into many different sub-branches such as machine learning, deep learning, natural language processing, expert systems, artificial neural networks and genetic algorithms, have become widely used in areas such as engineering, health, finance, automotive, education, media and industrial production. The concept of artificial intelligence, which has occupied the thoughts of scientists such as ancient Greek and Egyptian philosophers since ancient times, was introduced in the early period of today, and the concept of "expert systems" that combine techniques such as logical thinking, symbolic calculation and problem solving to reveal human-like logical judgments and decision abilities (Turban and Watkins, 1986). With the combination of modern computer science based on the algorithmic perspective and a series of innovative ideas and discoveries based on statistical studies, the concept of artificial intelligence made further development in the mid-20th century. The Dartmouth Conference, which took place in 1956, was an important milestone for the introduction and development of the concept of artificial intelligence as a branch of science, which was officially put forward by scientists such as John McCarthy, Marvin Minsky, Nathaniel Rochester and Claude Shannon (Moor, 2006). The main goal of artificial intelligence-oriented scientific studies is that computer systems have human-like intelligence, and that they reach results and perform better than humans in many processes such as data analysis, pattern recognition, and making predictions, and as of today, an artificial intelligence structure equivalent to human intelligence has not yet been revealed and continues to develop in many ways (Shinde and Shah, 2018).

2.2 Machine Learning and Deep Learning

Machine learning (ML) is a sub-branch of artificial intelligence and refers to the ability of computers to perform certain tasks by providing learning using data. Machine learning structures, which have different structures from traditional programming logic, are structures that have the ability to create patterns by processing data and to make predictions and decisions by learning the relationships between these patterns, rather than operating based on pre-programmed rules. It is examined in 3 subcategories as supervised learning, unsupervised learning and reinforcement learning. Supervised learning is a type of machine learning that is mostly used in studies such as classification and regression, and enables the matching of input data with the right outputs by providing learning on labeled data. Unsupervised learning is based on the principle of discovering the differences by the learning model itself by applying it on unlabeled data, which is preferred in studies such as clustering and size reduction. Reinforcement learning, robotic education and game development are followed with a learning methodology based on a reward or punishment system, which is preferred. While the decision-maker is rewarded when he makes the right decisions, he provides learning by receiving negative signals in the wrong decisions.

The concept of deep learning (DL), on the other hand, is a machine learning technique performed using artificial neural networks and is generally used in studies that need to develop learning ability using large and complex data sets. There are many subtypes of deep learning, and the term "deep" in the concept of deep learning, which refers to the "concept of deep artificial neural networks", is related to the use of a large number of layers (Shinde and Shah, 2018). Deep learning is a sub-application of machine learning, and machine learning is under artificial intelligence applications, which is the widest scope. To give an example of the main areas where deep learning is successfully applied; We see that studies on applications such as image recognition and processing, natural language processing, autonomous driving, and voice recognition come to the fore. Model structures, called artificial neural networks, are mathematical models inspired by the functions of the human brain. Deep learning refers to the situation where these networks are made up of multiple layers (usually a large number of hidden layers). Thanks to these layers, deep learning models have the ability to perform an automatic feature extraction by starting from simple features on the data and progressing to more complex features (Sahu and Dash, 2021).

2.3 Key Elements for Deep Learning Application

Deep learning applications are carried out in the computer environment using various programming languages. Within the scope of these studies, researchers need to master many subjects and make the necessary preparations for applications in order to reveal an efficient code structure and to operate it effectively. In this context, the correct and appropriate selection of the programming language, compiler environment, and hardware capacity of the computer to be used is important for a successful deep learning application. In addition, a good understanding of concepts such as many libraries, layers, activation functions, metrics that should be used under the deep learning architecture, learning the working principles, and determining the relationships and parameters affecting the operation correctly are important issues for model performance. We can explain the importance of these basic elements and the reasons for their preference by summarizing them as follows.

Today, Python is the most widely used programming language in similar studies, and it was preferred to take this language as a basis in our study. In order to create a deep learning architecture on Python, it is necessary to first select a computer, operating system and compiler (IDE) to run this programming language on (Raschka and Mirjalili, 2019).

In our study, it was possible to carry out code development experiments in different environments and compilers by using 2 different computers with Windows and Linux operating systems, Visual Studio Code, Kaggle and Google Colab compilers, and the Python program directly from the terminal on a Linux-based computer. In the deep learning architecture we are working on, it is aimed to use the Keras API (API, Application Programming Interface) and sub-APIs under the TensorFlow library. TensorFlow is an open-source machine learning library developed by the Google Brain team and published by Google. It is designed for complex data processing tasks and has been shown to be particularly effective in large-scale deep learning applications. Its main features include flexibility due to its support for various computational operations and its ability to run on different platforms, the ability to perform calculations in parallel and efficiently by converting operations into a structured graph using a data flow graph, and the ability to automatically adjust model parameters using optimization techniques such as gradient descent with automatic derivative calculation (Helms et al., 2018).

Keras; TensorFlow is a high-level neural network API that runs on core libraries such as Theano and CNTK, offers a user-friendly and modular structure, enabling rapid prototyping of deep learning models (Manaswi, 2018). Thanks to Keras, which is integrated into TensorFlow, the application becomes user-friendly and provides practicality to practitioners.

Groups with different features formed by artificial neural networks in a deep learning architecture can be defined as "layers". Deep learning models are made up of several layers of compute that process data from the input layer to the output layer. Layers act as filtering structures designed to learn a specific set of features from data. The characteristics of the layers used in the study and why they are preferred are explained in detail in the following sections. The types of layers used in deep learning studies are generally classified as input layers, hidden layers, and output layers. The neurons in each layer receive and process the incoming signals and transmit them to the next one. With these complex interactions between layers, the systematic working function of deep learning structures takes place (LeCun et al., 2015).

The mathematical expressions used to calculate the output of each neuron in the network are called activation functions. Non-linear activation functions (e.g., ReLU, sigmoid, tanh) allow the model to learn nonlinear and more complex relationships. It is possible to process the data coming to a neuron in the artificial neural network by subjecting it to the mathematical process defined by the specified activation function and to transform it as a different element for the next stage as the output of the neuron. The mathematical expression of the activation function and the way it works is very important for the performance of deep learning architecture. Instead of applying the trial-and-error method for the selection of the right activation function for the deep learning architecture built for each different purpose, choosing inspired by case studies will speed up the process. The activation functions used in the study are discussed in detail in the relevant section (Rasamoelina et al., 2020).

Each neuron contains weights and biases that are applied to the input data. During the training of the network, these parameters are adjusted to provide the best performance over the data. Bias is a constant added to the activation function that the neuron will process, and it is useful to get results in different ranges by changing the function curve. Weight, on the other hand, is a numerical element of information that is processed in one neuron and transferred to another neuron to reveal a feature. The weights randomly selected at the beginning of the training process are optimized by the learning algorithm in accordance with the data set during the training process (Dung and Mizukawa, 2007).

The loss function is used to evaluate model performance during the training of the model, to be an indicator of the optimization of parametric settings, and to optimize algorithms. It is used to measure how close their predictions are to the actual data. Designing the training process to minimize this loss is essential for a successful model training. There are varieties such as Mean Squared Error (MSE), Mean Absolute Error (MAE), Cross Entropy Loss, Hinge Loss, Poisson Loss, Huber Loss, each of which can be expressed mathematically separately. Details about the loss function used in the study are given in the relevant section (Wang et al., 2022).

Optimization algorithms are used to improve the training process of the deep learning model and to obtain the best performance. It has basic tasks such as updating the model parameters, minimizing the loss function, adjusting the learning rate, preventing the problem of overfitting, and accelerating the training process.

Different types of algorithms such as Stochastic Gradient Descent (SGD), Momentum, Adagrad, RMSProp (Root Mean Square Propagation), Adam (Adaptive Moment Estimation), Adadelta, Nadam (Nesterov-accelerated Adaptive Moment Estimation) are used, and in our study, it was decided to use the "Adam" optimizer due to its performance in similar studies. The relevant section provides the necessary explanations about the Adam optimizer (Haji and Abdulazeez, 2021).

3. EXPERIMENTAL STUDY

The establishment of deep learning architecture requires the application of theoretical knowledge in the field of practical experience, that is, the introduction of coding work. For this, it is essential to run the code by working on a Python compiler. During this coding study, it is possible to construct different architectures, to achieve high or low performance results by using different libraries or layers with different parameters, or to reveal application details. In addition, it is possible to optimize the accuracy and lost output values, which are the training result metrics, by trying different parametric values during the construction of the model.

3.1 Dataset

It is the dataset that contains the data on which the deep learning model will apply the feature layers. Depending on the type of deep learning study to be conducted, this data may include different types of data such as audio, image, numbers, lists, video footage, etc. In addition, the data files that make up the data set should consist of the same type of data and should have forms and features ready to be used in the training process. The dataset we will work on is the dataset containing image files of a large number of metal plate surface defects, which have been shared as open source under the name of "NEU Metal Plate Surface Defects Dataset" (Song and Yan, 2019). Surface defect image files in 6 different categories are distributed in folders with different names and divided into training, test and verification sets. Each image file is a bitmap (BMP) file with a size of 200x200 pixels and a color depth of 8 bits. Thanks to Keras' ImageDataGenerator sub-API, there is no need for labeling for images, and tags can be matched automatically thanks to the nested folder structure (Lv et al., 2020).

3.2 Preparation and Data Pre-Processing

It is ensured that the libraries and layers to be used in coding are transferred to the program, called (imported), and the address definitions of the location where the training, test and verification sets are located in the computer environment are made at this stage. Importing basic Python libraries such as NumPy, Pandas, Matplotlib and TensorFlow into the program is essential to reveal the functions required in the working process of the Python program. At this point, in order to facilitate the operation of the program, instead of importing the entire large-sized library, it is generally preferred to import the small cube sub-modules needed in the code group. Thus, it is possible for the program to run faster with lower dimensional data.

At this stage, a data generator is created for the training dataset. With this generator, various data boosting techniques have been applied on the images, such as scaling, random rotation, random panning in width and height, and horizontal flipping. With these techniques, it is possible to generalize the model and reduce the problem of overfitting. Scaling is also implemented for test and validation datasets through the creation of a data generator. In addition, the creation of image streams from data generators is ensured (Maharana et al., 2022).

3.3 Setting Up the Model

Tensorflow and Keras libraries and sub-APIs and sub-APIs and layers, such as Sequential, Conv2D, MaxPooling2D, Activation, Flatten, Dense, Dropout, were imported at this stage and parametric definitions were made (Sobhana et al., 2023). Figure 1 shows an example deep learning architecture image that matches the structure in our original model.

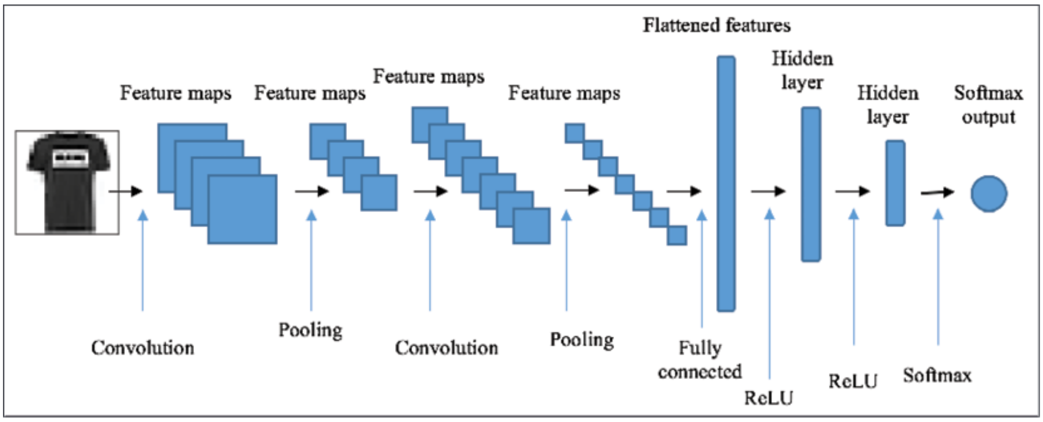

Figure 1. A representative structure of deep learning architecture (Bbouzidi et al., 2024)

Sequential is a class used to build models in Keras, and it is a library that allows layers to be ordered in relation to each other (Gulli and Pal, 2017).

The Functional model structure, which is another type of Sequential, can provide multiple inputs and outputs and enables a more complex architectural setup. In our study, it was preferred to use Sequential architectural structure. In Figure 2, ordered and functional API structures are shown schematically.

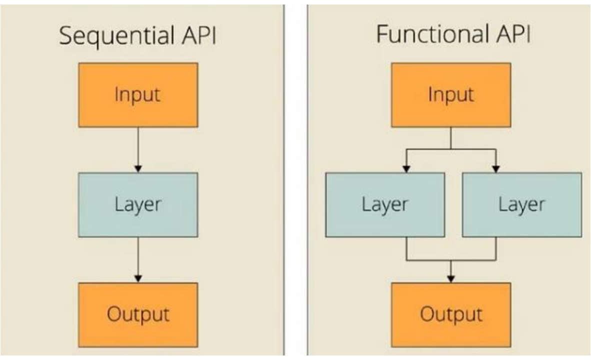

Figure 2. Algorithmic expression of the Sequential and Functional API difference (Vansh, 2022)

Conv2D is the convolution layer used to extract features from such data that has been shown to be successful on 2D data, such as image data. A representative comparison of the input data and the convolution kernel is presented in Figure 3.

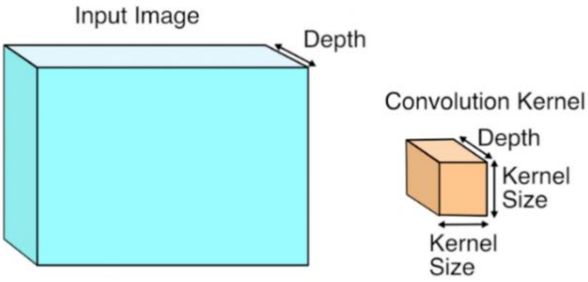

Figure 3. Representative expression of the Conv2D convolution layer (Warden, 2015)

MaxPooling2D is used in the architectural structure of deep learning models, it is the pooling layer that usually follows the convolution layers. Thanks to this layer, it is possible to reduce feature maps, while preserving important features and reducing data size (Mastromichalakis, 2023). In Figure 4, the effect of applying Max Pooling is expressed on the image.

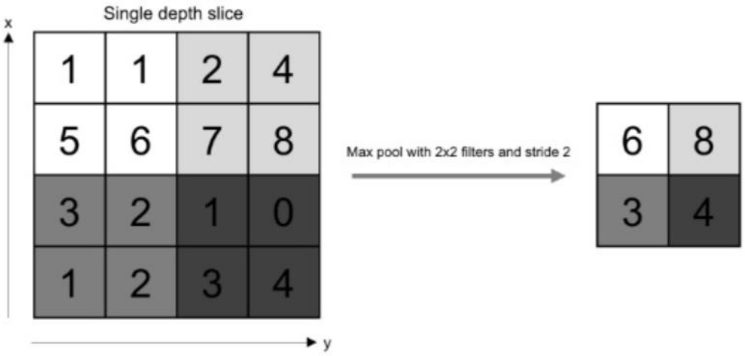

Figure 4. Example demonstration of the effect of the MaxPooling2D digestion layer

Flatten is the layer used for converting multidimensional feature maps into a one-dimensional vector. Preparation is made for the processing of the data in the "Dense" layer by providing a size reduction transformation (Jin et al., 2015). The effects of the flattening layer are expressed in the image given in Figure 5.

Figure 5. Example illustration of the size reduction transformation of the flatten layer

Dense is the layer in which all the neurons in the previous layer are fully connected to each other. In this layer, parametric transformations are performed that express the complexity of a data set and help the model learn. The process of reducing the input data to a certain size and producing various feature outputs by using the representation of this data is carried out in this layer. Dense layers are commonly used in many tasks such as classification, regression, language processing, and so on, and they play an important role within the architecture to increase the complexity of the model and learn patterns in the data set. The image in Figure 6 schematically expresses the dense layer.

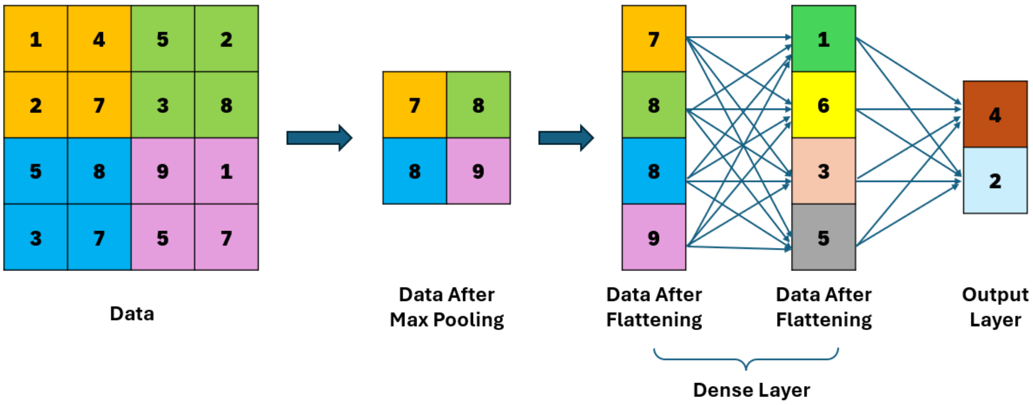

Figure 6. The location of dense layers in the order of layers

The so-called overfitting or overlearning condition refers to the situation in which a model loses its ability to make predictions in real-world data due to over-adaptation to training data and occurs when the model overreacts to noise or randomness in the training data. Underfitting or underlearning, on the other hand, means that the model fails by failing to catch even the basic patterns due to its simplicity and failing to show the expected performance (Rice et al., 2020).

In Figure 7, the under-fitting, right-fit and over-fitting situations encountered in classification studies are shown on the graph depending on the time.

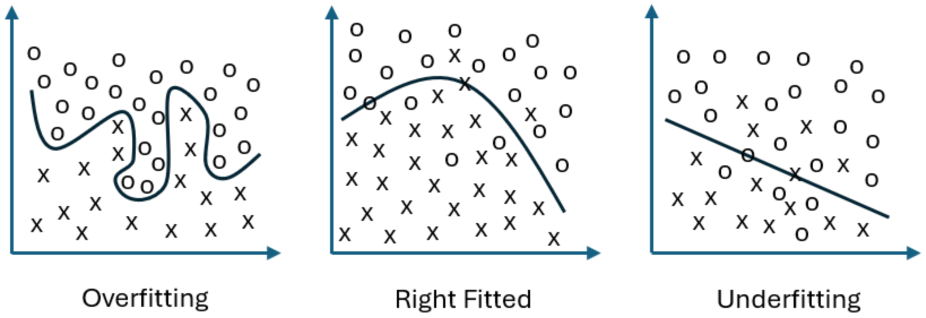

Figure 7. Representation of overfit, right-fit, underfit graphical representation

Dropout is a layer used to ensure that the model is resistant to overfitting. Overfitting, right fitting and underfitting situations can be seen in Figure 7. This layer is based on the principle of covering a certain proportion of neurons randomly determined in each iteration during the training of the model, that is, stopping their activity. Thanks to the neurons that remain dysfunctional, it is possible for the remaining network elements to gain the ability to learn more independently (Baldi and Sadowski, 2013).

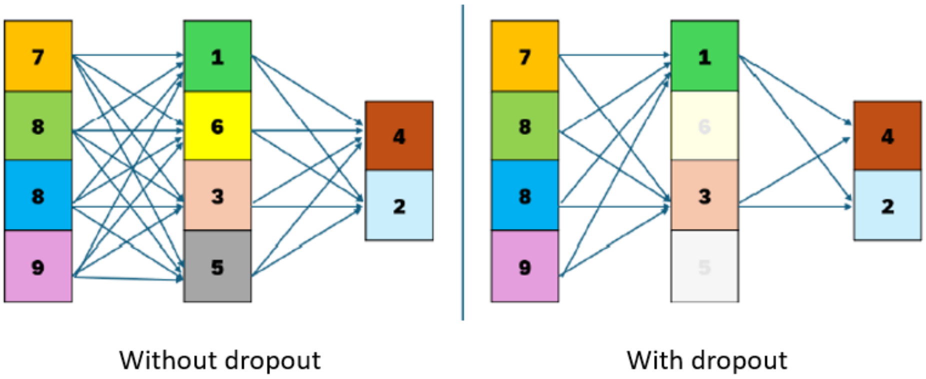

Figure 8. Representative expression of with and without dropout layers

EfficientNetB7 is a ready-to-use model developed by the Google Brain team for use in computer vision studies, which has been previously trained on the ImageNet data set and allows large data sets consisting of complex images to be processed in a short time with high performance. For this reason, the use of this model was preferred in the study (Helms et al., 2018).

Relu is an abbreviation of "Rectified Linear Unit" and is a popular activation function used in deep learning models. This function checks whether the value it receives as input is greater than zero, leaves the value as it is if it is greater than zero, and works to define it as zero if the value is less than zero. Its mathematical equation (1) and graphical representation are as follows (Agarwal et al., 2021).

$$ReLU(x) = max(0, x) \tag{1}$$

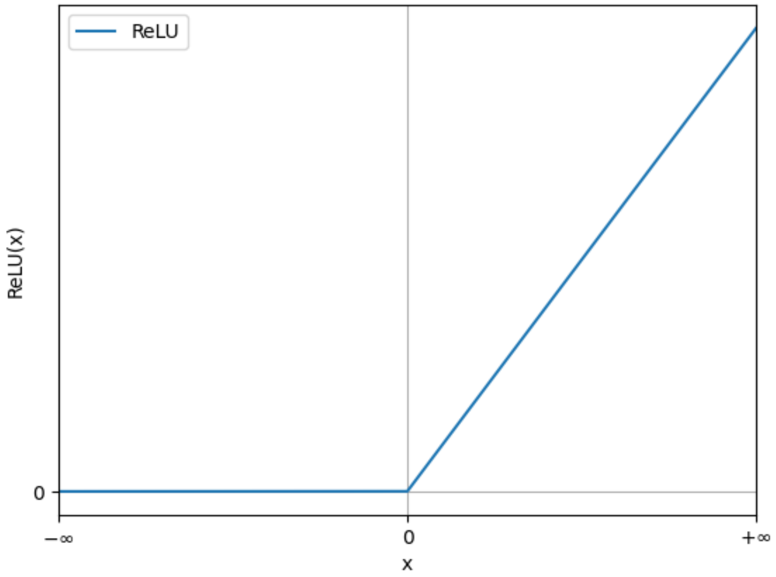

Figure 9. Graph of the ReLU activation function

This function helps to speed up the training process of neural networks. Since the derivative is 1 for values greater than zero, gradients are propagated quickly and efficiently. For values less than zero, it is possible for the model to work more efficiently by causing some neurons to remain dysfunctional and closed since the derivative is zero.

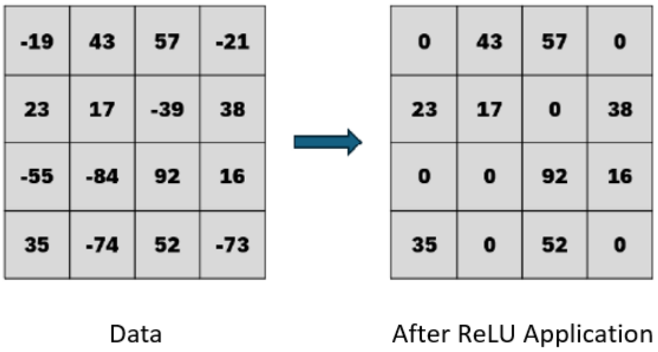

Data

-19	43	57	-21
23	17	-39	38
-55	-84	92	16
35	-74	52	-73

After ReLU Application

0	43	57	0
23	17	0	38
0	0	92	16
35	0	52	0

Figure 10. Transformed matrix with the ReLU activation function applied

Softmax function is a mathematical function that takes a set of real numbers, converts them to values between 0 and 1, and normalizes them by equalizing the sum of all outputs to 1. With the Softmax function, which is frequently used in the output layer in multi-class classification problems, the probability distribution for each class is revealed. The Softmax function works with the logic of normalization by starting by transforming each element with an exponential function and dividing it by the sum of these transformations. Mathematically, the Softmax i-th element for a vector "z" is calculated by the following equation (2) (M. Wang et al., 2018).

$$\text{Softmax}(z_i) = \frac{e^{z_i}}{\sum_j e^{z_j}} \tag{2}$$

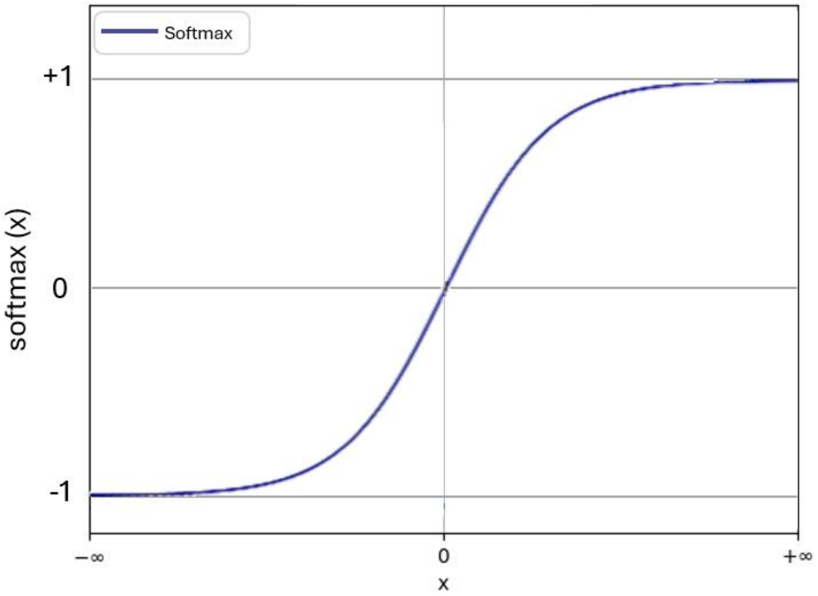

Figure 11. Graphical representation of the Softmax function

Where z is the input vector, e is Euler's number (about 2.718), zi is the i-th element of the input vector, and addition is done over all the elements in the vector. In addition to modeling the probability of each class, this function is also used to ensure that the model's predictions are more stable and balanced (Kılıçarslan et al., 2021).

3.4 Optimization and Compilation

In the optimization and compilation phase, which is one of the processes that should be applied before model training, the optimizer must be defined first. The optimizer of choice in the study is the Adam optimizer. Adam optimizer is an effective stochastic gradient descent algorithm that is widely used in the fields of machine learning and deep learning. The name "Adam" is an abbreviation for "Adaptive Moment Estimation". This optimizer provides adaptive learning rates for each parameter by calculating the unique learning speeds of each parameter. This feature allows different parameters to be updated more evenly and effectively, and often helps to achieve faster and more efficient results than different optimization algorithms. One of the main advantages of the Adam optimizer is that it uses both the first moment (average) and the second moment (variance) values, as shown in the following equations (3,4,5,6). Thus, it is possible for the algorithm to dynamically adjust the learning speed according to the size of the gradients.

$$v_t = \beta_1 * v_{t-1} - (1 - \beta_1) * \ g_t \tag{3}$$

$$s_t = \beta_2 * s_{t-1} - (1 - \beta_2) * \ g_t^2 \tag{4}$$

$$\Delta\omega_t = -\eta \frac{v_t}{\sqrt{s_t + \epsilon}} * \ g_t \tag{5}$$

$$\omega_{t+1} = \omega_t + \ \Delta\omega_t \tag{6}$$

v_t refers to the moving exponential average of time-varying gradients. s_t stands for the exponential moving average of the square of the gradients. β_1, β_2 are the exponential deceleration rates for the first and second moment estimates of gradients. Values can be taken as 0.9 for β_1 and

0.999 for β_2. η (Learning Rate) refers to the speed of the learning process. This value is typically set with a low initial value (for example, 0.001). g_t refers to the gradient of the parameters that the algorithm tries to optimize at time t.

Adam uses learning rates that can be individually adapted for each parameter. In each training step, the first moment estimate of the gradients (moving average of the gradients) and the second moment estimate (the moving average of the squares of the gradients) are calculated first. Subsequently, these calculated values are initially used to update the parameters by correcting the gradients and gradient squares with bias-correlation steps against low estimates (Bock and Weiß, 2019).

3.5 Metrics

In this study, the categorical cross-entropy function, which is highly preferred in multiclass classification problems, is used as the loss function. This function (7,8) is used to maximize the agreement between the probability distributions predicted by the model and the actual labels. In Figure 12, this issue is schematized.

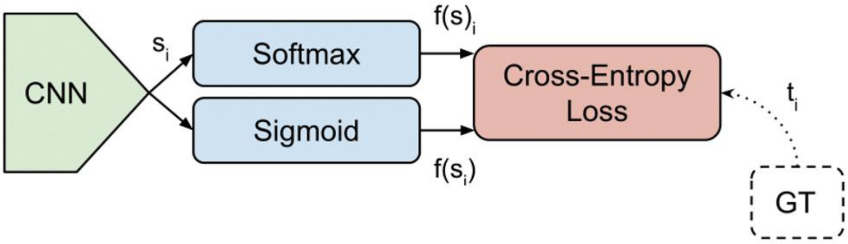

Figure 12. Loss function expression in CNN architecture (Swasthik, 2020)

$$CE = -\sum_{i}^{C} t_i \log(f(s)_i) \tag{7}$$

$$CE = -\sum_{i=1}^{C'=2} t_i \log\big(f(s_i)\big) = -t_1 \log\big(f(s_1)\big) - (1 - t_1) \log(1 - f(s_1)) \tag{8}$$

c Represents the number of classes. This is the number of different categories that the model tries to predict. ti, represents the actual labels. These values are usually 0 or 1; If it belongs to a class, it is encoded as 1, if not, it is encoded as 0. f(si) refers to the probabilities that the model predicts. log is a logarithm function. In cross-entropy loss, the logarithm of the estimated probabilities is taken. Logarithms play an important role in measuring the accuracy of the predictions made by the model; Correct predictions reduce loss, while incorrect predictions increase loss (Barz and Denzler, 2020).

In the study, accuracy metric was used to evaluate the performance of the model. Accuracy indicates the ratio of the model's correct predictions to total predictions and is often considered a measure of success in classification problems. Accuracy ratio can be calculated with the equation (9) below accorting to values determined in the matrix (Figure 13).

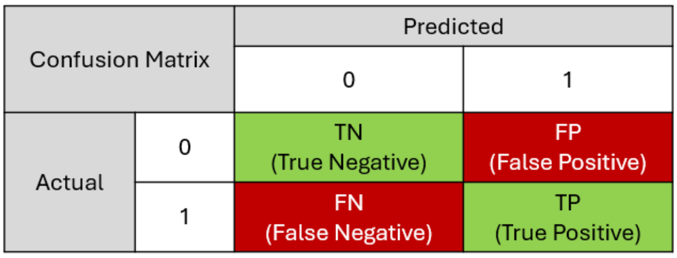

Confusion Matrix		Predicted	
		0	1
Actual	0	TN (True Negative)	FP (False Positive)
	1	FN (False Negative)	TP (True Positive)

Figure 13. Confusion matrix

$$Accuracy = \frac{TP + TN}{TP + TN + FP + FN} \tag{9}$$

The table above is a confusion matrix used to evaluate the performance of the classification model. The confusion matrix is used to show the classification success of the model in detail by comparing the predictions of the model with the actual values. The terms used here are; TP (True Positive) is the number of cases that the model predicts as positive and that are actually positive. That is, it refers to the number of positive cases that are correctly classified. FP (False Positive) is the number of cases that the model predicted as positive but were actually negative. This can also be referred to as a false alarm. FN (False Negative) is the number of cases that the model predicted as negative but were actually positive. This can also be considered a missed opportunity. TN (True Negative) is the number of cases that the model predicts as negative and that are actually negative. That is, it is the negative cases that are correctly classified (Maxwell et al., 2021).

3.6 Model Training

After the optimization process, the training process of the model is started within the scope of a certain number of batches and epochs. The cycle can be schematized as seen in Figure 14.

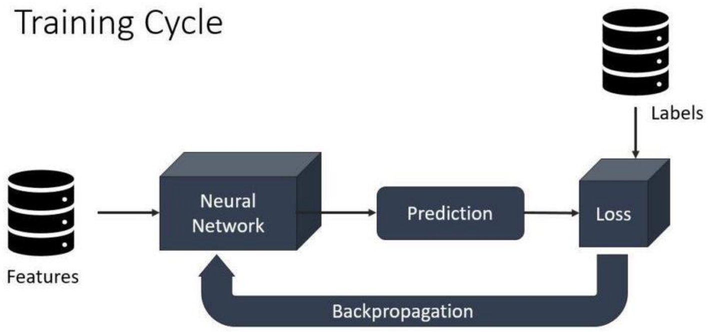

Figure 14. Representation of the model training process in the form of a flow diagram (Glasmacher, 2022)

Batch size specifies the number of instances that the model will use for training in each iteration. The batch_size parameter allows the model to make its updates more frequently, helping the training process go faster. The epoch number, on the other hand, indicates how many full cycles the training process will be run. For example, if 30 epochs are specified in the model, it means that the training data set will be processed by the model 30 times from start to finish. Figure 15 schematizes the iterations within 1 epoch.

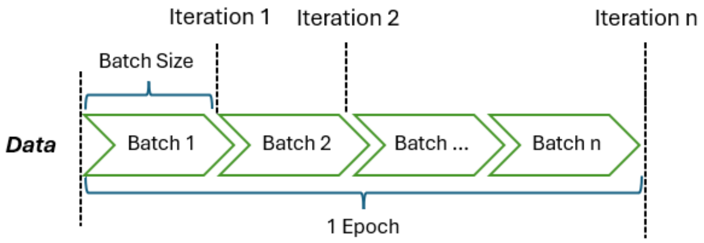

Figure 15. Formal expression of the concepts of Batch and Epoch

The duration of this process can take quite a long time, in the order of hours or days, depending on the complexity of the model and data set, and the performance of the computer hardware (Smith et al., 2018).

3.7 Accuracy and Loss Values, Confusion Matrix

The success indicator of a deep learning model can be considered as the convergence of the accuracy rate to 1 and the convergence of the loss rate to 0 as the number of iterations progresses in the training process. It is important to record the accuracy and loss values obtained during the iterations and to graph them at the end of the training in order to visualize the model performance (Figure 16, 17). The loss and accuracy values reached as of the last iteration emerged as follows for the model we created and trained within the scope of our study.

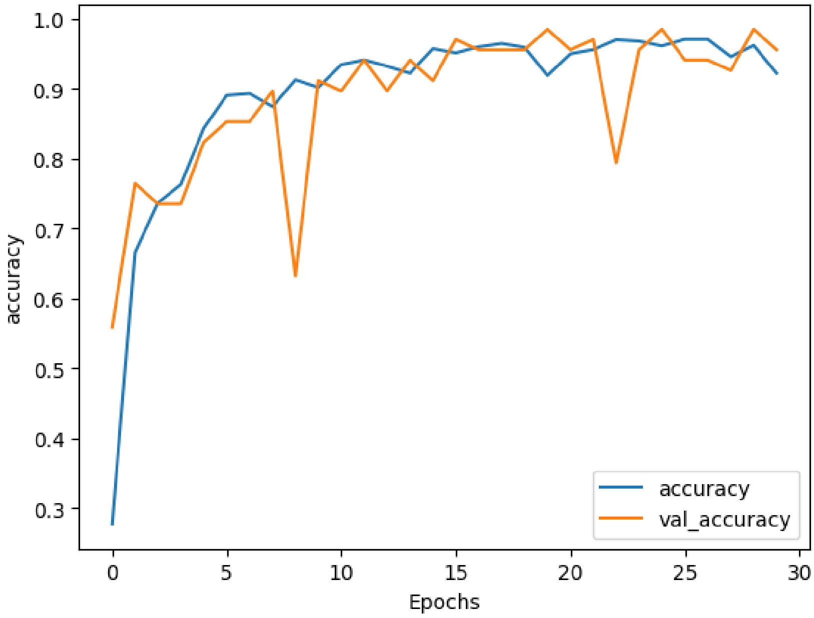

Figure 16. “Accuracy – Epoch” graph created at the end of the training

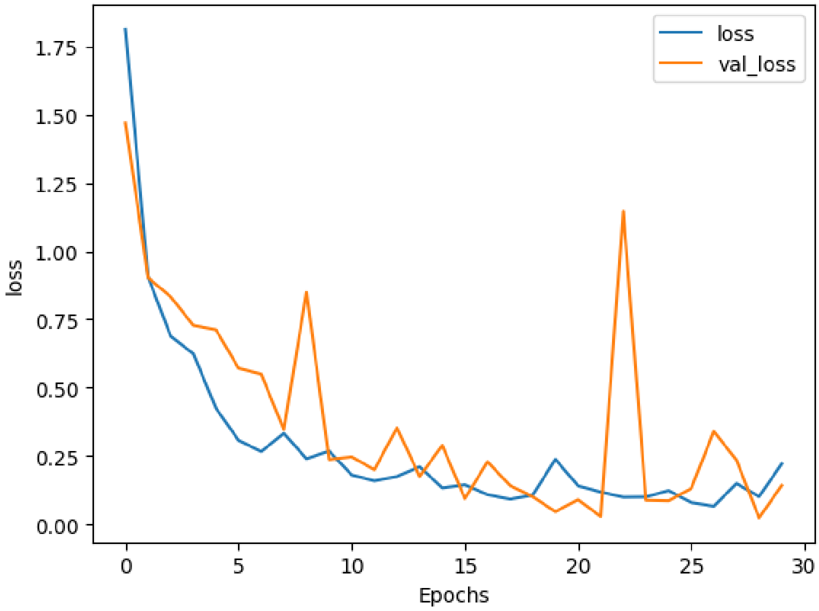

Figure 17. “Loss – Epoch” graph created at the end of the training

As a result of the training of the model, a confusion matrix was Created. The actual label values and the numbers of the estimated impact values were presented in the confusion matrix shown in Figure 18.

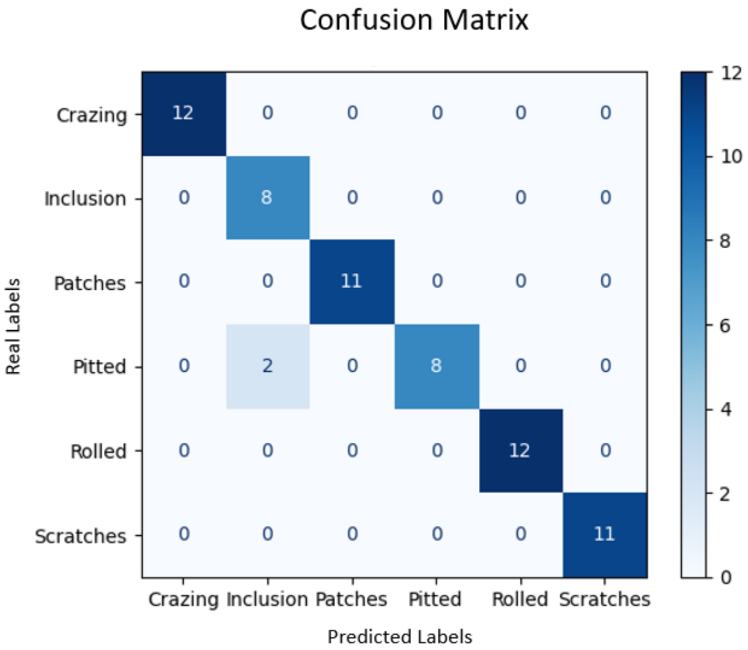

Figure 18. Confusion Matrix obtained after model training

3.8 Testing the Model

After the training process of the model was completed, the test process was applied. At this stage, the performance of the model on the test data set was evaluated by visualizing. First, 9 images were randomly selected from the test data set and the model was provided with prediction. The prediction results were then compared with the actual labels. The images are visualized in a 3x3 matrix layout, and actual class information is added to each along with the model's prediction. If the prediction is correct, the label is shown in blue, and if it is incorrect, the classification accuracy of the model is easily understood visually. As a result of testing whether the sample images randomly taken from the test set were correctly predicted, the following result was reached. In the first test, it was seen that all 9 images examined were correctly estimated and can be seen in Figure 19.

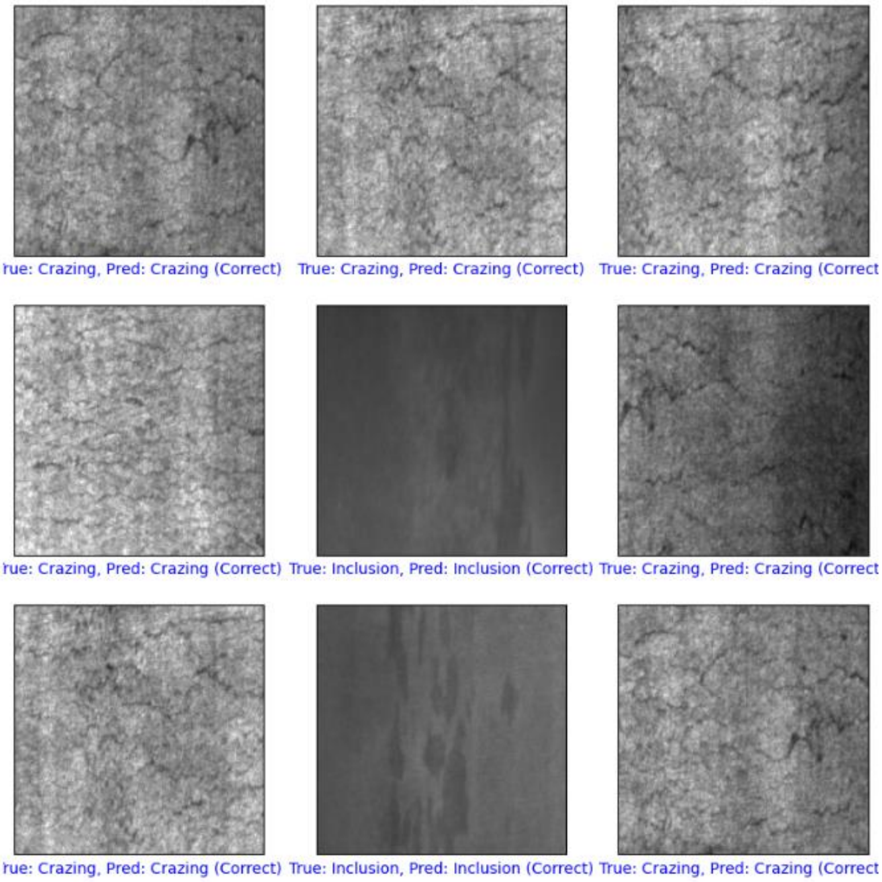

Figure 19. Estimation of 9 randomly selected images from the test set. Incorrect predictions are expressed in red and correct predictions are expressed in blue writing, in this test all predictions are correct

In addition, the model was installed on the Nvidia Jetson Nano device and run in the python environment. This device is a developer computer with high graphics processing capability and can be used to analyze instant live video data with external cameras that can be integrated onto it. In the Linux environment, which is the operating system of the device, the model file was converted to the required format (.onnx) in order to run the relevant Python code, and the Python program was coded and run, where both the live image and how many errors were detected with how many probabilities can be read on the screen connected to the device, by performing the error classification function by detecting live images with the camera using this model file on the device (Oranen, 2021). Under real conditions, the errors on the samples were detected with a camera and tested in real time and the model was verified to work successfully as shown in Figure 20. As an example, the Patches error could be detected more than once with a performance rate of more than 90%.

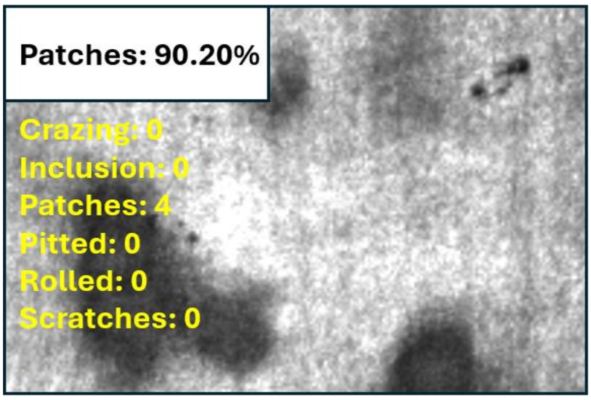

Figure 20. Testing the model with a camera

4. RESULTS AND DISCUSSION

After the completion of the training of the model, the status of the training performance was revealed by the metrics used. These metrics are accuracy and loss graphs and confusion matrix. Accuracy and loss graphs were created using the accuracy values reached at the end of each of the 30 cycles conducted in the model training. The values that make up the chart are given in the table below.

Epoch	Accuracy	Validation Accuracy (Val_Accuracy)
1	0.2111	0.5588
2	0.6227	0.7647
3	0.7344	0.7353
4	0.7618	0.7353
5	0.8407	0.8235
6	0.8917	0.8529
7	0.8878	0.8529
8	0.8999	0.8971
9	0.8958	0.6324
10	0.8746	0.9118
11	0.9257	0.8971
12	0.9470	0.9412
13	0.9261	0.8971
14	0.9306	0.9412
15	0.9572	0.9118
16	0.9607	0.9706
17	0.9455	0.9559
18	0.9722	0.9559
19	0.9550	0.9559
20	0.9471	0.9853
21	0.9403	0.9559
22	0.9568	0.9706
23	0.9616	0.7941
24	0.9664	0.9559
25	0.9564	0.9853
26	0.9598	0.9412
27	0.9769	0.9412
28	0.9489	0.9265
29	0.9644	0.9853
30	0.9159	0.9559

The tests carried out with the numerical and graphical results obtained have shown that the model creation and training work has sufficient reliability. The "Test loss" obtained using the test dataset was 0.1437525451183319, while the "Test accuracy" was 0.96875. In other words, it is understood that the success of the model has reached the level of 96.88%. The confidence interval was calculated as CI=[0.92621,1.01139] by using the test accuracy and test loss values obtained at the end of the testing of the model. A 95% confidence interval is acceptable between 0.926 and 1.0, as the confidence interval cannot be greater than 1. It is also aimed to calculate the p-value in order to support the successful result. However, in order to calculate the p-value, there must be two different groups of comparable results. Since validation results are obtained during the training process, it may be misleading to use them for calculating the p-value together with the test results. However, since we do not have any other comparison elements, it was decided to obtain the p value using validation data.

The values obtained at the end of the T-Test were "T-Statistic: -2.9503" and "P-Value: 0.0046". Since the value of 0.0046 is considerably smaller than the generally accepted significance value of 0.05, it can be said that there is a statistically significant difference between the two groups. If the T-statistic value is negative, it means that the Validation results are lower than the Test results. In other words, it is possible to say that the model exhibits a higher success in the Test set, that is, it produces a more successful result in real-world conditions that it does not encounter in the training process. On the other hand, some important parameters such as learning rate, number of batches, number of epochs, and optimizer type used in the establishment of the CNN model are factors that can affect the performance of the model. These values were selected based on the mean values used in the sample studies found in the literature, and the evaluation of the effects of different parameters on the model can be considered as a new study.

This study has many similarities and differences with similar studies in the literature. For example, in a similar study, innovative improvements were made to the Faster R-CNN algorithm, such as restructuring the network structure and using a deformed convolution network, to improve the detection of small and complex steel surface defects. In this way, the detection accuracy was increased by 12.8% to 75.2% (Zhao et al., 2021).

Another study is developing a CCVAE model that generates data for each type of defect using a Convolutional Variational Autoencoder (CVAE) to generate sufficient data for rare defects. This improves the generalization performance of DCNN-based classification, enabling defect detection with high accuracy in industrial applications (Yun et al., 2020).

In another application, a combination of improved ResNet50 and improved Faster R-CNN algorithms is proposed to enable automatic detection of steel surface defects. This method aims to overcome the limitations of traditional and existing deep learning-based methods by offering a 98.2% accuracy rate and faster uptime (Wang et al., 2021).

This model is ready for both academic and industrial use. At the end of the training process of the model, the final model file, which includes the weights and configuration properties learned, is saved out of the code as an external file. By using the weights in this file, it has become possible to make industrial-level applications using different data sets and real test samples (metal plates). In order to test the model in real conditions, it was decided to use the Nvidia Jetson Nano Developer Kit hardware to be used in the application development phase. It has been shown that these and similar devices can exhibit sufficient success for beginner and intermediate industrial applications.

It will be useful to work with a larger data set to increase the level of performance of the study. In addition, it may be possible to obtain a lower loss rate with a higher accuracy, as different results are obtained when model training is reconsidered using different layers, activation functions and parametric values. In this context, studies can be carried out on the use of different parameters to shorten the training time of the model. For example, the model can be retrained using different values for filter sizes and quantities, either individually or in different combinations. Thus, optimization can be made for model training in a shorter time with lower batch and epoch values. On the industrial application side of the study, application performance will increase when higher resolution cameras and industrial computers with higher image processing capabilities are used. The prototype devices to be developed can be equipped with many functions at the simple or advanced robotic level to record and transmit data, make statistical evaluations, perform mechanical marking or repair.

In this context, the study has been presented to the literature as a basic study in order to shed light on scientific, technological or industrial studies to be carried out in the future.

5. CONCLUSION

In this study, the developed model demonstrated sufficient reliability and robustness, confirming its readiness for both academic and industrial applications. The final model file, incorporating the learned weights and configuration properties, enables industrial-level applications with varied data sets and real test samples, such as metal plates. The use of the Nvidia Jetson Nano Developer Kit for real-world testing confirmed its capability for beginner and intermediate industrial applications. Future work with larger datasets could enhance the model's performance. Moreover, retraining the model with different layers, activation functions, and parametric values could yield lower loss rates and higher accuracy. Optimizing training time by adjusting filter sizes, quantities, batch, and epoch values is another avenue for improving the model. Industrial applications could benefit from higher resolution cameras and more powerful image processing computers. Enhanced prototype devices could incorporate functions for data recording, statistical evaluations, mechanical marking, or repairs at both simple and advanced robotic levels. This study contributes to the literature as a foundational work, providing valuable insights for future scientific, technological, and industrial research.

6. ACKNOWLEDGEMENTS

We would like to thank Bandırma Onyedi Eylül University Scientific Research Projects Unit for their support throughout our project numbered BAP 22-1010-002.

7. CONFLICT OF INTEREST

Author approve that to the best of their knowledge, there is not any conflict of interest or common interest with an institution/organization or a person that may affect the review process of the paper.

8. AUTHOR CONTRIBUTION

Can Tuncer and Cemil Közkurt contributed to the conceptualization, writing-original draft and visualation of the study. Can Tuncer, Cemil Közkurt, and Serhat Kılıçarslan contributed to the methodology and writing review and editing. Can Tuncer contributed to data curaiton and software. Cemil Közkurt contributed to the formal analysis.

9. REFERENCES

Agarwal M., Gupta S., Biswas K. K., A new Conv2D model with modified ReLU activation function for identification of disease type and severity in cucumber plant. Sustainable Computing: Informatics and Systems 30, 100473, 2021.

Baldi P., Sadowski P. J., Understanding Dropout. Advances in Neural Information Processing Systems 26, 2013.

Barz B., Denzler J., Deep Learning on Small Datasets without Pre-Training using Cosine Loss, In Proceedings of the IEEE/CVF winter conference on applications of computer vision, 2020, pp: 1371-1380.

Bbouzidi S., Hcini G., Jdey I., Drira F., Convolutional Neural Networks and Vision Transformers for Fashion MNIST Classification: A Literature Review. arXiv preprint arXiv:2406.03478, 2024.

Bock S., Weiß M., A Proof of Local Convergence for the Adam Optimizer. 2019 International Joint Conference on Neural Networks (IJCNN), July, 2019, pp: 1-8.

Dung L., Mizukawa M., A Pattern Recognition Neural Network Using Many Sets of Weights and Biases. 2007 International Symposium on Computational Intelligence in Robotics and Automation, 2007, pp: 285–290.

Glassmacher S., https://galaxyinferno.com/epochs-iterations-and-batch-size-deep-learning-basics-explained/, 2022, (24 October 2022).

Gulli A., Pal S., Deep Learning with Keras. Packt Publishing Ltd., 2017.

Haji S. H., Abdulazeez A. M., Comparison of Optimization Techniques Based on Gradient Descent Algorithm: A Review. PalArch's Journal of Archaeology of Egypt / Egyptology 18(4), 2715-2743, 2021.

Helms M., Ault S. V., Mao G., Wang J., An Overview of Google Brain and Its Applications. Proceedings of the 2018 International Conference on Big Data and Education, March, 2018, pp: 72-75.

Jin J., Dundar A., Culurciello E., Flattened Convolutional Neural Networks for Feedforward Acceleration, arXiv preprint arXiv:1412.5474,2015.

Kılıçarslan S., Adem K., Çelik M., An overview of the activation functions used in deep learning algorithms. Journal of New Results in Science, 10(3), 2021.

LeCun Y., Bengio Y., Hinton G., Deep learning. Nature 521(7553), 436-444, 2015.

Lv X., Duan F., Jiang J., Fu X., Gan L., Deep Metallic Surface Defect Detection: The New Benchmark and Detection Network. Sensors 20(6) 1562, 2020.

Maharana K., Mondal S., Nemade B., A review: Data pre-processing and data augmentation techniques. Global Transitions Proceedings 3(1), 91-99, 2022.

Manaswi N. K., Understanding and Working with Keras. In N. K. Manaswi (Ed.), Deep Learning with Applications Using Python: Chatbots and Face, Object, and Speech Recognition With TensorFlow and Keras, Apress, pp:1–43, 2018.

Mastromichalakis S. Parametric Leaky Tanh: A New Hybrid Activation Function for Deep Learning arXiv preprint arXiv:2310.07720, 2023.

Maxwell A. E., Warner T. A., Guillén L. A., Accuracy Assessment in Convolutional Neural Network-Based Deep Learning Remote Sensing Studies—Part 2: Recommendations and Best Practices. Remote Sensing 13(13), 2591, 2021.

Mo X., Tao K., Wang Q., Wang G., An Efficient Approach for Polyps Detection in Endoscopic Videos Based on Faster R-CNN. 2018 24th International Conference on Pattern Recognition (ICPR), August, 2018, pp: 3929-3934.

Montesinos López O. A., Montesinos López A., Crossa J., Overfitting, model tuning, and evaluation of prediction performance. In Multivariate statistical machine learning methods for genomic prediction. Cham: Springer International Publishing, pp: 109-139, 2022.

Moor J., The Dartmouth College Artificial Intelligence Conference: The Next Fifty Years. AI Magazine 27(4), 87-87, 2006.

Oranen L., Utilizing deep learning on embedded devices, 2021.

Rasamoelina A. D., Adjailia F., Sinčák P., A Review of Activation Function for Artificial Neural Network. 2020 IEEE 18th World Symposium on Applied Machine Intelligence and Informatics (SAMI), 281–286, 2020.

Raschka S., Mirjalili V., Python Machine Learning: Machine Learning and Deep Learning with Python, scikit-learn, and TensorFlow 2. Packt Publishing Ltd., 2019.

Rice L., Wong E., Kolter Z., Overfitting in adversarially robust deep learning. Proceedings of the 37th International Conference on Machine Learning, November, 2020, pp: 8093-8104.

Sahu M., Dash R., A Survey on Deep Learning: Convolution Neural Network (CNN). In D. Mishra, R. Buyya, P. Mohapatra, & S. Patnaik (Eds.), Intelligent and Cloud Computing, Springer, pp: 317-325, 2021.

Shinde P. P., Shah S., A Review of Machine Learning and Deep Learning Applications. 2018 Fourth International Conference on Computing Communication Control and Automation (ICCUBEA), August, 2018, pp: 1-6.

Smith S. L., Kindermans P. J., Ying C., Le Q. V., Don’t Decay the Learning Rate, Increase the Batch Size arXiv preprint arXiv:1711.00489v2, 2018.

Sobhana M., Hindu K., Girishma N., Bhavani P. S., Rajeswari S., A Comparitive Evaluation Of Custom CNN, Sequential CNN & Dense-Net Models to forecast Dementia. 2023 Second International Conference on Augmented Intelligence and Sustainable Systems (ICAISS), 2023 pp: 287-293,2023.

Song K., Yunhui Y., NEU surface defect database. Northeastern University, 2019.

Swasthik, “Understanding Entropy and Losses and all those confusing names of losses,”, 2020, https://medium.com/@swasthik0304/understanding-entropy-and-losses-and-all-those-confusing-names-of-losses-d7444711cf3c>, (21 April 2020).

Turban E., Watkins P. R., Integrating Expert Systems and Decision Support Systems. MIS Quarterly, 10(2), 121-136, 1986.

Vansh, “Predicting House Prices Using Keras Functional API” 2022, <https://www.analyticsvidhya.com/blog/2022/04/predicting-house-prices-using-keras-functional-api/>, (9 May 2022).

Wang M., Lu S., Zhu D., Lin J., Wang Z., A High-Speed and Low-Complexity Architecture for Softmax Function in Deep Learning. 2018 IEEE Asia Pacific Conference on Circuits and Systems (APCCAS), October, 2018, pp: 223-226.

Wang Q., Ma Y., Zhao K., Tian Y., A Comprehensive Survey of Loss Functions in Machine Learning. Annals of Data Science 9(2), 187-212, 2022.

Wang S., Xia X., Ye L., Yang B., Automatic detection and classification of steel surface defect using deep convolutional neural networks. Metals 11 (3), 1-23, 2021.

Warden, Pete, “Why GEMM is at the heart of deep learning” 2015, <https://petewarden.com/2015/04/20/why-gemm-is-at-the-heart-of-deep-learning/>, (20 April 2015)

Yun J. P., Shin W. C., Koo G., Kim M. S., Lee C., Lee S. J., Automated defect inspection system for metal surfaces based on deep learning and data augmentation. Journal of Manufacturing Systems 55, 317-324, 2020.

Zhao W., Chen F., Huang H., Li D., Cheng W., A new steel defect detection algorithm based on deep learning. Computational Intelligence and Neuroscience 2021(1), 5592878, 2021.

JOURNAL of
MATERIALS and MECHATRONICS:A

e-ISSN 2717-8811
JournalMM, 2024, 5(2), 286-302
https://doi.org/10.55546/jmm.1566700

Araştırma Makalesi / Research Article

Optimization of Printing Parameters of PLA and ABS Produced by FFF

İsmail Aykut KARAMANLI[1*], Kadircan TAHNAL[2]

[1*] Bozok University, Sorgun Vocational School, Department of Motor Vehicles and Transportation Technologies, Yozgat, Türkiye,
ORCID ID: https://orcid.org/0000-0002-6725-2662, aykutkaramanli@gmail.com
[2] Toyota Plaza Mezcar Otomotiv, İstanbul, Türkiye,
ORCID ID: https://orcid.org/0009-0005-4336-9419, kadirtahnal2209@gmail.com

Geliş/ Received: 14.10.2024; **Revize/Revised:** 15.11.2024 **Kabul / Accepted:** 18.11.2024

ABSTRACT: In this study, the changes in tensile strength of PLA and ABS specimens, the most commonly used materials in additive manufacturing with FFF, were investigated as a function of fill rate and print speed. Tensile specimens were fabricated for different fill rates and speeds and tensile tests were performed. Increasing the fill rate increases the tensile strength. Increasing or decreasing the print speed too much has a negative effect on tensile strength. Filament usage and printing times were also calculated. With the data obtained, an optimization model was created using response surface methodology. The aim of this study is to optimize the strength/cost of ABS and PLA, the two preferred FFF materials. The novelty of the study is to investigate the strength/cost optimization for different material types in terms of UTS, filament consumption and printing speed. For each material type, high tensile strength, low printing time and low filament used conditions were determined for the optimization model. The optimum parameters for PLA are obtained at 66.77% fill level and 78.43% speed rate. For ABS, optimum values are obtained at 79.5% fill rate and 135% speed rate. Then, samples were produced for optimum conditions and experiments and calculations were repeated. The numerical results obtained with the model were compared with the experimental results. It is found that the model estimates the output parameters with high accuracy. This proves the accuracy of the proposed optimization model.

Keywords: 3D printing, Tensile strength, ABS, PLA, Optimization

---

*Sorumlu yazar / Corresponding author: aykutkaramanli@gmail.com

Bu makaleye atıf yapmak için /To cite this article

Karamanlı, İ. A., Tahnal, K. (2024). Optimization of Printing Parameters of PLA and ABS Produced by FFF. Journal of Materials and Mechatronics: A (JournalMM), 5(2), 286-302.

1. INTRODUCTION

Metal Fused filament fabrication (FFF), a type of additive manufacturing (AM), is a method based on converting the designs prepared with computer aided design (CAD) data programs into G codes, and then melting the raw material (filament) with an extruder in accordance with the G codes and depositing it in layers (Khan et al., 2018). This method has rapidly popularized due to its low equipment and raw material costs, short production time and easy applicability (Alabd and Temiz, 2024). With this rapid expansion, FFF has been used in various fields such as aerospace industry (Yao et al., 2019), robotics (Kaya et al., 2023), biomedical applications (Pehlivan et al., 2024). This method is also preferred because infill rate, infill pattern and printing speed are adjustable (Fontana et al., 2022). In addition, the process allows for functional grading and manufacturing at different fill rates, making it possible to create regions with different mechanical properties on the same product (Temiz, 2024b). This is especially desirable for biomedical structures such as individually specialized prosthesis-orthotics (X. Wang et al., 2016).

Although there are many positive aspects, there are also negative aspects of the FFF process. The mechanical properties and dimensional stability of the products obtained as a result of the process vary as a function of many parameters such as fill rate and fill pattern, layer height (Srinivasan et al., 2020), build orientation (Öz and Öztürk, 2023), extrusion temperature (Hikmat et al., 2021), operating conditions of the product (Grasso et al., 2018). The fact that the mechanical performance of FFF, which is quite new and developing day by day, depends on many parameters has caused researchers to focus on this field. The most preferred filament types as printing raw materials are polylactic acid (PLA), acrylonitrile butadiene styrene (ABS) and polyethylene terephthalate glycol (PETG) (Güdür et al., 2023). In the study performed by Rajpurohit and Dave in which the variation of the ultimate tensile strength (UTS) value of PLA according to the printing parameters was investigated; raster angle, raster width, layer height indicating layer angle were selected as variables (Rajpurohit and Dave, 2019). Tensile tests demonstrated that all variables were effective on UTS. It was also found that the raster angle has an effect on fracture mechanics (Rajpurohit and Dave, 2019). In another study, the effect of fill pattern on UTS and flexural strength was investigated. Rectilinear, concentric, HoneyComb and HilbertCurve patterns were selected as fill patterns. The tests showed that the fill pattern was effective on the mechanical properties and the best strength was obtained with rectilinear fill pattern (Khan et al., 2018). In the study by Dwiyati et al. in which the variation of tensile strength of ABS according to layer thickness was investigated, it was found that the decrease in layer thickness increased the tensile strength (Dwiyati et al., 2019). Rifuggiato et al. examined the effect of fill rate and fill pattern on UTS and reported that the gaps formed in the microstructure and the distribution of these gaps are effective in the differentiation of UTSs (Rifuggiato et al., 2022).

The changes in mechanical properties depending on quite different parameters require optimization studies to be carried out on production parameters. In the study by Samykano et al. layer height, raster angle and filler density for ABS material were optimized according to UTS and production costs. According to the results, the best UTS/cost ratio was obtained with 0.5 mm layer height, 65^o raster angle and 80% fill density (Samykano et al., 2019). In another study, optimization of layer height, raster angle and layer width for UTS and surface roughness of PLA specimens was performed. Optimum results were obtained for 0 ^{o} raster angle, 0.1 mm layer height and 0.6 mm layer width (Temiz, 2024a). Although optimization studies focus on changing the printing parameters, there are also comparative optimization of specimens produced by different AM methods. Bayraklılar et al. compared the mechanical properties of ultraviolet radiation (UVR) polymer produced by stereolithography (SLA) with ABS and PLA produced by FFF. The comparisons were made on tensile and flexural strengths and hardnesses. The best results for all input parameters were obtained with UVR. Differences in mechanical properties were found to be based on differences in microstructure (Bayraklılar et al., 2023).

Although there are studies in the literature on both the mechanical properties of the specimens produced with FFF and the optimization of printing parameters, there is no study in which both the mechanical properties and strength/cost ratios of different materials are investigated in detailed. In addition, previous studies have investigated the effect of fill rate, layer height and printing orientation on mechanical properties for a single material type. However, the comparison of mechanical properties and cost changes for different material types is a gap in the literature. The parameters investigated were selected according to this gap in the literature. In the current study, tensile tests were performed on specimens produced from two different materials, ABS and PLA, at different fill rates and at different printing speeds. The data obtained were evaluated in terms of UTS, printing times and the amount of filament spent. The results were optimized by response surface methodology (RSM). The aim of this study is to optimize the strength/cost of ABS and PLA, the two preferred FFF materials. The novelty of the study is to investigate the strength/cost optimization for different material types in terms of UTS, filament consumption and printing speed. By establishing the optimum parameters, it will be possible to increase the strength of the parts produced with 3D printing for the manufacturing sector and reduce labor and production costs.

2. MATERIALS AND METHODS

2.1 Materilas

The specimens investigated in the study were produced from two different filaments compatible with FFF, namely PLA and ABS. The filaments were purchased from the same company and have a diameter of 1.75 mm. The mechanical properties of the filaments are detailed in Table 1. The fill pattern for all specimens is grid.

Table 1. Mechanical Properties of PLA and ABS (Esun, 2024b, 2024a)

Material	Density (g/cm^3)	Flexural Modulus (MPa)	Tensile Strength (MPa)	Bending Strength (MPa)	Elongation (%)
PLA	1.23	1973	60	74	20
ABS	1.04	1177	43	66	22

2.2 Optimization Methodology

Optimizations were performed using RSM. The reason for choosing this optimization method is that RSM allows the estimation of non-experiment conditions with great accuracy with a small number of experiments. (Karamanlı et al., 2024). The inputs for this study are material type, fill rate and speed rate. The outputs are UTS, spent filament and printing time. The aim of the optimization is to find the optimum printing parameters for high tensile strength, low spent filament and printing time conditions. The design matrix for RSM was created with MiniTab Software. The matrix used was L18 full factor design. The design matrix and printing parameters are given in Table 2. The inputs for the RSM model can be given as in equation 1(K. Wang and Lam, 1999):

$$y = F(x_1, x_2, x_3, \dots, x_m) \tag{1}$$

where $x_1, x_2, x_3, \ldots, x_m$ and y indicates input and output parameters respectively. The main principle of RSM is to relate inputs to outputs. This is obtained by modelling a quadratic equation (equation 2) (K. Wang and Lam, 1999);

$$y = b_0 + \sum_{i=1}^{m} b_i x_i + \sum_{i=1}^{m-1} \sum_{j \geq i}^{m} b_{ij} x_i x_j + \sum_{i=1}^{m} b_{ii} x_i^2 + \varepsilon \tag{2}$$

In the equation, i indicates the linear coefficient, j indicates the second-order coefficient, b indicates the regression coefficient, m indicates the number of parameters, and ε indicates the error defined in the response (K. Wang and Lam, 1999). Furthermore, the effect levels of the parameters were evaluated utilizing Analysis of Variance (ANOVA). The calculations regarding statistics occurred with a confidence level of 95%.

Table 2. L18 full factor design matrix for response surface methodology

Test No	Material Type	Fill Rate (%)	Speed Rate (%)
1	ABS	70	125
2	ABS	100	75
3	ABS	100	100
4	ABS	85	135
5	PLA	100	100
6	ABS	70	75
7	PLA	70	75
8	PLA	65	100
9	PLA	70	125
10	PLA	85	135
11	PLA	100	125
12	PLA	85	100
13	PLA	85	65
14	ABS	65	100
15	ABS	85	65
16	ABS	100	125
17	PLA	100	75
18	ABS	85	100

2.3 Specimen Production

For tensile tests, a tensile specimen in the shape of a dog-bone according to ASTM D638-14 Type-1 was preferred (ASTM, 2022). The dimensions of the specimen are illustrated in Figure 1. The computer aided design (CAD) model of the specimen was created with the student version of SOLIDWORKS and saved in STL format. Slicing and G-code generation was performed with Creality's slicing software.

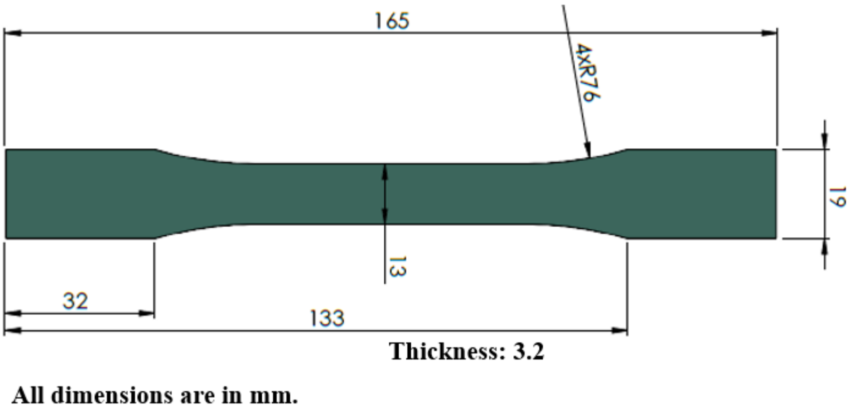

Figure 1. ASTM D638-14 Type-1 tensile test specimen (ASTM, 2022)

The specimens were produced with a Creality K1 model 3D printer. Printing parameters were selected according to the parameters recommended by Esun company for Creality K1 model 3D printer (Esun, 2024c). The recommended printing speeds were accepted as 100% speed rate. Printing parameters for 100% speed rate are given in Table 3. All of the printing speed parameters were changed in the same percentages according to the optimum value of each material type. For example, for a PLA sample produced under 75% speed rate conditions, the infill production speed is 225 mm/s, while for ABS it is 37.5 mm/s. During printing operations, the in-cab conditions were controlled by a temperature and humidity meter. The whole production was carried out at 26-38 °C in-cabinet temperature and 32-44% humidity conditions. At least 3 specimens were produced for each condition. The heating table temperature for PLA specimens was 60 °C and for ABS was 105 °C. No adhesion enhancing adhesive was used in the production of both specimens.

Table 3. Printing parameters for 100% speed rate (Esun, 2024c)

Material Type	Printing Temperature (°C)	Layer Height (mm)	Printing Speed (mm/s)	
PLA	220	0.2	Infill	:300
			Outer Wall	:200
			Inner Wall	:300
			Top/Bottom	:200
			Travel	:500
			Layer	:50
			Skirt	:50
ABS	240	0.2	Infill	:50
			Outer Wall	:30
			Inner Wall	:25
			Top/Bottom	:25
			Travel	:100
			Layer	:20
			Skirt	:20

2.3 Tensile Tests

Tensile tests were performed using a 60 kN tensile machine at room temperature at a speed of 5 mm/min in accordance with ASTM D638 (ASTM, 2022). The specimens were subjected to tensile tests until fracture. The tests were repeated at least three times for each condition and the final values were determined by averaging the results. The process steps of the study are presented in Figure 2.

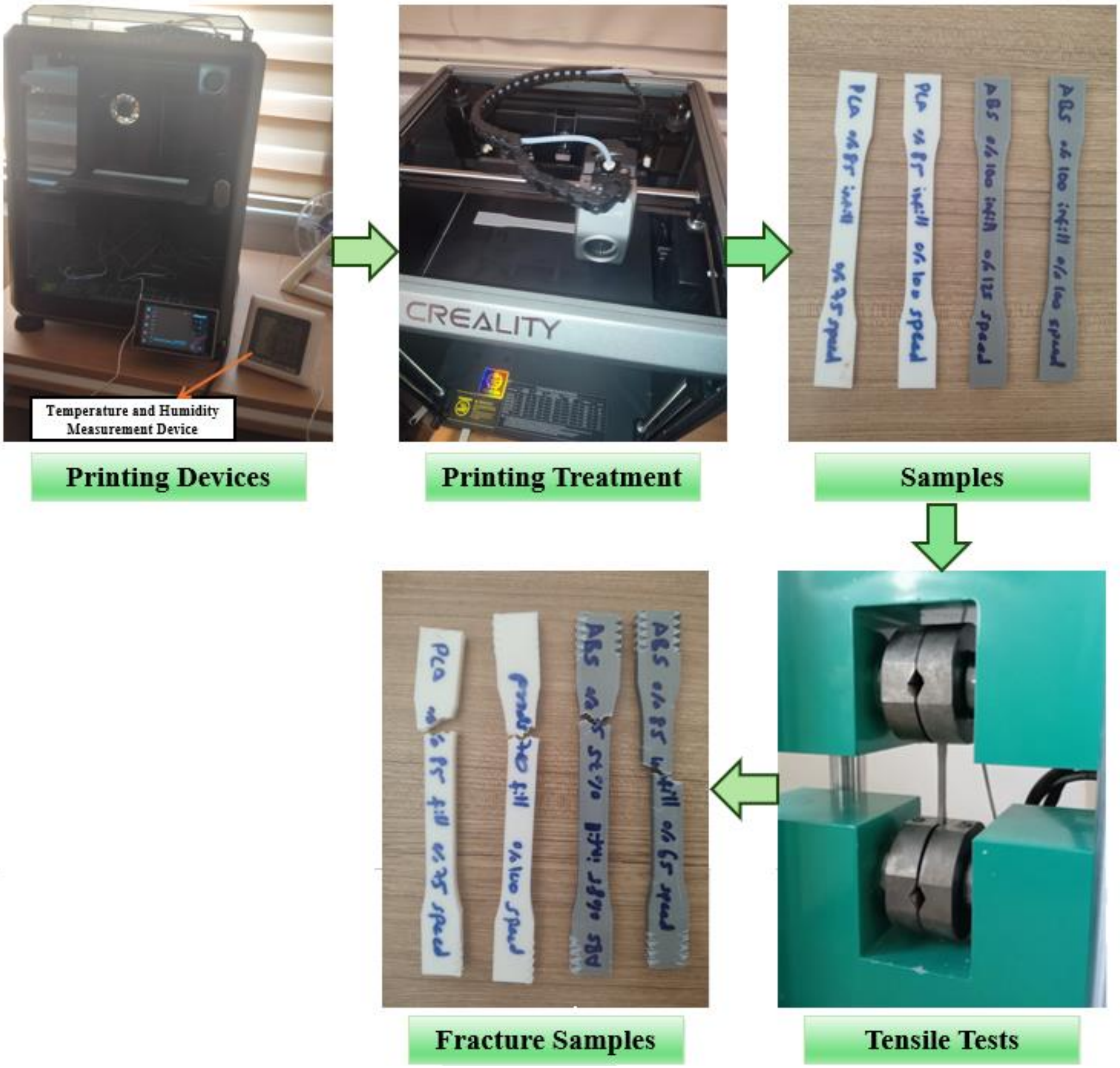

Figure 2. Specimen production and tensile tests processes

3. RESULTS AND DISCUSSION

3.1 Tensile Tests Results

In this section, tensile test results were analyzed and evaluated. The results obtained are given in Table 4. The stress-elongation curves obtained as a result of the tests are shown in Figure 3. When the results for 85% fill rate (Figure 3(a)) were analyzed; it was found that all PLA specimens reached better tensile strength values than ABS specimens. The best UTS were obtained in PLA specimens for 100% speed rate with 39.02 MPa. The UTS of the specimens produced at 65% speed rate with 35.45 MPa were close to the maximum. When the speed rate increased to 135%, a decrease in UTS was observed. This indicates that increasing the speed rate too much negatively affects the tensile strength. When the UTSs of ABS were analyzed, it was found that the specimens produced with 135% speed rate exhibited the best performance with 29.56 MPa. The specimens produced with 100% speed rate exhibited similar UTS performance. However, the UTS of the specimens produced with 65% speed rate decreased by approximately 29% with 20.96 MPa. ABS materials require higher printing and table temperature. When the printing speeds are reduced, the material melted with the extruder cools faster than desired. The decrease in UTSs for 65% speed rate could be explained by layer adhesion and delamination defects (Darsin et al., 2022; Singaravel et al., 2024). Analyzing the elongation ratios, it was observed that ABS performed better in contrast to the UTS results. For ABS, the transformation from the elastic to the plastic region occurs at higher elongation ratios. This difference could be explained by the better ductility of ABS (Esun, 2024b, 2024a). The results demonstrated that the yield strength of PLA specimens was better than that of ABS. The best yield strength of 34.03 MPa was obtained for PLA specimens for 100% speed rate. The best yield strength for ABS was 24.95 MPa for 135% speed rate. The yield strength results were in parallel with the tensile strength results.

Table 4. Tensile test results

Material Type	Fill Rate (%)	Speed Rate (%)	UTS (MPa)	Spent Filament (m)	Printing Time (min)
ABS	70	125	23.123	6.15	47.5
ABS	100	75	29.987	7.54	86.5
ABS	100	100	32.915	7.54	65.5
ABS	85	135	29.559	6.99	51
PLA	100	100	45.191	7.53	23.5
ABS	70	75	23.253	6.15	72.5
PLA	70	75	34.29	6.18	21
PLA	65	100	28.094	5.9	20
PLA	70	125	33.502	6.18	20
PLA	85	135	33.807	6.94	21.5
PLA	100	125	42.365	7.53	23
PLA	85	100	39.204	6.94	22
PLA	85	65	38.448	6.94	23.5
ABS	65	100	20.958	5.94	55
ABS	85	65	26.316	6.99	81.5
ABS	100	125	32.79	7.54	55
PLA	100	75	39.204	6.94	22
ABS	85	100	27.605	6.99	61

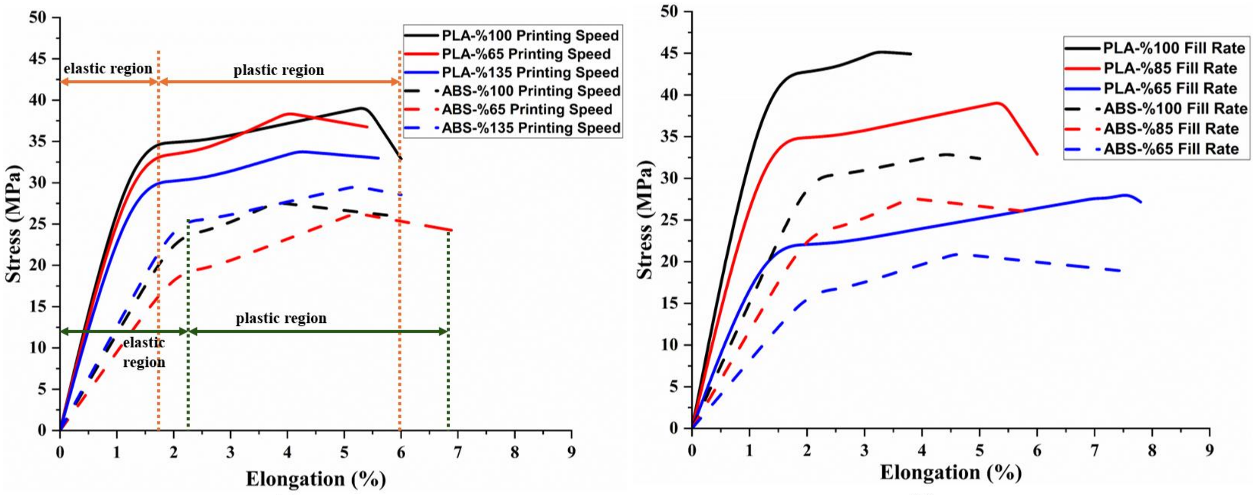

(a) (b)

Figure 3. Stress-elongation curves for 85% fill rate (a) and stress-elongation curves for 100% speed rate (b)

Figure 3(b) shows the stress-elongation curves for different fill rates at 100% speed rate. The results clearly indicate that the UTS increases with the increase in the fill rate. The highest UTS of 45.19 MPa was obtained for PLA specimens produced at 100% filling rate. For 85% fill rate, this value decreased to 39.20 MPa and for 65% fill rate it decreased to 28.09 MPa. The reason for this is that the air gap decreases with the increase in the fill rate and the product exhibits a more homogeneous property. Air gaps affect the heat distribution during production, causing residual stresses and reducing the UTS (Atakok et al., 2022). For ABS, the results are parallel to PLA results and UTS increases as the fill rate increases. Another significant result is that the ductility increases with the decrease in the fill rate for the specimens with the same properties. The reason for this is that the specimens have a more homogeneous structure and show more rigid behavior with the increase in the fill rate as in UTS (Atakok et al., 2022; Rifuggiato et al., 2022). As stiffness increases, ductility decreases and therefore elongation decreases.

Similarly, in a study examining the tensile strength of ABS for three different filling ratios, it was found that increasing the filling rate increased the UTS. In addition, SEM analyses showed that the changes in tensile strength were caused by internal gaps (Rifuggiato et al., 2022). In another study in which the change of the tensile strength of PLA according to the printing parameters was examined, it was found that the increase in the fill rate increases the UTS in parallel with the results obtained (Rismalia et al., 2019). Although the increase in the fill rate also increases the UTS, it also increases the printing times and the amount of filament spent. This has a negative impact on production costs. This situation requires an optimization study examining the printing parameters.

3.2 Statistical Evaluation and Optimization

In this section, ANOVA and optimization results are evaluated. The summary of the optimization model is presented in Table 5. Here, it is observed that the R^2 value, which expresses the realism of the model, is greater than 94% for all output parameters. This indicates that the model is highly compatible with experimental data and has a high representation ability. Pred. R^2 value, which expresses the predictive ability of the model, varies between 84-97%. It means that the prediction accuracy is between 84-97% for specimens that have not been examined experimentally and this indicates that the model has a very high prediction accuracy.

Table 5. Model summary

	S	**R^2**	**Adj. R^2**	**Pred. R^2**
UTS (MPa)	1.996	94.47%	91.45%	84.11%
Flament Spent (%)	0.156	95.58%	93.17%	85.71%
Printing Time (%)	2.647	99.19%	98.74%	97.70%

ANOVA results are given in Table 6. The results obtained show that material type and fill rate are effective in the change of UTS ($p<0.05$). Speed rate had no significant effect on UTS ($p>0.05$). The most effective parameter in the change of UTS was material type with 53.83%, while the effect of fill rate was found to be 38.68%. The related regression equations are given in equation 3(a) and equation 3(b).

When the filament spent results were analyzed, the only output that was effective on this parameter was the fill rate with 93.09%. Other parameters had no significant effect on filament spent ($p>0.05$). The related regression equations are shown in equation 4(a) and equation 4(b). All parameters have an effect on printing time change. The most effective parameter on printing time is material type with 84.06%, followed by speed rate with 6.92% and fill rate with 1.45%. Although the fill rate is significant ($p<0.05$), the reason for the low effect rate is that the preparation time for printing is quite high and most of the printing time is spent here. The regression equations for filament spent are given in equation 5(a) and equation 5(b).

Table 6. ANOVA results

	Source	DF	Contribution	F-Value	P-Value
UTS (MPa)	Fill Rate	1	38.68%	76.92	0.000
	Speed Rate	1	0.08%	0.01	0.922
	Material Type	1	53.83%	103.30	0.000
	2-Way Interaction	3	1.88%	1.25	0.340
	Error	11	5.53%		
	Total	17	100%		
Flament Spent (m)	Fill Rate	1	93.09%	231.73	0.000
	Speed Rate	1	0.36%	0.39	0.548
	Material Type	1	0.52%	0.91	0.361
	2-Way Interaction	3	1.61%	1.33	0.313
	Error	11	4.42%		
	Total	17	100%		
Printing Time (%)	Fill Rate	1	1.45%	19.58	0.001
	Speed Rate	1	6.92%	86.26	0.000
	Material Type	1	84.06%	1086.63	0.000
	2-Way Interaction	3	6.77%	30.56	0.000
	Error	11	0.81%		
	Total	17	100%		

$$UTS\ for\ PLA = 30.50 + 0.104\ Fill\ Rate - 0.216\ Speed\ Rate + 0.00229\ Fill\ Rate\ x\ Speed\ Rate \tag{3a}$$

$$UTS\ for\ ABS = 17.90 + 0.071\ Fill\ Rate - 0.159\ Speed\ Rate + 0.00229\ Fill\ Rate\ x\ Speed\ Rate \tag{3b}$$

$$Flament\ Spent\ for\ PLA = 4.80 + 0.0201\ Fill\ Rate - 0.0137\ Speed\ Rate + 0.000197\ Fill\ Rate\ x\ Speed\ Rate \tag{4a}$$

$$Flament\ Spent\ for\ ABS = 4.64 + 0.0265\ Fill\ Rate - 0.0167\ Speed\ Rate + 0.000197\ Fill\ Rate\ x\ Speed\ Rate \tag{4b}$$

$$Printing\ Time\ for\ PLA = 3.70 + 0.230\ Fill\ Rate + 0.113\ Speed\ Rate - 0.0015\ Fill\ Rate\ x\ Speed\ Rate \tag{5a}$$

$$Printing\ Time\ for\ ABS = 72.20 + 0.495\ Fill\ Rate - 0.374\ Speed\ Rate - 0.0015\ Fill\ Rate\ x\ Speed\ Rate \tag{5b}$$

3D surface plots and contour plots were generated for each parameter to analyze the interactions of the optimization parameters UTS, speed rate and fill rate with respect to each other. 3D surface plots and counter plots generated for UTS are illustrated in Figure 4. When the results for PLA (Figure 4(a) and (b)) were analyzed; the best UTS values were found to be at 100% fill rate and 80-110% speed rate conditions. Reducing the fill rates and increasing the speed rate could negatively affect the UTS. When produced at lower speeds, PLA has more time to absorb heat, which increases the degree of crystallization of PLA. Increased crystallinity could improve tensile strength as the material transforms from a more amorphous form to a semi-crystalline form (Hsueh et al., 2021; Tichý et al., 2021). If the printing speed is reduced too much, it may cause separation between layers (delamination) with excessive solidification. When the printing speed is increased too much, internal stress may occur and this may cause delamination (Balasubramanian et al., 2024).

When the plots for ABS (Figure 4(c) and (d)) were analyzed, it was found that the best UTS values were obtained at high speeds in opposite to PLA. At very low printing speeds, the time between two sequential layers increases. This may cause interlayer non-bonding and thermal problems (Guimarães et al., 2020). Another remarkable issue was that for ABS specimens produced at speed rates above 130% and low fill rates, the UTS was minimum. The reason for this situation could be explained by the fact that the time required for cooling between the 2 overlapping layers cannot be fulfilled with both the decrease in the fill rate and the decrease in the printing speed and there is not enough cooling time for the molten material (Daly et al., 2023). The increase in the fill rate increased the tensile strength as in PLA specimens. The reason for this increase is related to the decrease in the micro gaps in the specimen and the more homogeneous structure as mentioned before (Atakok et al., 2022).

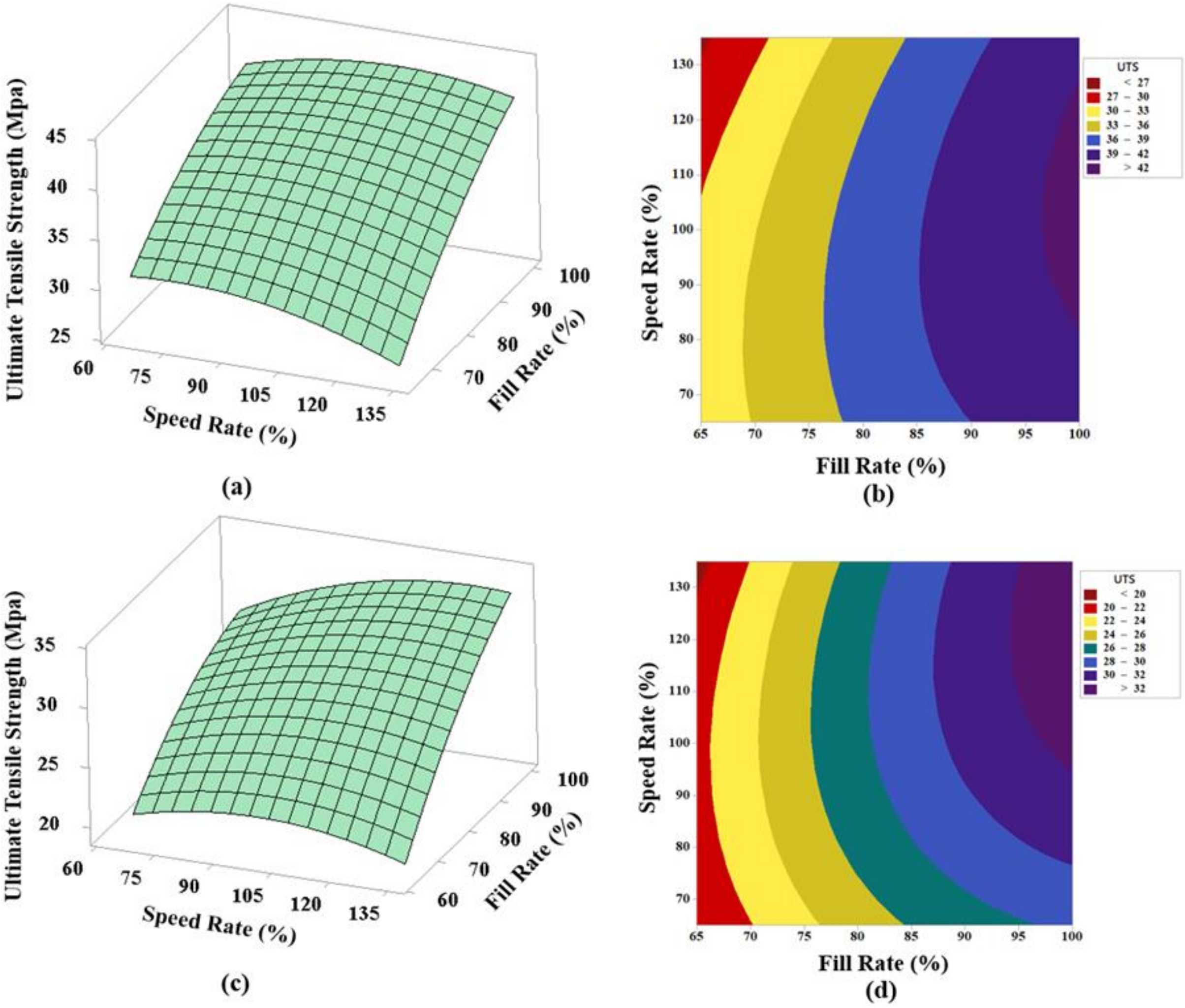

Figure 4. 3D surface plots of PLA (a) and ABS (c), contour (2D) plots of PLA (b) and ABS (d) for UTS

In Figure 5, changes of printing time for PLA and ABS according to the input parameters are given. According to the plots; as the fill rates decrease and the speed rate increases, the printing time decreases. This result was more evident in the plots of ABS samples due to the longer production times (Figure 5(c) and (d)). According to the optimization plots for PLA (Figure 4(a) and (b)), after 115% speed rate, the printing time increases slightly as the speed rate increases. The experimental data (Table 4) clearly indicates that the increase in speed rate decreases the printing time for all speeds. This difference is within the range of errors for the model formed and is since the production times for PLA samples are considerably shorter than ABS samples. In addition, the fact that the material type and fill rate are highly effective on the printing time causes deviations for the speed rate results. This caused a mismatch within the optimizations model for rates above 115%. A further study examining only high speed rate values could be performed to eliminate these variations and errors.

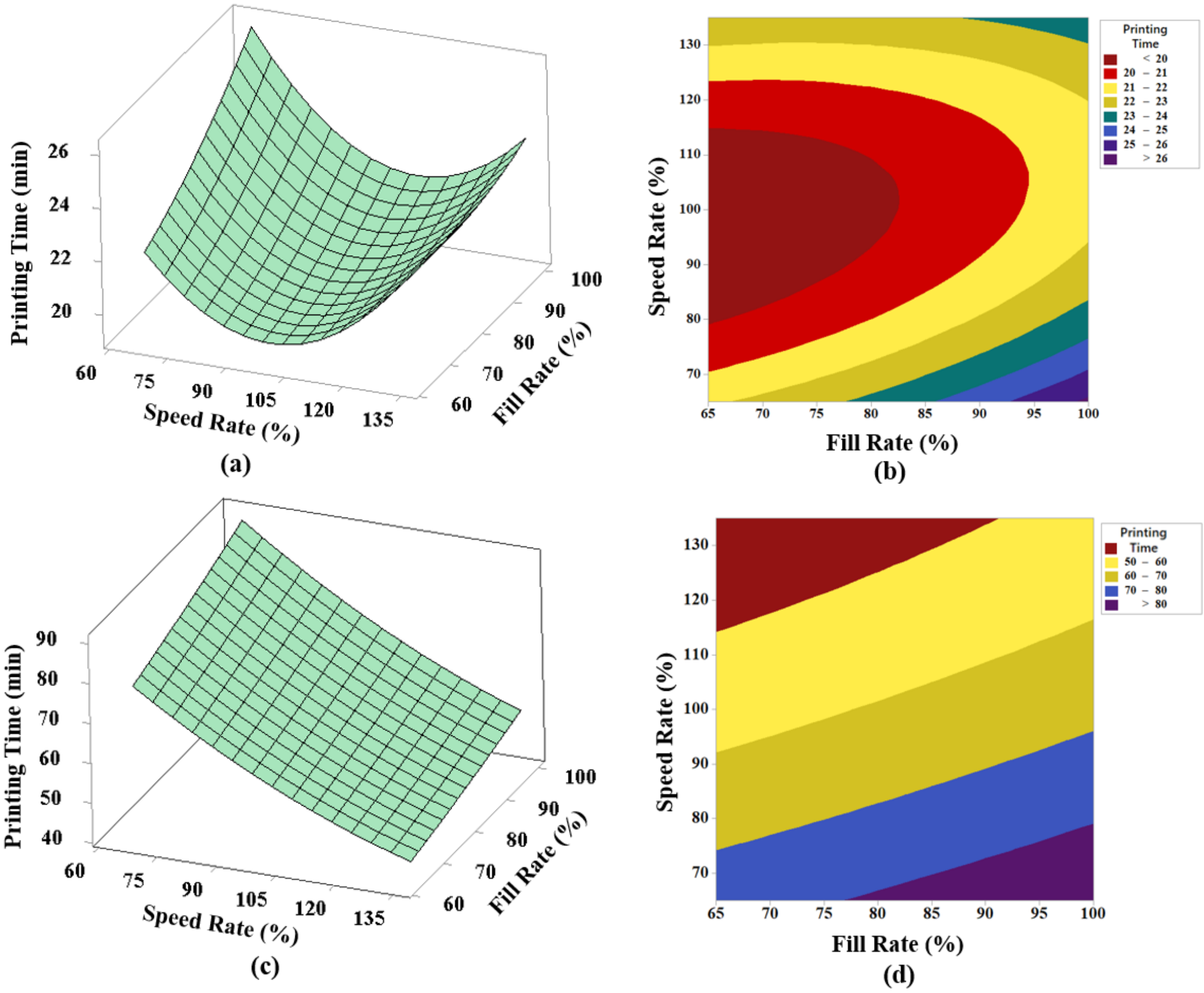

Figure 5. 3D surface plots of PLA (a) and ABS (c), contour (2D) plots of PLA (b) and ABS (d) for printing time

The change plots of filament spent according to the input parameters are given in Figure 6. The effective parameter in the change of filament spent is the fill rate. Speed rate and material type have no effect on filament spent. For a sample produced at 65% fill rate, 6 meters of filament was spent. When the fill rate was increased to 100%, the amount of filament spent increased to over 7.5 meters.

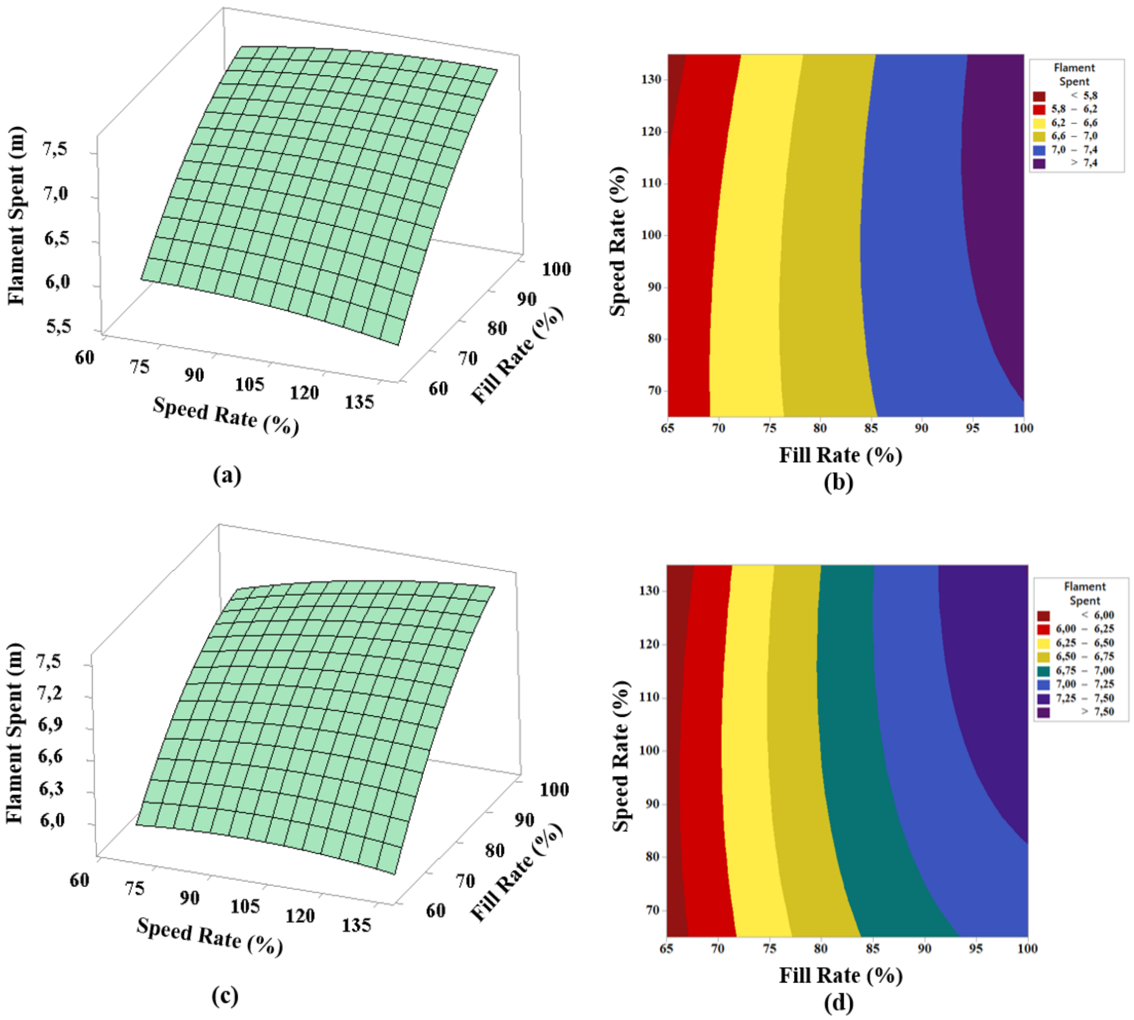

(a) (b)

(c) (d)

Figure 6. 3D surface plots of PLA (a) and ABS (c), contour (2D) plots of PLA (b) and ABS (d) for filament spent

Optimization was performed with the obtained data. Optimum values were found for both PLA and ABS. The values found for PLA also represented the optimum results for the model. Optimizations were performed in attempts to maximize UTS and minimize filament spent and printing time. Optimization curves are shown in Figure 7. According to the results, optimum values for PLA were obtained at 66.77% fill rate and 78.43% speed rate conditions. In addition, predictions were made to the optimization model for these conditions. The model predicted UTS as 32.08 MPa, filament spent as 6.01 m and printing time as 20 min. Optimum values for ABS were obtained at 79.5% fill rate and 135% speed rate. For these conditions, the model predicted UTS as 26.5 MPa, filament spent as 6.67 m and printing time as 46.5 min. For optimum parameters, 3 samples were produced and tensile tests were performed The optimum input-output values and experimental results for both material types are given in Table 7. According to this, the optimization model can predict the UTS with an error of 4.02% for PLA and 10.52% for ABS. Likewise, the model was able to predict the printing time with an error of 6.98% for PLA and 2.11% for ABS. For filament spent, these values decrease to 0.17% and 1.37% respectively. The prediction errors are very low, which proves the accuracy of the optimization model.

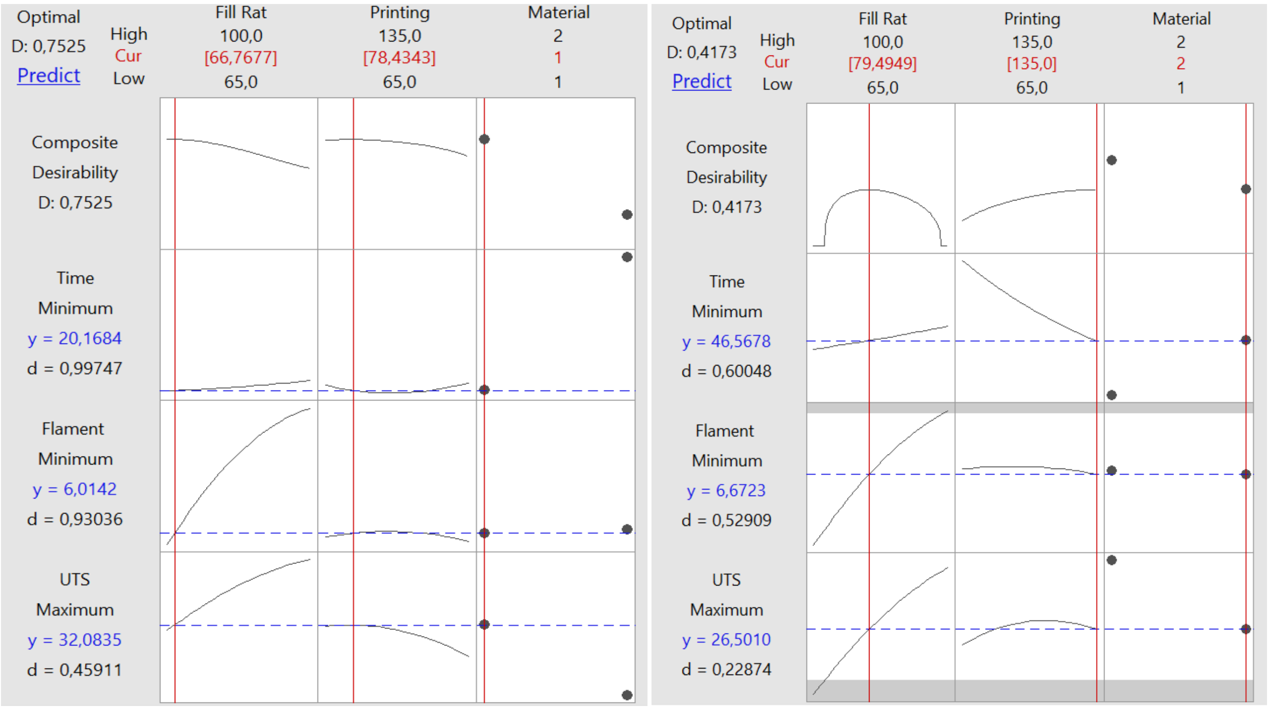

(a) (b)

Figure 7. Optimization curves for PLA (a) and for ABS (b)

Table 7. Results of optimization and experimental evaluation

	Input Parameters		**Output Parameters**		
	Fill Rate (%)	**Speed Rate (%)**	**UTS (MPa)**	**Flament Spent (m)**	**Printing Time (min)**
Optimization Results					
For PLA	66.77	78.43	32.084	6.01	20.0
For ABS	79.50	135	26.501	6.67	46.5
Experimental Results					
For PLA	66.77	78.43	30.842	6.00	21.5
For ABS	79.50	135	29.615	6.58	47.5

The results were consistent with previous optimization studies. In the study in which the optimum conditions of the printing parameters of ABS specimens were investigated with RSM, it was found that the increase in fill rate increased the UTS (Srinivasan et al., 2020). Similarly, the optimization study by Samykano et al. confirms the results (Samykano et al., 2019). In another study investigating the optimum production parameters of PLA specimens, it was stated that the speed rate increases the UTS at up to certain speed rates, but very high speed rates cause a decrease in UTS (Hikmat et al., 2021).

PLA is a biodegradable material, non-toxic (Yao et al., 2020) and particularly suitable for biomedical applications (Mishra et al., 2021). Tensile strength is also higher than ABS. However, working conditions begin to undergo structural deformation at temperatures above 60-65 °C. It is not suitable for applications operating under high temperature conditions. ABS begins to undergo structural deformation above 100 °C. This could make ABS the preferred choice of applications with high temperature operating conditions. However, contrary to PLA, ABS is toxic (Pellejero et al., 2020). By using the optimization model, predictions can be made for different applications according to material preference. In applications where durability is more important, fill rate, speed rate and calculations can be made according to the desired UTS values. Similarly, in applications where production speed and costs are important, production can be realized by decreasing fill rate and increasing speed rate. Due to the optimization model proposed in this study, all desired properties could be predicted with great accuracy without the need for experimental investigation.

4. CONCLUSION

In this study, tensile strength, filament spent and printing time changes of PLA and ABS produced by FFF according to printing parameters were investigated and optimized. According to the results obtained:

- Tensile strength of PLA specimens is higher than ABS specimens. The UTS of PLA produced at 100% fill rate and 100% speed rate is 45.19 MPa, while the UTS of ABS produced with the same printing parameters is approximately 32.92 MPa. However, the elongation rate of ABS specimens is higher.
- For both PLA and ABS, the tensile strength increases as the fill rate increases. However, the amount of filament spent and production times also increase. Thus, this increases production costs.
- Increasing the speed rate too much negatively affected the UTS of PLA samples. On the other hand, the best UTSs of ABS samples were obtained at 135% speed rate. It is obvious that increasing the speed rate too much for ABS will have negative effects. The fact that the speed increase rate used for the optimization model is the same for PLA and ABS is an obstacle for investigating the effect of higher speeds on ABS, in this study. In another study, the effect of higher speed rates on ABS could be investigated in more detail.
- The optimum parameters for PLA are obtained under 66.77% fill rate and 78.43% speed rate. For ABS, optimum values are obtained at 79.5% filling rate and 135% speed rate.
- The optimization model was able to predict the tensile strength with an error of 4.02% for PLA and 10.52% for ABS. Likewise, the model was able to predict the printing time with an error of 6.98% for PLA and 2.11% for ABS. For filament spent, these values decrease to 0.17% and 1.37% respectively.
- Through optimization, printing parameters could be selected according to the desired tensile strength and the time spent for trial and error could be reduced. In addition, by selecting the correct printing parameters according to the desired mechanical properties, the material and labor costs and the time spent for printing could also be reduced.

5. ACKNOWLEDGEMENTS

This study was supported by Scientific and Technological Research Council of Turkey (TÜBİTAK) with Project number of 1919B012302277.

6. CONFLICT OF INTEREST

Authors approve that to the best of their knowledge, there is not any conflict of interest or common interest with an institution/organization or a person that may affect the review process of the paper.

7. AUTHOR CONTRIBUTION

İsmail Aykut KARAMANLI contributed to determining and managing the concept and/or design process of the research, data collection, data analysis and interpretation of the results, preparation of the manuscript, critical analysis of the intellectual content, as well as providing final approval and full responsibility. Kadircan TAHNAL contributed to data collection, and data analysis and interpretation of the results.

8. REFERENCES

Alabd M. U., Temiz A., Optimization of Annealing and 3D Printing Process Parameters of PLA Parts. International Journal of 3D Printing Technologies and Digital Industry 8(2), 185-201, 2024.

ASTM D638-14, Standard Test Method for Tensile Properties of Plastics, 2022.

Atakok G., Kam M., Koc H. B., Tensile, Three-Point Bending and Impact Strength of 3D Printed Parts Using PLA and Recycled PLA Filaments: A Statistical Investigation. Journal of Materials Research and Technology 18, 1542-1554, 2022.

Balasubramanian M., Saravanan R., Shanmugam V., Impact of Strain Rate on Mechanical Properties of Polylatic Acid Fabricated by Fusion Deposition Modeling. Polymers for Advanced Technologies 35(3), 2024.

Bayraklılar M. S., Kuncan M., Buldu A., Koçak M. T., Ülkir O., Comparison of Mechanical Properties of Samples Fabricated by Stereolithography and Fused Deposition Modelling. Journal of Materials and Mechatronics: A 4(2), 475-491, 2023.

Daly M., Tarfaoui M., Chihi M., Bouraoui C., FDM Technology and the Effect of Printing Parameters on the Tensile Strength of ABS Parts. The International Journal of Advanced Manufacturing Technology 126(11-12), 5307-5323, 2023.

Darsin M., Mauludy R. R., Hardiatama I., Fachri B. A., Ramadhan M. E., Parningotan D., Analysis of The Effect 3D Printing Parameters on Tensile Strength Using Copper-PLA Filament. SINERGI 26(1), 99, 2022.

Dwiyati S. T., Kholil A., Riyadi R., Putra S. E., Influence of Layer Thickness and 3D Printing Direction on Tensile Properties of ABS Material. Journal of Physics: Conference Series 1402(6), 066014, 2019.

Esun, (a), Esun ABS+ Mechanical Properties. https://www.esun3d.com/abs-product/, 2024.

Esun, (b), Esun PLA+ Mechanical Properties. https://www.esun3d.com/tr/pla-pro-product/, 2024.

Esun, (c), Recommended printing parameters for Creality K1. https://www.esun3d.com/uploads/eSUN-Fast-filaments-print-parameters.pdf, 2024.

Fontana L., Minetola P., Iuliano L., Rifuggiato S., Khandpur M. S., Stiuso V., An Investigation of The Influence of 3D Printing Parameters on The Tensile Strength of PLA Material. Materials Today: Proceedings 57, 657-663, 2022.

Grasso M., Azzouz L., Ruiz-Hincapie P., Zarrelli M., Ren G., Effect of Temperature on The Mechanical Properties of 3D-printed PLA Tensile Specimens. Rapid Prototyping Journal 24(8), 1337-1346, 2018.

Güdür C., Türkoğlu T., Eren İ., Effect of Lattice Design and Process Parameters on the Properties of PLA, ABS AND PETG Polymers Produced by Fused Deposition Modelling. Journal of Materials and Mechatronics: A 4(2), 561-570, 2023.

Guimarães A. L. A., Neto V. G., Foschini C. R., Azambuja M. dos A., Hellmeister L. A. V., Influence of ABS Print Parameters on a 3D Open-Source, Self-Replicable Printer. Rapid Prototyping Journal 26(10), 1733-1738, 2020.

Hikmat M., Rostam S., Ahmed Y. M., Investigation of Tensile Property-Based Taguchi Method of PLA Parts Fabricated by FDM 3D Printing Technology. Results in Engineering 11, 100264, 2021.

Hsueh M. H., Lai C. J., Wang S., Zeng Y., Hsieh C. H., Pan C. Y., Huang W. C., Effect of Printing Parameters on the Thermal and Mechanical Properties of 3d-Printed PLA and PETG, Using Fused Deposition Modeling. Polymers 13(11), 1758, 2021.

Karamanlı İ. A., Gök M. S., Küçük Y., Ünal O., Study of the Wear Resistance Plasma Nitrided GGG60 by Optimization of Surface Treatment Conditions Using Response Surface Methodology. International Journal of Metalcasting 1-17, 2024.

Kaya Z., Aksoy B., Özsoy K., Eklemeli İmalat Yöntemiyle Üretilen Altı Eksenli Robot Kol ile Görüntü İşleme ve Yapay Zeka Tabanlı Ürünlerin Tasniflemesi. Journal of Materials and Mechatronics: A 4(1), 193-210, 2023.

Khan S. F., Zakaria H., Chong Y. L., Saad M. A. M., Basaruddin K., Effect of Infill on Tensile and Flexural Strength of 3D Printed PLA Parts. IOP Conference Series: Materials Science and Engineering 429(1), 012101, 2018.

Mishra A. K., Chavan H., Kumar A. Effect of Material Variation on The Uniaxial Compression Behavior of FDM Manufactured Polymeric TPMS Lattice Materials. Materials Today: Proceedings 46, 7752-7759, 2021.

Öz Ö., Öztürk F. H., Yazdırma Açısının 3B Yazıcıda Üretilen PLA Numunenin Mekanik Özellikleri Üzerine Etkisinin Deneysel ve Sonlu Elemanlar Metodu ile İncelenmesi - Investigation of the Effects of Printing Angle on Mechanical Properties of PLA Specimen Fabricated with 3D P. Politeknik Dergisi 26(2), 529-540, 2023.

Pehlivan F., Öztürk F. H., Demir S., Temiz A., Optimization of Functionally Graded Solid-Network TPMS Meta-Biomaterials. Journal of the Mechanical Behavior of Biomedical Materials 157, 106609, 2024.

Pellejero I., Almazán F., Lafuente M., Urbiztondo M. A., Drobek M., Bechelany M., Julbe A., Gandía L. M., Functionalization of 3D Printed ABS Filters with MOF for Toxic Gas Removal. Journal of Industrial and Engineering Chemistry 89, 194-203, 2020.

Rajpurohit S. R., Dave H. K., Analysis of Tensile Strength of a Fused Filament Fabricated PLA Part Using an Open-Source 3D Printer. The International Journal of Advanced Manufacturing Technology 101(5-8), 1525-1536, 2019.

Rifuggiato S., Minetola P., Stiuso V., Khandpur M. S., Fontana L., Iuliano L., An Investigation of The Influence of 3D Printing Defects on The Tensile Performance of ABS Material. Materials Today: Proceedings 57, 851-858, 2022.

Rismalia M., Hidajat S. C., Permana I. G. R., Hadisujoto B., Muslimin M., Triawan F., Infill Pattern and Density Effects on The Tensile Properties of 3D Printed PLA Material. Journal of Physics: Conference Series 1402(4), 044041, 2019.

Samykano M., Selvamani S. K., Kadirgama K., Ngui W. K., Kanagaraj G., Sudhakar K., Mechanical Property of FDM Printed ABS: Influence of Printing Parameters. The International Journal of Advanced Manufacturing Technology 102(9-12), 2779-2796, 2019.

Singaravel B., Devaraj S., Niranjan T., Chakradhar B., Chaitanya P., Effect of Material Type and Process Parameters on Tensile Strength of 3D Printed Specimen. Journal of Physics: Conference Series 2779(1), 012077, 2024.

Srinivasan R., Pridhar T., Ramprasath L. S., Charan N. S., Ruban W., Prediction of Tensile Strength in FDM Printed ABS Parts Using Response Surface Methodology (RSM). Materials Today: Proceedings 27, 1827-1832, 2020.

Temiz A., (a), A Response Surface Methodology Investigation into The Optimization of Manufacturing Time and Quality for FFF 3D Printed PLA Parts. Rapid Prototyping Journal 2024.

Temiz A., (b), The Tensile Properties of Functionally Graded Materials in MSLA 3D Printing as a Function of Exposure Time. Journal of Materials and Mechatronics: A, 5(1), 49–59, 2024.

Tichý T., Šefl O., Veselý P., Dušek K., Bušek D., Mathematical Modelling of Temperature Distribution in Selected Parts of FFF Printer during 3D Printing Process. Polymers 13(23), 4213, 2021.

Wang K., Lam F., Quadratic RSM Models of Processing Parameters for Three-Layer Oriented Flakeboards. Wood and Fiber Science, 173-186, 1999.

Wang X., Xu S., Zhou S., Xu W., Leary M., Choong P., Qian M., Brandt M., Xie Y. M., Topological Design and Additive Manufacturing of Porous Metals for Bone Scaffolds and Orthopaedic Implants: A Review. Biomaterials 83, 127-141, 2016.

Yao T., Deng Z., Zhang K., Li S., A method to Predict the Ultimate Tensile Strength of 3D Printing Polylactic Acid (PLA) Materials with Different Printing Orientations. Composites Part B: Engineering 163, 393-402, 2019.

Yao T., Ye J., Deng Z., Zhang K., Ma Y., Ouyang H. Tensile Failure Strength and Separation Angle of FDM 3D Printing PLA Material: Experimental and Theoretical Analyses. Composites Part B: Engineering 188, 107894, 2020.

JOURNAL of
MATERIALS and MECHATRONICS:A

e-ISSN 2717-8811
JournalMM, 2024, 5(2), 303-315
https://doi.org/10.55546/jmm.1552182

Araştırma Makalesi / Research Article

Investigation of Mechanical Behavior of Carbon Fiber Reinforced Sandwich Composites with Different Weights

Ercan ŞİMŞİR[1*]

[1*] Afyon Kocatepe Üniversitesi, Teknoloji Fakültesi, Otomotiv Mühendisliği Bölümü, Afyonkarahisar, Türkiye,
ORCID ID: https://orcid.org/0000-0001-6655-2324, esimsir@aku.edu.tr

Geliş/ Received: 18.09.2024; **Revize/Revised:** 12.11.2024 **Kabul / Accepted:** 25.11.2024

ABSTRACT: In this study, the impact and three-point bending performances of sandwich structures produced using carbon fiber-reinforced composite materials and XPS foam core with different fiber weights were investigated. Carbon fiber weighing 200 g/m² and 400 g/m² were used in sandwich structures. The reinforced layers were formed by placing four layers above and four layers below the XPS foam core. For the impact resistance test, low-speed impact tests and three-point bending tests were performed at 30 J, 50 J, and 70 J energy levels. As a result of the tests, it was determined that the increase in fiber weight has a significant effect on the impact resistance and bending strength of the materials. While the samples with a fiber weight of 200 g/m² reached a maximum force value of 1200 N under 30 J energy, the samples with a weight of 400 g/m² reached a force value of 6400 N. Similarly, at energy levels of 50 J and 70 J, heavier fiber samples provided higher maximum force and energy absorption. In three-point bending tests, samples with a fiber weight of 200 g/m² reached a maximum force value of 200 N, while samples with a weight of 400 g/m² reached up to 450 N. As a result, increasing the fiber weight significantly increased the mechanical strength and energy absorption capacity of sandwich structures, indicating that materials are a critical parameter for engineering applications.

Keywords: Carbon fiber, Laminated composite, Low speed impact test, XPS foam

---

*Sorumlu yazar / Corresponding author: esimsir@aku.edu.tr

Bu makaleye atıf yapmak için /To cite this article

Şimşir, E. (2024). Investigation of Mechanical Behavior of Carbon Fiber Reinforced Sandwich Composites with Different Properties. Journal of Materials and Mechatronics: A (JournalMM), 5(2), 303-315.

1. INTRODUCTION

Sandwich structures consist of core material and fiber-reinforced layers placed on this core. According to the literature research, it has been observed that these structures have been examined in a wide range of mechanical properties, especially impact strength (Abid et al., 2020; He et al., 2021) and bending strength (Djafar et al., 2021; Adin and Adin, 2022). These studies show that the mechanical performance of structures is directly related to important engineering parameters. Composite materials are used in many sectors, such as the automotive sector (Bhong et al., 2023; Gebrehiwet et al., 2023), defense, aviation (Ozturk et al., 2023) and construction (Fan, 2024), especially due to their properties such as low weight and high strength (Khan et al., 2024). In addition to these features, the processability of sandwich composites is also important in industrial applications. The easy-to-process structure accelerates the production processes of these materials and increases their adaptability to different designs (Ceritbinmez et al., 2021; Ceritbinmez et al., 2022; Doğan et al., 2024) The most preferred of these composite materials are carbon fiber reinforced composite materials (Wu et al., 2023). (Wu et al., 2023). In engineering application areas, carbon fiber-reinforced materials exhibit good performance in terms of strength as well as lightness. The mechanical behavior of these materials has been studied in the literature using different weights and parameters (Muthukumarana et al., 2023). These materials offer both high strength and durability and are advantageous in terms of energy efficiency with their low weight (Mohanty et al., 2023). The factors affecting the mechanical properties of carbon fiber include fiber weight and number of layers. Increasing the fiber density can increase impact resistance and flexural strength but reduce deformation resistance (Burley and Aitharaju, 2023).

Within the realm of sandwich composites design framework, the core material is just as critical, as the fiber layers (Habib et al., 2024). Core materials that possess properties, like energy absorption and being lightweight and flexible are usually favored choices. In scenarios where impact and bending resilience're vital factors extruded polystyrene foam (XPS) is a preferred option because of its low water absorption rate, exceptional insulation capabilities and lightweight nature (Ižvolt et al., 2023; Karpenko et al., 2023; Yavuz et al., 2024). Many studies in the literature have shown the impact of XPS on structures; XPS contributes to the lightweight nature of sandwich composite structures due, to its low-density feature and simultaneously enhances their mechanical strength. XPS is highly favored as a material, in industries like automotive and aviation due to its unique qualities (Tawil et al., 2022). The cellular makeup of XPS enhances its impact absorption capabilities significantly. Studies indicate that the use of XPS core sandwich composites can improve impact resistance effectively (Zhang et al., 2023). XPS protects the structural integrity of the composite structure with its capacity to absorb impact energy. Using XPS as a material helps minimize distortions that may develop in the material post impact (Özcan, 2024).

Impact resistance is an important criterion when comparing the overall performance of composite materials. Low-velocity impact tests are often used to determine the post-impact behavior of materials. (Acanfora et al., 2023; Mohammadi et al., 2023). For safety purposes, especially in the automotive and aerospace industries, impact tests are used to evaluate how long materials can maintain their structural integrity during impact. The relationship between fiber weight and type of core material and impact toughness has been discussed in detail in many studies.

At the same time, bending resistance is likewise the most extensively used approach to deciding the electricity of composite substances. Three-factor bending assessments are used to degree how composite systems react below bending forces (Acanfora et al., 2023; Mohammadi et al., 2023). Studies show that bending strength varies depending on the weight of the fiber. The range of fiber layers and the weaving form make a contribution to the cloth turning into extra immune to bending forces. The number of layers of fibers and the texture properties (such as weight, density, and expansion) increase the strength, resistance to bending forces; However, this increase causes a decrease in the flexibility capacity. In this study, XPS foam and carbon fiber composites with different weights were used as core materials. Different carbon fiber weights and mechanical properties of XPS core material were investigated. The combination of core material and fiber weights used contributes to the literature and presents a new technique.

2. MATERIALS AND METHODS

Sandwich composites are a special class of composite materials produced by bonding two rigid shells to a core. In this study, extruded polystyrene (XPS) foam was used as the core material (Figure 1). Different carbon fiber woven fabrics with weight ratios of 200 g/m² and 400 g/m² have been favored because of the layer fabric (Figure 2). The thickness of the carbon fiber fabrics used in this study was measured as 0.25 mm for those with a density of 200 g/m² and 0.50 mm for those with a density of 400 g/m². The 200 g/m² fabric was used in 1 cm thickness in the upper and lower layers, and the 400 g/m² fabric was used in 2 cm thickness. In the layout of those systems, a total of 8 layers of carbon fiber woven cloth have been used, positioned 4 layers above and 4 layers underneath the XPS middle fabric. Carbon fiber woven fabric stands out as a crucial fabric in lots of commercial packages with their excessive power and lightness properties. This fabric, which might be broadly favored in terms of electricity performance due to their low weight, additionally permits the manufacturing of long-lasting and dependable merchandise via means of displaying excessive resistance to corrosion and chemical effects.

Figure 1. XPS foam core material

Porous structures are widely used in many sectors due to their lightness and superior energy absorption ability (Yavuz and Yildirim, 2023). The energy absorption capacity of these structures is directly determined by many factors, such as the shape, length and distribution of the air voids they contain. Extruded polystyrene (XPS) foam is a polymer foam cloth produced through extrusion beneath excessive temperature and pressure. During the production process, polystyrene granules are melted and passed through various molds in the extrusion line. These molds allow the material to take the desired form, and the formation of the cell structure is achieved by adding foaming agents. In addition, XPS is resistant to chemical and biological effects, which allows the material to maintain its structural integrity even in various difficult environmental conditions. As a result, a dense, lightweight, waterproof, and highly insulating material is obtained.

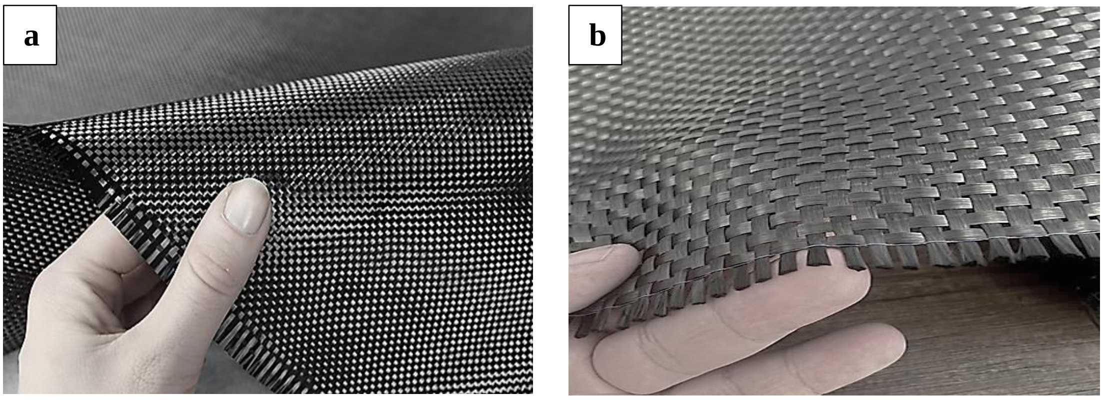

Figure 2. Carbon fiber woven fabrics used a) 200 g/m², b) 400 g/m²

Figure 3 shows the production process of the composite sample with XPS core material and carbon fiber coating. The production process starts with the homogeneous mixing of MGS LR 285 epoxy resin and LH 285 hardener with a mixer. This mixture is applied to the XPS core material and the surface of the carbon fiber layers. The composite structure is created with the carbon fiber layer placed four layers above and four layers below the XPS core material. Then, these prepared layers are processed in a hot-pressing machine for about two hours at a temperature of 40 °C and turned into composite panels. After the process is finished, the produced panels are cut with a bandsaw according to the test dimensions, and the samples are prepared. Finally, these samples are prepared for testing by subjecting them to low-speed impact and three-point bending tests.

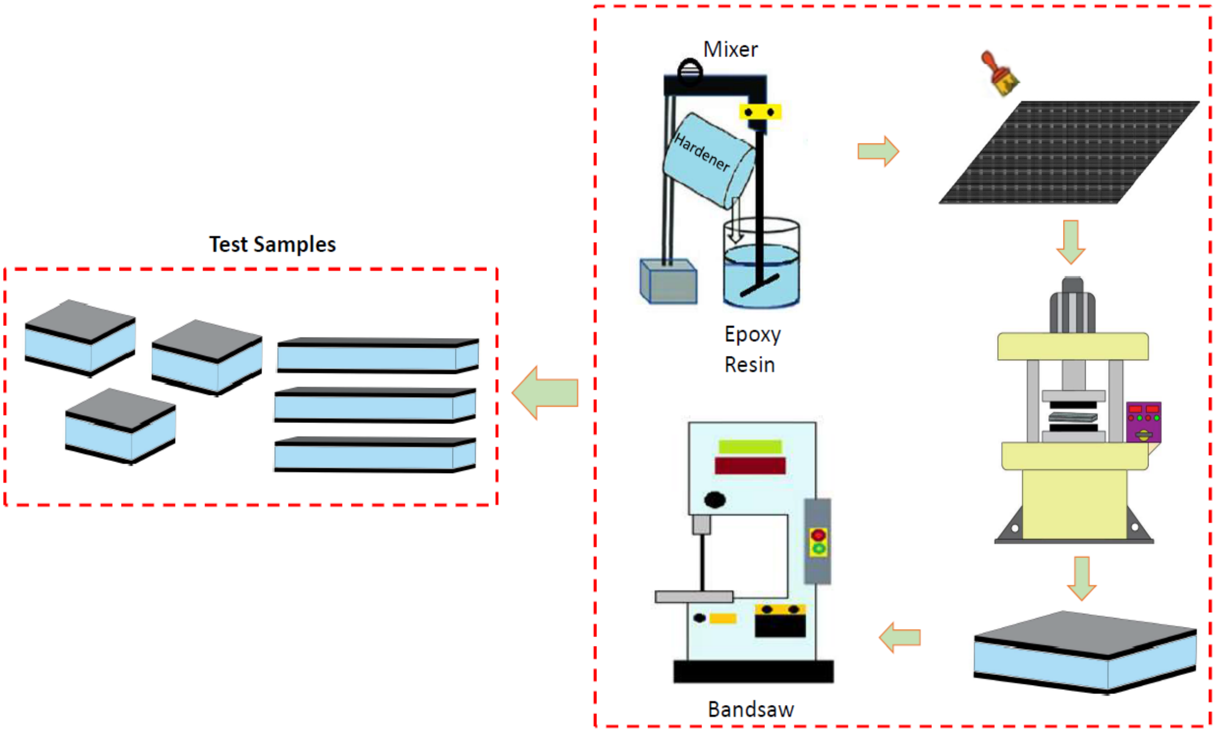

Figure 3. Schematic representation of the manufacturing process

2.1 Low Speed Impact Test

This test method measures the response of materials to impact energy. This technique is used to determine the impact resistance, energy absorption, and damage mechanisms of composite materials. Low-velocity impact events provide important information about the durability and strength of the material. Test results are very important in the safety and performance analysis of materials used in sectors such as construction, automobiles, and aviation. Thus, the structural integrity of materials after impact is evaluated, and the service life of the materials can be predicted. Low-velocity impact testing is a valuable method for improving safety and durability in engineering applications.

In this study, impact tests were carried out at Hitit University Scientific Technical Application and Research Center (HÜBTUAM). A CEAST 9350-Fractovis Plus impact testing machine was used, shown in Figure 4. The testing machine used in this study is presented in Figure 1. The striking tip used in the tests is 20 mm in diameter and made of steel in a hemispherical shape; this tip weighs 4.926 kg. The experiments were carried out at room temperature (20 °C), the released height was set as 1.657 m, and the impact energy was determined as 30, 50, and 70 Joules. All tests were performed in accordance with ASTM D7136 standard (Şimşir et al., 2021; Ferreira et al., 2023).

Figure 4. Low speed impact tester

The impact energy (joule) values applied in the study were calculated using the weight of the striking tip and the free fall height. Impact energy calculation is made with the equation given below:

$$E = m \, . \, g \, . \, h \tag{1}$$

In the equation, E is the impact energy (joule), m is the mass of the striking tip (kg), g is the acceleration due to gravity (9.81 m/s²) and h is the free fall height. These calculations were made automatically by the data logger system used during the low-speed impact test. Thus, energy levels of 30, 50 and 70 joules were achieved.

2.2 Three Point Bending Test

The three-point bending test was performed using the Shimadzu Autograph tensile device with a capacity of 10 kN located in the Mechanical Engineering Laboratory of Afyon Kocatepe University. The feed rate in the test was determined as 1 mm/min. The tests were carried out in accordance with the ASTM D7264 standard (Mohamad et al., 2023; Burkov et al., 2024), and the feed rate was determined as 1 mm/min. Samples were prepared in accordance with ASTM D7264 standards, with a width of 13 mm and a length of 125 mm. Sample thicknesses were measured as 22 mm for 200 g/m² fabrics and 24 mm for 400 g/m² fabrics. Figure 5 shows images of the samples during the test.

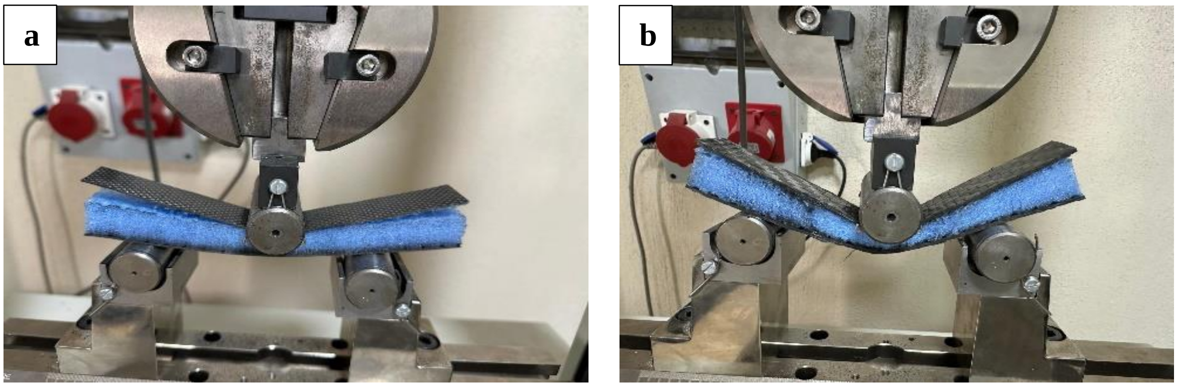

Figure 5. a) 200 g/m², b) 400 g/m² Three point bending test

3. RESULTS AND DISCUSSION

3.1 Low Speed Impact Test Results

In this study, the results of the experiments carried out using carbon fiber fabrics with two different weights of 200 g/m² and 400 g/m² and XPS core material were investigated. Three test samples were prepared for each energy value with dimensions of 100 mm x 100 mm and thickness of 22 mm and 24 mm to be used in the impact test. Force-deformation graphs were obtained at energy levels of 30 Joule, 50 Joule and 70 Joule.

3.1.1 Effect of fiber weight on strength under 30 Joule energy

Figure 6 shows the Force-Deformation graph of carbon fiber-reinforced composites at different weights and 30 joules of energy.

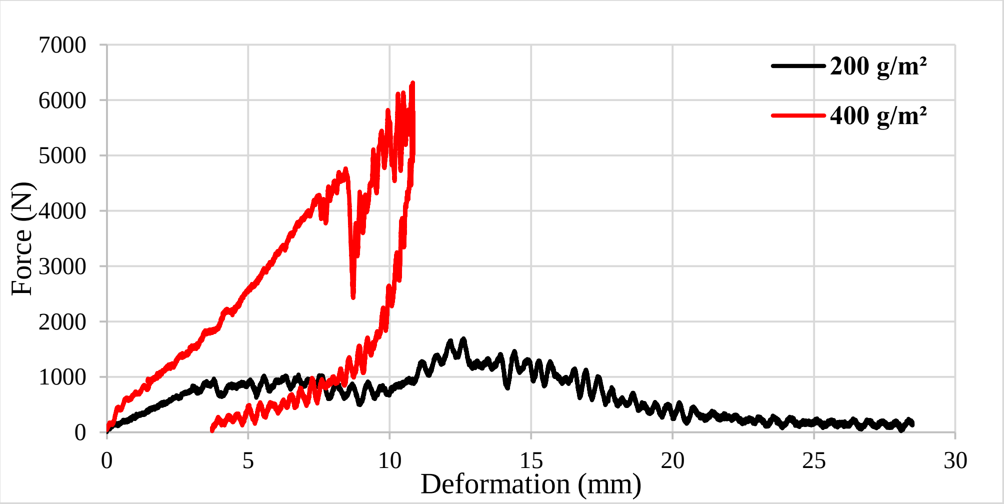

Figure 6. Effect of fiber weight on 30 Joule impact energy

30 Joule impact energy was applied to samples with fiber weights of 200 g/m² and 400 g/m². The sample weighing 200 g/m² reached a maximum force value of approximately 1200 N, and a puncture occurred on both surfaces, creating an open curve. The sample weighing 400 g/m², on the other hand, created a closed curve by bouncing back to the upper surface of the striking tip. This sample reached a maximum force value of approximately 6400 N and showed a deformation of approximately 10 mm at this level. The damage types in the upper-lower surfaces and core material of the samples as a result of the 30 Joule impact are given in Figure 7.

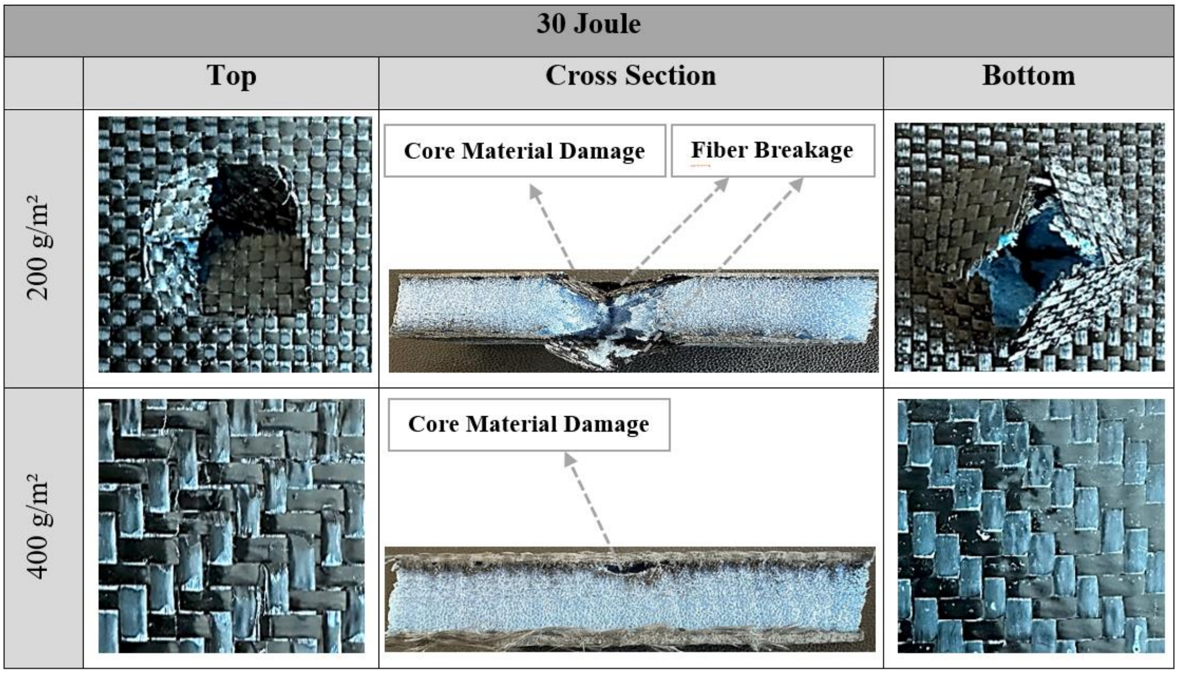

Figure 7. Damage image of the sample after a 30 Joule impact

3.1.3 Effect of fiber weight on strength under 50 Joule energy

Figure 8 shows the Force-Deformation graph of carbon fiber-reinforced composites at different weights and 50 Joules of energy.

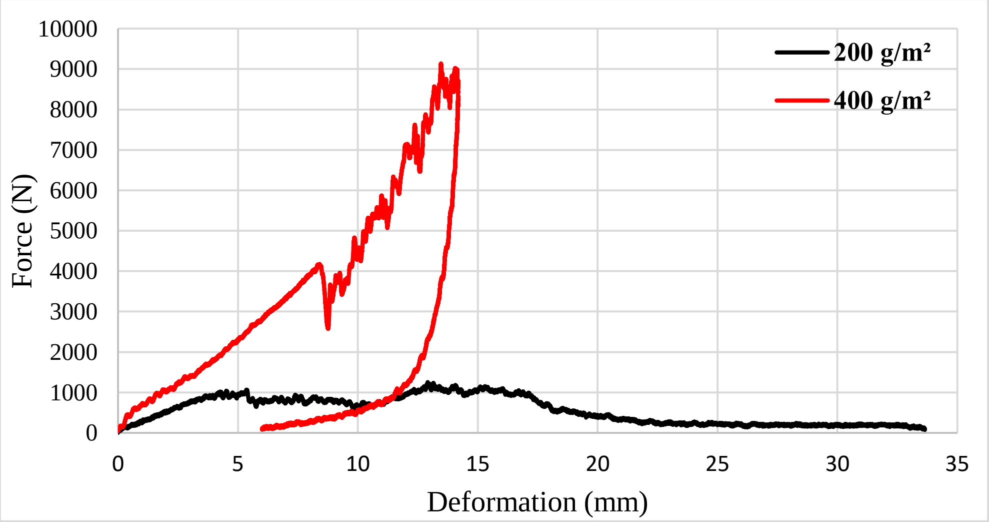

Figure 8. Effect of fiber weight on 50 Joule impact energy

50 Joule impact energy was applied to samples with fiber weights of 200 g/m² and 400 g/m². The sample weighing 200 g/m² reached a maximum force value of approximately 1000 N, and an open curve was formed by perforation on both surfaces. The test sample weighing 400 g/m² had a closed curve formed by bouncing back from the striking tip of the sample. The sample showed a deformation of about 12 mm and reached a max. value of about 9000 Newtons. The damage types in the upper-lower surfaces and core material of the samples as a result of the 50 Joule impact are given in Figure 9.

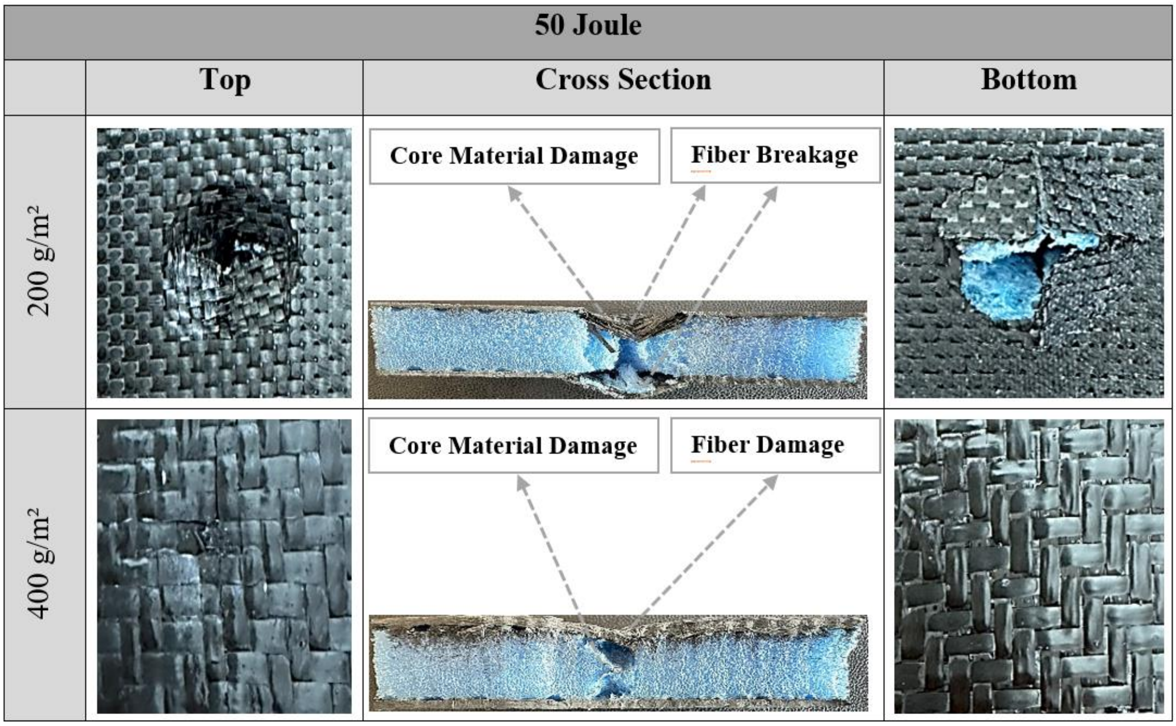

Figure 9. Damage image of the sample after a 50 Joule impact

3.1.4 Effect of fiber weight on strength under 70 joule energy

Figure 10 shows the Force-Deformation graph of carbon fiber-reinforced composites at different weights and 70 Joules of energy.

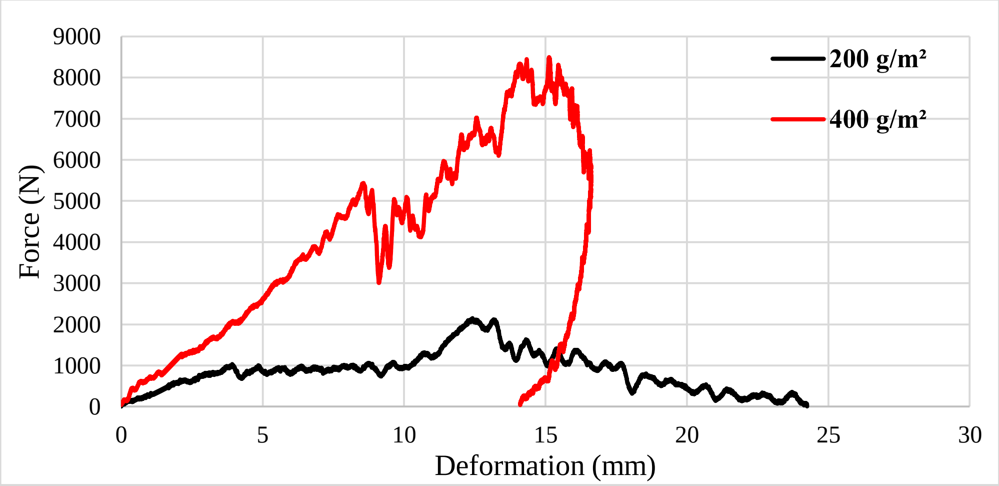

Figure 10. Effect of fiber weight on 70 Joule impact energy

70 Joule impact energy was applied to samples with fiber weights of 200 g/m² and 400 g/m². The sample weighing 200 g/m² reached a maximum force value of approximately 2000 N, and an open curve was formed by perforation on both surfaces. The sample weighing 400 g/m², on the other hand, created a closed curve by bouncing back to the upper surface of the striking tip. This sample reached a maximum force value of approximately 8000 N and showed a deformation of approximately 15 mm at this level. The damage types in the upper-lower surfaces and core material of the samples as a result of the 70 Joule impact are given in Figure 11.

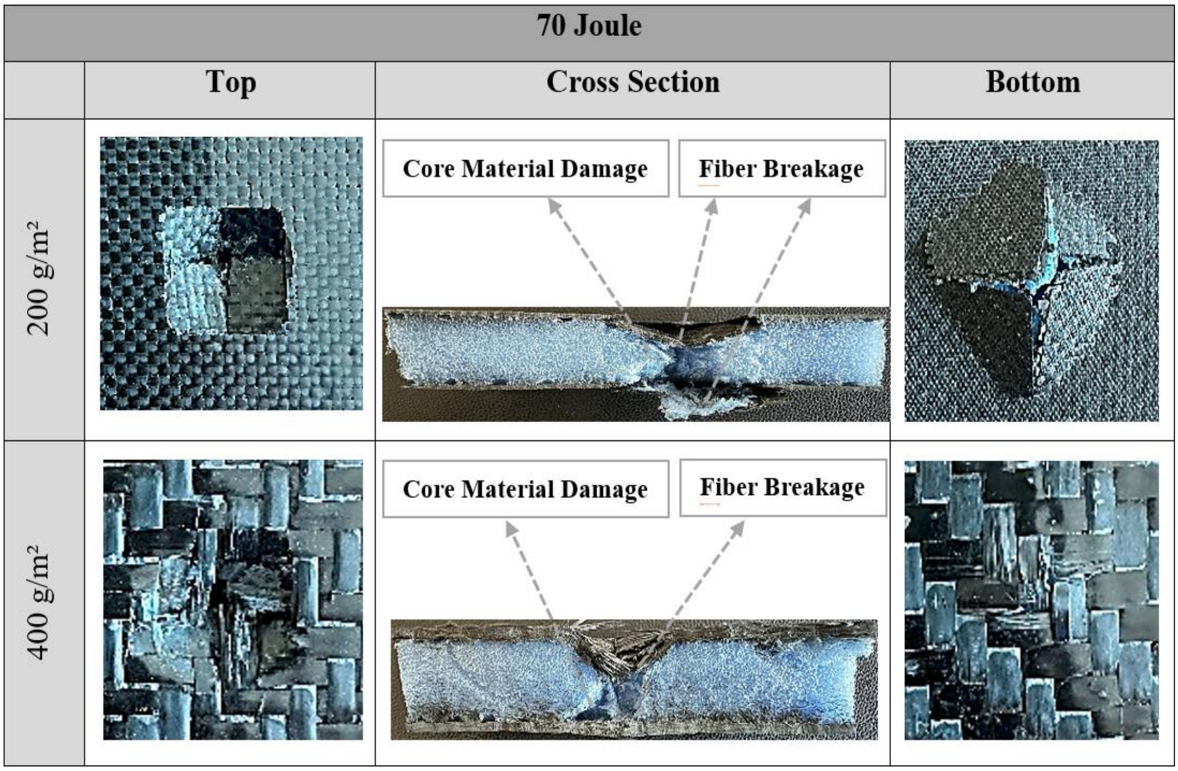

Figure 11. Damage image of the sample after a 70 Joule impact

3.2 Three Point Bending Test Results

The graph in Figure 12 shows the Force-Displacement curves of carbon fiber-reinforced composite samples with different fiber weights subjected to three-point bending tests.

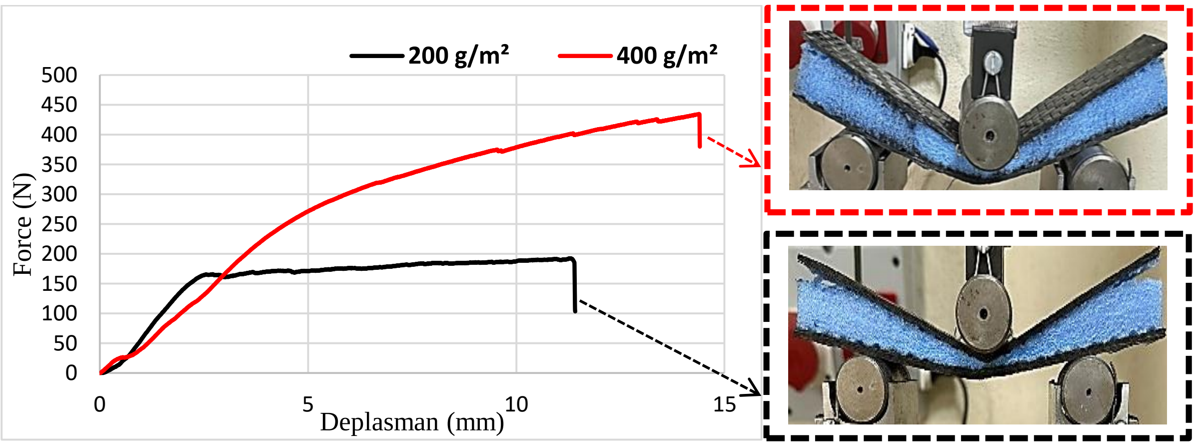

Figure 12. Three point bend test chart

In the three-point bending tests, the sample with a fiber weight of 200 g/m² reached a maximum force value of approximately 200 N and showed the lowest force-carrying capacity. The 200 g/m² sample showed little resistance to bending resistance, and the first fracture occurred. The sample with a density/weight of 400 g/m² showed the highest performance. This sample reached a maximum force value of approximately 450 N and showed the highest force-carrying capacity. The 400 g/m² sample was found to be more resistant to bending resistance than the 200 g/m² sample. Therefore, the increase in fiber density/weight significantly increased the strength of the material.

4. CONCLUSION

In this study, mechanical tests of sandwich structures prepared using carbon fiber-reinforced composite materials and XPS foam cores of different weights were carried out. Impact resistance and bending strength of these structures were investigated at 30 J, 50 J, and 70 J energy levels. According to the results:

Low-speed impact tests applied to carbon fiber-reinforced samples with different fiber weights showed that fiber weight significantly increased impact resistance In the 30 J, 50 J and 70 J impact test results, it is revealed that the sample with a fiber weight of 200 g/m² reached the maximum force elements of approximately 2000 N and punctured on both surfaces. In contrast, the sample with a fiber weight of 400 g/m² reached the maximum force of approximately 9000 N and less damage was observed after the new impact. However, less deformation was observed in heavier fiber materials at the same energy level. The first increase and then the decrease in forces for the 400 g/m² fabric is due to the material being able to absorb energy up to 50 J and being pushed to its structural limits at 70 J. Addition, it was determined that the sample with a fiber weight of 400 g/m² reached a deformation of approximately 10 mm. Three-point bending tests also showed similar results. The sample with a fiber weight of 200 g/m² reached a maximum force of 200 N, while the sample with a fiber weight of 400 g/m² showed the highest performance with 450 N. It was observed that the bending strength improved significantly by increasing the fiber weight in the produced samples. These results show that increasing the fiber weight has a positive effect on both impact strength and bending strength.

As a result, the weight of the fibers must be taken into account as a factor when selecting materials and designing products. It is stressed that this aspect needs to be evaluated to enhance performance, in engineering applications. These results suggest that enhancing the impact resistance and flexural strength of materials can lead to the creation of robust and dependable structures particularly in the automotive and aviation sectors.

5. ACKNOWLEDGEMENTS

This study did not benefit from any support.

6. CONFLICT OF INTEREST

The author accepts that, to the best of his knowledge, he has no conflict of interest or common interest with any institution/organization or person that could influence the evaluation process of the article.

7. AUTHOR CONTRIBUTION

Ercan ŞİMŞİR has the full responsibility of the paper about determining the concept of the research, data collection, data analysis and interpretation of the results, preparation of the manuscript and critical analysis of the intellectual content with the final approval.

8. REFERENCES

Abid S. R., Abdul-Hussein M. L., Ayoob N. S., Ali S. H., Kadhum A.L., Repeated Drop-Weight Impact Tests on Self-Compacting Concrete Reinforced with Micro-Steel Fiber. Heliyon 6 (1), 2020.

Acanfora V., Sellitto A., Russo A., Zarrelli M., Riccio A., Experimental Investigation on 3D Printed Lightweight Sandwich Structures for Energy Absorption Aerospace Applications. Aerospace Science and Technology 137, 108276, 2023.

Adin H., Adin M. Ş., Effect of Particles on Tensile and Bending Properties of Jute Epoxy Composites. Materials Testing 64 (3), 401-411, 2022.

Alabd M. U., Temiz A., Optimization of Annealing and 3D Printing Process Parameters of PLA Parts. International Journal of 3D Printing Technologies and Digital Industry 8(2), 185-201, 2024.

Alagesan P. K., Recent Advances of Hybrid Fiber Composites for Various Applications. Hybrid Fiber Composites 381-404, 2020.

ASTM D638-14, Standard Test Method for Tensile Properties of Plastics, 2022.

Bhong M., Khan T. K. H., Devade K., Vijay Krishna B., Sura S., Eftikhaar H. K., Pal Thethi H., Gupta N., Review of Composite Materials and Applications. Materials Today, Proceedings 2023.

Burkov M. V., Kononova A. A., Eremin A. V., Effect of SWCNT Deposition by Spraying Technique on Mechanical Properties and Electrical Conductivity of Peek Laminates. Mechanics of Composite Materials 60 (3), 561-574, 2024.

Burley A., Aitharaju V., Enhanced Ductility in In-Layer Glass-Carbon Fiber/Epoxy Hybrid Composites Produced Via Tailored Fiber Placement. Composites Part A: Applied Science and Manufacturing 168, 107488, 2023.

Ceritbinmez F., Özkan V., Saracoglu G., Yapici A., MWCNTs Doped GFRPs Drilling: Crosscheck Among Holes Obtained by Alternative Manufacturing Methods, The International Journal of Advanced Manufacturing Technology 118(1), 33-4, 2022.

Ceritbinmez F., Yapici A., Kanca E., The Effect of Nanoparticle Additive on Surface Milling in Glass Fiber Reinforced Composite Structures, Polymers and Polymer Composites 29(9), 575-585, 2021.

Djafar Z., Renreng I., Jannah M., Tensile and Bending Strength Analysis of Ramie Fiber and Woven Ramie Reinforced Epoxy Composite. Journal of Natural Fibers 18 (12), 2315-2326, 2021.

Doğan M. A., Gemi L., Yazman Ş., Ceritbinmez F., Yapici A., Effect of Hybridization and Stacking Sequence on Damage Development in AWJ Machining of Al/FRP/Al FML Composites, Journal of Manufacturing Processes 131, 141-159, 2024.

Fan Y., Mechanical Performance of Advanced Composite Materials and Structures. Materials 17 (10), 2172, 2024.

Ferreira L. M., Aranda M. T., Muñoz-Reja M., Coelho C. A. C. P., Távara L., Ageing Effect on The Low-Velocity Impact Response of 3D Printed Continuous Fibre Reinforced Composites. Composites Part B: Engineering 267, 111031, 2023.

Gebrehiwet L., Abate E., Negussie Y., Teklehaymanot T., Abeselom E., Application of Composite Materials In Aerospace and Automotive Industry: Review. International Journal of Advances in Engineering and Management (IJAEM) 5, 697, 2023.

Habib A., Rajoni H., Sayeed A., Islam M., Taher A., Sajedujjaman M., Saifullah A., Sarker F., Habib A., Rajoni H., Sayeed A., Islam M., Sajedujjaman A.T.M., Sarker F., Saifullah A., Sustainable Jute Fiber Sandwich Composites with Hybridization of Short Fiber and Woven Fabric Structures in Core and Skin Layers. Macromolecular Materials and Engineering 2400138, 1-12, 2024.

He W., Wang L., Liu H., Wang C., Yao L., Li Q. and Sun G., On Impact Behavior of Fiber Metal Laminate (FML) Structures: A State of The Art Review. Thin-Walled Structures 167, 1-33, 108026, 2021.

Ižvolt L., Kardoš J., Dobeš P., Navikas D., Comprehensive Assessment of The Effectiveness of The Application of Foam and Extruded Polystyrene In The Railway Substructure. Buildings 14 (1), 31, 2023.

Karpenko M., Stosiak M., Deptuła A., Urbanowicz K., Nugaras J., Królczyk G., Żak K., Performance Evaluation of Extruded Polystyrene Foam for Aerospace Engineering Applications Using Frequency Analyses. International Journal of Advanced Manufacturing Technology 126, 5515-5526, 2023.

Khan F., Hossain N., Mim J. J., Rahman S. M., Iqbal M. J., Billah M., Chowdhury M. A., Advances of Composite Materials In Automobile Applications – A review. Journal of Engineering 2307-1877, 2024.

Mohamad M. A., Jumahat A., Sapiai N., Flexural Analysis of Hemp, Kenaf and Glass Fibre-Reinforced Polyester Resin. Biopolymer Composites: Production and Modification from Tropical Wood and Non-Wood Raw Materials 9 (1), 231-246, 2023.

Mohammadi H., Ahmad Z., Petru M., Mazlan S. A., Faizal Johari M. A., Hatami H., Rahimian Koloor S. S., An Insight From Nature: Honeycomb Pattern In Advanced Structural Design for Impact Energy Absorption. Journal of Materials Research and Technology 22, 2862-2887, 2023.

Mohanty A. K., Vivekanandhan S., Tripathi N., Roy P., Snowdon M. R., Drzal L. T., Misra M., Sustainable Composites for Lightweight and Flame Retardant Parts for Electric Vehicles to Boost Climate Benefits: A perspective. Composites Part C: Open Access 12, 100380, 2023.

Muthukumarana T. V., Arachchi M. A. V. H. M., Somarathna H. M. C. C., Raman S. N., A Review on The Variation of Mechanical Properties of Carbon Fibre-Reinforced Concrete. Construction and Building Materials 366, 130173, 2023.

Ozturk F., Cobanoglu M., Ece R. E., Recent Advancements In Thermoplastic Composite Materials in Aerospace Industry. Journal of Thermoplastic Composite Materials 37(9), 3084-3116, 2023.

Özcan Z., Effects of Core and Surface Materials on the Flexural Behavior of Lightweight Composites Sandwich Beams, Düzce Üniversitesi Bilim ve Teknoloji Dergisi 12(4), 2387-2399, 2024.

Şimşir E., Yavuz İ., Çağdaş E. M., Comparison of Energies Absorbed at Different Speeds of Polymer Materials Used in Vehicle Bumpers. Konya Journal of Engineering Sciences 4 (9), 2667-8055, 2021.

Tawil H., Tan C. G., Sulong N. H. R., Nazri F. M., Sherif M. M., El-Shafie A., Mechanical and Thermal Properties of Composite Precast Concrete Sandwich Panels: A Review, Buildings 12(9), 1429, 2022.

Wu M., Sadhukhan J., Murphy R., Bharadwaj U., Cui X., A Novel Life Cycle Assessment and Life Cycle Costing Framework for Carbon Fibre-Reinforced Composite Materials in The Aviation İndustry. International Journal of Life Cycle Assessment 28 (5), 566-589, 2023.

Yavuz I. and Yildirim A., Mechanical Properties of PLA Based Closed Porous Structures Manufactured Using FDM Process. Multidiscipline Modeling in Materials and Structures 19 (3), 493–506, 2023.

Yavuz İ., Şimşir E., Şenol B., Investigation of Mechanical Behavior of Glass Fiber Reinforced Extruded Polystyrene Core Material Composites. RSC Advances 14 (19), 13311-13320, 2024.

Zhang T., Yuan J., Pang H., Huang Z., Guo Y., Wei J., Yu Q., UHPC-XPS Insulation Composite Board Reinforced By Glass Fiber Mesh: Effect of Structural Design on The Heat Transfer, Mechanical Properties and Impact Resistance, Journal of Building Engineering 75, 106935, 2023.

JOURNAL of
MATERIALS and MECHATRONICS:A

e-ISSN 2717-8811
JournalMM, 2024, 5(2), 316-326
https://doi.org/10.55546/jmm.1565104

Araştırma Makalesi / Research Article

Measurement of Charpy Impact Durability of Intraply Hybrid Composites Under Ultraviolet Light and Nanoparticle Reinforcement

Zeynal Abidin OĞUZ[1*]

[1*] Adıyaman Üniversitesi, Mühendislik Fakültesi, Makine Mühendisliği Bölümü, Adıyaman, Türkiye,
ORCID ID: https://orcid.org/0000-0002-8566-2331, zoguz@adiyaman.edu.tr

Geliş/ Received: 11.10.2024; **Revize/Revised:** 13.11.2024 **Kabul / Accepted:** 25.11.2024

ABSTRACT: This study investigates the effects of nanoclay reinforcement and UV aging on the low-velocity impact resistance of polymer-based intraply carbon/aramid composites. Nanoclay particles, in concentrations ranging from 0% to 3% by weight, were incorporated into the composites. The impact resistance was examined experimentally, focusing on both the particle reinforcement and the impact of UV aging. Charpy impact tests were conducted on specimens subjected to 450 and 900 hours of UV exposure, alongside a control group. The results revealed that the composite reinforced with 2% by weight of nanoclay exhibited the highest impact resistance, with an improvement of 57.89% compared to the baseline. Although a reduction in impact resistance was observed after 450 hours of UV exposure, partial recovery occurred after 900 hours. Nonetheless, UV aging had an overall negative effect on the impact resistance of the materials. Additionally, scanning electron microscopy (SEM) was used to analyze the failure morphologies of the samples, providing insights into the damage mechanisms.

Keywords: Polymer, Intraply compsites, Nanoclay, Charpy impact test, UV aging

---

*Sorumlu yazar / Corresponding author: zoguz@adiyaman.edu.tr

Bu makaleye atıf yapmak için /To cite this article

Oğuz, Z. A. (2024). Measurement of Charpy Impact Durability of Intraply Hybrid Composites Under Ultraviolet Light and Nanoparticle Reinforcement. Journal of Materials and Mechatronics: A (JournalMM), 5(2), 316-326.

1. INTRODUCTION

Composite materials are of critical importance due to their ability to combine the advantageous properties of different constituent materials, resulting in superior mechanical, thermal, and chemical performance compared to traditional materials. They offer a high strength-to-weight ratio, enhanced durability, and excellent resistance to environmental factors such as corrosion, fatigue, and wear. These properties make composites particularly valuable in applications where lightweight and high-performance materials are essential. Composite materials are widely used in a variety of industries, including aerospace, automotive, marine, and construction. In aerospace and automotive sectors, for instance, composites reduce vehicle weight, leading to improved fuel efficiency and lower emissions. In civil engineering, they are utilized in bridge reinforcement, building structures, and pipelines for their superior durability and resistance to harsh environmental conditions. Furthermore, composites are increasingly found in sporting goods, medical devices, and renewable energy systems, such as wind turbine blades, due to their versatile and customizable nature. This broad range of applications highlights the significance of composite materials in advancing modern technology and engineering solutions (Demircan et al., 2021).

Nanoparticle-reinforced composite materials are important due to their ability to significantly enhance the mechanical, thermal, and functional properties of conventional composites (Ekici et al., 2022). The incorporation of nanoparticles, such as nanoclay, carbon nanotubes, or graphene, into composite matrices can improve properties like strength, stiffness, toughness, and thermal stability without substantially increasing the material's weight. This is particularly advantageous in applications requiring high-performance materials with a low density. Additionally, nanoparticles contribute to enhanced resistance against environmental degradation factors, such as UV radiation, moisture, and chemical exposure, thus extending the lifespan of the composite materials in harsh conditions. Nanoparticles also facilitate better load transfer at the microscopic level due to their high surface area and interaction with the polymer matrix, resulting in superior damage tolerance and impact resistance. As a result, nanoparticle-reinforced composites are increasingly used in cutting-edge technologies, including advanced electronics, medical devices, and energy storage systems, where multifunctionality and superior performance are required.

The impact test is crucial for assessing the mechanical performance of composite materials and ensuring their reliability in various applications. Composite materials, known for their lightweight, high strength, and corrosion resistance, exhibit complex fracture behaviors when subjected to sudden impacts. Impact testing provides critical insights into their energy absorption capacity, fracture toughness, and damage propagation under dynamic loading conditions (Kösedağ et al., 2022) By evaluating the interaction between different layers of composite structures and identifying potential weak points, impact testing helps in optimizing material design and selection for enhanced durability and safety. Thus, the impact test plays a vital role in advancing the application of composites in high-performance environments.

Literature review has shown that composite materials are subjected to single or repeated impact tests (Zhou et al., 2020; Doğan et al., 2022; Kueh et al., 2023). Additionally, the impact properties of composites after hydrothermal aging conditioning was investigated by researchers (Ferreira et al., 2023; Oğuz et al., 2021a; Oğuz et al., 2021b).

In addition to composite materials subjected to impact testing without exposure to any environment or by exposure to hydrothermal/hygrothermal environments, the effect of UV aging on the impact resistance of various composite materials was also investigated. Doğan and Arman (2019) applied drop weight impact test to glass fiber reinforced composite materials after keeping them in different environments including UV aging. It was reported that aging affected the perforation threshold and absorbed energy values. Especially at low impact energies, delamination emerged as the main failure mode, while fiber fracture became more pronounced at higher energies. UV aging was found to reduce impact resistance by approximately 33% compared to the unaged group. Alsaadi and Erkliğ (2021) investigated the mode I fracture properties of glass/epoxy samples with micro particle reinforcement ranging from 0 to 20 wt% after 1000 hours of UV aging. It was found that the addition of 10% of micro particles improved the fracture toughness of aged samples by 14.3%, while the improvement in unaged samples was 1.7%. Ovalı and Sancak (2022) added various UV protective agents to jute fiber reinforced low density polyethylene materials and left the materials in the UV environment for 120 and 240 hours. Impact tests were applied to the samples at the end of two different aging periods. While the change in impact strength was seen as minor after short-term aging, dramatic decreases were observed in the impact strength of the samples after long-term aging. In addition, samples containing protective agents were less affected by UV aging than the group without. Nasri et al. (2022), evaluated the drop weight properties of natural fiber reinforced polypropylene after UV radiation. All samples were aged for 960 h. This study showed that flax fiber reinforced polypropylene (PP30-F) was more sensitive to UV radiation, with its impact strength decreasing by 33% after 960 hours of UV exposure. In addition, pine fiber reinforced polypropylene (PP30-P) showed a lower decrease, with the impact strength decreasing by around 10%.

In contrast to previous studies, this research focuses on the Charpy impact resistance of intraply carbon/aramid hybrid composites reinforced with six different weight percentages of nanoclay particles, both before and after UV aging. Specifically, the samples were subjected to UV exposure for 450 and 900 hours, without the use of UV stabilizers, in order to investigate the effect of varying nanoclay content on impact resistance over different aging periods. The absence of UV retardants and the exploration of the influence of nanoclay on UV-induced degradation marks a critical distinction from existing literature. This study aims to provide new insights into how nanoclay reinforcement alters the impact performance of hybrid composites under prolonged UV exposure, offering valuable data for outdoor and high-durability applications of such materials.

2. MATERIALS AND METHODS

2.1 Materials

The reinforcing material utilized in this study was a carbon/aramid twill woven fabric. To fabricate the composite laminates, epoxy resin MGS L 160 was mixed with hardener MGS H 160 in a stoichiometric ratio of 100:25 by weight. The fabric and chemical components used in the production of the composite plates were supplied by Dost Kimya (Turkey), while the nanoparticles were sourced from Grafen Kimya (Turkey). The physical properties of these materials are summarized in Table 1.

Table 1. Physical properties of materials

Material	Specifications	Dimensions
Carbon/aramid intraply fabric	Areal density	210 g/m^2
	Fiber thickness	0.12 mm
Epoxy Resin MGS L160	Density	1.13-1.17 g/m^3
	Viscosity	700-900 mPas
	Flexural Strength	110-140 (N/mm^2)
	Modulus of Elasticity	3.2-3.5 (kN/mm^2)
	Tensile Strength	70-80 (N/mm^2)
	Impact Strength	40-50 (kJ/m^2)
Nanoclay	Lateral width	0.5-2 µm
	Thickness	1-10 nm
	Bulk Density	200-500 kg/m^3

Composite samples were produced by vacuum-assisted hand lay-up method that include two primary steps. In the first step the MGS L 160 epoxy resin was mixed with varying weight percentages of nanoclay particles (0, 0.5, 1.0, 1.5, 2.0, and 3.0 wt.%) using an ultrasonic mixer. Then MGS H 160 hardener was added till a homogenous mixture was achieved. Epoxy resin and hardener were combined using a mechanical stirrer set at 8000 rpm for 10 minutes. After the first step was completed, the mixture prepared in the first step was applied to 12 layers of intraply carbon/aramid fabrics with 0°/90° stacking sequence by means of a roller. Attention was paid to the curing times of the resin system according to the manufacturer's recommendations and plate production was completed under 700 mm-Hg vacuum pressure. The sample thicknesses for each weight group are given in Table 2.

Table 2. Thickness of the composite groups

Thickness (mm)					
0 wt%	**0.5 wt%**	**1 wt%**	**1.5 wt%**	**2 wt%**	**3 wt%**
3.12±0.05	3.07±0.02	3.16±0.01	3.11±0.07	3.08±0.04	3.09±0.02

In this article, coding has been done for sample groups in the text or in their graphical representations. For example, in a name like CA0.5-450, CA represents carbon/aramid intraply fabric. The numerical expression immediately following CA (0.5, 1.0 etc.) refers to the reinforcement ratio. The number in the last part (0, 450 or 900) indicates the aging period.

2.2 UV Aging of Samples

For this study, an OSRAM brand UV lamp was used in a cabin according to ASTM G 154 standards. In addition, a fan was used for homogeneous heat distribution in the cabin. Two-thirds of the prepared samples were subjected to UV aging. Two different aging periods were determined for UV aging as 450 and 900 hours.

2.3 Charpy Impact Test

The impact strength of the samples was assessed using a Charpy impact testing machine (Köger 3/70) in compliance with the ISO 179/92 standard. The specimens, each with dimensions of 55 x 10 mm, were prepared for testing in a flatwise impact direction. An impact hammer with an energy capacity of 15 J was used for the tests. Fig. 1 illustrates the flatwise impact testing setup. The absorbed energy and impact strength values were calculated using Eqs. 1 and 2, based on the energy differences between the initial (E_1) and final (E_2) energy levels,

$$E = E_1 - E_2 \tag{1}$$

$$U = \frac{E}{bh} \tag{2}$$

Where E and U represent the absorbed energy and impact strength values. The width b and thickness h of the samples were used to calculate the impacted area.

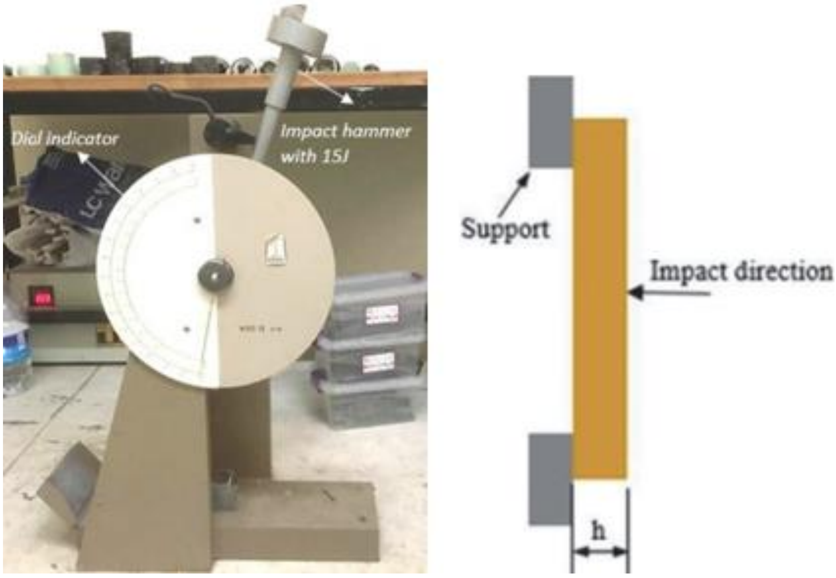

Figure 1. Illustration of Charpy impact test

After the Charpy impact test, the SEM images were taken to identify the damage character of samples.

3. RESULTS AND DISCUSSION

3.1 Charpy Impact Test Results

The Charpy impact test results of the samples are clearly shown in Figure 2. The Charpy impact test results for intraply carbon/aramid hybrid composites reinforced with varying weight percentages of nanoparticles (0, 0.5, 1.0, 1.5, 2.0, and 3.0 wt.%) showed a clear enhancement (45.95, 53.4, 56.74, 64.94, 72.55 and 72.04 kJ/m²) in impact strength with increasing nanoparticle content up to a certain threshold. The impact strength values for the composites ranged from 45.95 kJ/m² for the unreinforced (0 wt.%) sample to a peak value of 72.55 kJ/m² at 2.0 wt.% nanoparticle reinforcement. This represents a significant improvement in impact performance, particularly between 0 and 2.0 wt.% reinforcement, indicating that the inclusion of nanoparticles effectively increases energy absorption during impact. However, beyond 2.0 wt.%, a slight decrease to 72.04 kJ/m² was observed at 3.0 wt.%, suggesting a potential saturation point or agglomeration effect, where the addition of further nanoparticles may no longer contribute positively to the composite's impact strength. These findings highlight the optimal nanoparticle concentration for improving the mechanical properties of hybrid composites and emphasize the importance of controlling filler content to maximize performance.

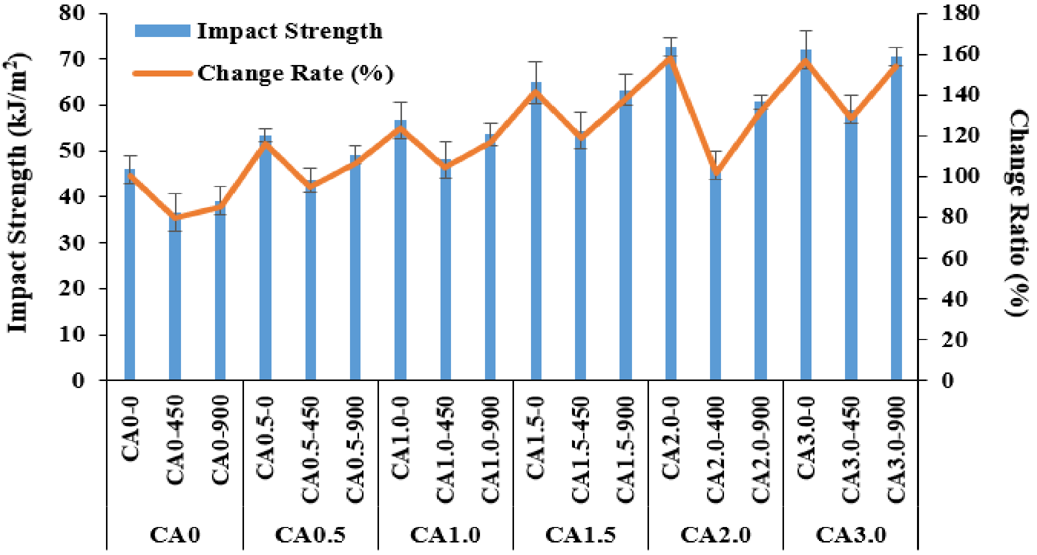

Figure 2. Impact strength results of samples

The Charpy impact test results for hybrid carbon/aramid intraply composites reinforced with varying weight percentages of nanoparticles (0, 0.5, 1.0, 1.5, 2.0, and 3.0 wt.%) demonstrated notable differences in impact performance after 450 and 900 hours of UV aging. For the 450-hour UV-aged samples, impact strengths were found as 36.6, 43.62, 48.09, 54.47, 46.78 ve 59.03 kJ/m^2 for 0, 0.5, 1.0, 1.5, 2.0, and 3.0 wt.%, respectively. It is clear that the impact strengths decreased across all nanoparticle concentrations compared to the unaged composites, with the maximum impact strength observed at 1.5 wt.% reinforcement (54.47 kJ/m^2), followed by a significant drop at 2.0 wt.% (46.78 kJ/m^2). This suggests that prolonged UV exposure up to 450 hours induces degradation that weakens the composite, particularly at higher nanoparticle concentrations, potentially due to UV-induced surface microcracking or material embrittlement. After 900 hours of UV aging, however, the impact strength values showed a recovery trend compared to the 450-hour aged samples, with a peak value of 70.61 kJ/m^2 at 3.0 wt.% reinforcement. For the 0, 0.5, 1.0, 1.5, 2.0, and 3.0 wt.% nanoparticle reinforced composite samples the impact strengths were found as 39.18, 49.04, 53.59, 63.35, 60.69 ve 70.61 kJ/m^2, respectively. This improvement after extended UV exposure might be attributed to the relaxation or reformation of the polymer matrix after prolonged aging, allowing better load distribution during impact. Although the 900-hour aged samples did not fully regain the initial impact strengths of the unaged composites, the results indicate that nanoparticle reinforcement helps mitigate UV degradation over time, particularly in higher concentrations.

These findings imply that the extended UV aging period increased the cross-linking and rigidity on the outermost layer of the samples by allowing the free radicals produced during radiation exposure to recombine. This durability improvement can be ascribed to a potential crosslinking among adjacent molecules from both resin and particles, which results in a stronger durability against UV aging after 900 hours of UV aging degradation (Silva et al., 2020; Azim, 2016).

However, when the impact test results were examined in general, it was observed that UV aging reduced the impact strength of nanoclay reinforced intraply samples. UV aging negatively affects impact strength due to several key mechanisms that degrade the material's structural integrity over time. Prolonged exposure to UV radiation leads to both physical and chemical changes in the polymer matrix of composite materials, resulting in a reduction in their ability to absorb and dissipate energy during impact events (Doğan and Arman, 2019). UV exposure induces photo-oxidation in the polymer matrix, breaking down polymer chains and leading to a loss of mechanical properties. This chemical degradation weakens the polymer structure, making the material more brittle. As a result, the material's ability to resist impact diminishes, as it becomes more prone to cracking and failure under stress (Alsaadi and Erkliğ, 2021; Ovalı and Sancak, 2022). In addition, UV aging typically causes the polymer matrix to stiffen, reducing its ductility and flexibility. As the material becomes more brittle, its capacity to deform and absorb energy during an impact event decreases. Instead of absorbing the impact energy through plastic deformation, UV-aged materials are more likely to fracture suddenly, leading to lower impact strength (Nicholas et al., 2016; Doğan and Arman, 2019). In fiber-reinforced composites, UV radiation can deteriorate the fiber-matrix interface. This weakening reduces the efficiency of load transfer between the fibers and the matrix, a critical factor in the composite's overall impact performance. The compromised interface leads to poor bonding and reduced ability to withstand impact forces, resulting in lower impact strength (Nasri et al., 2022; Silva et al., 2020).

The amount of energy absorbed by the samples during the flatwise Charpy impact test is shown in Figure 3. When the absorbed energy amounts are taken into consideration, it is clearly seen that the results are parallel to the impact strength results. An increase in the absorbed energy amounts was detected with particle reinforcement. The increasing trend continued up to 2.0 wt.%. Although a slight decrease was observed for the 3.0 wt.% samples, the amount of absorbed energy was still high for this ratio compared to the unreinforced samples. Also, similar to the impact strength results, the absorbed energy amounts decreased after 450 hours of UV aging. Although the absorbed energy amounts after 900 hours of UV aging improved compared to 450 hours, they were still lower than the unaged samples.

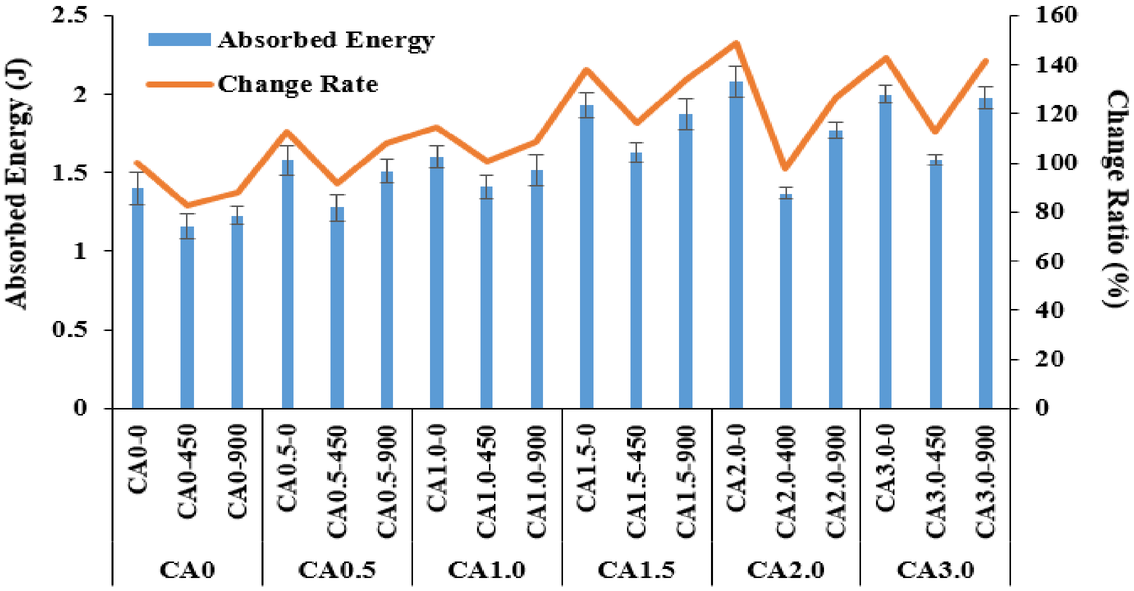

Figure 3. Absorbed energy values of samples

For the unaged samples, absorbed energies were found as 1.4, 1.58, 1.6, 1.93, 2.08 and 2.0 J for 0, 0.5, 1.0, 1.5, 2.0, and 3.0 wt.%, respectively. In addition, the absorbed energy amounts after 450-900 h of UV aging were 1.16-1.23, 1.28-1.51, 1.41-1.52, 1.63-1.87, 1.37-1.77 and 1.58-1.98 J for 0, 0.5, 1.0, 1.5, 2.0, and 3.0 wt.%, respectively.

3.2 SEM Results

SEM images were taken from the broken samples after the Flatwise Charpy impact test. Figure 4 displays the typical configuration of the impact damage and distributions across a laminate. In most cases, low-velocity impacts result from things like fallen tools and collision damage. The laminate displays a quasi-static behavior in these circumstances, with bending of the laminate being the predominant stress state (Bibo and Hogg, 1996). As a result, ply cracking and delamination are frequently the most common damage types. The SEM images of samples are shown in Figure 5. As clearly observed from the images, impact-induced fiber breakage, matrix breakage or crack, delamination between fiber-matrix and fiber-fiber were identified as the main types of failures.

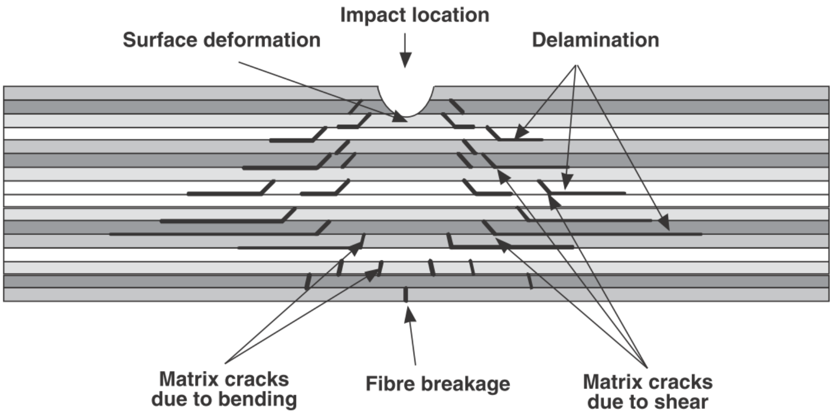

Figure 4. Schematic designation of a general low impact failure of a composite (Shyr and Pan, 2003)

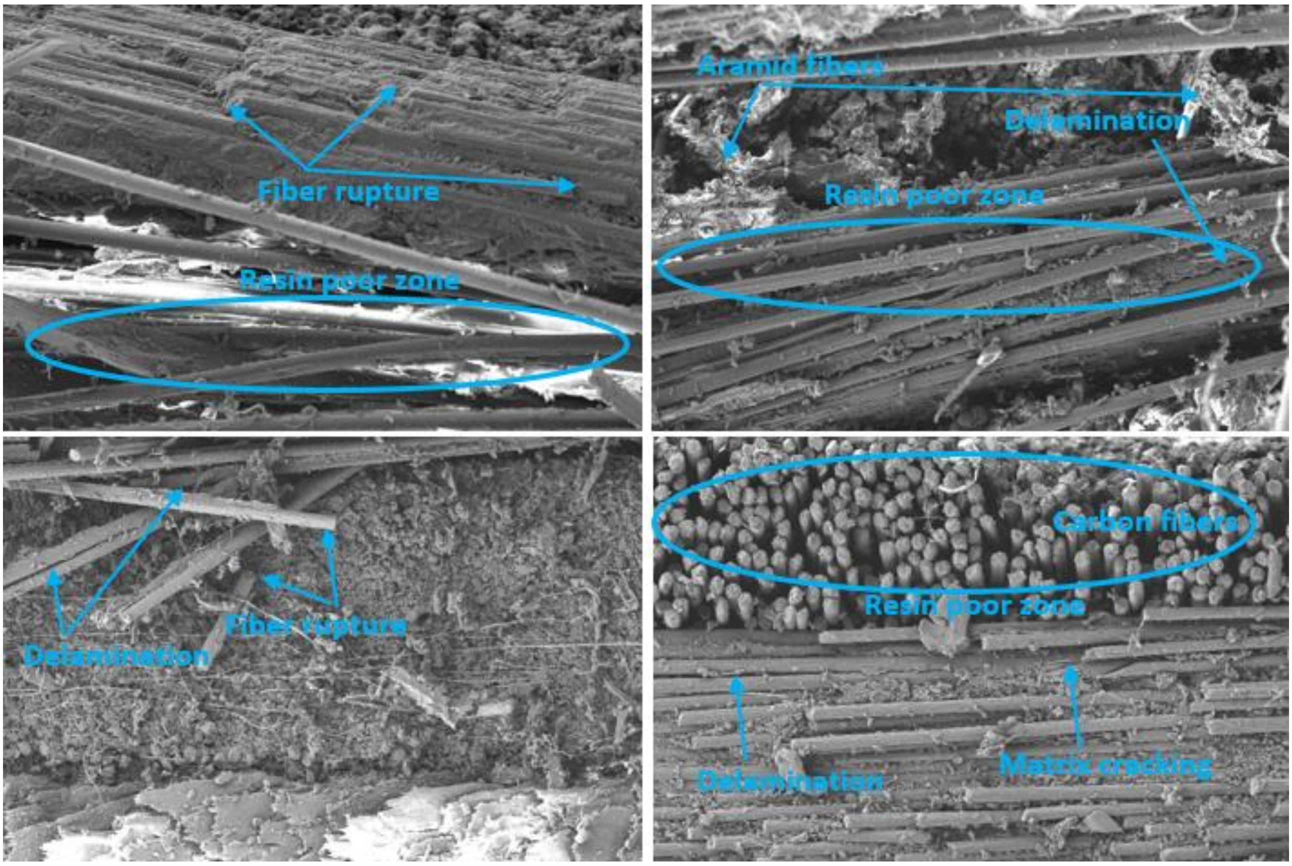

Figure 5. SEM images of samples

4. CONCLUSION

This study investigated the impact strength of nanoparticle-reinforced carbon/aramid hybrid composites subjected to various UV aging periods (450 and 900 hours) to assess the effect of UV exposure on mechanical performance. Charpy impact tests were performed on composites with different weight percentages of nanoclay reinforcement (0, 0.5, 1.0, 1.5, 2.0, and 3.0 wt.%).

The results for unaged samples showed a steady increase in impact strength as the nanoclay content increased, reaching a peak value of 72.55 kJ/m² at 2.0 wt.% reinforcement. Beyond this concentration, a slight decrease in impact strength was observed, with the 3.0 wt.% sample registering 72.04 kJ/m². This suggests that nanoparticle addition improves the energy absorption capacity of the composites up to an optimal threshold, after which further reinforcement does not provide additional benefits.

However, UV aging significantly impacted the composite's performance. After 450 hours of UV exposure, a notable decline in impact strength was observed across all samples. The impact strength of the 0 wt.% sample dropped from 45.95 kJ/m² to 36.6 kJ/m², indicating the material's sensitivity to UV degradation. The highest impact strength after 450 hours was recorded at 1.5 wt.% reinforcement (54.47 kJ/m²), but a significant drop occurred for the 2.0 wt.% sample (46.78 kJ/m²). This suggests that while nanoclay reinforcement initially improves UV resistance, higher concentrations may lead to diminished benefits under prolonged UV exposure due to potential agglomeration or interface weakening.

After 900 hours of UV aging, the impact strength of all samples recovered to some extent compared to their 450-hour values. The 3.0 wt.% sample exhibited the highest impact strength after 900 hours (70.61 kJ/m²), demonstrating a significant improvement over the 2.0 wt.% sample, which had the highest unaged performance. This recovery indicates that extended UV exposure may lead to matrix reorganization or relaxation, allowing for better load distribution during impact. Nonetheless, even after 900 hours of aging, the composites did not fully regain their unaged impact strength levels, reflecting the persistent effects of UV-induced degradation.

In conclusion, the addition of nanoclay particles significantly enhances the impact strength of carbon/aramid hybrid composites, particularly at concentrations up to 2.0 wt.%. However, UV aging introduces degradation mechanisms that reduce impact performance, particularly after shorter exposure periods. Despite some recovery in impact strength with prolonged aging, the results underscore the importance of optimizing nanoparticle content and UV stabilization strategies to improve the long-term durability of hybrid composites in outdoor applications.

5. ACKNOWLEDGEMENTS

This study did not receive funding support from any institution or organization.

6. CONFLICT OF INTEREST

Author approves that to the best of their knowledge, there is not any conflict of interest or common interest with an institution/organization or a person that may affect the review process of the paper.

7. AUTHOR CONTRIBUTION

Zeynal Abidin OĞUZ has the full responsibility of the paper about determining the concept of the research, data collection, data analysis and interpretation of the results, preparation of the manuscript and critical analysis of the intellectual content with the final approval.

8. REFERENCES

Alsaadi M., Erkliğ A., UV accelerated aging and sewage sludge ash particle effects on mode I interlaminar fracture properties of glass fiber/epoxy composites. Iranian Polymer Journal 30, 811-820, 2021.

ASTM G154 Standard Practice for Operating Fluorescent Light Apparatus for UV Exposure of Nonmetallic Materials.

Azim A.Y.M.A., Effect of Gamma Radiation on the Properties of Jute Reinforced Polyester Matrix Composites. Journal of Textile Science and Engineering 7 (2), 2016.

Bibo G., Hogg P., The role of reinforcement architecture on impact damage mechanisms and post-impact compression behaviour. Journal of Materials Science 31, 1115-1137, 1996.

Demircan G., Kısa M., Özen M., Açıkgöz A., Quasi-static penetration behavior of glass-fiber-reinforced epoxy nanocomposites. Mechanics of Composite Materials 57, 503-516, 2021.

Doğan A., Arman Y., The effect of hygrothermal aging and UV radiation on the low-velocity impact behavior of the glass fiber-reinforced epoxy composites. Iranian Polymer Journal 28, 193-201, 2019.

Doğan N.F., Özbek Ö., Erkliğ A., Effect of graphene nanoplatelets on mechanical and impact properties of an aramid/glass-reinforced epoxy composite. Materials Testing 64 (4), 490-501, 2022.

Ekici R., Kösedağ E., Demir M., Repeated low-velocity impact responses of SiC particle reinforced Al metal-matrix composites. Ceramics International 48 (4), 5338-5351, 2022.

Ferreira L.M., Aranda M.T., Muñoz-Reja M., Coelho C.A.C.P., Távara L., Ageing effect on the low-velocity impact response of 3D printed continuous fibre reinforced composites. Composites Part B: Engineering 267, 111031, 2023.

Kösedağ E., Çalışkan U., Ekici R., The effect of artificial aging on the impact behavior of SiC nanoparticle-glass fiber-reinforced polymer matrix composites. Polymer Composites 43 (2), 964-976, 2022.

Kueh A.B.H., Sabah S.H.A., Qader D.N., Drahman S.H., Amran M., Single and repetitive low-velocity impact responses of sandwich composite structures with different skin and core considerations: A review. Case Studies in Construction Materials 18, e01908, 2023.

Nasri K., Toubal L., Loranger E., Koffi D., Influence of UV irradiation on mechanical properties and drop-weight impact performance of polypropylene biocomposites reinforced with short flax and pine fibers. Composites Part C 9, 100296, 2022.

Nicholas J., Mohamed M., Dhaliwal G.S., Anandan S., Chandrashekhara K., Effects of accelerated environmental aging on glass fiber reinforced thermoset polyurethane composites. Composites Part B, 94, 370-378, 2016.

Oğuz Z.A., Erkliğ A., Bozkurt Ö.Y., Degradation of hybrid aramid/glass/epoxy composites hydrothermally aged in distilled water. Journal of Composite Materials 55 (15), 2043-2060, 2021a.

Oğuz Z.A., Erkliğ A., Bozkurt Ö.Y., Effects of hydrothermal seawater aging on the mechanical properties and water absorption of glass/aramid/epoxy hybrid composites. International Polymer Processing 36 (1), 79-93, 2021b.

Ovalı S., Sancak E., Investigating the effect of the aging process on LDPE composites with UV protective additives. Journal of Thermoplastic Composite Materials 35 (11), 1921-1939, 2022

Shyr T.W., Pan Y.H., Impact resistance and damage characteristics of composite laminates. Composite Structures 62, 193-203, 2003.

Silva A.O., Monsores K.G.C., Oliveira S.S.A., Weber R.P., Monteiro S.N., Vital H.C., Influence of gamma and ultraviolet radiation on the mechanical behavior of a hybrid polyester composite reinforced with curaua mat and aramid fabric. Journal of Materials Research and Technology, 9 (1), 394-403, 2020

Zhou J., Wen P., Wang S., Numerical investigation on the repeated low-velocity impact behavior of composite laminates. Composites Part B: Engineering 185, 107771, 2020.

JOURNAL of
MATERIALS and MECHATRONICS:A

e-ISSN 2717-8811
JournalMM, 2024, 5(2), 327-340
https://doi.org/10.55546/jmm.1584040

Araştırma Makalesi / Research Article

The Influence of B Content on the Microstructure and Hardness of in Situ Formed TiC-TiB_2 Reinforced Fe-Based Hardfacing Coatings

Bülent KILINÇ[1*]

[1*] Sakarya University of Applied Sciences, Machine and Metal Department, Vocational School of Arifiye, Sakarya, Türkiye,
ORCID ID: https://orcid.org/0000-0003-4928-7148, bkilinc@subu.edu.tr

Geliş/ Received: 13.11.2024; **Revize/Revised:** 26.11.2024 **Kabul / Accepted:** 01.12.2024

ABSTRACT: In this study, Fe-Cr-Ti-(B, C) based hardfacing coatings with different ratios were produced on DIN St37 steel plate surface using tungsten inert gas (TIG) welding method. It was investigated how increasing boron content affects the morphology of in situ TiC-TiB_2 phases expected to form in situ in the coating. The effects of these changes in microstructure on the microhardness of the hardfacing coatings were also determined. X-ray analyses revealed that phases such as α-(Fe, Cr), M_2B, TiC, and M_7C_3 were formed in coatings with 10% B content, and TiB_2 phase was also detected in coatings with 20% and 30% boron content. In addition, it was determined that the volume fraction ratio of TiB_2 phase increased in the coating microstructures and it was synthesised as a rod-like structure. Accordingly, the microhardness values of the hardfacing coatings increased significantly. The highest microhardness found was 1045 $HV_{0.2}$ for the coating produced from 30B-Ti composition, which is about 4.5 times higher than the base steel (234 $HV_{0.2}$).

Keywords: In situ, TiC-TiB_2, Hardfacing, Surface alloying, Hardness, Wear

---

*Sorumlu yazar / Corresponding author: bkilinc@subu.edu.tr

Bu makaleye atıf yapmak için /To cite this article

Kılınç, B. (2024). The Influence of B Content on the Microstructure and Hardness of in Situ Formed TiC-TiB_2 Reinforced Fe-Based Hardfacing Coatings. Journal of Materials and Mechatronics: A (JournalMM), 5(2), 327-340.

1. INTRODUCTION

Hardfacing is a powerful and inexpensive deposition method used to repair worn parts or to improve their wear properties. This method is widely used in heavy industries and extends the service life of components by improving their wear, corrosion and impact resistance (Ahn, 2013; Durmuş et al., 2018; Variables & Works, 2023). Various welding methods are used for hardfacing. Among these methods, plasma transfer arc (PTA) welding (Brezinová et al., 2021; D'Oliveira et al., 2006; Huang et al., 2022), laser cladding (Hu et al., 2024), gas metal arc welding (GMAW) (Pawlik et al., 2023) and tungsten inert gas (TIG) welding (Jozwik et al., 2018) etc. are the most common ones. Among these methods, hardfacing coatings made by TIG welding are more preferred due to the low cost of equipment (Kumar & Das, 2022; Lin et al., 2010). In the TIG method, an arc is created between the tungsten electrode and the workpiece, and the resulting high heat melts the layer previously placed on the steel surface. Thus, by melting the coating powder on the steel substrate, coating layers with high hardness and high wear properties are obtained. (Buytoz & Ulutan, 2006). For this reason, many researchers have successfully used the TIG method to produce a hard and wear-resistant coating in their work.

In composite coatings, the mixture of a highly ductile metal matrix and hard reinforcement phases improves wear and hardness properties. To produce these composites, firstly, high hardness ceramic particles are directly reinforced. In the second method, various reinforcement phases (TiB, TiB_2 and TiC, etc.) are formed by in-situ synthesis in a melt pool (Weng et al., 2022). TiB_2 and TiC ceramics are the most widely used ceramics to improve the mechanical performance of coatings due to their great features such as high melting point, high hardness, and high thermal stability (Chen et al., 2022; Gupta et al., 2022). Wang et al (Wang et al., 2008) produced composite hardfacing coatings reinforced with in situ TiC and TiB_2 particles by forming different mixtures of Fe, Ti and B_4C powders by argon arc welding. Zhang et al. (Zhang et al., 2017) fabricated Fe-based composite coatings reinforced with Fe-Ti-Cr-B-C particles by laser cladding technique. They prepared FeTi30 (Ti about 30 wt%), B_4C (90 wt%) and iron powders in a mixed ratio as precursor powders. The effects of ferrochrome (FeCr) addition to these powders on the microstructure and mechanical properties of the coatings were investigated. Tang (Tang, 2016), deposited TiC-TiB_2 composite coating on the surface of 40Cr steel by electrical discharge hardening with a TiC-TiB_2 composite rod as an electrode. The structure, phase compositions, hardness and wear properties of the composite coating were investigated. The composite rod used for the coating process was prepared by self-propagating high-temperature synthesis of Ti and B_4C powders. In the literature, the use of Ti and B_4C powders to produce in situ TiC-TiB_2 reinforced hardfacing coatings is common, but the use of ferroalloys is limited.

In this research, ferrous-boron, ferrous-chromium and ferrous-titanium were used as coating powders to produce TiC-TiB_2 reinforced Fe based hardfacing coating. The use of such ferroalloys as coating powders significantly reduces the cost of the coating material and also lowers the melting point of the coating material through eutectic reactions (Du et al., 2008). In this research, Fe-Cr-Ti-(C,B) based coatings with three different boron contents were deposited on low carbon steel surface by TIG welding method. The phase constituents, microstructure and hardness properties of the produced hardfacing coatings were systematically investigated.

2. MATERIALS AND METHODS

2.1 Materials

The steel substrate was first cut in dimensions of 30 mm × 80 mm × 10 mm and then grooved on its surfaces with a depth of 2 mm and a width of 10 mm on a milling machine. The surfaces of the prepared steel substrates to be subjected to the coating process were cleaned from dirt and oil.

Table 1. Chemical composition of the DIN St37 steel (wt.%)

C	Mn	S	P	Fe
0.22	1.5	0.03	0.033	Bal.

Ferrous-boron, ferrous-titanium, ferrous-chromium, and iron powder were used for the hardfacing process. The compositions of the ferroalloy powders used for the formation of Fe-Cr-Ti-(B,C) based hardfacing coatings are given in Table 2. Ferroalloys in rock form were first crushed. After crushing, they were ground in a Retch ring mill with a sieve size of 75 μm.

Table 2. Composition of used ferroalloys (wt.%)

Ferro-alloys	Fe	B	Ti	Cr	C	Al
Ferrous-boron	81.82	18.1	-	-	0.19	-
Ferrous-chromium	33.35	-	-	60	0.15	1.5
Ferrous-titanium	25.2	-	70.95	-	0.13	3.96
Pure iron	99.98	-	-	-	-	-

Iron powder, which was supplied in powder form, was directly sieved to a sieve size of 75 μm. A pre-written excel programmed was used to atomically determine the hardfacing compositions at the desired ratios. With the help of this program, the ferroalloys whose weight ratios are given in Table 2 were first converted into atomic ratios. Then, by entering the desired atomic values, the required amount of each ferroalloy by weight was calculated. Finally, the powders were weighed and mixed on a precision balance according to the composition ratios given in Table 3. Thus, the desired alloy ratios for hardfacing were formed.

Table 3. Atomic ratios of the compositions prepared for hardfacing (at.%)

Metal Alloys	Fe	Cr	Ti	C	B
10B-Ti	55	15	15	5	10
20B-Ti	45	15	15	5	20
30B-Ti	35	15	15	5	30

2.2 Hardfacing Process

The powders prepared in three different compositions were subjected to grinding and mixing process in MSE TECH brand mill at 200 rpm for 1 hour. In the mixing process, the powder/ball ratio was selected as 1/3. Steel balls with a diameter of 7 mm were used for mixing. The containers and balls were thoroughly cleaned with pure alcohol before mixing. The powder mixtures were mixed with potassium silicate (K_2O_3Si) with the help of a metal rod until a paste consistency was obtained. The powder mixture was plastered one by one to fill the channels in the substrate materials. The resulting sample was dried in the open air for 24 hours and then heated in an oven at 250°C for 2 hours.

The powders dried in channels on the steel substrate surface were melted by tungsten inert gas (TIG) welding method for hardfacing. Hardfacing operations were carried out using a Magmaweld ID 220T AC/DC Pulse brand TIG inverter welding machine with 160 A welding current, 20 V welding voltage, 12 L/min argon (99.9%) flow rate and Type W-2 pct ThO2 tungsten electrode. The coated specimens were then cooled in an open atmosphere and subjected to sandblasting to remove the oxide layer and slag formed during coating.

2.3 Metallographic Study

The samples coated by TIG process were cut perpendicular to the welding direction and bakelite was taken for microstructure examinations. The specimens were first subjected to sanding process for microstructure investigations. They were then polished with 1 μm Al2O3 paste and etched with 3% Nital solution. SEM-EDS examinations of the Fe-Cr-Ti-(C, B) based alloy formed on the surface were carried out with JEOL-JSM-6060 scanning electron microscope.

Phase analyses of the samples in which Fe-Cr-Ti-(C, B) based alloys were produced on their surfaces were carried out by using RIGAKU D/MAX/2200/PC brand x-ray diffractometer. CuKα (λ= 1,5408 A°) radiation was used during the analyses.

The microhardness measurements of the produced samples were carried out using FutureTech FM700 microhardness tester under 200 g load from the surfaces prepared for microstructure investigations. Measurements were made with a Vickers tool ($HV_{0.2}$) from the substrate to the surface at 0.2 mm intervals from three different areas as row hardness and the arithmetic mean was calculated.

3. RESULTS AND DISCUSSION

3.1 Microstructural and Phase Analysis

Figure 1 shows the SEM microstructure image of the cross-sectional area of the 30B-Ti sample coated on the DIN St37 steel surface. It can be seen that the hardfacing produced formed a metallurgical bond with the steel substrate and did not contain pores and any microscopic cracks. From the microstructure images, it is observed that there is a harmonious transition between the hardfacing and the substrate material, and a homogeneous coating structure is formed. In addition, the substrate, interface (fusion line), transition zone and coating layer can be clearly distinguished. In the hardfacing process performed by TIG welding, dilution of the coating layer may occur due to some melting of the substrate.

In this layer, called the transition zone in Figure 1, there is more iron content than the hardfacing coating layer. Therefore, the black rod-like (TiB_2) structures seen in the upper layers are not seen in this region. This is a result of solidification rate changes that are much higher in the upper regions of the coating layer. The solidification rate (R) from the fusion line (interface) to the coating surface increased and at the same time the temperature gradient (G) decreased. Therefore, this transition zone consists of planar growth, cellular and coaxial dendrite growth (Hajihashemi et al., 2015).

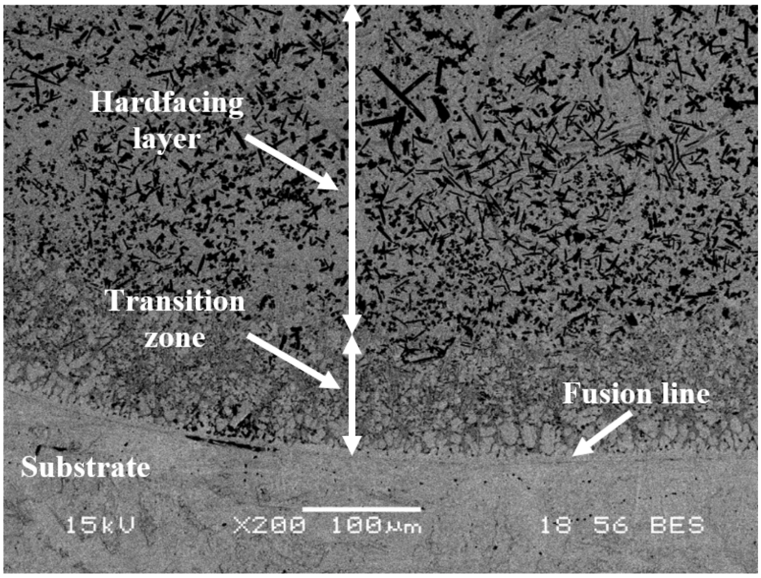

Figure 1. Cross-section of 30B-Ti sample

Figure 2 shows the XRD patterns of hardfacing coatings. As a result of XRD analyses, α-(Fe,Cr), M_2B (M= Fe,Cr), TiC and M_7C_3 phases were detected in the coating containing 10% B. In the coatings with 20% and 30% B content, the presence of TiB_2 phase was determined together with the above phases. Zhang et al. investigated the effect of Cr element in Fe-Cr-Ti-(C,B) based coatings and reported the presence of similar phases (Zhang et al., 2017).

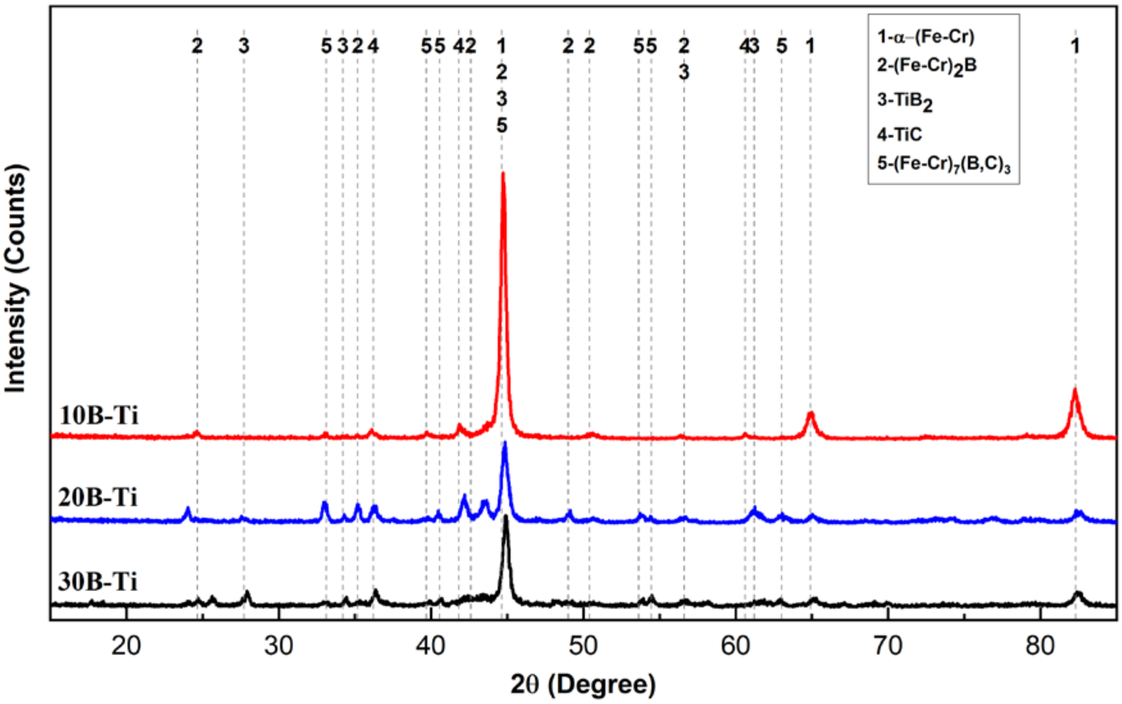

Figure 2. X-ray analysis patterns of hardfacing coatings

Figure 3 shows the SEM images, EDS, and MAP analyses of the 10B-Ti sample with an atomic boron content of 10%. SEM images show that the produced coating layer exhibits a hypoeutectic solidification. It is seen that Ti and C elements are dense in the EDS number 1 taken from the equiaxed dark regions distributed in the coating microstructure and in the MAP analysis given in Figure 3(i and j). In addition, the presence of TiC phase in this coating was found in the X-ray analysis given in

Figure 2, supporting that these regions consist of TiC phase. In the EDS analysis number 2 taken from the light grey regions in the coating microstructure, signals of Fe and Cr elements were obtained. The same situation is also observed in MAP analysis and these regions are thought to be the hypoeutectic α-(Fe,Cr) phase. In the EDS analysis number 3 taken from the eutectic region of the coating, Fe and Cr peaks were quite intense, but very few B and C peaks were measured (Figure 3 (e)). Again, when the elemental distribution maps of the eutectic region were analysed, Cr and Fe were found to be intense, and C and B elements were also detected in these regions, albeit slightly (Figure 3 (f-k).

As a result of the X-ray analysis given in Figure 2, it was determined that M_2B and M_7C_3 (M= Fe,Cr) phases were also present in this composition. Therefore, it is thought that the eutectic structure consists of α-Fe+M_2B and/or M_7C_3 phases.

Figure 4 shows the SEM images, EDS, and MAP analyses of the 20B-Ti sample in which the boron ratio atomically increases to 20%. SEM images show that the coating microstructure consists of complex structures (Figure 4 (a and b)). During coating on the steel surface by TIG welding method, the melt pool of this compound is rich in B and it is easier to form TiB_2 phase. For this reason, it is thought that the first structure formed in the melt pool due to cooling is the TiB_2 phase. It is expected that the TiC phase will be formed in the continuation of solidification. In their study, Weng et al. reported that thin TiB_2 lamellae were first formed in the melt pool and then the TiC phase nucleated on these lamellae by heterogeneous nucleation (Weng et al., 2022). SEM images, EDS and MAP analyses given in Figure 4 show that TiC phase is present around the polygonal TiB_2 structures.

As a result of the EDS analysis number 2 taken from the black colored polygonal regions shown in Figure 4 (d) and the MAP analysis given in Figure 4 (j and l), it is seen that these structures are rich in Ti and B elements. When evaluated with the X-ray analysis given in Figure 2, it can be assumed that these structures consist of TiB_2 phase. As a result of the EDS signal number 4 taken from the dark grey colored coaxial structures and the MAP analysis given in Figure 4 (j and k), it is clearly seen that these regions are rich in Ti and C elements. When compared with XRD results, it is possible to say that these regions consist of TiC phase.

EDS analyses of the light white regions in the coating layer showed that they are rich in iron, and also contain Cr and very little Ti elements (Figure 4 (c)). According to MAP analyses and XRD results, it was determined that these structures consist of α-(Fe,Cr). In addition, light grey long strip-like structures were observed in the microstructure in SEM images. Gramajo et al. identified these structures as $M_7(B,C)_3$ (Gramajo et al., 2020). In addition, it was determined by EDS analysis number 3 that these structures are rich in Cr and Fe elements. According to XRD analyses, these structures are thought to be $(Fe,Cr)_7$ $(B,C)_3$.

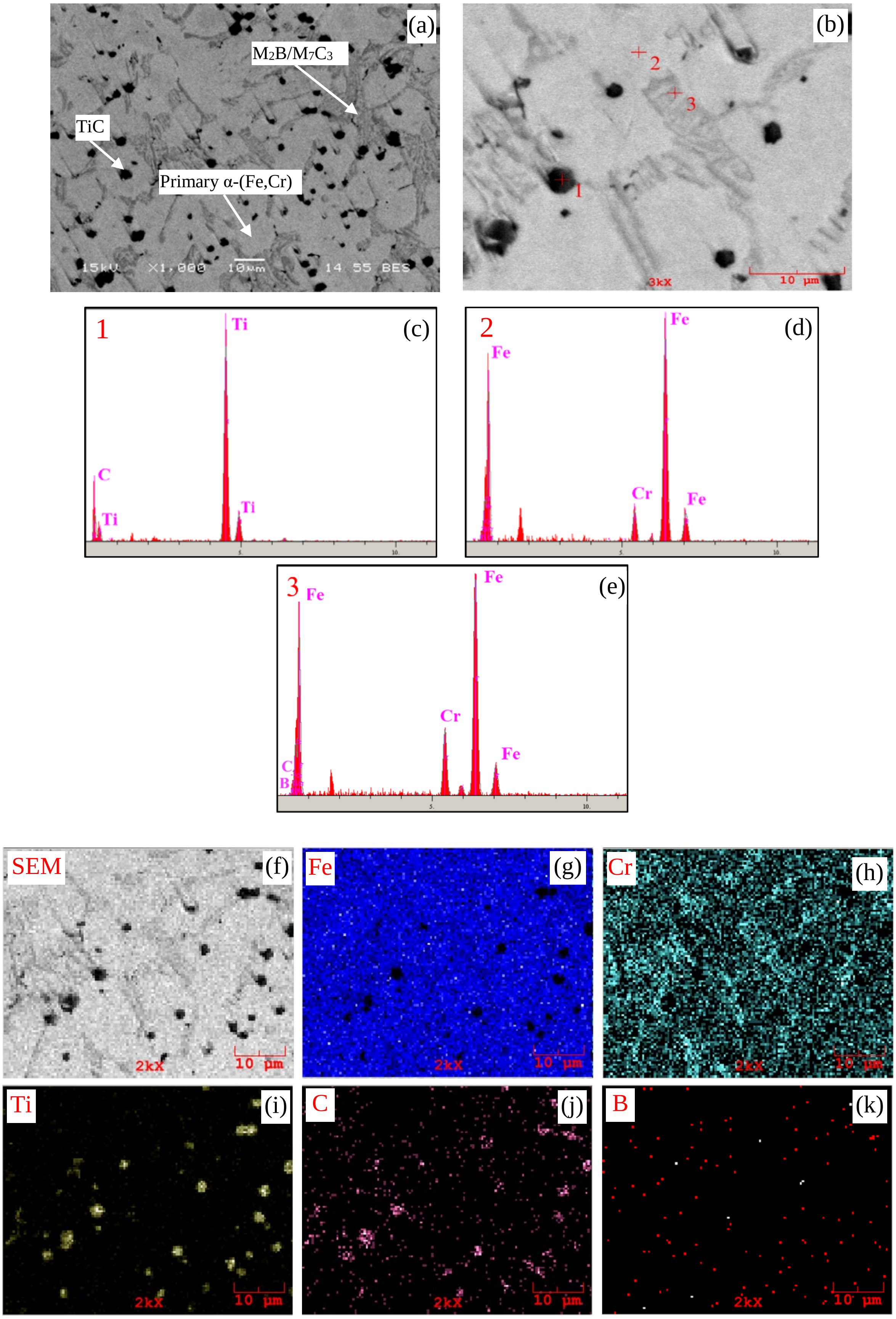

Figure 3. SEM images (a and b), EDS analyses (c-e) and elemental distribution maps (f-k) of 10B-Ti sample

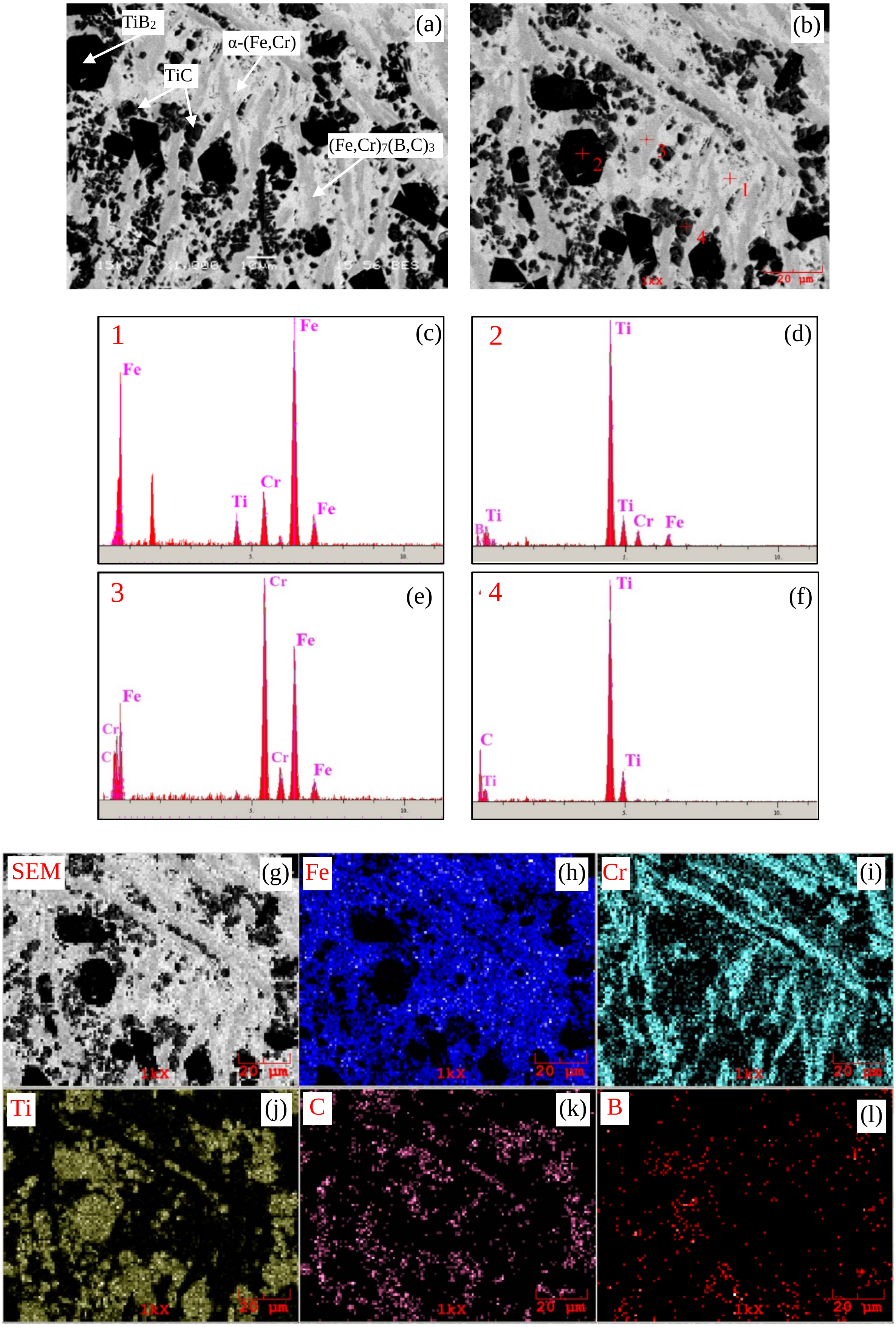

Figure 4. SEM images (a and b), EDS analyses (c-f) and elemental distribution maps (g-l) of 20B-Ti sample

SEM images, EDS and MAP analyses of 30B-Ti sample are given in Figure 5. This sample also exhibits a hypereutectic microstructure like the 20B-Ti sample. However, the black colored polygonal structures seen in the 20B-Ti sample are seen as black colored rod-like and long sharp-cornered phase formations in the 30B-Ti sample. It has been reported that increasing titanium and boron concentrations in the alloy system are effective in the formation of these structures. (Kaptanoglu & Eroglu, 2017; Kocaman et al., 2022).

As a result of the EDS and MAP analyses given in Figure 5, it was determined that these structures are also rich in Ti and B elements. Therefore, it can be said that these structures are TiB_2 phase. Ti and C elements were detected in the dark grey coloured equiaxed structures around the TiB_2 phase and in the matrix. As a result of the x-ray analysis given in Figure 2, these structures were determined to be TiC. A similar microstructure formation was shown in the study by Zhang et al. Two different types of coloured particles were identified in the coating layer. One is grey particles forming the cubic or flower-like TiC phase and the other is black particles forming the block-like TiB_2 phase (Zhang et al., 2020). Similar to our study, TiC phases are located in the matrix and around TiB_2 phases.

It can be said that the first structure to form during the solidification of the 30B-Ti sample formed on the steel surface is the TiB_2 phase. In the continuation of solidification, TiC phase was formed and clustered around the TiB_2 phase. As explained above, TiC phase will nucleate heterogeneously on thin TiB_2 lamellas solidified in the coating bath. With the nucleation and subsequent growth of the TiC phase on the TiB_2 lamellae, the B element dissociates at the liquid-solid interface. With the dissociated B element, TiB_2 is ready to nucleate and grow again. Therefore, the TiB_2 phase continues to grow by two-dimensional nucleation and lateral spreading (Li et al., 2013). Weng et al. stated that due to the rapid cooling and rapid solidification occurring in the coating layer, the lamellar structures formed from the TiB_2 phase in this layer will not transform into hierarchical tower-like and dendritic morphologies, but will remain in plate-like morphology (Weng et al., 2022). When the SEM images and EDS analyses of the 30B-Ti sample given in Figure 5 are examined, it is seen that the microstructure formation is in accordance with the above description.

As in the 20B-Ti sample, Cr and Fe elements are present in the light-colored regions of this sample. Therefore, it is possible to say that in addition to the iron-rich α-(Fe,Cr) phase, very little M_2B phase is also present in the structure. In this coating, the light grey long rod $(Fe,Cr)_7(B,C)_3$ phase is also present.

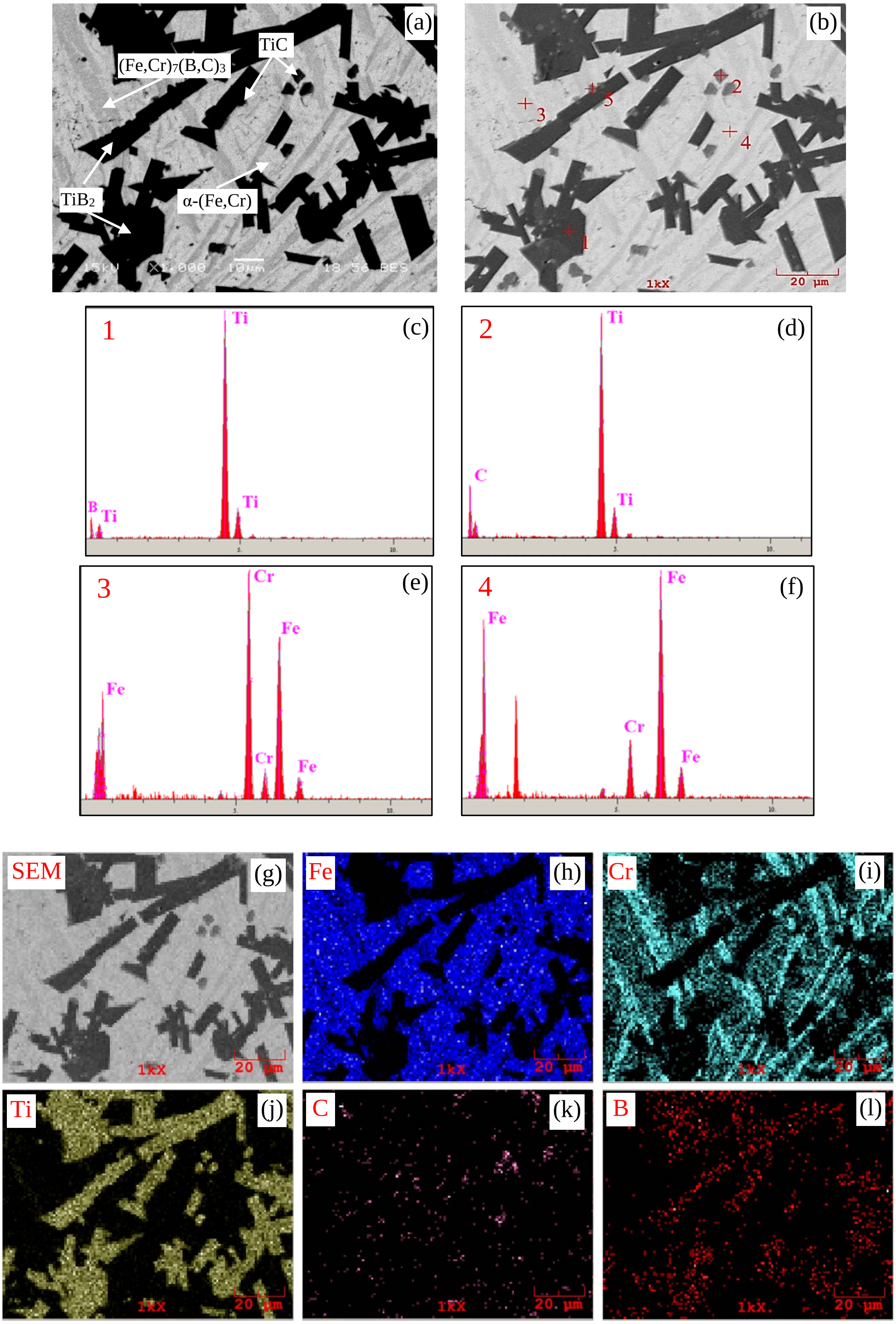

Figure 5. SEM images (a and b), EDS analyses (c-f) and elemental distribution maps (g-l) of 30B-Ti sample

3.2 Hardness

Figure 6 shows the microhardness values of the coated samples measured at 0.2 mm intervals from the substrate to the coating surface. In such composite coatings, the microhardness values are strongly influenced by the volume fraction of phases with high hardness values, such as borides and carbides, present in the structure as reinforcing phases (Amushahi et al., 2010; Du et al., 2008; Venkatesh et al., 2015). When the graph is examined, it is seen that the microhardness increases as the B content in the coating increases.

When the B content was increased from 10at.% to 30 at.%, the hardness of the coating increased from an average of 544 to 1045 $HV_{0.2}$. The maximum hardness was determined in the 30B-Ti sample with 30 at.% B content, which is approximately 4.5 times higher than the microhardness value of DIN St37 steel (234$HV_{0.2}$).

As determined in the microstructure examinations, the 10B-Ti sample with the lowest B ratio had a hypoeutectic microstructure and the hard particle phase TiC was homogeneously distributed in the structure. However, the volume fraction of the hard particle reinforcement phase in this sample was very low compared to the matrix phase. In addition, eutectic structures with M_2B and $(Fe,Cr)_7(B,C)_3$ phases were also observed to be present at lower rates compared to other samples. In the 20B-Ti and 30B-Ti samples, where the B ratio increased, a microstructure hypereutectic was detected. In these samples, TiB_2, which is a hard particle reinforcement phase, was observed to increase significantly in the microstructure. Therefore, the increase in the B ratio in the coating greatly affected the microstructure and significantly increased the microhardness of the hardfacing.

When the graph given in Figure 6 is analyzed, it is determined that there are fluctuations in microhardness values. It is known that these fluctuations in hardness results are due to hard particle reinforcement structures such as TiC and TiB_2 in the coating microstructure (Kocaman et al., 2020; Kumar & Das, 2022). It is also observed that the microhardness values for all specimens increase slightly from the substrate to the coating layer. Microhardness values depend on the concentration and shape of the coating layer as well as the distribution of the coating microstructure (Kumar & Das, 2022). Hardness values are expected to be lower in the coating layer close to the substrate due to the dilution effect. As you move to the upper layers of the coating layer, the volume fractions of hard phases such as TiB_2 and TiC increase, which leads to an increase in microhardness.

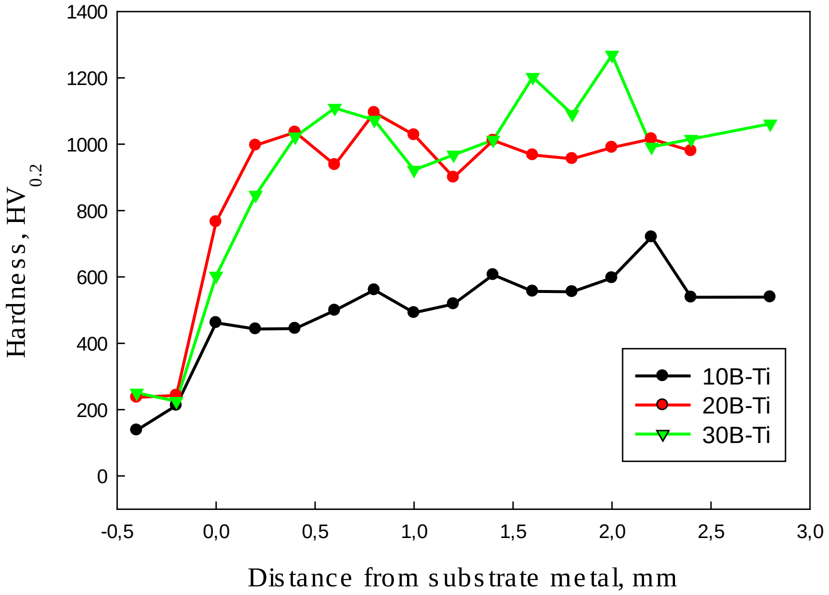

Figure 6. Microhardness values of Fe-Cr-Ti-(C, B) based hardfacing

4. CONCLUSION

This study presents the effects of B content on the microstructural changes and hardness of Fe-based in-situ TiC-TiB_2 hardfacing coatings. The main conclusions are as follows:

- Fe-Cr-Ti-(C,B) based coatings were successfully produced by TIG method and the coatings were found to be compatible with the substrate. No porosity and microscopic cracks were observed in the coating layer. The hardfacing layer, transition zone and interface (fusion line) were determined by microstructure images.
- Boron content significantly affected the microstructure of hardfacing coatings. The coating layer with a B content of 10% had a hypoeutectic microstructure. In this sample, a homogeneously distributed equiaxed dark colored TiC phase and α- (Fe, Cr) phase were detected. In eutectic regions, α-Fe+M_2B and/or M_7C_3 phases were found. The proportion of black colored polygonal TiB_2 phases was intense in the coating microstructure where the B ratio increased to 20%. In addition, $(Fe, Cr)_7(B,C)_3$ phases were also detected in the structure as long strips. Polygonal TiB_2 structures were observed as black colored rod-like and long sharp-cornered phases in the coating with 30% B content, which exhibited eutectic microstructure. TiC phase was detected around the TiB_2 phase and in the matrix. In this coating, the light grey long rod $(Fe, Cr)_7(B,C)_3$ phase is also present in this coating together with the M_2B phase.
- It was observed that the microhardness of Fe-Cr-Ti-(C,B) hardfacing coatings increased as the amount of B increased. The highest microhardness was found in 30B-Ti sample with 1045 $HV_{0.2}$. It was also observed that the microhardness values increased from the substrate to the surface of the coating layer.

5. ACKNOWLEDGEMENTS

This study did not receive funding support from any institution or organization.

6. CONFLICT OF INTEREST

Author approves that to the best of their knowledge, there is not any conflict of interest or common interest with an institution/organization or a person that may affect the review process of the paper.

7. AUTHOR CONTRIBUTION

Bülent KILINÇ has the full responsibility of the paper about determining the concept of the research, data collection, data analysis and interpretation of the results, preparation of the manuscript and critical analysis of the intellectual content with the final approval.

8. REFERENCES

Azzi M., Paquette M., Szpunar J.A., Klemberg-Sapieha J.E., Martinu L., Tribocorrosion behaviour of DLC-coated 316L stainless steel. Wear 267 (5-8), 860-866, 2009.

Ahn D. G., Hardfacing technologies for improvement of wear characteristics of hot working tools: A review. International Journal of Precision Engineering and Manufacturing, 14(7), 1271-1283, 2013.

Amushahi M. H., Ashrafizadeh F., Shamanian M., Characterization of boride-rich hardfacing on carbon steel by arc spray and GMAW processes. Surface and Coatings Technology, 204(16-17), 2723–2728, 2010.

Brezinová J., Viňáš J., Guzanová A., Živčák J., Brezina J., Sailer H., Vojtko M., Džupon M., Volkov A., Kolařík L., Rohan P., Puchý V., Selected properties of hardfacing layers created by pta technology. Metals, 11(1), 1-20, 2021.

Buytoz S., Ulutan M., In situ synthesis of SiC reinforced MMC surface on AISI 304 stainless steel by TIG surface alloying. Surface and Coatings Technology, 200, 3698-3704, 2006.

Chen L., Yu T., Guan C., Zhao Y., Microstructure and properties of metal parts remanufactured by laser cladding TiC and TiB2 reinforced Fe-based coatings. Ceramics International, 48(10), 14127-14140, 2022.

D'Oliveira A. S. C. M., Paredes R. S. C., Santos R. L. C., Pulsed current plasma transferred arc hardfacing. Journal of Materials Processing Technology, 171(2), 167-174, 2006.

Du B., Zou Z., Wang X., Qu S., Laser cladding of in situ TiB2 /Fe composite coating on steel. Applied Surface Science, 254(20), 6489-6494, 2008.

Durmuş H., Çömez N., Gül C., Yurddaşkal, M., Yurddaşkal, M., Wear performance of Fe-Cr-C-B hardfacing coatings: Dry sand/rubber wheel test and ball-on-disc test. International Journal of Refractory Metals and Hard Materials, 77(June), 37-43, 2018.

Gramajo J., Gualco A., Svoboda H., Study of the welding procedure in nanostructured super-hard Fe-(Cr, Mo, W) - (C, B) hardfacing. International Journal of Refractory Metals and Hard Materials, 88(December 2019), 1-6, 2020.

Gupta N. K., Pyla K. R., Debta M. K., Masanta M., Performance evaluation of TIG cladded in-situ TiC-TiB2 composite coating fabricated on AISI304 stainless steel. Materials Today: Proceedings, 62(P10), 5956-5961, 2022.

Hajihashemi M., Shamanian M., Azimi G., Physical, Mechanical, and Dry Sliding Wear Properties of Fe-Cr-W-C Hardfacing Alloys Under Different Tungsten Addition. Metallurgical and Materials Transactions B, 46, 919-927, 2015.

Hu Z., Zhang, D., Wu D., Zheng, X., Sun J., Geng P., Ma N., Enhanced mechanical properties of Fe-based hardfacing alloy with Al additions fabricated by laser cladding. Surface and Coatings Technology, 478(January), 130447, 2024.

Huang Y., Huang J., Yu X., Yu S., Fan D., Microstructure characterization and texture evolution of Ti-6Al-4V cladding layer fabricated by alterative current assisted TIG. Surface and Coatings Technology, 431, 128014, 2022.

Jozwik J., Dziedzic K., Usydus I., Ostrowski D., & Krolczyk G. M., Assessment of internal defects of hardfacing coatings in regeneration of machine parts. Journal of Central South University, 25(5), 1144-1153, 2018.

Kaptanoglu M., Eroglu M., Microstructure and wear of iron-based hardfacings reinforced with in-situ synthesized TiB2 particles. Kovove Materialy, 55(2), 123-131, 2017.

Kocaman E., Kılınç B., Şen Ş., Şen U., Effect of chromium content on Fe(18-x)CrxB2(X=3,4,5) hardfacing electrode on microstructure, abrasion and corrosion behavior. Journal of the Faculty of Engineering and Architecture of Gazi University, 36(1), 177-190, 2020.

Kocaman E., Kılınç B., Şen Ş., Şen U., In-situ TiB2 and Fe2Ti intermetallic assisted hard coatings by Fe-Ti-B based hardfacing electrodes. Journal of Alloys and Compounds, 900, 163478, 2022.

Kumar S., Das A. K., Wear resistance and hardness properties of TiB2– Fe coating developed on AISI 1020 steel by tungsten inert gas (TIG) cladding. Ceramics International, 48(20), 30052-30065, 2022.

Li P., Wu Y., Liu X., Controlled synthesis of different morphologies of TiB2 microcrystals by aluminum melt reaction method. Materials Research Bulletin, 48(6), 2044-2048, 2013.

Lin C. M., Chang C. M., Chen J. H., Hsieh C. C., Wu W., Microstructure and wear characteristics of high-carbon Cr-based alloy claddings formed by gas tungsten arc welding (GTAW). Surface and Coatings Technology, 205(7), 2590-2596, 2010.

Pawlik J., Bembenek M., Góral T., Cieślik J., Krawczyk J., Łukaszek-Sołek A., Śleboda T., Frocisz Ł., On the Influence of Heat Input on Ni-WC GMAW Hardfaced Coating Properties. Materials, 16(11), 2023.

Tang J., Mechanical and tribological properties of the TiC-TiB2 composite coating deposited on 40Cr-steel by electro spark deposition. Applied Surface Science, 365, 202-208, 2016.

Variables P., Works F., A Review on Hardfacing, Process Variables, Challenges, and Future Works. Metals, 13 (1512), 1-37, 2023.

Venkatesh B., Sriker K., Prabhakar V. S. V., Wear Characteristics of Hardfacing Alloys: State-of-the-art. Procedia Materials Science, 10(Cnt 2014), 527-532, 2015.

Wang Z. T., Zhou X. H., Zhao G. G., Microstructure and formation mechanism of in-situ TiC-TiB2/Fe composite coating. Transactions of Nonferrous Metals Society of China (English Edition), 18(50075085), 831-835, 2008.

Weng F., Yu H., Du X., Tian H., Chen C., In situ formed TiB2/TiC complex structure in laser-alloyed coatings with improved wear property. Ceramics International, 48(5), 7056-7062, 2022.

Zhang M., Qu K. L., Luo S. X., Liu S., Effect of Cr on the microstructure and properties of TiC-TiB2 particles reinforced Fe-based composite coatings. Surface and Coatings Technology, 316, 131-137, 2017.

Zhang M., Zhao G. L., Wang X. H., Liu S. S., Ying W. L., Microstructure evolution and properties of in-situ ceramic particles reinforced Fe-based composite coating produced by ultrasonic vibration assisted laser cladding processing. Surface and Coatings Technology, 403, 126445, 2020.

JOURNAL of
MATERIALS and MECHATRONICS:A

e-ISSN 2717-8811
JournalMM, 2024, 5(2), 341-353
https://doi.org/10.55546/jmm.1576256

Araştırma Makalesi / Research Article

Effect of Graphene Reinforcement on Boronization in FeCo Medium Entropy Alloys Produced by Different Methods

Nazmiye Nur KÜÇÜKELÇİ[1],Ersan MERTGENÇ[2*], Rıza KARA[3]

[1] Afyon Kocatepe University, Institute of Science, Department of Nanoscience and Nanotechnology, Afyonkarahisar, Türkiye,
ORCID ID: https://orcid.org/0000-0003-4937-6626, nkelci@hotmail.com
[2*] Afyon Kocatepe University, Afyon Vocational High School, Department of Railway Systems, Afyonkarahisar, Türkiye,
ORCID ID: https://orcid.org/0000-0001-8247-2922, ersanmertgenc@hotmail.com
[3] Usak University, Vocational School of Technical Sciences, Faculty of Technology, Department of Mechanical and Metal Technologies, Usak, Türkiye,
ORCID ID: https://orcid.org/0000-0002-0820-2577, riza.kara@usak.edu.tr

Geliş/ Received: 30.10.2024; **Revize/Revised:** 24.11.2024 **Kabul / Accepted:** 03.12.2024

ABSTRACT: With the developing technology, studies on the production and development of new materials are intensifying as traditional materials are inadequate to meet the needs of the industry. As an alternative to traditional steels, the use of low, medium and high entropy alloys and nanomaterials has recently become one of the most suitable solutions. Based on these solutions, in this study; the effect of nanoparticle reinforcement material on the boride layer structure in pack boriding of FeCo alloy, which is described as a soft magnetic alloy and produced by different methods, was investigated. Firstly, 2% and 4% graphene reinforced, medium entropy FeCo alloy was produced by 2 different methods melt casting (MC) and powder metallurgy (PM). Then, medium entropy alloys (MEAs) produced by both methods were subjected to a pack boronizing process at 1073 K temperature for 2 hours. Both the produced MEAs and the boride layers of the borided MEAs were characterized. When the microstructures of the produced alloys are examined, it is seen that with the increase in graphene reinforcement, the tendency for dendritic structure increases in alloys using the MC method, while crack formation increases in alloys using the PM method. According to the XRD pattern analysis of the alloys produced by both methods, peaks belonging to the CoFe phase were detected in the main peaks of the alloys. The microhardness of the alloys ranges between 258 $HV_{0.05}$ and 314 $HV_{0.05}$. In the boride layer structures obtained by pack boronizing, no transition zone is formed, they are columnar and have a sawtooth appearance. Boride layer thicknesses range between 22 μm and 34 μm. According to the XRD pattern analysis of the boride layers of the alloys produced by both methods, FeB, Fe_2B, CoFe phases were detected in the main peaks, while the Co_2Fe phase was also present in the alloys produced by the MC method. The surface microhardness of the boride layers varies between 1922 $HV_{0.05}$ and 2124 $HV_{0.05}$.

Keywords: Medium entropy alloy, Graphene, Melt casting, Powder metallurgy, Pack boriding

---

*Sorumlu yazar / Corresponding author: ersanmertgenc@hotmail.com

Bu makaleye atıf yapmak için /To cite this article

Küçükelçi, N. N., Mertgenç, E., Kara, R. (2024). Effect of Graphene Reinforcement on Boronization in FeCo Medium Entropy Alloys Produced by Different Methods. Journal of Materials and Mechatronics: A (JournalMM), 5(2), 341-353.

1. INTRODUCTION

With the rapid development of technology in recent years, traditional commercial materials may be inadequate to meet the needs of the industry. In order to provide the expected properties, intensive studies are being carried out by researchers to develop different alloys. Especially high entropy alloys (HEA), medium entropy alloys (MEA) and low entropy alloys (LEA) are among the leading solutions in obtaining the desired properties in recent years.

Entropy, in physics, refers to the thermal energy of a system that cannot be converted into mechanical work. It is defined as disorder and randomness in the system. In the literature, the concept of entropy is divided into 2 classes. It is defined as alloys consisting of at least five elements and their concentrations are between 5% and 35% On the other hand, according to the entropy-based definition, it is examined in 3 classes as low, medium and high entropy alloys according to the amount of elements they contain. When determining the class to which the alloy belongs, calculations are made according to the configuration entropy; alloys formed up to 2 elements are called low entropy, alloys containing 3 and 4 elements are called medium entropy, and alloys containing 5 and more elements are called high entropy.

Magnetic materials constitute a significant portion of engineering alloys. Among commercial magnetic materials, FeCo alloys are considered to have the highest saturation. These alloys are soft magnetic materials and are used in high temperature applications because they have low coercivity, high Curie temperature and high magnetization (Küçükilhan et al., 2024; Yu et al., 1999). In the production of alloys, melting and powder metallurgy methods are mostly preferred.

In cases where alloys are exposed to wear or work in corrosive environments, surface coating applications are also carried out as in conventional steels. The most common surface coating methods used are laser coatings (Riquelme & Rodrigo, 2021) aluminization (Bölükbaşı et al., 2023), atmospheric plasma spray (APS) (Michalak et al., 2021), electro spark deposition (Padgurskas et al., 2017), high-velocity oxygen fuel injection (HVOF) (Pulido-González et al., 2020) and boronization (Elias-Espinosa et al., 2015; Mishigdorzhiyn et al., 2020).

Boriding is based on the formation of a hard boride layer on the surface depending on the chemical composition of the substrate material in liquid, solid and gas environments. The process is a thermochemical method based on diffusion performed at high temperatures. Therefore, the boride layer formed on the surface of the material has low roughness, is solid and permanent. The pack-boriding method is widely used due to its easy applicability and economic operation. The process can be performed in a wide range of temperatures ranging from 973 K to 1273 K and durations of 1-10 hours.

According to literature research; There are quite a few studies on the production method and magnetic properties of FeCo alloy. However, studies on the effect of nanoparticle reinforcement elements on the alloy system and the effects of reinforcement elements on surface coatings are quite limited in these alloys. In this study, the manufacturability of FeCo alloy was investigated using MC and PM methods. In addition, different amounts of graphene reinforcement were added to FeCo alloys produced with different methods. The effect of graphene on the boride layer to be formed on the alloys was examined in detail using the pack-boriding method of FeCo alloys containing different amounts of graphene reinforcement.

2. MATERIALS AND METHODS

In this study, iron (Fe) and cobalt (Co) powders with a size of -325 mesh and graphene (G) powder with a size of 3 nm supplied by Nanografi company were used. The chemical equivalents of the Fe/Co alloy used are given in Table 1, and the powder mixing ratios of the prepared MEAs are given in Table 2.

Table 1. Information on Fe/Co alloy

Element	Atomic weight (u)	Mixing ratio (%wt)	Mixing ratio (%at)
Fe	55.845	50	51.3444
Co	58.933	50	48.6556

Table 2. MEA codes, production methods and mixing ratios

Alloy code	Production method	Graphene (%)	Fe (g)	Co (g)	Graphene (g)	Total (g)
MC-0	Melt Casting	0	5.00	5.00	-	10.00
MC-2	Melt Casting	2	4.90	4.90	0.20	10.00
MC-4	Melt Casting	4	4.80	4.80	0.40	10.00
PM-0	Powder Metallurgy	0	5.00	5.00	-	10.00
PM-2	Powder Metallurgy	2	4.90	4.90	0.20	10.00
PM-4	Powder Metallurgy	4	4.80	4.80	0.40	10.00

A lathe machine was used to mix the powders whose compositions were determined and weighed, and they were mixed at 120 rpm for 12 hours. A Seles brand JTA model scale with a 0.001 gr sensitivity was used to weigh the powders. The powders, which were mixed and made homogeneous, were pressed in a Ø20 mm diameter mold, with a single-axis press at 400 bar pressure, and turned into cylindrical pellets for powder metallurgy and melt casting.

The alloys to be produced with the powder metallurgy method were sintered for 1 hour at 1273 K in a protective gas atmosphere and made ready for boronization. In the alloys to be produced with the melt casting method, pellets shaped in the press were used. Two molds were designed for the melting process; the first was used for the master alloy production and the second was used for the final alloy production. In the master alloy production, the alloys were turned upside down in each melting process and melting was done 4 times and all processes were carried out in an argon protective gas atmosphere. In the mold used in the production of the final alloy, a reverse vacuum system was used and when the alloy reached the liquid phase during melting, the air previously collected in the air accumulator chamber with a vacuum pump was drawn (-0.1 atm) to produce the final alloy. In the production of the alloys, a Welder TIG 400 DC pulse model TIG welding machine was used at 210 A. The copper melting molds used for the production of the alloys is given in Figure 1(a) and the alloy production system is given in Figure 1(b).

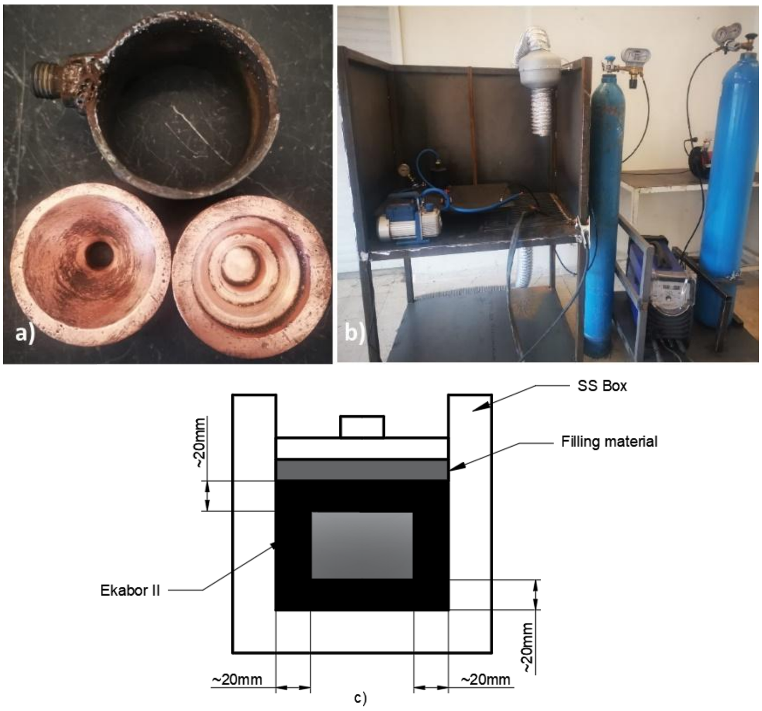

Figure 1. a) Copper mold and b) production system used in the MC process c) Schematic view of the pack-boronizing method

Boriding of alloys produced by MC and PM methods was carried out in a chamber type furnace with commercial Ekabor II (90% SiC, 5% B_4C and 5% KBF_4) coating powder environment at 1073 K for 2 hours by package boronizing method. Alloys to be coated were placed in Ekabor II powder in the center of the box made of stainless steel (at least 20 mm distance from the box edges).

For microstructural examination of boronized and non-boronized alloys, non-boronized alloys were prepared metallographically and SEM analyses were performed by LEO 1430VP brand SEM imaging, SEM analyses of boronized alloys were performed without metallographic preparation. X-ray diffraction analysis using CuKα (α= 1.5406˚A) radiation, Shimadzu XRD-6000 brand X-ray diffractometer and microhardness measurements were performed at three separate points at 10 µm intervals under a 50 g load for 15 seconds, Shimadzu HMV-2L model microhardness measuring device were used. The flow chart of this study is given in Figure 2.

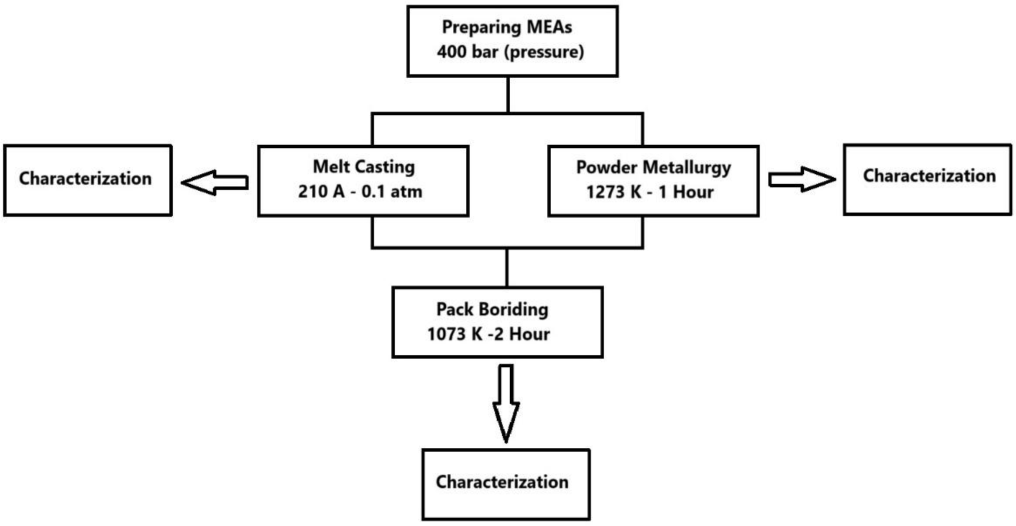

Figure 2. Flow chart of the study

3. RESULTS AND DISCUSSION

3.1 Characterization of MEAs

In Figure 3, SEM (backscatter electrons) microstructure images of unreinforced, 2% and 4% graphene reinforced alloys produced by melt casting (MC) and powder metallurgy methods (PM) are given together with EDS elemental analysis.

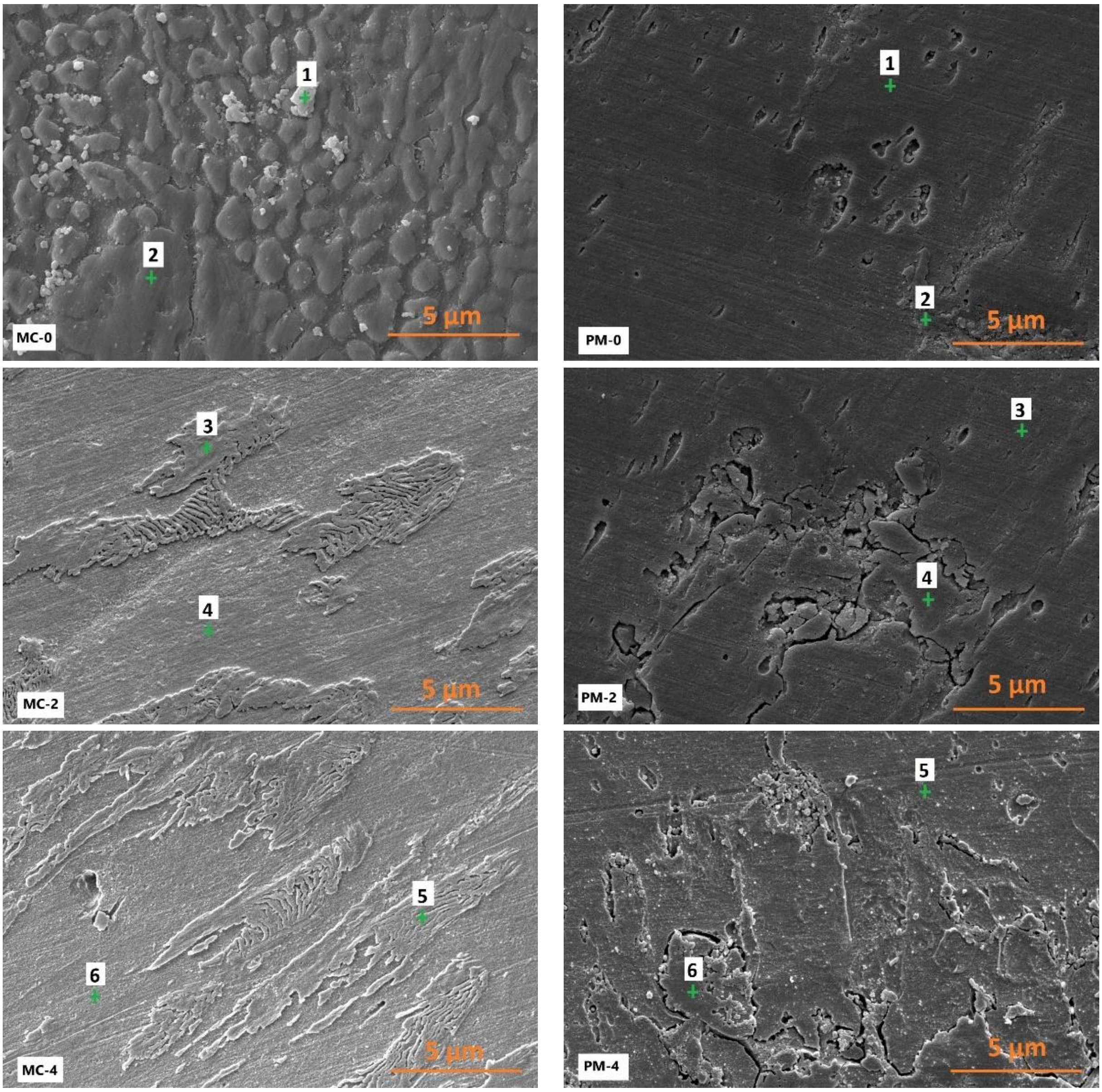

MC

Point	Fe (%)	Co (%)	C (%)	Al (%)	O (%)
1	11.73	9.35	--	52.41	23.36
2	49.78	45.96	--	--	4.26
3	48.92	43.79	2.87	1.04	3.38
4	45.42	48.28	1.71	0.46	4.13
5	49.82	39.23	5.14	0.75	5.06
6	42.44	50.25	3.07	0.22	4.02

PM

Point	Fe (%)	Co (%)	C (%)	Al (%)	O (%)
1	46.73	50.75	--	0.28	2.24
2	48.64	43.92	--	2.02	5.42
3	47.68	49.78	1.14	0.44	0.96
4	52.12	37,70	2.92	3.14	4.12
5	45.64	46.76	3.56	0.32	3.72
6	47.84	34.14	5.02	4.26	8.74

Figure 3. MEAs, SEM(BE) microstructure and EDS point analyses (%wt)

When the microstructures of the samples produced by the melt casting and powder metallurgy methods are examined together, the microstructure of those produced by the casting method has a multiphase structure, while the single-phase structure is dominant in the production with powder metallurgy. In the production with melt casting, due to the unstable solidification of alloy elements with different melting temperatures in the system with graphene reinforcement, the matrix structure tends to form dendritic (Li et al., 2022). In powder metallurgy production, an increase in inclusions and cracks is observed with the increase in the amount of graphene reinforcement. This situation is attributed to the fact that the alloy elements in the system have different thermal properties and that there are weak bonds on the surfaces (Zhu et al, 2023). On the other hand, according to the EDS elemental analyses in production with both methods, the Fe and Co ratios are approximately at the production amounts, and the C amount increases with graphene reinforcement. In addition, according to elemental analysis, the dendritic parts formed in production by arc melting are carbon-rich regions. Although the melting process is carried out in a protective gas (argon) atmosphere, since there is no vacuum system, there is oxygen in the structure, albeit in low amounts. The increase in oxygen amounts in carbon-rich dendritic regions is due to the increase in the melting temperature of carbon during melting. The fact that the amount of aluminum is high (in the elemental analysis of MC-0 sample) along with oxygen at point number 1 shows that this grain is not due to production, but rather due to alumina suspension during polishing at the sample preparation stage. The amount of oxygen in production with powder metallurgy is higher than in production with melt casting. The biggest disadvantage of production with powder metallurgy method is that the oxide phases formed in the material cannot be removed due to their stable structure and do not decompose easily. Therefore, even if protective gas is used both during production and sintering, if the temperature does not reach a sufficient value, the oxides continue to exist in the structure, albeit partially (Fang et al., 2018).

Figure 4 shows the XRD pattern analysis of the unreinforced and graphene reinforced MEA produced by MC (Figure 4a) and PM (Figure 4b) methods.

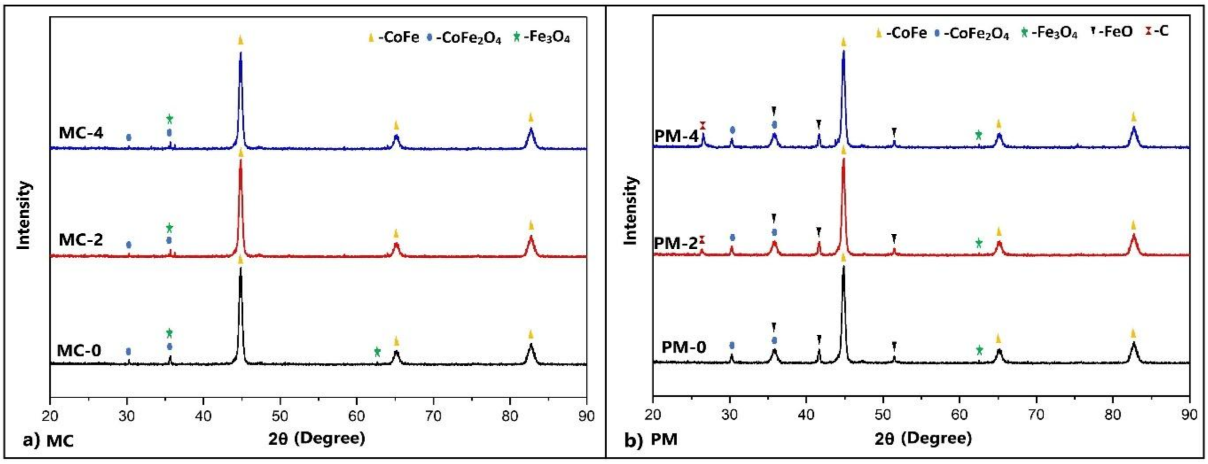

Figure 4. XRD pattern analysis of unreinforced and graphene reinforced MEAs a) melt casting, b) Powder Metallurgy

CoFe (PDF: 01-071-5029) phase with a single-phase solution crystal structure and a body-centered cubic (BCC) structure is located in the main peaks. In the secondary peaks, there are peaks belonging to the oxide phases $CoFe_2O_4$ (PDF: 01.074.6403) and Fe_3O_4 (PDF: 00-026-1136) due to Fe and Co (Allaedini et al., 2015; Gill et al., 2019). In the MEAs produced by powder metallurgy, the peaks belonging to the FeO (PDF: 00-006-0615) phase and the C (graphite) (PDF: 00-056-0159) phase become more pronounced, and the volume of these phases increases with the increase in the amount of graphene reinforcement. This result is also consistent with the EDS analysis in Figure 3. While the C peak is not present in the productions made with the melt casting method, its presence in the productions made with powder metallurgy can be attributed to the insufficient sintering temperature or time. The increase in the peaks of oxide phases in production by powder metallurgy method is due to insufficient protective gas environment or temperature (Tan et al., 2021).

Figure 5 shows the graph of microhardness values of MEA alloys.

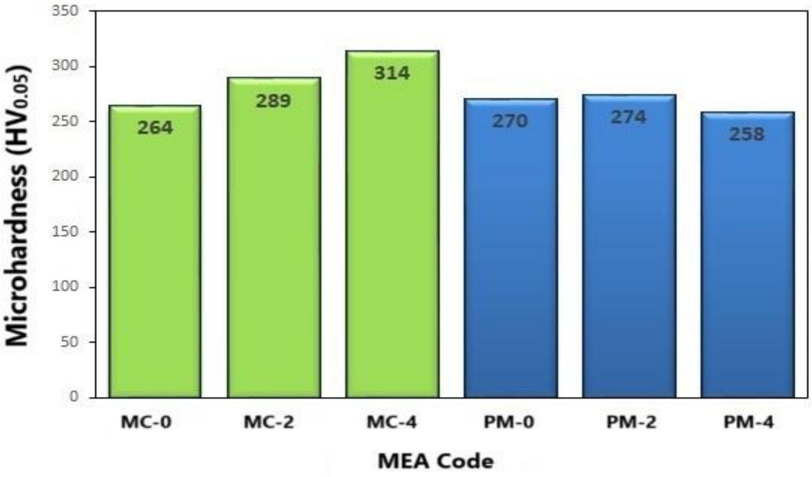

Figure 5. Microhardness of MEAs

The microhardness values of the graphene unreinforced alloys (MC-0 and PM-0) were measured as 264 $HV_{0.05}$ - 270 $HV_{0.05}$. 2% and 4% graphene reinforced alloys (MC-2, MC-4, PM-2 and PM-4) MEAs produced by MC and PM methods were measured as 289 $HV_{0.05}$ - 274 $HV_{0.05}$ and 314 $HV_{0.05}$ - 258 $HV_{0.05}$, respectively. In literature studies on FeCo alloys, it has been recorded that hardness values are evaluated between 235 HV and 314 HV (Albaaji et al., 2017; Mani et al., 2014). It has been recorded in the literature that graphene reinforcement to different alloys causes an increase in properties such as hardness, density, corrosion and wear resistance of the alloys (Liang et al., 2025; Zhang et al., 2022). In samples produced with the melt casting method, microhardness values also increase with the increase in the reinforcement ratio. It is thought that this situation is due to the more homogeneous distribution of the carbon element in the alloy system by using the melt casting method. On the other hand, in the samples produced with the powder metallurgy method, although the hardness values were close to each other, there was no stable change depending on the reinforcement ratio. As can be seen in the SEM images of the samples produced with powder metallurgy (Figure 3), there are cracks in the samples with graphene reinforcement and their distribution is irregular. The instability of the measurement values may be due to phase differences at the points where the hardness values are measured and discontinuities such as porosity, precipitation and cracks.

3.1 Characterization of Boride Layers

Figure 6 shows the SEM microstructure images of the boride layers of unreinforced, 2% and 4% graphene reinforced FeCo alloy produced by melt casting and powder metallurgy methods, which were boronized at 1073 K for 2 hours, and Figure 7 shows the graph of boride layer thicknesses.

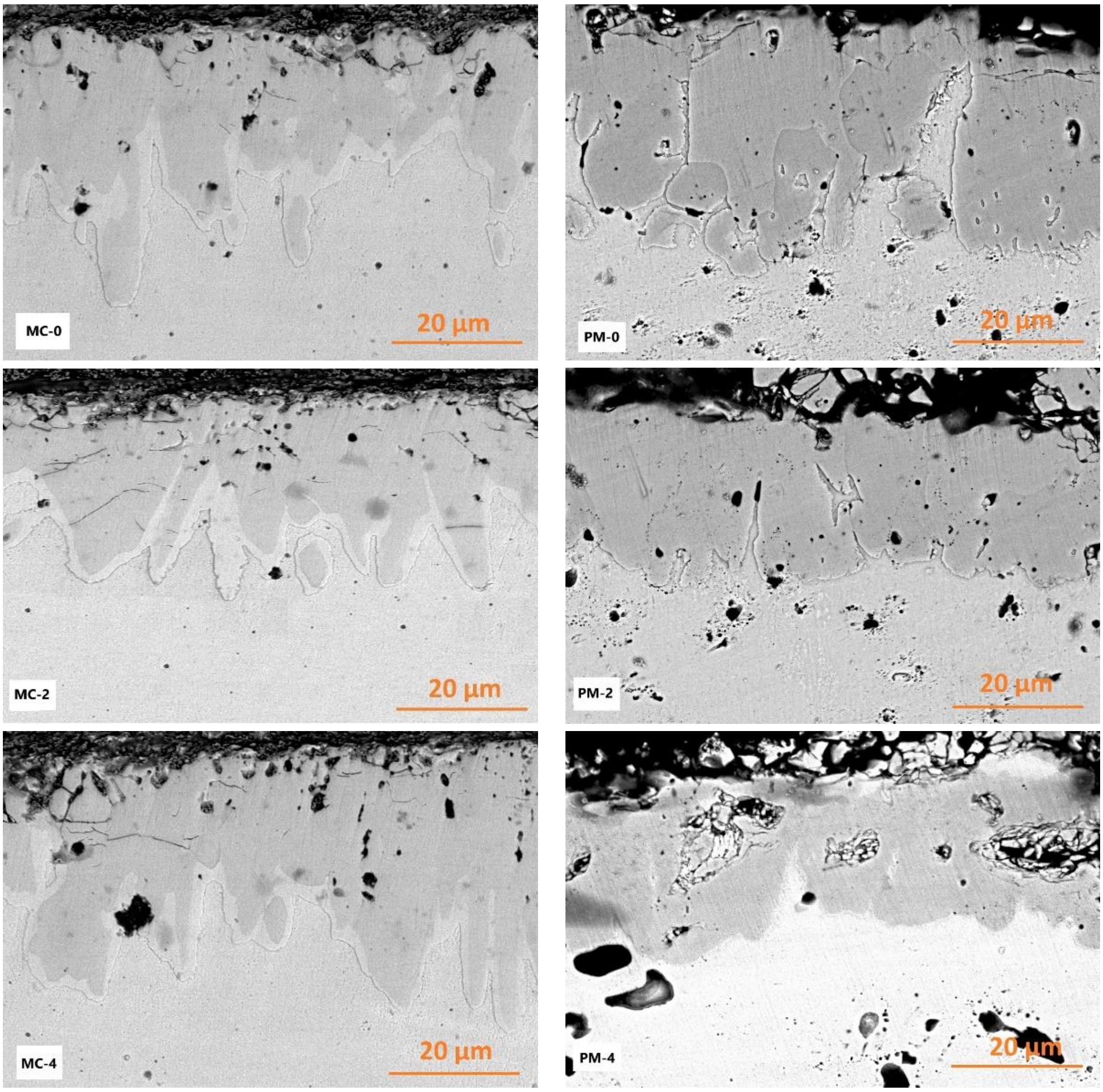

Figure 6. SEM (BE) images of boron layer of unreinforced and graphene reinforced MEAs

When the boride layer structures of MEAs produced by melt casting and powder metallurgy methods are examined, it is seen that no transition region is formed and the boride layers are columnar and have a sawtooth appearance.

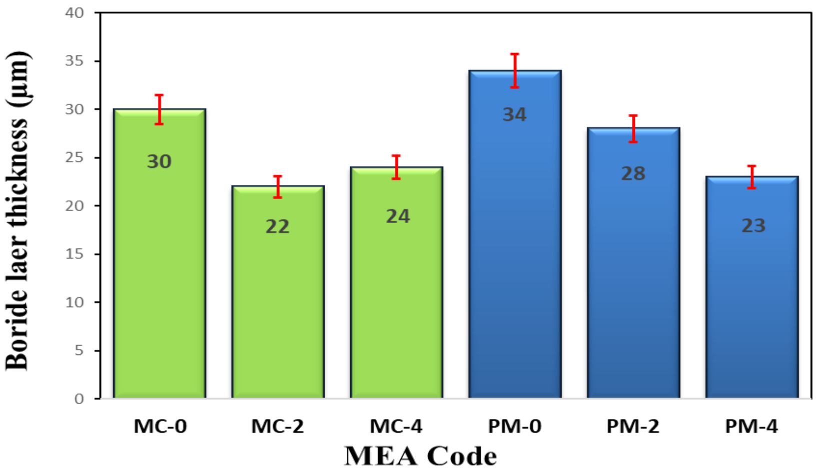

Figure 7. Boride layer thicknesses of unreinforced, 2% and 4% graphene reinforced MEAs

In the boriding of unreinforced, 2% and 4% graphene reinforced FeCo alloy produced using melt casting and powder metallurgy methods at 1073 K for 2 hours, the boride layer thicknesses were obtained as 30 µm - 34 µm, 22 µm - 28 µm and 24 µm - 23 µm, respectively. The formation of a thicker boride layer in unreinforced alloys is thought to be due to the absence of graphene reinforcement in these alloys and the interstitial atom behavior of boron atoms allowing them to diffuse to longer distances without any carbon element barrier.

When the microstructure images in Figure 6 is evaluated together with the boride layer thicknesses in Figure 7; it is seen that the boride layer thicknesses decrease as the amount of graphene reinforcement increases. It can be thought that as the amount of the element in the alloy increases, the boron element strengthens the diffusion to enter deeper distances. (Gao et al., 2022; Mertgenç and Kayali, 2022). Again, as the amount and ratio of alloying elements increase, the cracks in the boride layer increase, their lengths tend to extend, and fractures occur in the boride layer. This is due to the different thermal expansion properties of the alloy elements with different properties in the system (Cengiz, 2021).

Figure 8 shows the XRD pattern analysis taken from the boride layer surface of unreinforced, 2% and 4% graphene reinforced MEAs produced by melt casting and powder metallurgy methods, after boronizing at 1073 K for 2 hours.

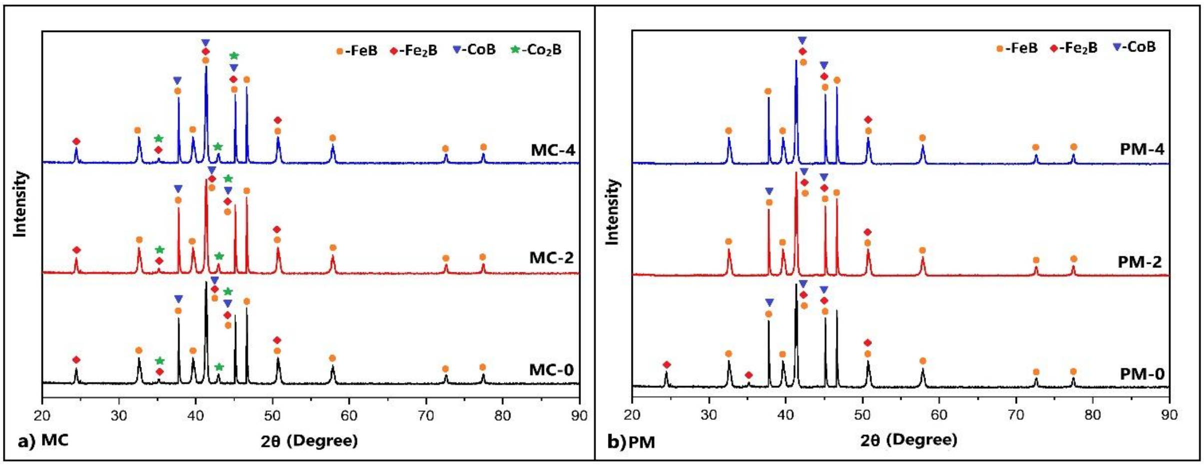

Figure 8. XRD pattern analysis of boride layer of MEAs a) Melt casting, b) Powder Metallurgy method

According to the XRD pattern analyses there are peaks belonging to the FeB (PDF: 03-065-2599), Fe_2B (PDF: 01-072-1301), CoB (PDF: 03-065-2596) phases in the main peaks of the boride layers (Alkan, 2023). While there are also low amounts of Co_2B (PDF: 03-065-2962) phase peaks in MEAs produced by the casting method, peaks belonging to this phase cannot be found in MEAs produced by the PM method. In addition, in the boronization of alloys produced by PM, the Fe_2B phase decreases in volume as the reinforcement ratio increases compared to the alloy without graphene reinforcement. In the microstructure images of the coated MEAs (Figure 6, Figure 7), it can be seen that the coating layers of the samples produced by PM are composed of similar phases compared to those produced by the casting method. This supports the absence of the Co_2B phase in the samples produced by powder metallurgy and the decrease in volume of the Fe_2B phase. On the other hand, cobalt and iron, which are the main elements that make up MEA, have very close atomic radii (r_{Co} = 0.125 nm, r_{Fe} = 0.126 nm). Therefore, they have a high solid solution degree with each other in iron and cobalt alloys (Wang et al., 2021) and it is very difficult to separate the two elements from each other in these systems.

Figure 9 shows the graph of microhardness values taken from the surface towards the matrix of unreinforced and graphene reinforced MEAs with different ratios produced by melt casting and powder metallurgy methods, after boronizing at 1073 K for 2 hours.

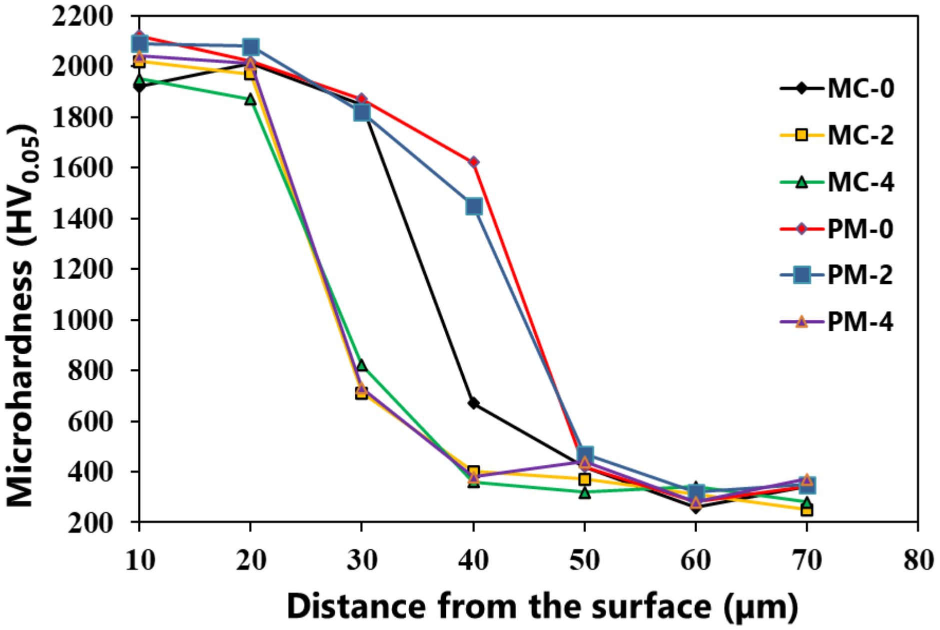

Figure 9. Microhardness graph of boride layers of MEAs

When Figure 9 is examined, the borided surface hardness of the MC-0, MC-2 and MC-4 alloys produced by the casting method were measured as 1922 $HV_{0.05}$, 2018 $HV_{0.05}$ and 1956 $HV_{0.05}$, respectively, and the surface hardness of the PM-0, PM-2 and PM-4 alloys produced by the powder metallurgy method were measured as 2124 $HV_{0.05}$, 2086 $HV_{0.05}$ and 2040 $HV_{0.05}$, respectively. In the literature, it has been recorded that in previous studies conducted on the surfaces of different materials by pack boronizing, the hardness of the FeB phase obtained is around 2350 HV (Kulka et al., 2017), the hardness of the CoB phase is between 2200 HV and 2753 HV (Campos-Silva et al., 2013; Rodríguez-Castro et al., 2015), the hardness of the Fe_2B phase is between 1748 HV and 1866 HV (Kulka et al., 2017), and the hardness of the Co_2B phase is around 1835 HV (Campos-Silva et al., 2013). So, in the present study, the measured boride layer surface hardnesses are compatible with the literature.

4. CONCLUSION

The results obtained in the investigation of the production of FeCo alloys produced without reinforcement, with 2% and 4% graphene reinforcement by melt casting and powder metallurgy methods and their boronization at 1073 K for 2 hours using the pack boronizing method are given below;

- While the microstructures of the alloy produced with the PM method graphene unreinforcement (PM-0) consist of a single phase, it was observed that the microstructure of the alloy produced with the MC method graphene unreinforcement (MC-0) consists of a double phase. With the increase in the graphene reinforcement ratio, the tendency for dentritic structure in MEAs produced by the melt casting method increases, while cracks and porosities increase in MEAs produced by the powder metallurgy method.

- Peaks belonging to CoFe, $CoFe_2O_4$ and Fe_3O_4 phases were detected in alloys produced by the melt casting method, while peaks belonging to CoFe, $CoFe_2O_4$, Fe_3O_4, FeO and C phases were detected in alloys produced by the powder metallurgy method.
- The microhardness of unreinforced and graphene reinforced MEAs varies between 264 $HV_{0,05}$ and 314 $HV_{0,05}$.
- The boride layers of MEAs produced by both methods and boronized at 1073 K for 2 hours are columnar and have a sawtooth appearance.
- The boride layer thicknesses of the MEAs produced by the melt casting method and boronized were 30 µm in the unreinforced alloy, 22 µm in the 2% graphene reinforced alloy, and 24 µm in the 4% graphene reinforced alloy. The boride layer thicknesses of the MEAs produced by the powder metallurgy method were 34 µm in the unreinforced alloy, 28 µm in the 2% graphene reinforced alloy, and 23 µm in the 4% graphene reinforced alloy.
- Peaks belonging to FeB, Fe_2B, CoB and Co_2B phases were detected on the boride layer surfaces of MEAs produced by the melt casting method, and peaks belonging to FeB, Fe_2B and CoB phases were detected on the boride layers of MEAs produced by the powder metallurgy method.
- The boride layer hardnesses of the reinforced and graphene reinforced MEAs ranged between 1922 $HV_{0.05}$ and 2086 $HV_{0.05}$, and the surface hardnesses of the boronized alloys produced by both methods increased by 8 to 10 times.

5. ACKNOWLEDGEMENTS

This study was supported by Afyon Kocatepe University Scientific Research Projects Coordination Unit with Project number of 22.FEN. BİL.26.

6. CONFLICT OF INTEREST

Authors approve that to the best of their knowledge, there is not any conflict of interest or common interest with an institution/organization or a person that may affect the review process of the paper.

7. AUTHOR CONTRIBUTION

Ersan MERTGENÇ contributed to the management of the concept and/or design process of the research, preparation of the manuscript, and final approval and full responsibility for the work. Rıza KARA contributed to the data analysis and interpretation of the results, as well as the critical analysis of the intellectual content. Nazmiye Nur KÜÇÜKELÇİ contributed to the data collection.

8. REFERENCES

Albaaji A. J., Castle E. G., Reece M. J., Hall J. P., Evans S. L., Effect of ball-milling time on mechanical and magnetic properties of carbon nanotube reinforced FeCo alloy composites. Materials and Design 122, 296-306, 2017. https://doi.org/10.1016/j.matdes.2017.02.091.

Allaedini G., Tasirin S. M., Aminayi P., Magnetic properties of cobalt ferrite synthesized by hydrothermal method. International Nano Letters 5(4), 183-186, 2015. https://doi.org/10.1007/s40089-015-0153-8.

Alkan S., Effect of Boron-Aluminide Coating Applied on R4 Grade Offshore Mooring Chain Steel on Pitting and Tribo-Corrosion Behaviour. Journal of Materials and Mechatronics: A 4(1), 302-317, 2023. https://doi.org/10.55546/jmm.1296633.

Bölükbaşı Ö. S., Serindağ T., Gürol U., Günen A., Çam G., Improving oxidation resistance of wire arc additive manufactured Inconel 625 Ni-based superalloy by pack aluminizing. CIRP Journal of Manufacturing Science and Technology 46, 89-97, 2023. https://doi.org/10.1016/j.cirpj.2023.07.011.

Campos-Silva I., Bravo-Bárcenas D., Meneses-Amador A., Ortiz-Dominguez M., Cimenoglu H., Figueroa-López U., Andraca-Adame J., Growth kinetics and mechanical properties of boride layers formed at the surface of the ASTM F-75 biomedical alloy. Surface and Coatings Technology 237, 402-414, 2013. https://doi.org/10.1016/j.surfcoat.2013.06.083.

Cengiz S., Effect of refractory elements on boronizing properties of the CoCrFeNi high entropy alloy. International Journal of Refractory Metals and Hard Materials, 95, 205418, 2021. https://doi.org/10.1016/j.ijrmhm.2020.105418.

Elias-Espinosa M., Ortiz-Domínguez M., Keddam M., Gómez-Vargas O. A., Arenas-Flores A., Barrientos-Hernández F. R., West A. R., Sinclair D. C., Boriding kinetics and mechanical behaviour of AISI O1 steel. Surface Engineering 31(8), 588-597, 2015. https://doi.org/10.1179/1743294415Y.0000000065.

Fang Z. Z., Paramore J. D., Sun P., Chandran K. S. R., Zhang Y., Xia Y., Cao F., Koopman M., Free M., Powder metallurgy of titanium–past, present, and future. International Materials Reviews 63(7), 407-459, 2018. https://doi.org/10.1080/09506608.2017.1366003.

Gao Z., Wang L., Wang Y., Lyu F., Zhan X., Crack defects and formation mechanism of FeCoCrNi high entropy alloy coating on TC4 titanium alloy prepared by laser cladding. Journal of Alloys and Compounds 903, 163905, 2022. https://doi.org/10.1016/j.jallcom.2022.163905.

Gill N., Sharma A. L., Gupta V., Tomar M., Pandey O. P., Singh D. P., Enhanced Microwave absorption and suppressed reflection of polypyrrole-cobalt ferrite-graphene nanocomposite in X-band. Journal of Alloys and Compounds, 797, 1190-1197, 2019. https://doi.org/10.1016/j.jallcom.2019.05.176.

Küçükilhan M., Mertgenç E., Çolak F., The effect of powder-pack aluminising on the corrosion performance of FeCoGx low entropy. International Journal of Surface Science and Engineering 18(3), 229-244, 2024. https://doi.org/10.1504/IJSURFSE.2024.141505.

Kulka M., Makuch N., Piasecki A., Nanomechanical characterization and fracture toughness of FeB and Fe2B iron borides produced by gas boriding of Armco iron. Surface and Coatings Technology, 325, 515-532, 2017. https://doi.org/10.1016/j.surfcoat.2017.07.020.

Li Y., Yang Z., Ma Z., Bai Y., Wu C., Li J., Effect of element V on the as-cast microstructure and mechanical properties of Al0.4Co0.5VxFeNi high entropy alloys. Journal of Alloys and Compounds 911, 165043, 2022. https://doi.org/10.1016/j.jallcom.2022.165043.

Liang L., Wu J., Wang B., Kong C., Pervikov A., Shi H., Li X., Microstructure and electromagnetic wave absorption properties of FeCo/graphene composites prepared by electrical wire explosion method. Applied Surface Science 681, 161577, 2025. https://doi.org/10.1016/j.apsusc.2024.161577.

Mani M. K., Viola G., Reece M. J., Hall J. P., Evans S. L., Influence of coated SiC particulates on the mechanical and magnetic behaviour of Fe-Co alloy composites. Journal of Materials Science 49(6), 2578-2587, 2014. https://doi.org/10.1007/s10853-013-7954-9.

Mertgenç E., Kayali Y., Diffusion kinetics and boronizing of high entropy alloy produced by TIG melting reverse suction method. Canadian Metallurgical Quarterly 62(2), 362-371, 2022. https://doi.org/10.1080/00084433.2022.2082203.

Michalak M., Sokołowski P., Szala M., Walczak M., Łatka L., Toma F. L., Björklund S., Wear behavior analysis of Al2O3 coatings manufactured by APS and HVOF spraying processes using powder and suspension feedstocks. Coatings 11(8), 879, 2021. https://doi.org/10.3390/coatings11080879.

Mishigdorzhiyn U., Chen Y., Ulakhanov N., Liang, H., Microstructure and wear behavior of tungsten hot-work steel after boriding and boroaluminizing. Lubricants 8(3), 26, 2020. https://doi.org/10.3390/lubricants8030026.

Padgurskas J., Kreivaitis R., Rukuiža R., Mihailov V., Agafii V., Kriūkienė R., Baltušnikas A., Tribological properties of coatings obtained by electro-spark alloying C45 steel surfaces. Surface and Coatings Technology 311, 90-97, 2017. https://doi.org/10.1016/j.surfcoat.2016.12.098.

Pulido-González N., García-Rodríguez S., Campo M., Rams J., Torres B., Application of DOE and ANOVA in Optimization of HVOF Spraying Parameters in the Development of New Ti Coatings. Journal of Thermal Spray Technology 29(3), 384-399, 2020. https://doi.org/10.1007/s11666-020-00989-9.

Riquelme A., Rodrigo P., An introduction on the laser cladding coatings on magnesium alloys. Metals 11(12), 1993, 2021. https://doi.org/10.3390/met11121993.

Rodríguez-Castro G. A., Reséndiz-Calderon C. D., Jiménez-Tinoco L. F., Meneses-Amador A., Gallardo-Hernández E. A., Campos-Silva I. E., Micro-abrasive wear resistance of CoB/Co2B coatings formed in CoCrMo alloy. Surface and Coatings Technology 284, 258-263, 2015. https://doi.org/10.1016/j.surfcoat.2015.06.081.

Tan Z. Q., Engström U., Li K., Liu Y., Effect of furnace atmosphere on sintering process of chromium-containing steel via powder metallurgy. Journal of Iron and Steel Research International 28(7), 889-900, 2021. https://doi.org/10.1007/s42243-020-00549-z.

Wang L., Zhang F., Yan S., Yu G., Chen J., He J., Yin F., Microstructure evolution and mechanical properties of atmosphere plasma sprayed AlCoCrFeNi high-entropy alloy coatings under post-annealing. Journal of Alloys and Compounds 872, 159607, 2021. https://doi.org/10.1016/j.jallcom.2021.159607.

Yu R. H., Basu S., Zhang Y., Xiao J. Q., Magnetic domains and coercivity in FeCo soft magnetic alloys. Journal of Applied Physics 85, 6034-6036, 1999. https://doi.org/10.1063/1.369073.

Zhang R., Lv K., Du Z., Chen W., Ji P., Wang M., Effects of Graphene on the Wear and Corrosion Resistance of Micro-Arc Oxidation Coating on a Titanium Alloy. Metals 12(1),70, 2022. https://doi.org/10.3390/met12010070.

Zhu Z. X., Liu X. B., Liu Y. F., Zhang S. Y., Meng Y., Zhou H. B., Zhang S. H., Effects of Cu/Si on the microstructure and tribological properties of FeCoCrNi high entropy alloy coating by laser cladding. Wear 512-513, 204533, 2023. https://doi.org/10.1016/j.wear.2022.204533.

JOURNAL of
MATERIALS and MECHATRONICS:A

e-ISSN 2717-8811
JournalMM, 2024, 5(2), 354-368
https://doi.org/10.55546/jmm.1562715

Araştırma Makalesi / Research Article

Ağır Hizmet Araçlarının Kabin İçi İzolasyonunda Kullanılmak Üzere Geliştirilen Hibrit Kompozitlerin Termal ve Akustik Performanslarının İncelenmesi

Sena ARSLAN ATMACA[1*], Öznur İSKENDER[2], Tuğay SEVİNÇ[3]

[1*] Formfleks Otomotiv A.Ş., Bursa, Türkiye,
ORCID ID: https://orcid.org/0009-0008-2806-2656, sena.arslan@ff-rd.com
[2] Formfleks Otomotiv A.Ş., Bursa, Türkiye,
ORCID ID: https://orcid.org/0009-0007-0858-6201, oznur.iskender@ff-rd.com
[3] Formfleks Otomotiv A.Ş., Bursa, Türkiye,
ORCID ID: https://orcid.org/0009-0007-5105-0226, tugay.sevinc@ff-rd.com

Geliş/ Received: 07.10.2024; **Revize/Revised:** 11.11.2024 **Kabul / Accepted:** 04.12.2024

ÖZET: Kamyon, tır vb. ağır hizmet araçlarında sürüş konforunu artırmak ve motor bölgesinde ortaya çıkan ses ve yüksek sıcaklığın kabin içerisine geçişini engellemek amacıyla, kompozit yapılar kullanılmaktadır. Bu çalışmada, kamyon, tır vb. gibi ağır hizmet araçlarında, motor bölgesinde ortaya çıkan ses ve yüksek sıcaklığın ortamlar arası geçişini engelleyip, kabin içi sürüş konforu sağlamak üzere, ses ve darbe izolasyonu sağlamakla görevli alt ve üst katmanda fenolik keçe, akustik ve termal dayanımı arttırmakla görevli ara katmanda aerojel, seramik kumaş, cam kumaş ve kombinasyonları kullanılarak düz kalıpta, 185 °C sıcaklıkta ve 170 bar basınç altında hibrit kompozit yapılar oluşturulmuş ve bu yapıların empedans tüpünde ses yutum katsayıları, ısıl iletkenlik ölçüm cihazında ısıl iletkenlik katsayıları ölçülerek birbiriyle karşılaştırılmıştır. Akustik performans test sonuçları incelendiğinde, geniş frekans aralığında kararlı bir ses yutum performansı gösteren hibrit kompozit yapının ısı üreten yapıya bakacak yönde iki kaplama telası arası fenolik keçe, cam kumaş, toz formda aerojel ve fenolik keçe içeren malzeme kompozisyonu 5 olduğu tespit edilmiştir. Termal izolasyon performansı en yüksek hibrit kompozit yapının ise sırayla, iki kaplama telası arası fenolik keçe, toz formda aerojel ve fenolik keçe içeren malzeme kompozisyonu 3 ve iki kaplama telası arası fenolik keçe, cam kumaş, toz formda aerojel ve fenolik keçe içeren malzeme kompozisyonu 5 olduğu tespit edilmiştir. Elde edilen veriler göz önüne alındığında hem akustik hem de termal izolasyon performansını bir arada sunabilecek kompozit yapı malzeme kompozisyonu 5 ile sağlanmıştır.

Anahtar Kelimeler: Isıl iletkenlik, Akustik, Kompozit, Yalıtım malzemesi, Aerojel

---

Sorumlu yazar / Corresponding author: sena.arslan@ff-rd.com

Bu makaleye atıf yapmak için /To cite this article

Arslan Atmaca, S., İskender, Ö., Sevinç, T. (2024). Ağır Hizmet Araçlarının Kabin İçi İzolasyonunda Kullanılmak Üzere Geliştirilen Hibrit Kompozitlerin Termal ve Akustik Performanslarının İncelenmesi. Journal of Materials and Mechatronics: A (JournalMM), 5(2), 354-368.

Investigation of Thermal and Acoustic Performance of Hybrid Composites Developed to be Used in Cabin Insulation of Heavy-Duty Vehicles

ABSTRACT: Composite structures are used in heavy-duty vehicles, such as trucks and lorries, to improve driving comfort by reducing noise and heat transmission from the engine compartment into the passenger area. This study develops such structures using phenolic felt in the upper and lower layers for sound and impact insulation, with aerogel, ceramic fabric, and glass fabric in the intermediate layer to enhance acoustic and thermal resistance. The composite structures were fabricated using a flat mold at 185 °C and 170 bar pressure, employing glass fabric and various combinations of materials. Their sound absorption coefficients were measured with an impedance tube, and thermal conductivity coefficients were determined using a thermal conductivity meter. The results were then compared for performance evaluation. The results showed that hybrid composite structure 5, which included phenolic felt, glass fabric, aerogel powder, and phenolic felt between two coating interlinings, achieved stable sound absorption across a wide frequency range. Additionally, structure 3, made with phenolic felt and aerogel powder, offered the best thermal insulation. Structure 5 was also identified as a promising option for providing both acoustic and thermal insulation benefits. Overall, the study demonstrates that composite structures can effectively enhance both acoustic and thermal insulation in heavy-duty vehicles, contributing to improve in-cabin comfort.

Keywords: Thermal conductivity, Acoustic, Composite, Insulation material, Aerogel

1. GİRİŞ

Dünya genelindeki ağır CO_2 emisyon yönetmeliklerinden kaynaklı, otomotiv endüstrisinde önemli ölçüde ağırlık azaltılması ihtiyacı oluşmaktadır (European Environment Agency, 2018). Araç ağırlığındaki %10'luk bir azalmanın yakıt ekonomisinde %6-8 oranında iyileşme sağladığı da görülmüştür (Kazan, 2019). Son zamanlarda, gelişen teknoloji ve teknik ile araç performansını ve yakıt verimliliğini arttırırken, yayılan emisyonu en aza indirmek, araç içi kabinlerde gürültü ve ısı izolasyonu sağlayarak sürücü ve yolcuların iç mekân konforunu arttırıp, sürüş deneyimini iyileştirmek gibi pek çok hedefe, düşük üretim maliyetleriyle ulaşmayı sağlayacak araştırma geliştirme faaliyetlerine ağırlık verilmiştir (Ahmed, 2023; Keskin, 2023). Bu çalışmalar doğrultusunda, amaca uygun özellikleri barındıran, birden fazla malzemenin bir araya getirilmesiyle elde edilen kompozit malzemelerin kullanımı da hızla yaygınlaşmıştır.

Kompozit malzemeler, makroskobik düzeyde bir araya getirilmiş ve birbiri içinde çözünmeyen iki veya daha fazla bileşenden oluşan yapı malzemeleridir (Kaw, 2005). Kompozit malzemeler, bileşenlerde tek başına olmayan mukavemet, hafiflik, estetik, termal dayanım ve akustik performans gibi özelliklerin geliştirilmesi ve bir araya getirilmesi amacıyla elde edilmektedir (Danyıldız, 2023). Kompozit malzemelerin otomotiv endüstrisinde kullanımı ise, araçların tasarımında kolaylık sağlaması, çevreci olması ile 80 yıllık bir geçmişe dayanmaktadır (Ağırgan, 2024). Aynı kompozit yapıda iki ya da daha fazla takviye elemanı çeşidinin bulunduğu kompozitlere ise hibrid kompozitler denilmektedir (Göz, 2016). Hibrit kompozitlerin, tek malzemeli kompozitlere oranla daha iyi özellik kombinasyonu sunduğundan yeni tip kompozitlerin geliştirilmesine en uygun kompozit sınıfı olduğu düşünülmektedir. Ancak, kullanılacak olan kompozit malzemenin kalınlığıyla ilgili belirli sınırlamalar bulunmaktadır. Buna ek olarak, aracın hızı ve sürüş koşullarıyla değişkenlik gösteren gürültü miktarı kontrolünün de kalınlığı azaltılmış hafif malzemeler ile etkin bir şekilde sağlanması gerekmektedir. (Nayak ve Padhye, 2016).

Gelişen teknoloji ile üretimi ve kullanımı yaygınlaşan elektrikli araçlarda, tahrik sistemi olarak kullanılan elektrik motorları, fosil yakıtla çalışan günümüz araçlarındaki içten yanmalı motorlara göre farklı termal ve akustik izolasyon ihtiyaçlarına sahiptir. İçten yanmalı motorlarda, gürültü frekans dağılımı düşük frekanslarda (100-1500 Hz) yoğunlaşırken; elektrik motorlarında bu yoğunlaşma yüksek frekans bandında (1250-6000 Hz) gerçekleşmektedir. Akustik banttaki bu değişim, elektrikli araçlarda bambaşka akustik izolasyon ihtiyaçlarını da beraberinde getirmektedir (Karabulut, 2022). Akustik performansı iyileştirmeye yönelik olarak literatürde yapılan bir çalışmada, araç kabinlerinde gürültü seviyesini azaltmak üzere, özellikle 2000-6300 Hz aralığında ses yutum katsayısı (α) 1 değerine yakın olan, dıştan içe doğru iki kaplama telası arasında PP/GF, PE film, taş yünü içeren bir kompozit sandviç yapı ortaya koyulmuştur (Aydın ve ark., 2024). Elektrikli araçlarda (EV), bataryaların konumlandırıldığı batarya muhafazalarında, termal ve mekanik özelliklerin yanı sıra hafiflik sağlamak üzere, alüminyuma alternatif olarak polimer kompozit malzemelerin kullanılmasına yönelik çalışmalar da bulunmaktadır (Cebe ve İrez, 2024). Elektrikli araç (EV) batarya muhafazalarında kullanılmak üzere, hem elektromanyetik girişim (EMI) koruma hem de termal yalıtım sağlama kapasitesine sahip yeni bir sandviç yapının geliştirildiği çalışmada, yazarlar karbon fiber takviyeli kompozit malzeme üzerine odaklanmışlardır. Çalışma sonucunda, önerilen kompozit malzemenin dış katmanlarında karbon fiber takviyeli kompozit, ara katmanlarda ise bakır kaplı polyester, melamin köpük ve grafit parçacıkları ile zenginleştirilmiş reçine bulunmaktadır (Hu ve ark., 2024).

Termal ve ses izolasyonu sağlamak amacıyla düşük termal iletkenliğe sahip olan, poliüretan köpük, keçe, mineral katkılı malzemeler ve elyaflarla takviye edilmiş polimer malzemeler tek başına veya farklı kombinasyonlarda yaygın olarak kullanılmaktadır. Bu malzemelere ek olarak, havadan bile daha düşük ısı iletim katsayısı değerine sahip olan aerojeller, bu özelliği nedeniyle ısı yalıtım malzemesi olarak çok iyi bir alternatif oluşturmakta ve birçok alanda başarıyla kullanılmaktadır (Caps ve Fricke, 2004). 21. yüzyılın en ilgi çekici malzemelerinden biri olarak kabul edilen aerojeller, inorganik (metal ve metal oksitler), organik (sentetik polimerler ve biyopolimerler) ve hibrid (organik–inorganik) malzemeler olmak üzere temel olarak üç ana kategoriye ayrılmaktadır (Meti ve ark., 2023). İnorganik aerojeller, genellikle metal oksitlerden ve diğer inorganik malzemelerden özel bir süreçle türetilen malzemeler olarak tanımlanırken (Aegerter ve ark., 2022), organik aerojeller, genellikle polimerlerin süperkritik kurutma yöntemiyle aerojel formuna dönüştürülmesiyle elde edilen özel malzemelerdir. Organik aerojellerin belirgin özellikleri, düşük yoğunluk ve esnek yapıya sahip olmasıdır (Mazraeh-shahi ve ark., 2015). Hibrit aerojeller ise, inorganik ve organik bileşenlerin entegre edilmesiyle oluşturulan özel malzemelerdir (Zuo vd., 2015).

Termal ve akustik yalıtım açısından yüksek performans gösteren gözenekli ve hafif yapılara sahip olan aerojellerin kompozit malzemeler ile birlikte kullanılmasına yönelik literatürde çeşitli çalışmalar yer almaktadır (Karabulut, 2022; Gündoğdu, 2023). Cam lifi/ silika aerojel ve cam lifi/ karbon lifi/ silika aerojel kompozit yapıların ısı yalıtım performanslarının karşılaştırıldığı çalışmada, sandviç termal yalıtım battaniyesi olarak oluşturulan silika aerojel/ cam lifi/ karbon lifi kompozit yapısının, cam lifi/ silika aerojel kompozit yapısına göre daha iyi eğilme mukavemeti ve daha düşük termal iletkenlik gösterdiği belirlenmiştir (Hung ve ark., 2020). Isı yalıtımı sağlamak üzere, silika-elyaf keçeleri ve silika-aerojel çekirdek tabakasından katmanlı bir sandviç yapıların oluşturulduğu çalışmada, elde edilen bu yapının, otomotiv katalitik konverterleri için termal genleşme matı olarak kullanılacağı varsayılmıştır. Söz konusu çalışma, iki farklı hazırlama sürecini ve karşılaştırılmasını içermektedir. Sunulan karakterizasyon analizleri, ısı radyasyonunu önlemek için SiC parçacıklarının aerojel çekirdek tabakasına ve ısıtılmış yüzeye yakın konumlandırıldığı yapılarda daha iyi sonuç elde edileceğini göstermiştir (Kawaoka ve ark., 2020). Bir diğer çalışmada, silika aerojel, poliüretan aerojel, poliimid aerojel, silika-poliimid hibrit aerojel, silika-poliüretan hibrit aerojel, poliimid-poliüretan hibrit aerojel ve silika-poliimid-poliüretan hibrit aerojellerin sentezleri gerçekleştirilmiş ve bu aerojellerin toz/ parçacık formda farklı şekillerde otomotiv trim malzemelerine aktarımı sağlanmıştır. Elde edilen yeni aerojel katkılı keçe malzemelerin, termal ve akustik özellikleri hem birbiri ile hem de aerojel içermeyen katmanlı keçe malzemeler ile karşılaştırılmıştır. Yapılan bu çalışma ile gözenekliliğin, literatürdeki verilerle uyumlu olarak termal ve akustik özellikleri arttırıcı sonuçları gözlemlenmiştir (Karabulut, 2022).

Bu çalışmada, literatürdeki çalışmalardan farklı olarak kamyon, tır vb. ağır hizmet araçlarında, sürüş konforunu artırmak ve motor bölgesinde ortaya çıkan ses ve yüksek sıcaklığın kabin içerisine geçişini engelleyen kompozit sandviç plaka elde edilmesine yönelik, ses ve darbe izolasyonu sağlamakla görevli alt ve üst katmanda fenolik keçe, akustik ve termal dayanımı arttırmakla görevli ara katmanda aerojel, seramik kumaş, cam kumaş ve kombinasyonları kullanılarak hibrit kompozit yapıların oluşturulması üzerine çalışmalar gerçekleştirilmiştir. Bahsedilen yapıların oluşturulmasında kullanılan malzeme kombinasyonları, benzer izolasyon malzemelerinin test şartnameleri, maliyet, akustik ve termal izolasyon ihtiyaçları dikkate alınmıştır. Belirlenen malzemelerin düz bir kalıpta preslenmesiyle sandviç plaka numuneleri elde edilmiştir. Üretilen numunelerin, termal ve akustik performansları, ısıl iletkenlik ve empedans tüpü testleriyle değerlendirilmiş ve hedefe yönelik en iyi performansı gösteren malzeme kompozisyonu seçilmiştir. Bu çalışmanın amacı, akustik performanstan ödün vermeden özellikle kamyon, tır gibi ağır hizmet araçlarının motor boşluk bölgelerinde oluşan yüksek ısının kabin içerisine transferini engelleyen ve bu sayede kabin içi iklimlendirmeden kaynaklı enerji ve yakıt sarfiyatını azaltırken araç ağırlığına olumsuz etki yaratmayan bir kompozit yapının ortaya koyulmasıdır.

2. MATERYAL VE YÖNTEM

2.1 Malzeme Kompozisyonunun Geliştirilmesi

Bu çalışmada, kamyon, tır vb. ağır hizmet araçlarında sürüş konforunu artırmak ve motor bölgesinde ortaya çıkan ses ve yüksek sıcaklığın kabin içerisine geçişini engellemek amacıyla, hibrit kompozit plaka elde edilmesine yönelik Çizelge 1'de verilen malzeme kombinasyonları üzerine çalışmalar gerçekleştirilmiştir. Malzeme kombinasyonları, benzer izolasyon malzemelerinin test şartnameleri, maliyet, akustik ve termal izolasyon ihtiyaçları dikkate alınarak belirlenmiştir. Belirlenen malzemeler düz bir kalıpta preslenerek hibrit kompozit plakalar elde edilmiştir. Üretilen numunelerin termal ve akustik performansları, ısıl iletkenlik ve empedans tüpü testleriyle değerlendirilmiş ve hedefe yönelik en iyi performansı gösteren malzeme kompozisyonu seçilmiştir.

Çizelge 1. Malzeme kompozisyonları (MK)

	İçerik					
MK 1	%4.89 Tela	%30.08 Fenolik Keçe	%30.08 Seramik Kumaş	%30.08 Fenolik Keçe	%4.89 Tela	
MK 2	%5.51 Tela	%33.90 Fenolik Keçe	%21.19 Cam Kumaş	%33.90 Fenolik Keçe	%5.51 Tela	
MK 3	%6.64 Tela	% 40.86 Fenolik Keçe	%5 Aerojel	% 40.86 Fenolik Keçe	%6.64 Tela	
MK 4	%4.84 Tela	%29.77 Fenolik Keçe	%29.77 Seramik Kumaş	%1 Aerojel	%29.77 Fenolik Keçe	%4.84 Tela
MK 5	%5.45 Tela	%33.56 Fenolik Keçe	%20.97 Cam kumaş	%1 Aerojel	%33.56 Fenolik Keçe	%5.45 Tela

Motor bölgesinde konumlanan parçalar su ve yağ ile temas halindedir. Bu nedenle en dış katmanda, su ve yağ itici özellikli, kolay deforme olmayan bir kaplama malzemesi olan tela kullanımı ve bununla birlikte özellikle akustik performansı yüksek ve diğer keçelere oranla maliyet avantajı sağlaması sebebiyle ana bileşen olarak fenolik keçe kullanımı kararlaştırılmıştır. Ara katmanda ise akustik ve termal izolasyonu desteklemesi adına, ısıya dayanıklı kumaşlar ve aerojel malzeme kombinasyonları eklenmiştir.

2.2 Prototip Ürünlerin Hazırlanması

Tüm prototip ürünlerde üst ve alt katmanda tela & fenolik keçe yapısı sandviç oluşturabilmek amacıyla sabit olarak kullanılmıştır. Şekil 1'de gösterilen bu yapı, akustik performans ve termal yalıtım özellikleri açısından, ağır hizmet araçlarının bulunduğu zorlu koşullarda çalışan sistemlerin gereksinimlerini karşılamak için ideal kombinasyondur. Fenolik keçe, termoset bir malzemedir. İçeriğinde bulunan fenol formaldehit reçine, malzemenin yüksek ısılara dayanıklı olmasını sağlarken, keçenin gözenekli yapısı akustik performansın artmasını sağlamaktadır. Kullanılan kaplama telası ise, yapıya mekanik dayanım ve esneklik kazandırmakta ve bu sayede, yapısal stabilite sağlayarak deformasyonu önlemektedir. Aynı zamanda hafif bir malzeme olması sebebiyle de toplam ağırlığı arttırmamaktadır. Kullanılan kaplama telası, piyasada PANOX® ticari ismi ile bilinen, %50 karbon içerikli NW kumaştan mamul olup, yoğunluğu 130 kg/m^3'tür. Fenolik keçe ise, %60 oranında polyester & pamuk karışımından oluşan elyaf ve %40 oranında fenol formaldehit reçine içermektedir. 800 kg/m^3 yoğunluğa sahiptir. Ara katman olarak, MK 1'de 800 gr/m^2 seramik kumaş, MK 2' de 500 gr/m^2 cam kumaş kullanılmış olup, MK 3'te Ömer Lütfü Özgül Kimyevi Maddeler firmasından tedarik edilen, Çizelge 2'de teknik özellikleri verilen ve OSIL SUPER S220 ticari ismiyle bilinen hidrofilik ve amorf yapıda üretilen silika bazlı aerojel malzeme kullanılmış olup, kompozit yapının toplam ağırlığının %5'i oranında katkılandırılmıştır. Aerojel malzeme, geniş yüzey alanı, düşük yoğunluk, nano gözenekli yapı, yüksek saflıkta SiO_2 içeriği, yüksek su absorpsiyon kapasitesi ve nötr pH ile üstün termal ve akustik yalıtım özellikleri ile ön plana çıkmaktadır. Seramik kumaş, alüminyum oksit ve silisyum dioksit bazlı seramik liflerden üretilmiş, yüksek performansa sahip bir tekstil malzemesidir. Yüksek sıcaklıklarda yapısal bütünlüğü bozulmamakta ve termal bir bariyer görevi görmektedir. Cam kumaş, S-cam liflerinden dokunan, hafif ve yüksek mukavemetli bir tekstil malzemesidir. Yüksek sıcaklıklarda yapısal özelliklerini koruyabilmekte ve zorlu ortamlara dayanıklılık göstermektedir. MK 4 ve MK 5 ‘de sırayla seramik kumaş-aerojel, cam kumaş-aerojel kombinasyonları uygulanmıştır. Aerojel katkısı kompozit yapının ağırlıkça %1’i olacak şekilde kullanılmıştır.

Çizelge 2. OSIL SUPER S220 teknik özellikleri

Özellik	**Test metodu**	**Değer**	**Birim**
Görünüm	-	Beyaz, ince kokusuz toz	-
Spesifik yüzey alanı	BET	220±30	m^2/g
Gözenek boyutu	BJH	3-5	nm
SiO_2 içeriği	ISO 3262/19	98.64	%
Na_2SO_4, çözünmüş tuz içeriği	ISO 787/13	1.36	%
Yoğunluk	ISO 787/11	92	g/l
Kurutmada kütle kaybı	ISO 787-2	4.38	%
pH değeri 50 g/l	ISO 787-9	6.87	-
Su absorplama kapasitesi	W_1-QCP-03	262	%
Partikül boyutu (Dv50)	ISO 13320-1	13.11	µm

Çizelge 1’de verilen malzemeler, 1 x 1 m ebatlarında kesilerek, üst üste olacak şekilde dizilmiş ve Şekil 1’de gösterilen katmanlı bir yapı oluşturulmuştur.

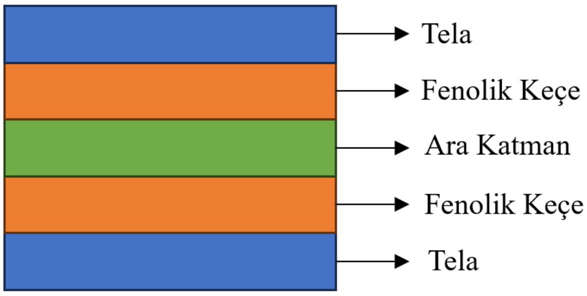

Şekil 1. Malzeme kompozisyonu katmanları

Ardından düz yüzeye sahip bir kalıp kullanılarak (Şekil 2), 185 °C sıcaklıkta ve 170 bar basınç altında 120 saniye preslenerek, sandviç panel formunda prototip ürün üretimleri gerçekleştirilmiştir.

Şekil 2. Pres ve kalıp görseli

Makine parametreleri belirlenirken, kompozisyonun ana yapısını oluşturan fenolik keçenin kürleşerek sert bir form alması için gerekli değerler dikkate alınmıştır. Fenolik keçe içerisinde bulunan fenol formaldehit reçinenin kürleşerek termoset bir hal alması için minimum 170 °C sıcaklık kullanılması gerekmektedir. Bununla birlikte, 185 °C sıcaklık, reaksiyonu hızlandırarak kürleşme sürecinin daha kararlı bir yapıda olmasını sağlamaktadır. Daha düşük sıcaklıklar, kürleşme süresini uzatarak bağ yapısının zayıflamasına neden olabilmektedir. Daha yüksek sıcaklıklar ise, reçinenin yanmasına sebep olarak, ürünün mekanik ve termal özelliklerini olumsuz etkilemektedir. 170 bar basınç ve 120 saniye presleme süresi, sandviç yapıda bulunan katmanların, homojen birleşmesini ve aralarında kuvvetli bir bağ oluşmasını sağlamaktadır. Yeterli basınç uygulanmadığı takdirde, katmanlar arasında istenen birleşme sağlanamamaktadır. Bu durumda yapısal bütünlüğü bozmaktadır. Daha yüksek basınç değerleri ise, malzemede deformasyona neden olabilmektedir. Çalışma kapsamında, benzer malzemelerin üretimine yönelik daha önce yapılmış çalışmalar temel alınarak, en uygun makine parametreler belirlenmiştir.

Kompozit malzemelerin üretiminde, numune kalınlığının sabit tutulması, performans özelliklerinin karşılaştırılabilmesi ve deneysel sonuçların güvenilirliği açısından kritik öneme sahiptir. Otomotiv sektöründe, termal ve akustik izolasyon amacıyla üretilen sandviç paneller genellikle 0.025 m kalınlığında üretilmektedir. Bu kalınlık, hafiflik ve performans beklentileri açısından ideal bir seçimdir. Tüm numunelerin 0.025 m kalınlıkta olması için, presleme esnasında farklı kalınlıklarda stoperler kullanılmıştır. Stoper, kalıpta sıkıştırmayı sınırlayan fiziksel bariyerlerdir.

2.3 Empedans Tüpü Ölçümleri

Ses yutum katsayısının ölçümlerinde kullanılan yaygın yöntemlerden biri, empedans tüpünde gerçekleştirilen ses şiddeti ölçümleridir. Ses yutum katsayısı, emilen dalganın kaynaktan gelen dalgaya oranı olarak tanımlanmaktadır (Aydın, 2008). Empedans tüpü içerisine yerleştirilen, 0.03 m ve 0.1 m boyutlarındaki numunenin ses yutum katsayısı ve ses iletim kaybı değerleri, numune üzerine yerleştirilen mikrofonlar aracılığıyla ölçülmektedir (Doğru, 2020).

Ses yutum katsayısı (α), gelen ses dalgası enerjisi ile yansıyan ses dalgası enerjisi arasındaki farkın oranı olup, genellikle aşağıdaki formülle hesaplanmaktadır.

$$\alpha = 1 - |r^2| = 1 - r_r^2 - r_i^2 \tag{1}$$

Formülde ‘’r’’ yansıma katsayısını ifade etmektedir. Yansıma katsayısı, ses dalgalarının malzeme yüzeyinde ne kadarının yansıdığını göstermekte ve empedans tüpünde yapılan hassas basınç ölçümleri ile belirlenmektedir. Ölçümlerde, ses basıncı, yansıma katsayısı, ses yutum gücü ve farklı frekanslardaki dalgaların özellikleri dikkate alınmaktadır. Genellikle, malzemenin ses yutum davranışı geniş bir frekans aralığında incelenerek değerlendirilmektedir. Bu yöntem sayesinde, malzemenin akustik performansı, özellikle gürültü kontrolü ve akustik tasarım alanlarında kullanılabilecek şekilde analiz edilmektedir (Batmaz ve Aydın, 2013).

Test işlemi, TS EN ISO 10534-2 standardına uygun olarak Formfleks Ar-Ge laboratuvarında gerçekleştirilmiştir. Bu test yöntemi, ses yutucu malzemelerin ses yutum katsayısının belirlenmesi için bir empedans tüpü (Şekil 3), iki mikrofon ve bir frekans analiz sisteminin kullanımını kapsamaktadır. TS EN ISO 10534-2 standardına göre, transfer-fonksiyon yöntemi ile malzemenin ses yutma katsayısı belirlenmektedir. Bu test, malzemenin yüzeyine gönderilen ve geri yansıyan ses dalgalarının analiziyle gerçekleştirilmiştir.

Şekil 3. Empedans tüpü

Test edilecek malzemelere ait numuneler, Şekil 4’te gösterildiği üzere, tüpün çapına uygun olacak şekilde 0.03 m ve 0.1 m boyutlarında kesim presinde hazırlanmaktadır. Empedans tüpü içerisinde herhangi bir kir olup olmadığı ve mikrofon giriş noktalarının temizliği kontrol edilmekte ve kullanılacak mikrofonların kalibrasyonları yapılmaktadır. Akabinde, kullanılan yazılım ve sistem bağlantıları kontrol edilmektedir. Laboratuvar ortamı, 23 °C sıcaklık ve %45 bağıl neme sahip olacak şekilde şartlandırılmaktadır. Test esnasında dış ortamdan gelen gürültü minimum seviyede olacak şekilde ortam izole edilmektedir.

Test malzemesi, tüpün uç kısmına yerleştirilip, sızdırmazlık sağlanmaktadır. Hoparlör aracılığıyla tüp içerisine 200 Hz ila 6300 Hz arasında değişen frekanslarda ses dalgaları gönderilmektedir. Bu kısımda, sinyal tipi olarak beyaz gürültü ve pembe gürültü kullanılmaktadır. Tüp üzerinde farklı noktalara yerleştirilmiş mikrofonlar tüp boyunca ilerleyen ve numuneden yansıyan ses dalgalarını ölçmektedir.

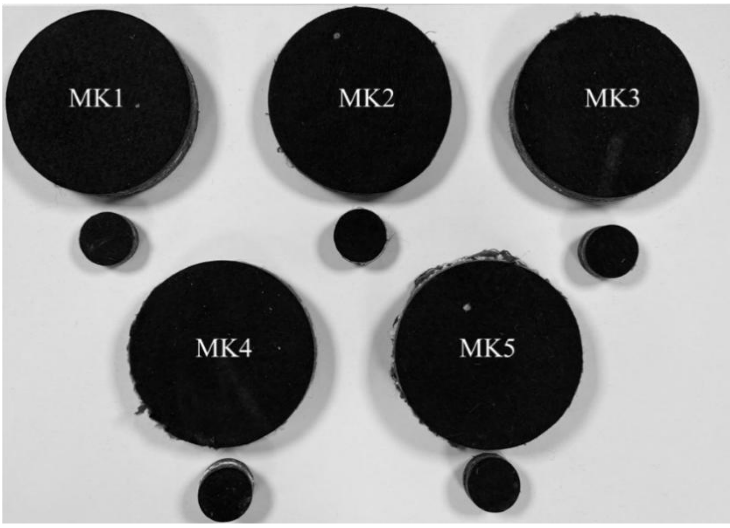

Şekil 4. 0.03 m ve 0.1 m empedans tüpü numuneleri

2.4 Isıl İletkenlik Ölçümleri

Isı İletkenlik Katsayısı λ (W/m.K), bir malzemenin fiziksel ve kimyasal yapısına bağlı olarak o malzemenin ısıyı ne kadar ilettiğinin ifadesidir. Isı iletimi, bir katı malzeme veya durgun akışkan içindeki sıcak bir bölgeden daha soğuk bir bölgeye doğru ısının geçişi olarak tanımlanmaktadır. Bir katı cisim içinde sıcaklık farkları varsa, yüksek sıcaklık bölgesinden düşük sıcaklık bölgesine iletim yoluyla aktarılmaktadır. (Variyenli ve Arslan, 2017).

Üretilen tüm numunelerin ısıl iletkenlik testleri, Şekil 5'te gösterilen TA Instruments markalı, Lasercomp Fox 314 modeli cihazda, TS ISO 8301 standardına uygun olarak gerçekleştirilmiştir. Bu standart düz levha halindeki deney parçalarında, kararlı ısı aktarımını ölçmek için ısı akış sayacının kullanılmasını ve deney parçalarının ısı aktarım özelliklerinin hesaplanmasını kapsamaktadır. Isıl iletkenlik ölçüm cihazı, iki plaka arasına yerleştirilen numune boyunca bir sıcaklık farkı oluşturarak ısıl iletkenliği ölçmektedir. Plakalara yerleştirilen hassas termokupllar, numune yüzeyindeki sıcaklık ve ısı akışını doğru bir şekilde algılanmaktadır.

Test numuneleri, 0.3 x 0.3 x 0.025 m ebatlarında hazırlanmaktadır. Test cihazında alt plaka sıcaklığı 10 °C, üst plaka sıcaklığı 30 °C olarak ayarlanmakta ve plakalar arası sıcaklık farkı oluşturulması sağlanmaktadır. Bu sayede, numune boyunca ısı akışı oluşturulmaktadır. Hassas termokupllar, numune yüzeyine yerleştirilerek 10 farklı noktadan sıcaklık ölçümü yapılmaktadır. Tüm ölçümlerin ortalama değeri alınarak, ısıl iletkenlik katsayısı λ (W/m.K) belirlenmektedir.

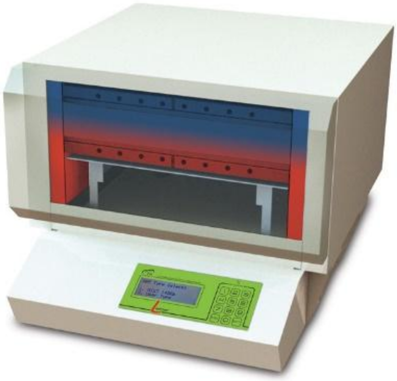

Şekil 5. Isıl iletkenlik ölçüm cihazı

3. BULGULAR VE TARTIŞMA

3.1 Empedans Tüpü Test Sonuçları

Aynı proses parametreleri kullanılarak (185 °C, 170 Bar, 120 saniye) malzeme kompozisyonu 1 ile prototip numune 1, malzeme kompozisyonu 2 ile prototip numune 2, malzeme kompozisyonu 3 ile prototip numune 3, malzeme kompozisyonu 4 ile prototip numune 4 ve malzeme kompozisyonu 5 ile de prototip numune 5 elde edilmiştir. Tüm prototip numunelerde, hibrit kompozit yapının oluşturulmasında, sesin yanı sıra darbe izolasyonu sağlamak üzere, en alt ve en üst katmanda fenolik keçe kullanılırken, tüm yapıyı saracak şekilde kaplama katmanı olarak tela kullanılmıştır. Şekil 6'da tüm prototip numunelere ait ses yutum katsayısı-frekans grafiği, Çizelge 3'te prototip numunelere ait ses yutum katsayıları (α) verilmiştir. X ekseninde verilen frekans değerleri, sesin titreşim hızını ifade etmektedir. Bu eksende, sesin düşük frekanslardan (200 Hz) yüksek frekanslara (6300 Hz) kadar nasıl davrandığı analiz edilmektedir. Y ekseninde verilen ses yutum katsayısı, bir malzemenin ses enerjisini ne kadar iyi emdiğini göstermektedir. 0 ile 1 arasında değişmekte olup, 0, sesin tamamen yansıtıldığını, 1 ise tamamen yutulduğunu ifade etmektedir.

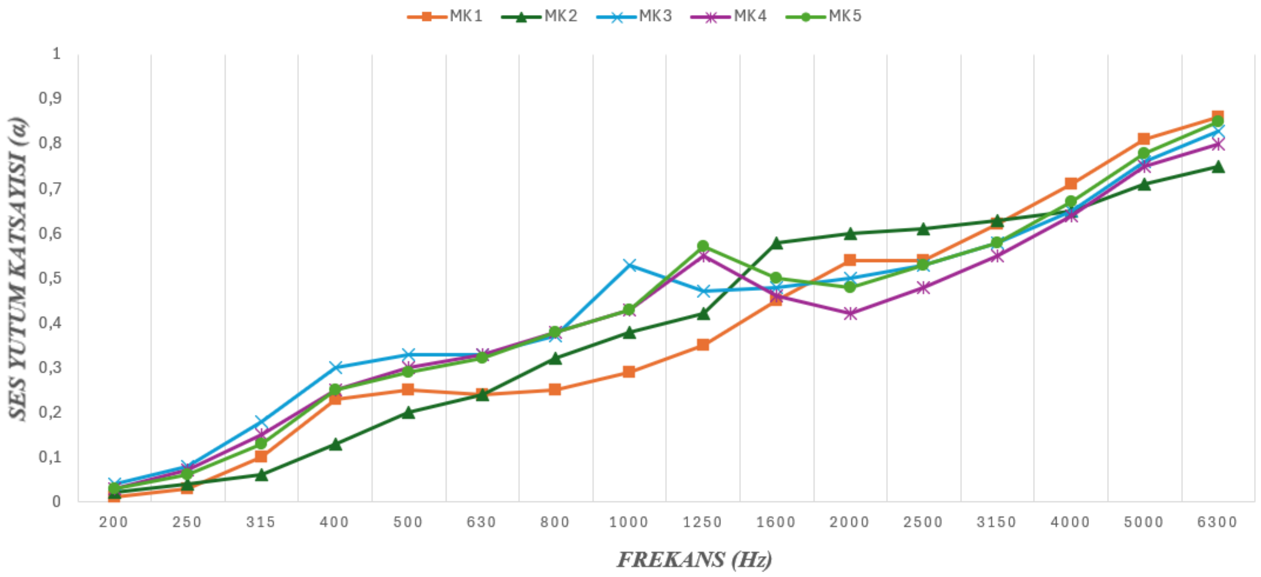

Şekil 6. Tüm prototip numunelere ait ses yutum katsayısı(α)-frekans (Hz) grafiği

Çizelge 3. Prototip numunelere ait ses yutum katsayıları (α)

Frekans [Hz]	MK 1 [α]	MK 2 [α]	MK 3 [α]	MK 4 [α]	MK 5 [α]
200	0.01	0.02	0.04	0.03	0.03
250	0.03	0.04	0.08	0.07	0.06
315	0.1	0.06	0.18	0.15	0.13
400	0.23	0.13	0.3	0.25	0.25
500	0.25	0.2	0.33	0.3	0.29
630	0.24	0.24	0.33	0.33	0.32
800	0.25	0.32	0.37	0.38	0.38
1000	0.29	0.38	0.53	0.43	0.43
1250	0.35	0.42	0.47	0.55	0.57
1600	0.45	0.58	0.48	0.46	0.5
2000	0.54	0.6	0.5	0.42	0.48
2500	0.54	0.61	0.53	0.48	0.53
3150	0.62	0.63	0.58	0.55	0.58
4000	0.71	0.65	0.65	0.64	0.67
5000	0.81	0.71	0.76	0.75	0.78
6300	0.86	0.75	0.83	0.8	0.85

Ses yalıtımının yanı sıra termal dayanımı arttırmak üzere, fenolik keçeler arasına cam kumaş ve seramik kumaşın konumlandırıldığı MK1 ve MK2 kompozisyonlarından üretilen prototip numunelerinin ses yutum performansı incelendiğinde; özellikle 630-3150 Hz frekans aralığında, cam kumaş içeren prototip 2 numunesinin ses yutum performansının, seramik kumaş içeren prototip 1 numunesine göre daha iyi olduğu, 3150Hz frekanstan sonra ise prototip 1 numunesinin ses yutum performansının prototip 2 numunesine oranla iyileştiği görülmüştür. Düşük frekanslı sesler uzun dalga boyuna, yüksek frekanslı sesler kısa dalga boyuna sahiptir. Cam kumaşın sahip olduğu gözenekli ve hafif yapı, 630-3150Hz frekanstaki seslerin malzeme içinde daha iyi absorbe edilmesini sağlarken yoğun ve sert yapıya sahip seramik kumaşın, kısa dalga boylarına sahip yüksek frekanslı seslerde daha etkin performans sergilediği düşünülmektedir (Kaya ve Dalgar, 2017).

Ses yalıtımı ve termal dayanımı arttırmak üzere, fenolik keçeler arasına toz formda aerojel katkılandırılarak üretilen prototip 3 numunesinin düşük frekanslarda, prototip 1 numunesi ve prototip

2 numunesine oranla daha yüksek ses yutum performansı sağladığı görülmüştür. Aerojeller, nano ölçekli gözeneklere sahip çok düşük yoğunluklu ve son derece gözenekli malzemelerdir. Gözeneklerin içindeki hava, düşük frekanslı ses dalgalarının yayılmasında önemli bir rol oynamaktadır. Düşük frekanslı ses dalgaları, uzun dalga boylarına sahiptir ve malzemenin gözenekli yapısında daha uzun süre hapsolmaktadır. Aerojelin içindeki hava boşlukları sayesinde, ses dalgalarının bu gözenekler içinde defalarca yansımasını sağlamaktadır. Bu süreç sırasında, ses enerjisi sürtünme ve viskoz direnç nedeniyle kaybolurken düşük frekansta ses yutumu artmaktadır (Begum ve ark., 2022). Bunun yanı sıra, aerojelin akustik empedansı hava ile uyum sağlamaktadır. Bu uyumluluk, sesin malzeme tarafından soğurulmasına yardımcı olmaktadır. Çalışmada kullanılan aerojel, hidrofilik yapıda olması sebebiyle nem ve suyu hapsetmektedir. Su emilimi, malzemenin yoğunluğunu artırarak ağırlaşmasına sebep olmaktadır. Bu da yüksek frekanslarda ses yutumunu olumsuz etkilemektedir. Gelecek çalışmalarda, hidrofobik özellikli aerojel katkısı ile çalışma tekrarlanarak, yüksek frekanslarda ses yutum performansının incelenebileceği düşünülmektedir.

Termal dayanımı arttırmak üzere, ısı üreten yapıya bakacak yönde, fenolik keçe ile toz formda aerojel arasına seramik kumaş konumlandırılarak prototip 4 numunesi, yine fenolik keçe ile toz formda aerojel arasına cam kumaş konumlandırılarak prototip 5 numunesi elde edilmiştir. Ses yutum katsayısı-frekans grafiği incelendiğinde, düşük frekans aralığında (200- 1250Hz) benzer özellikler göstermiştir. Yüksek frekans aralığında (1250-6000Hz) ise prototip 5 numunesinin ses yutum performansında prototip 4 numunesine göre artış olduğu gözlenmektedir. Cam kumaş, özellikle yüksek frekanslı ses dalgalarını absorbe etmede etkili iken aerojel gözenekli yapısı ile düşük frekanslarda yüksek ses yutma kapasitesine sahiptir (Shao ve ark., 2024). Aerojelin gözenekli yapısının, ses dalgalarının malzeme içinde yayılmasına ve çok sayıda yansımasına izin verdiği düşünülmektedir. Ses dalgaları, aerojel katmanını geçtikten sonra cam kumaşa çarptığında, cam kumaşın lifli yapısı, sesin daha fazla difüze olmasını sağlamaktadır. Dolayısıyla, prototip 5 numunesinde kullanılan cam kumaş ve aerojel kombinasyonunun sinerjik bir etki yaratarak geniş bir frekans aralığında etkili ses yalıtımı sağladığı düşünülmektedir. Seramik kumaşlar ise, genellikle daha sert ve yoğun yapıları nedeniyle, yüksek frekanslı ses dalgalarını geri yansıtma eğilimindedir. Seramik kumaş, aerojel ile birleştiğinde, malzemenin gözenek yapısı ve hava geçirgenliği azaldığı için ses emilim performansının düşebileceği ön görülmektedir. Elde edilen ses yutum katsayısı-frekans grafiği de bu öngörüyü doğrular niteliktedir. Tüm malzeme kompozisyonları göz önüne alındığında, prototip 5'in literatürle uyumlu olarak geniş frekans aralığında kararlı bir ses yutum performansı sergilediği gözlenmiştir. Özetle, düşük frekanslı sesler daha uzun dalga boylarına sahip oldukları için, malzeme içinde derinlere inebilmektedir. Bu sebeple, aerojel gibi nano ölçekli gözenekli malzemeler, bu frekans bandında daha etkili olmaktadır. Yüksek frekanslı sesler kısa dalga boylarına sahip oldukları için, yüzeye yakın kısımlarda yutum gerçekleşmektedir. Bu nedenle, lifli yapılar ses dalgalarının yayılmasını sağlayarak etkili olmaktadır.

3.2 Isıl İletkenlik Test Sonuçları

Gözenekli yapıya sahip izolasyon malzemelere ait kombinasyonların kullanıldığı hibrit kompozitlerin ısıl iletkenlik performanslarını incelemek üzere, her bir prototip numunenin ısı iletkenlik katsayısı ölçülerek sonuçları Çizelge 4 ve Şekil 7'de verilmiştir. Tela & fenolik keçeden oluşan alt katman ve üst katman arasına seramik kumaş, cam kumaş ve toz formda aerojelin konumlandırılarak elde edilen prototip numune 1, 2 ve 3'ün ölçülen ısıl iletkenlik katsayıları birbiri ile kıyaslandığında, termal izolasyon performansı en yüksek numunenin aerojel katkılı prototip 3 numunesi olduğu tespit edilmiştir. Aerojel, düşük ısıl iletkenlik özellikleri ile bilinmektedir (Alan ve ark., 2021). Dolayısıyla en düşük ısıl iletkenlik katsayısına sahip numunenin, prototip 3 numunesinin olması beklenen bir sonuçtur. Aerojel katkılı kompozitler, gözeneklik yapıları sayesinde, -200°C ile 650°C aralığında etkin bir ısı yalıtımı sağlamaktadır (Köken ve Kanık, 2022). Kararlı yapıları sayesinde, ani sıcaklık değişimlerinden minimum seviyede etkilenmektedirler. Bu da aerojel katkılı kompozitlerin, otomotiv, inşaat, petrol, doğalgaz ve uzay sanayi gibi çok çeşitli alanlarda etkin bir şekilde kullanılmasına olanak sağlamaktadır. Seramik kumaş ve cam kumaş içeren numuneler birbiri ile kıyaslandığında ise, prototip 2 numunesinin, prototip 1 numunesine kıyasla seramik kumaşın daha düşük ısıl iletim özellikleri sergilediği gözlemlenmiş olup, elde edilen bu sonuç, cam kumaşın seramik kumaşa göre daha etkili bir ısı yalıtımı sağlama kapasitesine sahip olduğunu destekler niteliktedir. Cam kumaşın üstün ısı yalıtım performansının temelinde, cam liflerinin gözenekli ve hafif yapısı ile düşük ısıl iletkenlik katsayısı yatmaktadır. Cam liflerinin sahip olduğu bu yapısal özellikler, ısının etkin bir şekilde emilmesini ve dağıtılmasını sağlayarak ısıl iletkenliği minimize etmektedir. Bununla birlikte, seramik kumaşlar daha sert ve yoğun olduğundan daha düşük bir yalıtım özelliğine sahiptir. Bu durum, seramik kumaşların ısı yalıtımı açısından cam kumaşlara göre daha az etkili olmasına yol açmaktadır (Li ve ark., 2002). Cam kumaş ve seramik kumaşa ayrıca aerojelin katkılandırılması ile oluşturulan prototip 4 ve prototip 5 numunelerinin ısıl iletkenlik katsayıları incelendiğinde, söz konusu kumaşların tek başına kullanıldığında ölçülen sonuçlara paralel olarak prototip 5 numunesinin prototip 4 numunesine kıyasla daha iyi bir ısı yalıtımı sağladığı görülmektedir. Yine bu kumaşlara aerojel katkısının etkisi incelendiğinde ise, elde edilen ısıl iletkenlik ölçümlerinde farklı bir sonuç elde edilmemiştir fakat, aerojel katkısı cam kumaş ve seramik kumaşın ısı yalıtım özelliğini anlamlı bir biçimde arttırmıştır. Tek başına seramik kumaşın kullanıldığı prototip 1 numunesine göre aerojel katkılı seramik kumaşın kullanıldığı prototip 4'ün ısıl iletkenlik katsayısında %16.4'lük düşüş kaydedilmişken, sadece cam kumaşın kullanıldığı prototip 2 numunesine göre aerojel katkılı cam kumaşın kullanıldığı prototip 5'in ısıl iletkenlik katsayısında %8.03'lük düşüş elde edilmiştir. Cam kumaş ve seramik kumaşın aerojel ile kombinasyonunda ısıl iletkenlik düşüşü farklı olabilmektedir. Cam kumaşın ısıl iletkenliği orta seviyede olduğu için aerojelin etkisi seramik kumaşa göre daha az belirgin olmuştur. Seramik kumaşın yüksek ısıl iletkenliği ise aerojelin etkisini daha belirgin hale getirmiştir.

Çizelge 4. Prototip numunelere ait ısıl iletkenlik katsayısı (W/m.K) sonuçları

	Test sonuçları				
Ölçüm Sayısı	MK 1	MK 2	MK 3	MK 4	MK 5
1	0.04276	0.03738	0.03388	0.03601	0.03436
2	0.04274	0.03728	0.03383	0.03591	0.03428
3	0.04273	0.03722	0.03379	0.03581	0.03423
4	0.04271	0.03716	0.03376	0.03575	0.03417
5	0.04269	0.0371	0.03373	0.03567	0.03414
6	0.04268	0.03708	0.03371	0.03564	0.03411
7	0.04267	0.03705	0.03368	0.03558	0.03408
8	0.04265	0.03703	0.03368	0.03554	0.03404
9	0.04264	0.03702	0.03367	0.03553	0.03404
10	0.04263	0.03701	0.03366	0.03551	0.03402
Ortalama Değer	0.04269	0.03713	0.03374	0.03570	0.03415

Bu çalışma, herhangi bir malzemeye/ yapıya aerojel eklenmesinin ısı yalıtımı üzerinde belirgin bir iyileştirme sağladığını göstermektedir. Düşük yoğunluklu ve yüksek gözenekliliğe sahip yapısı, aerojelin çok düşük ısıl iletkenlik katsayılarına (0,018 W/m.K) sahip olmasına olanak tanınmaktadır. Bu özellikleri, aerojeli son derece etkili bir ısı yalıtım malzemesi yapmaktadır. Düşük ısıl iletkenlik, aerojelin ısının geçişini sınırlandırarak ısıl yalıtıma doğrudan etki ettiğini ortaya koymaktadır (Koebel ve ark., 2012; Chang ve ark., 2014).

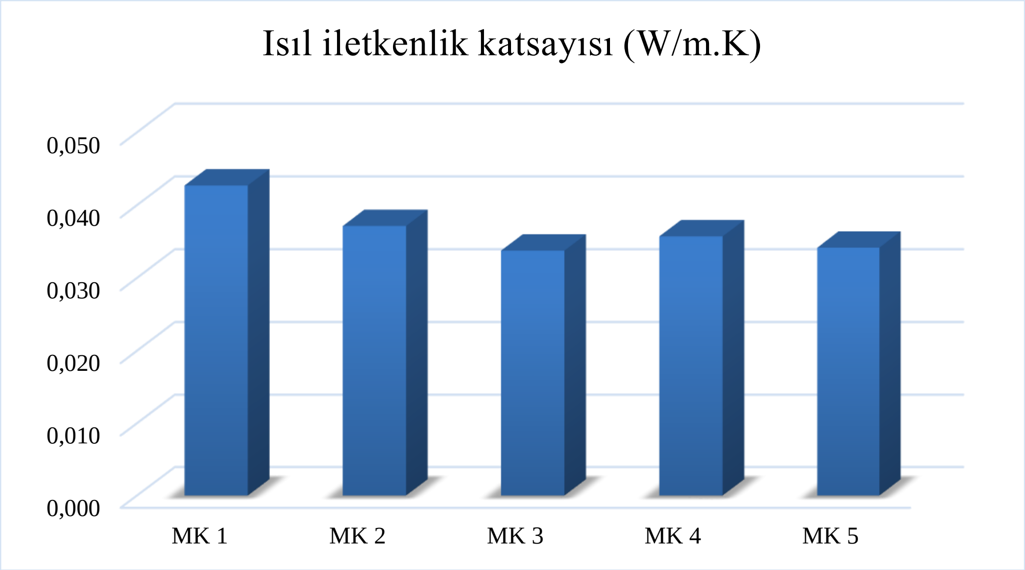

Şekil 7. Prototip numunelere ait ısıl iletkenlik katsayısı (W/m.K) sonuçları

4. SONUÇ

The Bu çalışmada, kamyon, tır vb. gibi ağır hizmet araçlarında, motor bölgesinde ortaya çıkan ses ve yüksek sıcaklığın ortamlar arası geçişini engelleyip, kabin içi sürüş konforu sağlamak üzere, ses ve darbe izolasyonu sağlamakla görevli alt ve üst katmanda fenolik keçe, akustik ve termal dayanımı arttırmakla görevli ara katmanda aerojel, seramik kumaş, cam kumaş ve kombinasyonları kullanılarak düz kalıpta, 185 °C sıcaklıkta ve 170 bar basınç altında hibrit kompozit sandviç yapılar oluşturulmuştur. Akabinde, bu yapıların empedans tüpünde ses yutum katsayıları, ısıl iletkenlik ölçüm cihazında ısıl iletkenlik katsayıları ölçülerek birbiriyle karşılaştırılmıştır. Ses yutum katsayısı, ses enerjisinin yansıma ve emilim oranıyla ilgilidir ve genellikle frekansa bağlı olarak ölçülmektedir. Isıl iletim katsayısı ise, malzemenin ısı enerjisini iletme kapasitesini tanımlamakta ve sabit bir değer olarak alınmaktadır. Gözenekli yapıların ısı iletim katsayısı, malzemenin yoğunluğu ve termal özelliklerine göre değişmekte iken, ses yutum özellikleri akustik dalga yayılımına bağlıdır. Ses yutum katsayısı ile ısıl iletim katsayısı arasında doğrudan bir orantı bulunmamakla birlikte, malzemelerin termal ve akustik performansı arasındaki ilişki, genellikle malzemenin yapısına ve yoğunluğuna bağlıdır. Malzemelerin gözenekliliği hem ısıl iletkenlik hem de ses yutum özelliklerini etkilemektedir. Örneğin, hafif, gözenekli malzemeler genellikle düşük ısıl iletim katsayısına ve yüksek ses yutum katsayısına sahip olması beklenmektedir. Buna karşılık literatürde, iyi bir ısı yalıtımının sağlanması durumunda, malzemelerin ses yalıtım özelliklerinin olumsuz yönde etkilendiği gözlemlenmiştir (Nurzyński, 2015).

Akustik performans test sonuçları incelendiğinde, geniş frekans aralığında kararlı bir ses yutum performansı gösteren hibrit kompozit yapının, ısı üreten yapıya bakacak yönde iki kaplama telası arası fenolik keçe, cam kumaş, toz formda aerojel ve fenolik keçe içeren malzeme kompozisyonu 5 olduğu tespit edilmiştir. Termal izolasyon performansı en yüksek hibrit kompozit yapının ise sırayla, iki kaplama telası arası fenolik keçe, toz formda aerojel ve fenolik keçe içeren malzeme kompozisyonu 3 ve iki kaplama telası arası fenolik keçe, cam kumaş, toz formda aerojel ve fenolik keçe içeren malzeme kompozisyonu 5 olduğu tespit edilmiştir. Elde edilen veriler göz önüne alındığında, hem akustik hem de termal izolasyon performansını bir arada sunabilecek hibrit kompozit yapı malzeme kompozisyonu 5 ile sağlanmıştır. Yapılan bu çalışmada, ağır hizmet araçlarının motor bölgesinde kullanılmaya yönelik hibrit kompozit yapılarının geliştirilmesinde uzmanlara destek olacak malzeme kompozisyonları ortaya koyulmuş olup, gelecekte farklı malzeme kompozisyonları ile NVH alanında çalışmak isteyen uzmanlara yol göstereceği düşünülmektedir. Bununla birlikte, geliştirilen malzeme kompozisyonunun kullanım alanları ağır hizmet araçları ile sınırlı değildir. Benzer akustik ve termal izolasyon beklentilerine sahip tarım makineleri (traktör), iş makineleri ve deniz taşıtlarının motor bölmeleri gibi diğer endüstriyel uygulama alanlarında da değerlendirilmesi mümkündür. Bu malzemeler, sıcaklık değişimlerine karşı dirençli yapıları sayesinde, enerji tasarrufu ve aynı zamanda üretim kolaylığı avantajlarına sahiptir. Bu özellikleri sayesinde, gelecek yıllarda yenilenebilir enerji sistemlerinde, soğutma ve ısıtma teknolojilerinde ve iklim değişikliğiyle mücadele için sürdürülebilir çözümler geliştiren sektörlerde önemli bir rol oynamasına olanak sağlayacağı düşünülmektedir.

5. TEŞEKKÜR

Bu çalışma, Formfleks Otomotiv A.Ş- Ar-Ge Merkezi bünyesinde gerçekleştirilmiştir. Yazarlar değerli katkılarından dolayı Ar-Ge Lideri Sn. İbrahim AYDIN’a teşekkür eder.

6. ÇIKAR ÇATIŞMASI

Yazarlar, bilinen herhangi bir çıkar çatışması veya herhangi bir kurum/kuruluş ya da kişi ile ortak çıkar bulunmadığını onaylamaktadırlar.

7. YAZAR KATKISI

Sena ARSLAN ATMACA çalışmanın kavramsal ve/veya tasarım süreçlerinin belirlenmesi, çalışmanın kavramsal ve/veya tasarım süreçlerinin yönetimi, veri toplama, veri analizi ve yorumlama, makale taslağının oluşturulması, fikirsel içeriğin eleştirel incelemesi, son onay ve tam sorumluluk kısımlarında katkıda bulunmuştur. Öznur İSKENDER veri toplama, veri analizi ve yorumlama, makale taslağının oluşturulması, fikirsel içeriğin eleştirel incelemesi, son onay ve tam sorumluluk kısımlarında katkıda bulunmuştur. Tuğay SEVİNÇ veri toplama, makale taslağının oluşturulması, son onay ve tam sorumluluk kısımlarında katkıda bulunmuştur.

8. KAYNAKLAR

Aegerter M. A., Leventis N., Koebel M. M., Steiner S. A. I., Springer Handbook of Aerogels, 2022.

Ağırgan M., Otomotiv endüstrisinde kompozit malzeme kullanımı, Electronic Journal of Vocational Colleges 13(2), 51-64, 2023.

Ahmed N. T., Otomotiv endüstrisinde karbon elyaf uygulamaları ile ilgili gelişmeler ve sürdürülebilirlik yaklaşımları, Pamukkale Üniversitesi Fen Bilimleri Enstitüsü, Yüksek Lisans Tezi (Basılmış), 2023.

Alan S., Gökçen Akkurt G., Akkurt S., Sezer H.Ç., Çam A., Aerojel Yalıtım Keçelerinin Isıl ve Higrotermal Karakterizasyonu, Harran Üniversitesi Mühendislik Dergisi, 6(Özel sayı): 58-69, 2021.

Aydın İ., Otomobillerde kullanılan izolasyon malzemelerinin emme katsayılarının ölçülmesi ve uygun malzeme kalınlığının belirlenmesi, Gazi Üniversitesi Fen Bilimleri Enstitüsü, Yüksek Lisans Tezi (Basılmış), 2008.

Aydın İ., Arslan S., Akduman M. Ç., Çay D., İskender Ö., Ağır hizmet araçlarının gürültü kalkanı parçasının akustik ve mekanik dayanım performansının incelenmesi, Journal of Advanced Research in Natural and Applied Sciences 10(2), 300-311, 2024.

Batmaz İ., Aydın İ. Taşıtlarda Kullanılan Yalıtım Malzemelerinin Ses Yutma Katsayılarının Belirlenmesi. Gazi Üniversitesi Mühendislik Mimarlık Fakültesi Dergisi 27(4), 2013.

Begum H., Xue Y., Bolton J. S., Horoshenkov K. V., The acoustical absorption by air-saturated aerogel powders, The Journal of the Acoustical Society of America 151(3), 1502-1515, 2022.

Caps R., Fricke J., Aerogels for thermal insulation. In Sol-Gel Technologies for Glass Producers and Users, 349-353, 2004.

Cebe E., İrez A. B., Elektrikli araçlarda batarya kutusu imali için termal özellikleri iyileştirilmiş hibrit polimer kompozitlerin geliştirilmesi ve mekanik özelliklerinin incelenmesi, International Journal of Advances in Engineering and Pure Sciences 36(3), 224-234, 2024.

Chang K. J., Wang Y. Z., Peng K. C., Tsai H. S., Chen J. R., Huang C. T., Lien W. F., Preparation of silica aerogel/polyurethane composites for the application of thermal insulation. Journal of Polymer Research 21, 1-9, 2014.

Danyıldız F. E., Hibrit fiber kompozit malzemelerin mekanik özelliklerinin deneysel olarak incelenmesi, Sakarya Üniversitesi Fen Bilimleri Enstitüsü, Yüksek Lisans Tezi (Basılmış), 2023.

Doğru T., Otomotiv iç trim malzemelerinde akuıstik özelliklerin ısı iletimi ile ilişkisinin araştırılması, Uludağ Üniversitesi Fen Bilimleri Enstitüsü, Yüksek Lisans Tezi (Basılmış), 2020.

European Environment Agency., Monitoring CO_2 Emissions from New Passenger Cars and Vans in 2017. EEA Technical Report, 15, 1-35, 2018.

Göz S., Elyaf dizilişinin karma kompozitlerin mekanik özellikleri üzerindeki etkisi, Dokuz Eylül Üniversitesi Fen Bilimleri Enstitüsü, Yüksek Lisans Tezi (Basılmış), 2016.

Hu S., Wang D., Večerník J., Křemenáková D., Militký J., Electromagnetic interference (EMI) shielding and thermal management of sandwich-structured carbon fiber-reinforced composite (CFRC) for electric vehicle battery casings. Polymers 16(16), 2291, 2024.

Hung WC., Horng R.S., Shia RE. Investigation of thermal insulation performance of glass/carbon fiber-reinforced silica aerogel composites, Journal of Sol-Gel Science and Technology 97, 414-421, 2021.

Gündoğdu İ., Aerojel Takviyesinin Farklı Metotlarla Tekstil Materyaline Aktarılması, Termal ve Akustik Yalıtım Özelliklerinin Incelenmesi, Bursa Uludağ Üniversitesi Fen Bilimleri Enstitüsü, Yüksek Lisans Tezi (Basılmış), 2023.

Karabulut C., Konvansiyonel malzemeler için aerojel takviyesi ile düşük termal iletkenlik, düşük akustik iletkenlik ve iyi mekanik özelliklere sahip süper yalıtım keçelerin geliştirilmesi, Bursa Uludağ Üniversitesi Fen Bilimleri Enstitüsü, Yüksek Lisans Tezi (Basılmış), 2022.

Kaw K., Mechanics of Composite Materials, CRC press, 2005.

Kawaoka S., Oya N., Sugiura K., Preparation and Characterization of Silica-Fiber/Aerogel Composite Heat Insulations, Journal of Mechanical Engineering Research and Developments 43(1), 228-234, 2020.

Kaya A. İ., Dalgar T., Ses Yalıtımı Açısından Doğal Liflerin Akustik Özellikleri, Mehmet Akif Ersoy Üniversitesi Fen Bilimleri Enstitüsü Dergisi 8(Özel (Special) 1), 25-37, 2017.

Kazan H., Hybrid Single Shot Manufacturing of MultiMaterials Structure for Automotive Applications. Phd Thesis of Clemson University, 2019.

Keskin E. N., Farklı monomer karışım oranları ile üretilen poliüretanların yüzey ve akustik özelliklerinin incelenmesi, Bursa Uludağ Üniversitesi Fen Bilimleri Enstitüsü, Yüksek Lisans Tezi (Basılmış), 2023.

Koebel M., Rigacci A., Achard P., Aerogel-based thermal superinsulation: an overview, Journal of sol-gel science and technology 63, 315-339, 2012.

Köken A., Kanık M., Aerojellerle Isı Yalıtımı ve Tekstil Uygulamaları. Tekstil ve Mühendis 29(128), 249-260, 2022.

Li Y., Zhu Q., Yeung K. W., Influence of Thickness and Porosity on Coupled Heat and Liquid Moisture Transfer in Porous Textiles, Textile Research Journal 72(5), 435-446, 2002.

Mazraeh-shahi Z. T., Shoushtari A. M., Bahramian A. R., A New Approach for Synthesizing the Hybrid Silica Aerogels. Procedia Materials Science 11, 571575, 2015.

Meti P., Wang Q., Mahadik D. B., Lee K. Y., Gong Y. D., Park H. H., Evolutionary Progress of Silica Aerogels and Their Classification Based on Composition: An Overview. Nanomaterials 13(9), 1498, 2023.

Nayak R., Padhye R., Acoustic textiles: an introduction, Acoustic Textiles, 1-32, 2016.

Nurzyński J., Is Thermal Resistance Correlated with Sound Insulation? Energy Procedia 78, 152-157, 2015.

Shao J., Lv Y., Xue Z., Pan Y., Liu J., Dai M., Qiu F., Preparation and Acoustic Performance of Porous Aerogel Composites of Graphene Oxide and Cellulose, Coatings 14 (4), 441, 2024.

Variyenli H. İ., Arslan C., Sıvıların ve Gazların Isıl İletkenlik Katsayısını Belirleyebilmek için Laboratuvar Tipi Bir Deney Cihazının Tasarımı, İmalatı ve Test Edilmesi, Politeknik Dergisi 20(3), 599-605, 2017.

Zuo L., Zhang Y., Zhang L., Miao Y. E., Fan W., Liu T., Polymer/carbon-based hybrid aerogels: preparation, properties and applications. Materials 8(10), 6806-6848, 2015.

JOURNAL of
MATERIALS and MECHATRONICS:A

e-ISSN 2717-8811
JournalMM, 2024, 5(2), 369-382
https://doi.org/10.55546/jmm.1582242

Araştırma Makalesi / Research Article

Ni-CoWB Kompozitlerinin Üretimi İçin Düşük Bor İçeriğine Sahip Ni-Co-W-B İri Hacimli Metalik Cam Alaşımlarının Geliştirilmesi

Cumali DİNCER[1*], Aytekin HİTİT[2], Selinnur AKSU[3]

[1*] Afyon Kocatepe Üniversitesi, Mühendislik Fakültesi, Malzeme Bilimi ve Mühendisliği Bölümü, Afyonkarahisar, Türkiye,
ORCID ID: https://orcid.org/0000-0001-7341-5993, cumalidincer@usr.aku.edu.tr
[2] Afyon Kocatepe Üniversitesi, Mühendislik Fakültesi, Malzeme Bilimi ve Mühendisliği Bölümü, Afyonkarahisar, Türkiye,
ORCID ID: https://orcid.org/0000-0003-2312-7840, hitit@aku.edu.tr
[3] Afyon Kocatepe Üniversitesi, Mühendislik Fakültesi, Malzeme Bilimi ve Mühendisliği Bölümü, Afyonkarahisar, Türkiye,
ORCID ID: https://orcid.org/0009-0002-8293-8803, selinnur.aksu@usr.aku.edu.tr

Geliş/ Received: 12.11.2024; **Revize/Revised:** 09.12.2024 **Kabul / Accepted:** 12.12.2024

ÖZET: Bu çalışmada yüksek sertliğe, yüksek kırılma tokluğuna, yüksek sıcaklık oksidasyon direncine ve yüksek korozyon dayanımına sahip bir kompozit malzeme grubu üretmek için kullanılacak öncül Ni-Co-W-B metalik cam alaşımları geliştirilmiştir. Düşük bor içeriğine sahip Ni-Co-W-B metalik cam alaşımlarının geliştirilmesi için yapılan çalışmalara temel oluşturan alaşım $Ni_{42.6}Co_{20}W_{20}B_{17.4}$ alaşımıdır. Camlaşma kabiliyeti en yüksek alaşımları belirlemek için Ni, Co ve W miktarları sistematik olarak değiştirilmiştir. Bu çalışmalar sonucunda %13 B ve %15 B içeren metalik cam alaşımları geliştirilmiştir. % 13 B ve % 15 B içerikli alaşımların hepsinin kritik döküm kalınlıklarının 0.3 mm olduğu belirlenmiştir.

Anahtar Kelimeler: Metalik cam, Camlaşma kabiliyeti, Termal özellikler

---

Sorumlu yazar / Corresponding author: cumalidincer@hotmail.com

Bu makaleye atıf yapmak için /To cite this article

Dincer, C., Hitit, A., Aksu, S. (2024). Ni-CoWB Kompozitlerinin Üretimi İçin Düşük Bor İçeriğine Sahip Ni-Co-W-B İri Hacimli Metalik Cam Alaşımlarının Geliştirilmesi. Journal of Materials and Mechatronics: A (JournalMM), 5(2), 369-382.

Development of Ni-Co-W-B Bulk Metallic Glass Alloys with Low Boron Content for the Production of Ni-CoWB Composites

ABSTRACT: In this study, Ni-Co-W-B metallic glass alloys were developed as precursors to produce a composite material group with high hardness, high fracture toughness, high temperature oxidation resistance and high corrosion resistance. The alloy that forms the basis for the studies carried out for the development of Ni-Co-W-B metallic glass alloys with low boron content is $Ni_{42.6}Co_{20}W_{20}B_{17.4}$ alloy. In order to determine the alloys with the highest glass forming ability, the amounts of Ni, Co and W were systematically changed. As a result of these studies, metallic glass alloys containing 13 at.% B and 15 at. % B were developed. It was determined that the critical casting thicknesses of all alloys with 13 at.% B and 15 at.% B content were 0.3 mm.

Keywords: Metallic glass, Glass forming ability, Thermal properties

1. GİRİŞ

Seramik malzemeler diğer geleneksel malzemelere göre yüksek sertlik, korozyon direnci ve yüksek sıcaklık dayanımı gibi özelliklere sahip olmaları nedeniyle pek çok uygulamada tercih edilirler. Ancak seramik malzemelerin gevrek yapıda olmaları kullanım alanlarını sınırlandırmaktadır. Bu nedenle daha az dayanıklı ve sınırlı alanlarda kullanıma sahip olan malzemelerin özelliklerini iyileştirmek ve uygulamada daha çok kullanım alanı bulabilen malzemeler üretmek amacıyla kompozit adı verilen malzemeler geliştirilmiştir. Bu amaç doğrultusunda kompozit malzemeler, yüksek kırılma tokluğuna sahip metal malzemeler ile yüksek mekanik özelliklere sahip seramik malzemelerin bir araya getirilmesi ile elde edilebilirler. Bu şekilde üretilen kompozit malzemeler literatürde sermet olarak adlandırılmaktadır. Sermetler takviye fazının seramik, matrisin ise metalik bir malzeme olduğu malzeme grubudur. Takviye fazı ile matrisin türünün ve hacim oranının değiştirilmesi ile sertlik-kırılma tokluğu kombinasyonunu elde etmek mümkündür (Lou vd. 2022). Takviye fazının içeriğine göre sermetleri; oksit esaslı (Cr-Al_2O_3), karbür esaslı (WC-Co), karbonitrür esaslı (TiC/TiN), nitrür esaslı (ZrN) ve borür esaslı (CrB-Mo) olarak sınıflandırmak münkündür.

Karbür esaslı sermetlerden en yaygın olarak kullanılan sermetin WC-Co olduğu gözlemlenmiştir. Kobaltın bağlayıcı faz (matris) ve tungsten karbürün takviye fazı olarak bir araya getirilmesi sonucunda oluşturulan WC-Co sermeti imalat, tıp, havacılık gibi birçok uygulama alanında tercih edilmektedir. WC-Co sermetler imalat alanında kesici uç olarak oldukça yaygın kullanılmaktadır. WC-Co sermetinin kullanımı esnasında yapı içerisindeki kobaltın zamanla oksidasyona uğraması ve yüksek kesme hızlarında tungsten karbürün ayrışması nedeniyle kesici ucun zamanla işlevselliğini kaybetmektedir. Bu da WC-Co sermetinin sektörel anlamda en büyük dezavantajı olarak kabul edilir.

Karbür esaslı sermetlerin bu gibi dezavantajları nedeniyle, borür esaslı sermetlerin üretimi daha fazla önem kazanmıştır. Borür esaslı sermetler yüksek sıcaklık oksidasyon direnci açısından karbür esaslı sermetlerden daha avantajlıdır (Zakhariev vd. 1986). Sermetlerin üretiminde takviye fazı olarak yaygın bir şekilde kullanılan WC, CoWB, TiB_2 ve TiC fazları, 1273 K sıcaklığında hava ortamında 4 saat boyunca oksidasyon sonucunda meydana gelen kütle artışlarını belirlemek amacıyla teste tabi tutulmuştur. Çizelge 1'de yapılan testler sonucunda meydana gelen kütle artışları verilmiştir. Çizelgeden de görüleceği üzere, CoWB takviye fazının karbür esaslı takviye fazlarına göre daha iyi oksidasyon direncine sahip olduğunu söylemek mümkündür. Karbür esaslı sermetlerin 600 ˚C ve üzeri sıcaklıklara çıkıldığında oksitlenmesinden kaynaklı aşınma dayanımları ve sertlik değerleri düşmektedir (Shi vd. 2008).

Çizelge 1. Bazı takviye fazlarının 1273 K sıcaklığında hava ortamındaki kütle kazanım değerleri (Zackariev vd. 1986)

Takviye Fazı	Kütle artışı (mg/cm^2)
WC	9.7
TiC	6
TiB_2	5.5
CoWB	3.5

Malzemelerin daha üstün özelliklere sahip olmasını sağlamak ve istenmeyen bazı mekanik özelliklerini iyileştirmek amacıyla, son 20 yıldır metalik cam kompozitleri çalışılan konular arasında yerini almaktadır. Metalik cam alaşımlarının kristalizasyonu sonucu takviye edilen fazlar yüksek çekirdeklenme hızına sahip olduklarından dolayı, matris içerisinde çökeltilmiş çok ince taneli ultra sert nanokompozitler meydana gelmektedir. Bu ve bunun gibi nedenlerden dolayı metalik camlar; kompozit malzeme eldesi amacıyla öncül olarak tercih edilirler (Igbal vd. 2008, Hitit vd. 2015).

Metalik cam alaşımlarınının kristalizasyonu ile ilgili son yıllarda yapılan çalışmalar, borür veya karbür takviyeli kompozit malzemelerinde metalik cam kristalizasyonu ile de mümkün olduğunu göstermiştir. Yüksek oranda bor ve/veya karbon içeriğine sahip Fe ve Co esaslı metalik camların kristalizasyonu ile çok yüksek sertlik değerine sahip kompozitler üretilmiştir (Hitit vd. 2019). Üretilen bu kompozit malzemeler yapıda çökelen $Cr_{23}C_6$, $(Fe, Cr)_{23}(C,B)_6$, Fe_3B, $(Co, Fe)_2B$, $(Co, Fe)_{21}Ta_2B_6$ ve CoWB fazları sayesinde yüksek sertlik değerlerine sahiptir. Ancak yapılan bu çalışmalar da üretilen kompozitlerin hiçbiri CoWB ile takviye edilen kompozit hariç sünek faz içermemektedir (Hitit vd. 2019). Ni-Co-W-B metalik camların kristalizasyonu yöntemi ile üretilen kompozitin yapısında hem sünek faz hem de yüksek sertliğe sahip CoWB fazı bulunmaktadır. Ni-CoWB kompozitinin içerisinde çökelen CoWB fazı borürler ve karbürler arasında bilinen en sert fazdır (Zakhariev vd. 1986). Literatür incelendiğinde $Ni_{37.6}W_{22.5}Co_{22.5}B_{17.4}$ alaşımının kristalizasyonu ile üretilen CoWB takviyeli kompozit malzemenin oldukça yüksek bir sertlik değerine sahip olduğu ortaya koyulmuştur (Akdağ 2022).

Bu çalışmada, yüksek kırılma tokluğuna ve yüksek korozyon dayanımına sahip Ni-CoWB kompozitlerinin üretiminde öncül olarak kullanmak amacıyla düşük bor ve yüksek nikel içeriğine sahip Ni-Co-W-B alaşımlarının gelişirilmesi hedeflenmiştir.

2. MATERYAL VE YÖNTEM

Çalışmada düşük bor içeriğine sahip alaşımların geliştirilmesi için sentezlenen alaşımların hazırlanması, dökülmesi ve karakterizasyon testleri uygulanmıştır.

2.1 Deney Numunelerin Üretimi

Çalışmada kullanılacak olan alaşım sistemi tasarlanırken, yüksek sertliğe ve yüksek kırılma tokluğuna sahip Ni-CoWB sermetlerinin üretiminde öncül olarak kullanılan Ni-Co-W-B iri hacimli metalik cam alaşımlarının bor içeriğini azaltmak amaçlanmıştır. Bu amaç doğrultusunda bor elementi miktarına bağlı olarak nikel, kobalt ve tungsten elementlerinin de miktarları farklı kombinasyonlar halinde sistematik olarak değiştirilmiştir. Alaşım tasarımı sırasında alaşımların Co ve W oranları sistematik olarak azaltılmış ve dolayısıyla Ni miktarı da sistematik olarak artırılmıştır. Co ve W miktarlarının azaltılmasının sebebi daha sonra kompozit üretiminde öncül olarak kullanılacak Ni-Co-W-B metalik cam alaşımının kristalizasyonu sırasında yapıda çökelen nikel katı çözeltisinin Co ve W içeriğini mümkün olduğunca düşük olmasını sağlamaktır. Bu sayede kompozitin kırılma tokluğu yüksek olacaktır.

Kompozisyon içerisindeki safsızlık oluşumunu engellemek ve homojen bir yapı elde edebilmek için alaşımlar hazırlanırken, mikron seviyesinde tane boyutuna sahip, oldukça yüksek saflıkta tozlar kullanılmıştır. Çizelge 2'de alaşımların hazırlanmasında kullanılan elementler ve bunların çeşitli özellikleri yer almaktadır.

Çizelge 2. Kullanılan elementlerin saflık dereceleri, tane boyutları ve atomik yarıçapları

Element	**Saflık (%)**	**Tane Boyutu (µm)**	**Atomik Yarıçap (nm)**
Nikel	99.9	3	0.124
Kobalt	99.8	<2	0.12510
Tungsten	99.9	1-5	1.367
Bor	98	<44	0.082

Atomik yarıçaplar (Senkov and Miracle 2001)

Düşük B içeriğine sahip Ni-Co-W-B metalik cam alaşımlarının geliştirilmesi için yapılan çalışmalar temel oluşturacak olan alaşım $Ni_{42.6}Co_{20}W_{20}B_{17.4}$ alaşımıdır. Bu çalışmalar sonucunda %13 B ve %15 B içeren alaşımlar geliştirilecektir. %15 B içeren alaşımların ilki $Ni_{45}Co_{20}W_{20}B_{15}$ olacaktır. Camlaşma kabiliyeti için en uygun Co ve W miktarlarını belirlemek için bu elementlerin miktarları sistematik olarak değiştirilecektir (Çizelge 3). %13 B içeren alaşımların ilki $Ni_{47}Co_{20}W_{20}B_{13}$ olacaktır. En iyi camlaşma kabiliyetine sahip alaşımı belirlemek için Co ve W içerikleri sistematik olarak değişttirilmiştir.

Çizelge 3. Düşük bor içeriğine sahip alaşımların geliştirilmesi amacıyla üretilecek alaşımlar (% atomik.)

Ni	**Co**	**W**	**B**
45	20	20	15
47	20	18	15
47	18	20	15
49	18	18	15
47	20	20	13
49	20	18	13
49	18	20	13
51	18	18	13
53	16	18	13
53	18	16	13
55	16	16	13

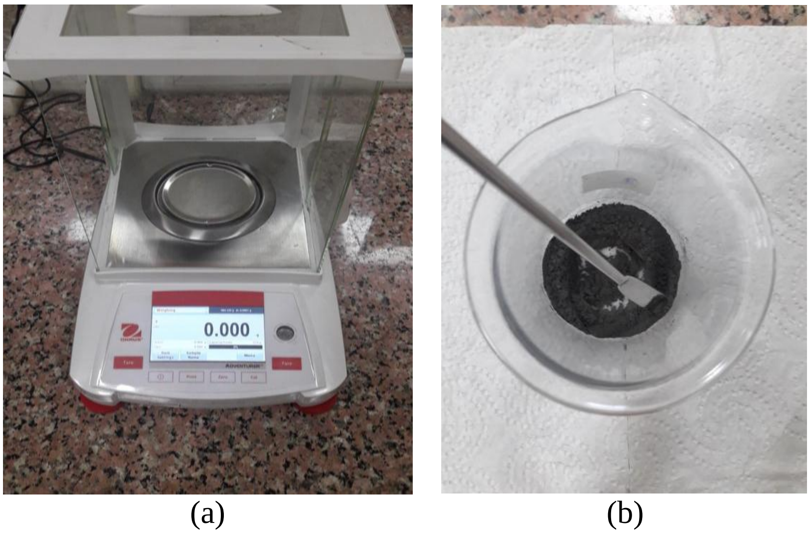

(a) (b)

Şekil 1. Hassas terazi yardımı ile 100 gr. tartılan toz karışımı. a) Kullanılan hassas terazi b) Toz karışımı

Karıştırma işlemi sonrasında homojen hale getirilen tozlar, çelik toz basma kalıbına konulmuştur. Tek etkili bir pres yardımı ile 80 MPa’lık basınç uygulanarak 12 mm çapa ve 6-7 mm yüksekliğe sahip tabletler halinde şekillendirilmiştir (Şekil 2).

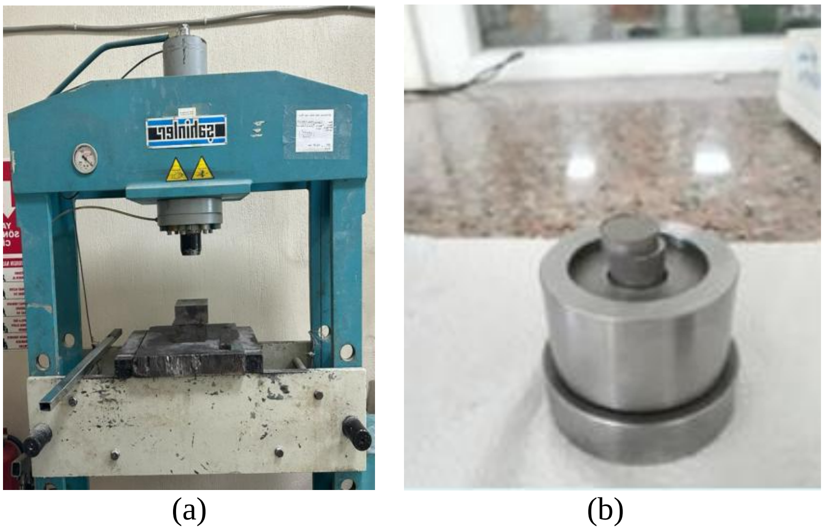

(a) (b)

Şekil 2. Hidrolik pres, çelik toz basma kalıbı ve şekillendirilen tablet. a) Hidrolik pres b) Şekillendirilen tablet

Tablet haline gelen alaşımlar, $5x10^{-5}$ mbar’ın altında basınç değerine indirilmiş ark ocağının (Şekil 3) içindeki haznede bulunan bakır kalıp içerisine ergitilmek üzere yerleştirilmiştir. Ergitme işlemleri öncesinde oksitlenme riskini en aza indirmek amacıyla hazne yaklaşık 1.3 atm basınç değerine sahip %99.999 saflıktaki Argon (Ar) gazı ile doldurulmuştur. Herhangi bir oksitlenme meydana gelip gelmediğini gözlemleyebilmek amacıyla Ti-Zr-Al fedai alaşımı hazne içerisinde ergitilmiştir (Şekil 4). Fedai alaşımda herhangi bir renk değişimi gözlemlenmediği takdirde bakır kalıp içerisindeki tabletlerin ark güç kaynağından gelen ve tungsten elektrod ile tabletlere aktarılan 350 A akım ile ilk ergitmeleri tamamlanmıştır. Tabletlerin daha homojen ergiyebilmeleri için, cihaz içerisinde bulunan manipülatör kol yardımı ile tabletler her defasında ters çevrilip tungsten elektrod ile üç kez ergitilerek bulk halde master alaşımlar (0.15 mol) elde edilmiştir (Şekil 4). Ergitme işlemi tamamlanarak döküm işlemi için hazır hale getirilen numuneler master alaşım olarak adlandırılır.

Şekil 3. Vakum ark ocağı ünitesi (1; Soğutma ünitesi, 2; Argon gazı, 3; X ve Y eksenlerinde hareketi sağlayan körük, 4; Manipülatör kol, 5; Ark ocağı haznesi, 6; Pnömatik emiş vanası, 7; Kontrol panosu, 8; Rotary vakum pompası ve turbo moleküler pompa, 9; Ark güç kaynağı)

Şekil 4. Vakum ark ocağında ergitme öncesi ve sonrası master alaşım numunesi. a) Ergitme öncesi master alaşımı b) Ergitme sonrası master alaşımı

Döküm işlemi için emme döküm yöntemi kullanılmıştır. Bu yöntem esnasında %99.999 saflığa sahip 0.3 mm ve 0.5 mm kesit kalınlığına sahip elekrolitik bakır kalıplar kullanılmıştır. Döküm işlemi öncesinde bakır kalıp cihaz içerisindeki hazneye oturtulmuştur. Ergitme işlemi tamamlanan master alaşımlar daha küçük parçalara ayrılmıştır. Yapılan denemeler sonucunda master alaşım belirlenen miktarlar da (0.6-0.7 gr.) tartılarak, bakır kalıp içerisine yerleştirilmiştir. Cihazın kapağı kapatılarak haznenin yaklaşık 3×10^{-4} mbar'ın altındaki basınç değerine inmesi beklenmiştir. Sonrasında koruyucu atmosfer için hazne yaklaşık 1.3 atm argon gazı ile doldurulmuştur. Emme döküm işlemi için tüm koşullar sağlandığında tungsten elektot yardımıyla master alaşımlar güç kaynağından gelen 100 ile 130 A arasında değişen akım değerinde ergitilmiştir. İşlem sırasında körük yatay ve düşey olarak hareket ettirilerek master alaşımın homojen bir şekilde ergimesi sağlanmıştır. Ergitme işlemi sonrası akışkan hale gelen master alaşımın, cihazın alt ve üst kısmındaki basınç farkından ve yerçekiminden yararlanılarak pnömatik emiş vanasının açılması ile kalıba emilmesi sağlanmış ve eş zamanlı olarak bakır kalıp içerisinde hızlı soğutma işlemi gerçekleştirilmiştir (Şekil 5).

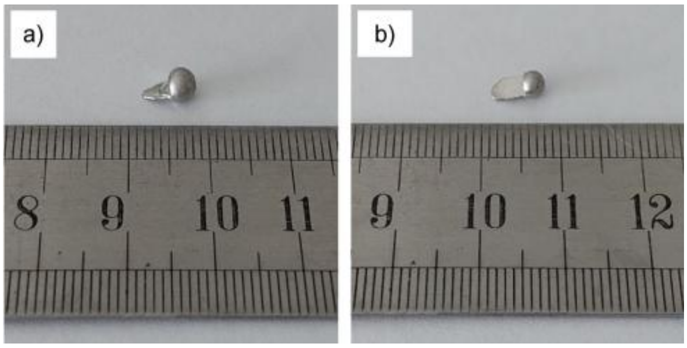

Şekil 5. Yüksek saflıktaki bakır kalıp ve emme döküm yöntemi ile elde edilmiş a) 0.3 mm, b) 0.5 mm kesit kalınlığına sahip numuneler

2.2 XRD Analizi

Elde edilen numunelerin içerisindeki fazların belirlenmesi amacıyla XRD analizi yapılmıştır. Bu analiz yöntemi, geneli temsil edecek şekilde malzemenin amorf yapıda olup olmadığını belirlemede oldukça kullanışlı ve verimlidir. XRD analizi sonucunda, amorf yapıya sahip malzemeler geniş difraksiyon desenine sahip tek bir pik sergilerken, kristal yapıdaki malzemeler dar ve keskin pikler halinde görüntülenirler.

Çalışmada gerçekleştirilen tüm XRD analizleri Afyon Kocatepe Üniversitesi bünyesinde bulunan Bruker D8 Advance marka XRD cihazında gerçekleştirilmiştir. Analiz öncesinde yeterli ve eşit miktardaki metalik cam numuneleri öğütülerek toz haline getirilmiştir. Toz halindeki numuneler cihaz içerisine konularak, Cu-K$_a$ (1.544 Å) X-ışını ile $2\Theta=10^{\circ}$ - 100° aralığında ve 1°/dk. tarama hızında analizleri gerçekleştirilmiştir. X-ışınlarının numuneye yönlendirmek ve paralel şekilde ulaşmasını sağlamak amacıyla 2 mm'lik slit ve 2 mm'lik kolimatör kullanılmıştır.

3. BULGULAR VE TARTIŞMA

%15 B içeren alaşımların 0.3 mm kesit kalınlığına sahip numunelerin XRD desenleri alaşımlarının tamamının amorf yapıda elde edildiğini göstermektedir (Şekil 6).

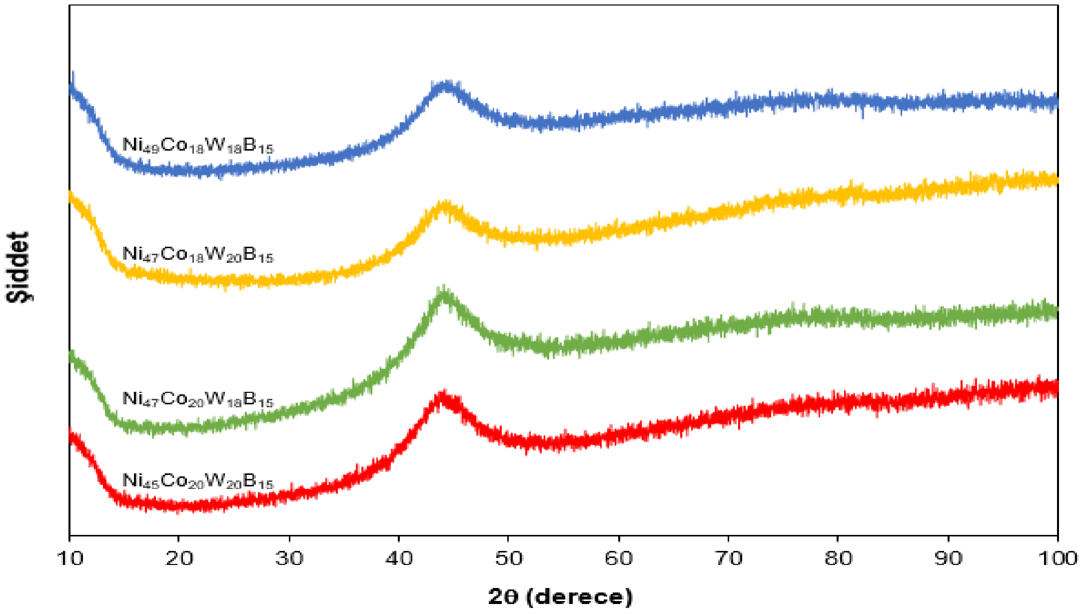

Şekil 6. %15 B içeren alaşımların 0.3 mm kesit kalınlığına sahip numunelerinin XRD desenleri

Ancak aynı alaşımların 0.5 mm kesit kalınlığına sahip numuneleri çok yüksek oranda Ni-katı çözeltisi çok az miktarda da CoWB fazı içermektedir (Şekil 7). Bu sonuçlar %15 bor içeren alaşımların kritik döküm kalınlıklarının 0.3 mm olduğunu göstermektedir.

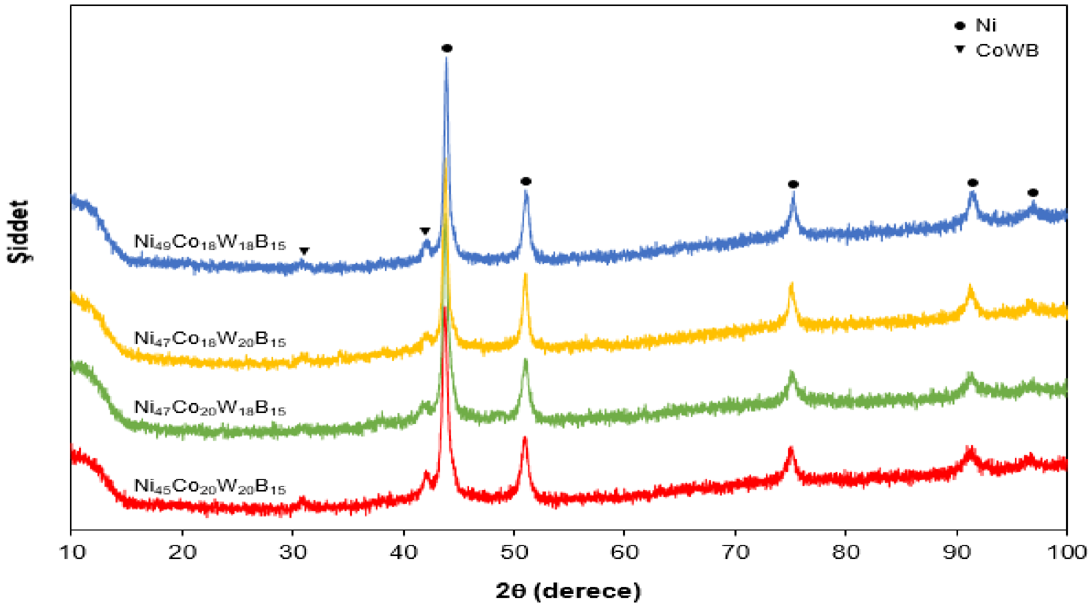

Şekil 7. %15 B içeren alaşımların 0.5 mm kesit kalınlığına sahip numunelerinin XRD desenleri

%15 B içeren alaşımların DSC analizleri yapılmış, T_g ve T_x sıcaklıkları belirlenmiş (Şekil 8) ve Çizelge 4'te verilmiştir. Sonuçlar %20 W içeriğine sahip alaşımların T_g ve T_x değerlerinin, %18 W içeriğine sahip alaşımların T_g ve T_x değerlerinden daha yüksek olduğunu göstermiştir. Bu da W içeriğinin termal kararlılığını etkileyen ana faktör olduğunu göstemektedir.

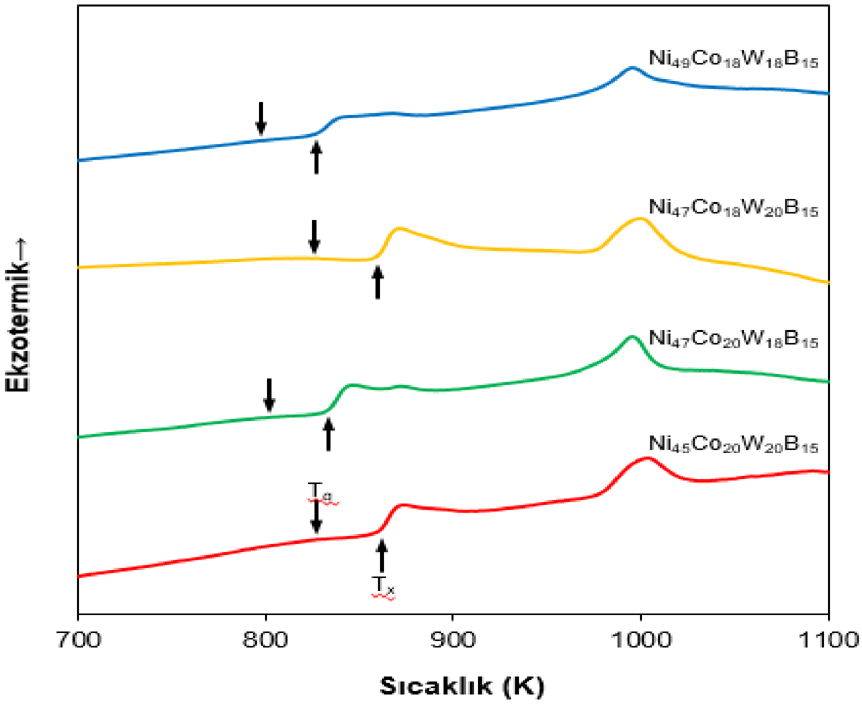

Şekil 8. %15 B içeren alaşımların DSC analizi sonuçları

Çizelge 4. %15 B içeren alaşımların termal özellikleri

Alaşım	**T_g (K)**	**T_x (K)**
$Ni_{45}Co_{20}W_{20}B_{15}$	827	861
$Ni_{47}Co_{20}W_{18}B_{15}$	802	833
$Ni_{47}Co_{18}W_{20}B_{15}$	826	860
$Ni_{49}Co_{18}W_{18}B_{15}$	797	827

%15 B içeren alaşımların 0.5 mm kesit kalınlığında yapılan dökümleri sırasında CoWB fazının oluşması alaşımın düşük Co, W ve B içeriğinden dolayı zordur. Bu yüzden de 0.5 mm kesit kalınlığındaki numunelerin CoWB içeriği oldukça düşüktür. Ancak alaşım çok yüksek oranda Ni içerdiği için Ni-katı çözeltisinin oluşabilmesi gerekli minimum çekirdeklenme zamanı daha düşük olmakta ve bunun sonucunda da çok yüksek oranda Ni-katı çözeltisi çökelmektedir (Şekil 9).

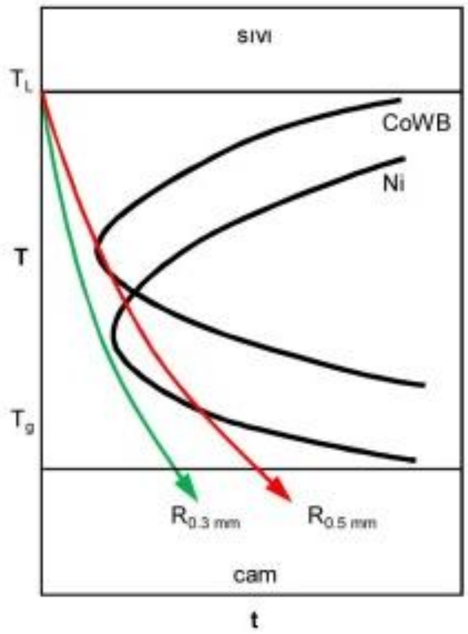

Şekil 9. %15 B içeren alaşımların şematik TTT diyagramı

%13 B içeren alaşımların 0.3 mm kesit kalınlığına sahip numunelerinin XRD desenleri $Ni_{47}Co_{20}W_{20}B_{13}$, $Ni_{49}Co_{20}W_{18}B_{13}$, $Ni_{49}Co_{18}W_{20}B_{13}$ ve $Ni_{51}Co_{18}W_{18}B_{13}$ alaşımlarının tamamen amorf yapıda olduğunu göstermektedir (Şekil 10). $Ni_{53}Co_{16}W_{18}B_{13}$ alaşımı yüksek oranda amorf faz içermesine rağmen bir miktar da Ni-katı çözeltisi içermektedir. $Ni_{53}Co_{18}W_{16}B_{13}$ ve $Ni_{55}Co_{16}W_{16}B_{13}$ alaşımları yüksek oranda Ni-katı çözeltisi ve bir miktar da CoWB fazı içermektedir.

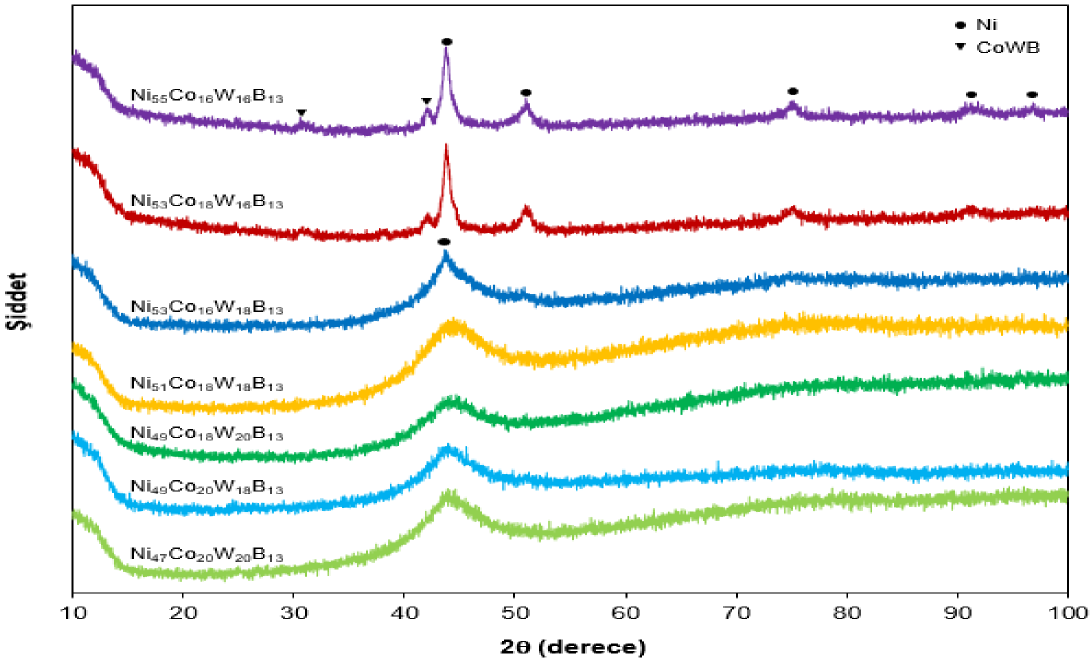

Şekil 10. %13 B içeren alaşımların 0.3 mm kesit kalınlığına sahip numunelerinin XRD desenleri

0.3 mm kesit kalınlığında tamamen amorf yapıda elde edilen alaşımların 0.5 mm kesit kalınlığına sahip numuneleri yüksek oranda Ni-katı çözeltisi ve bir miktar da CoWB fazı içermektedir (Şekil 11). Bu sonuçlar $Ni_{47}Co_{20}W_{20}B_{13}$, $Ni_{49}Co_{20}W_{18}B_{13}$, $Ni_{49}Co_{18}W_{20}B_{13}$ ve $Ni_{51}Co_{18}W_{18}B_{13}$ alaşımlarının kritik döküm kalınlıklarının 0.3 mm olduğunu ve diğer %13 B içeren alaşımların kritik döküm kalınlıklarının 0.3 mm'den küçük olduğunu göstermektedir. Ayrıca %13 B içeren alaşımların DSC analizleri yapılarak T_g ve T_x sıcaklıkları belirlenmiş (Şekil 12) ve Çizelge 5'te verilmiştir. %15 B katkılı alaşımlarda olduğu gibi %20 W içeriğine sahip alaşımların T_g ve T_x değerlerinin, %18 W içeriğine sahip alaşımların T_g ve T_x değerlerinden daha yüksek olduğunu göstermiştir. Bu da W içeriğinin termal kararlılığını etkileyen ana faktör olduğunu göstemektedir.

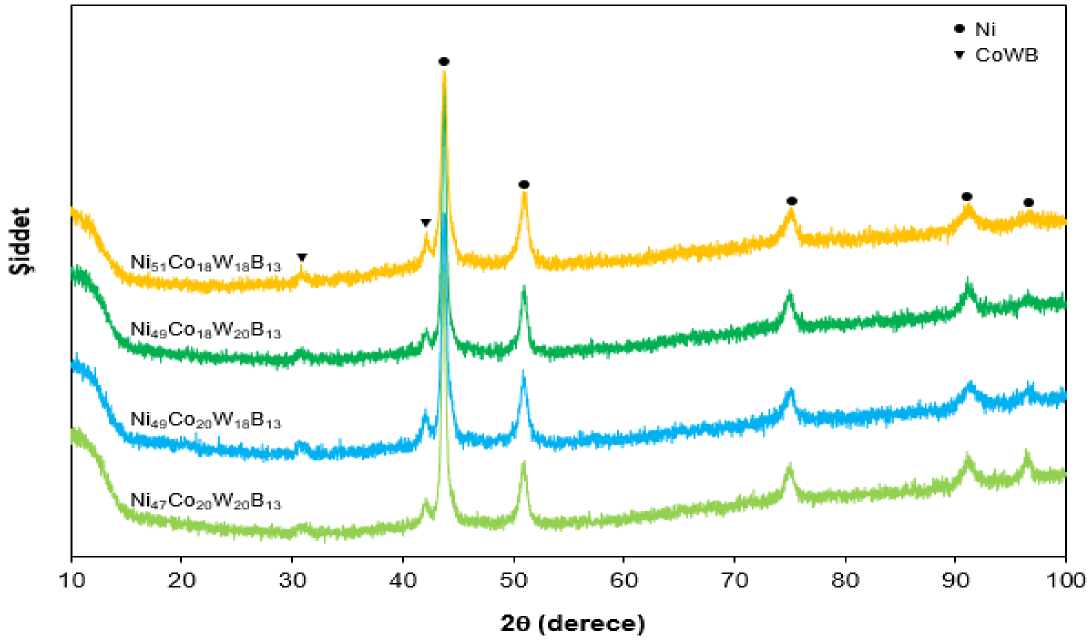

Şekil 11. %13 B içeren alaşımların 0.5 mm kesit kalınlığına sahip numunelerinin XRD desenleri

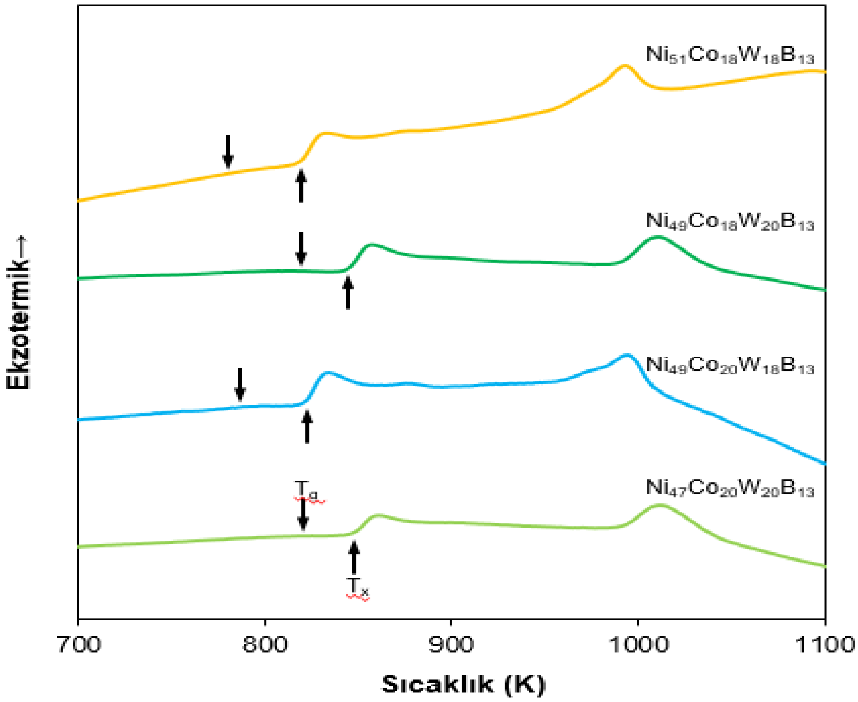

Şekil 12. %13 B içeren alaşımların DSC analizi sonuçları

Çizelge 5. %13 B içeren alaşımların termal özellikleri

Alaşım	**T_g (K)**	**T_x (K)**
$Ni_{47}Co_{20}W_{20}B_{13}$	820	848
$Ni_{49}Co_{20}W_{18}B_{13}$	786	822
$Ni_{49}Co_{18}W_{20}B_{13}$	819	845
$Ni_{51}Co_{18}W_{18}B_{15}$	780	819

%13 B içeren alaşımlarında Ni içeriğinin %53'e çıkarılması sonucu $Ni_{53}Co_{16}W_{18}B_{13}$ alaşımının 0.3 mm kesit kalınlığına sahip numune tamamen amorf yapı elde edilememiş, yapıda bir miktar Ni-katı çözeltisi çökelmiştir. Yine %53 Ni içeriğine sahip olan $Ni_{53}Co_{18}W_{16}B_{13}$ alaşımında ise yapıda çökelen Ni-katı çözeltisinin miktarının çok daha yüksek olduğu görülmektedir. Bunun sebebi $Ni_{53}Co_{16}W_{18}B_{13}$ alaşımının $Ni_{53}Co_{18}W_{16}B_{13}$ göre daha düşük W içeriğine sahip olmasından dolayı T_g sıcaklığının daha düşük olmasıdır. Daha düşük T_g sıcaklığından dolayı T_l-T_g farkı arttığı için aynı kesit kalınlığında elde edilebilecek soğuma hızı düşmektedir. Soğuma hızının düşmesinden dolayı da Ni-katı çözeltisinin çekirdeklenmesi söz konusu olmaktadır. % 55 Ni içeren $Ni_{55}Co_{16}W_{16}B_{13}$ alaşımı da hem daha yüksek Ni içeriğine sahip olduğu için hem de T_g sıcaklığı düşük olduğu için, 0.3 mm kesit kalınlığına sahip numunesinin yapısında yüksek oranda Ni-katı çözeltisi oluşumu meydana gelmiştir. 0.3 mm kesit kalınlığında amorf yapıda elde edilen %13 B içeren alaşımların 0.5 mm kesit kalınlığına sahip numuneleri aynı %15 B içeren alaşımlarının 0.5 mm kesit kalınlığına sahip numunelerinde olduğu gibi yüksek oranda Ni-katı çözeltisi içermektedir. Bunun sebebi %15 B içeren alaşımlarda olduğu gibi yüksek Ni içeriğinden dolayı Ni-katı çözeltisinin oluşumu için gerekli minimum çekirdeklenme zamanının oldukça düşük olmasıdır (Şekil 9).

%15 B içeren alaşımların tamamı 0.3 mm kesit kalınlığında amorf yapıda elde edilmiştir. Bu alaşımların tamamı da Ni-CoWB kompozitlerinin üretiminde öncül olarak kullanılabilir. Ancak bu alaşımlardan diğerlerine göre en düşük Co ve W içeriğine sahip olan $Ni_{49}Co_{18}W_{18}B_{15}$ alaşımı öncül olarak seçilmesi durumunda, alaşım diğerlerine göre en yüksek Ni içeriğine ve en düşük Co ve W içeriğine sahip olduğu için hem ısıl işlem sırasında çökelecek Ni-katı çözeltisinin hacim oranı yüksek olacaktır hem de Ni-katı çözeltisinin Co ve W içeriği diğerlerine göre düşük olacaktır. Böylece elde edilecek Ni-CoWB kompoziti hem yüksek kırılma tokluğuna hem de yüksek korozyon direncine sahip olacaktır.

%13 B içeren alaşımlardan sadece $Ni_{47}Co_{20}W_{18}B_{13}$, $Ni_{49}Co_{20}W_{18}B_{13}$, $Ni_{49}Co_{18}W_{20}B_{13}$ ve $Ni_{51}Co_{18}W_{18}B_{13}$ alaşımı 0.3 mm kesit kalınlığında tamamen amorf yapıda elde edilmiştir. Bu alaşımların tamamı da Ni-CoWB kompozitlerinin üretiminde öncül olarak kullanılabilir. Ancak bu alaşımlardan en yüksek Ni içeriğine ve en düşük Co ve W içeriğine sahip olan $Ni_{51}Co_{18}W_{18}B_{13}$ alaşımı öncül olarak seçilmesi durumunda, %15 B içeren alaşımlarda olduğu gibi elde edilecek kompozitin yapısında bulunan Ni-katı çözeltisinin miktarı diğerlerinden daha yüksek olacaktır. Ayrıca bu Ni-katı çözeltisi diğerlerinden daha düşük oranda Co ve W içerecektir. Böylece elde edilecek kompozitin kırılma tokluğu ve korozyon direncinin diğerlerinden daha yüksek olacaktır.

4. SONUÇ

Düşük bor içeriğine sahip alaşımlardan %15 B içeren alaşımların tamamı 0.3 mm kesit kalınlığında amorf yapıda elde edilmiştir. Bu alaşımların tamamı da Ni-CoWB kompozitlerinin üretiminde öncül olarak kullanılabilir. Ancak bu alaşımlardan diğerlerine göre en düşük Co ve W içeriğine sahip olan $Ni_{49}Co_{18}W_{18}B_{15}$ alaşımı öncül olarak kullanılması en uygun yaklaşım olacaktır. Bunun sebebi; söz konusu alaşım diğerlerine göre en yüksek Ni içeriğine ve en düşük Co ve W içeriğine sahip olduğu için hem ısıl işlem sırasında çökelecek Ni-katı çözeltisinin hacim oranı yüksek olacaktır hem de Ni-katı çözeltisinin Co ve W içeriği diğerlerine göre düşük olacaktır. Böylece elde edilecek Ni-CoWB kompoziti hem yüksek kırılma tokluğuna hem de yüksek korozyon direncine sahip olması beklenmektedir. Düşük bor içeriğine sahip alaşımlardan %13 B içeren alaşımlardan sadece $Ni_{47}Co_{20}W_{20}B_{13}$, $Ni_{49}Co_{20}W_{18}B_{13}$, $Ni_{49}Co_{18}W_{20}B_{13}$ ve $Ni_{51}Co_{18}W_{18}B_{13}$ alaşımı 0.3 mm kesit kalınlığında tamamen amorf yapıda elde edilmiştir. Bu alaşımların tamamı da Ni-CoWB kompozitlerinin üretiminde öncül olarak kullanılabilir. Ancak bu alaşımlardan en yüksek Ni içeriğine ve en düşük Co ve W içeriğine sahip olan $Ni_{51}Co_{18}W_{18}B_{13}$ alaşımı öncül olarak seçilmesi en uygun yaklaşım olacaktır. Bunun sebebi; %15 B içeren alaşımlarda olduğu gibi elde edilecek kompozitin yapısında bulunan Ni-katı çözeltisinin miktarı diğerlerinden daha yüksek olacaktır. Ayrıca bu Ni-katı çözeltisi diğerlerinden daha düşük oranda Co ve W içerecektir. Böylece elde edilecek kompozitin kırılma tokluğu ve korozyon direncinin diğerlerinden daha yüksek olması beklenmektedir.

5. TEŞEKKÜR

Bu çalışma 122M548 No'lu TÜBİTAK projesi kapsamında desteklenmiştir.

6. ÇIKAR ÇATIŞMASI

Yazarlar, bilinen herhangi bir çıkar çatışması veya herhangi bir kurum/kuruluş ya da kişi ile ortak çıkar bulunmadığını onaylamaktadırlar.

7. YAZAR KATKISI

Cumali DİNÇER çalışmanın kavramsal ve/veya tasarım süreçlerinin yönetimi, veri toplama, veri analizi ve yorumlama, makale taslağının oluşturulması, son onay ve tam sorumluluk kısımlarında katkıda bulunmuştur. Aytekin HİTİT çalışmanın kavramsal ve/veya tasarım süreçlerinin belirlenmesi, çalışmanın kavramsal ve/veya tasarım süreçlerinin yönetimi, veri analizi ve yorumlama, fikirsel içeriğin eleştirel incelemesi, son onay ve tam sorumluluk kısımlarında katkıda bulunmuştur. Selinnur AKSU çalışmanın kavramsal ve/veya tasarım süreçlerinin yönetimi, veri toplama, veri analizi ve yorumlama, fikirsel içeriğin eleştirel incelemesi, makale taslağının oluşturulması, son onay ve tam sorumluluk kısımlarında katkıda bulunmuştur.

8. KAYNAKLAR

Almound E. A., Roebuck B.W., Identification of optimum binder phase compositions for improved WC hard metals. Materials Science and Engineering 105, 237-248, 1998.

Borrel A., Salvador M. D., Rocha V. G., Fernandez A., Aviles A. M., Gotor J., Bulk TiCxN1-x – 15%Co cermets obtained by directs park plasma sintering of Mechanochemical synthesized powders. Materials Research Bulletin 47, 4487-4490, 2012.

Chang S. H., Chen S. L., Characterization and properties of sintered Wc-Co and WC-Ni-Fe hard metal alloys. Journal of Alloys and Compounds 585, 407-413, 2014.

Han J. J., Wang C. P., Kou S. Z., Liu X. J., Thermal stability, crystallization behavior, Vickers hardness and magnetic properties of Fe-Co-Ni-Cr-Mo-C-B-Y bulk metallic glasses. Transactions of Nonferrous Metals Society of China (English Edition), 23(1), 148-155, 2013.

Hitit A., Yazıcı Z. O., Öztürk P., Şahin H., Aşgın A. M., Hitit B., A Ni-CoWB composite developed by devitrification of Ni-Co-W-B bulk metallic glass. Materials Science and Engineering A, 803, 140479, 2021.

Iqbal M., Akhter J. I., Zhang, H. F., Hu Z. Q., Synthesis and characterization of Bulk amorphous steels. Journal of Non-Crystalline Solids 354, 3284-3290, 2008.

Kim H. V., Son I. J., Yoon J. K., Doh J. M., Munir Z. A., Rapid sintering of ultrafine WC-Ni cermets. Int. Journal of Refractory Metals and Hard Materials 24, 427-431, 2006.

Liu K., Wang Z., Yin Z., Gao L., Yuan J., Effect of Co content on microstructure and mechanical properties of ultra fine grained WC-Co cemented carbide sintered by Spark plasma sintering. Ceramics International 44, 18711-18718, 2018.

Marques B. J., Feranandes C. M., Senos A. M. R., Sintering, microstructure and properties of WC-AISI304 powder composites. Journal of Alloys and Compounds 562, 164-170, 2013.

Su W., Wen Y., Zhang O., Effects of Ni and Cu additions on microstructures, Mechanical properties and wear resistances of ultra-coar segrained WC-6Co Cemented carbides. International Journal of Refractory Metals and Hard Materials 70, 176-183, 2018.

Venkateswaran T., Basu B., Raju G. B., Kim D. Y., Densification and properties of transition metal borides-based cermets via spark plasma sintering. Journal of the European Ceramic Society, 26, 2431-2440, 2006.

Yu H., Liu W., Zheng Y., Microstructure and mechanical properties of liquid phase Sintered Mo_2FeB_2 based cermets. Materials and Design 32(6), 3521-3525, 2011.

Zakhariev Z., Zlateva R., Petrov K., Microhardness and High-Temperature Oxidation Stability of CoWB. Journal of the Less-Common Metals 117, 129-133, 1986.

Zhang G., Xiong W., Yang O., Yao Z., Chen S., Chen X., Effect of Moaddition on Microstructure and mechanical properties of (Ti,W)C solid solution based cermets. Int. Journal of refractory Metals and Hard Materials 43, 77-82, 2014.

Zhang T., Yin H., Zhang C., Zhang R., Yang Z., Elder S., Jiang X., Deng Z., Yang G., Zheng Q., Qu X., Synthesis and microstructure evolution of WCoB based cermets durings spark plasma sintering. Ceramics International 45, 17536-17544, 2019.

JOURNAL of
MATERIALS and MECHATRONICS:A

e-ISSN 2717-8811
JournalMM, 2024, 5(2), 383-397
https://doi.org/10.55546/jmm.1522909

Araştırma Makalesi / Research Article

Sodyum-iyon Pillerde Kullanılan MnFe-Bazlı Katotlarda Ni Etkisinin Araştırılması

Burcu KALYONCUOĞLU[1*], Serdar ALTIN[2], Metin ÖZGÜL[3,4]

[1*] Afyon Kocatepe Üniversitesi, Mühendislik Fakültesi, Malzeme Bilimi ve Mühendisliği Bölümü, Afyonkarahisar, Türkiye,
ORCID ID: https://orcid.org/0000-0002-3758-7111, bkalyoncuoglu@aku.edu.tr
[2] İnönü Üniversitesi, Fen-Edabiyat Fakültesi, Fizik Bölümü, Malatya, Türkiye,
ORCID ID: https://orcid.org/0000-0002-4590-907X, serdar.altin@inonu.edu.tr
[3] Afyon Kocatepe Üniversitesi, Mühendislik Fakültesi, Malzeme Bilimi ve Mühendisliği Bölümü, Afyonkarahisar, Türkiye,
ORCID ID: https://orcid.org/0000-0003-4273-5868, metinozgul@aku.edu.tr
[4] Afyon Kocatepe Üniversitesi, Teknoloji Uygulama ve Araştırma Merkezi (TUAM), Afyonkarahisar, Türkiye,
ORCID ID: https://orcid.org/0000-0003-4273-5868, metinozgul@aku.edu.tr

Geliş/ Received: 26.06.2024; **Revize/Revised:** 02.11.2024 **Kabul / Accepted:** 14.12.2024

ÖZET: P2-$NaMnO_2$ tabakalı metal oksit katot malzemeleri şarj edilebilir piller için yüksek kapasiteli ve ucuz bir pil malzemesi olarak bilinmektedir. Ancak Na^+ iyonlarının interkalasyonu sırasında oluşan “Jahn-Teller bozulması” uygulamalarda kısıtlamalara neden olmaktadır. Yapılan çeşitli katkılamalarla bu bozulmaların baskılandığına dair çalışmalar mevcuttur. Bu çalışmada, x=0-0.5 mol% aralığında değişen oranlarda Ni katkılama ile katı hal sentezi yöntemi ile $Na_{0.67}Mn_{0.5-x}Ni_xFe_{0.43}Al_{0.07}O_2$ kompozisyonlarında katot malzemesi tozları üretildi. Üretilen örneklerin mikro yapı incelemeleri için SEM, kristal yapı tayini için XRD ve bağ türlerinin tespiti için FTIR analizleri ile yapısal karakterizasyonları gerçekleştirildi. İncelenen örnekler arasında en düşük BET yüzey alanı katkısız kompozisyonda gözlemlenmiştir. Üretilen katotların elektrokimyasal analizleri için $Na_{0.67}Mn_{0.5-x}Ni_xFe_{0.43}Al_{0.07}O_2$/sodyum metali ile hazırlanan CR2032 düğme pil hücreleri kullanıldı. Oluşturulan hücrelerin CV, EIS ve kapasite ölçümleri oda sıcaklığında gerçekleştirildi. Hücrelerin en yüksek kapasitesi katkısız örneklerde C/3 ve C/20 hızlarında sırasıyla 172 mAh/g ve 203 mAh/g olarak bulundu. Ni'in $Na_{0.67}Mn_{0.5}Fe_{0.43}Al_{0.07}O_2$ içindeki içeriğinin artmasıyla Na tabakaları arasındaki mesafenin azaldığı görülmüştür. Bu durumun kristal yapıdaki Mn ve onunla yer değiştiren Ni iyonlarının iyonik yarıçaplarındaki farklılıktan kaynaklandığı söylenebilir.

Anahtar Kelimeler: Yeni nesil piller, Sodyum-iyon piller, MnFe-bazlı katotlar, Ni katkılama, $Na_{0.67}Mn_{0.5-x}Ni_xFe_{0.43}Al_{0.07}O_2$

Sorumlu yazar / Corresponding author: bkalyoncuoglu@aku.edu.tr

Bu makaleye atıf yapmak için /To cite this article

Kalyoncuoğlu, B., Altın, S., Özgül, M. (2024). Sodyum-iyon Pillerde Kullanılan MnFe-Bazlı Katotlarda Ni Etkisinin Araştırılması. Journal of Materials and Mechatronics: A (JournalMM), 5(2), 383-397.

Investigation of the Effect of Ni in MnFe-Based Cathodes Used in Sodium-Ion Batteries

ABSTRACT: P2-$NaMnO_2$ layered metal oxide cathode materials are known as high-capacity and cost-effective battery materials for rechargeable batteries. However, applications are restricted due to Jahn-Teller distortion occurring during the intercalation of Na^+ ions. Numerous studies have been conducted, suggesting that these distortions can be suppressed with various modifications. In this study, cathode material powders were produced via solid-state synthesis using varying ratios of Ni doping in the $Na_{0.67}Mn_{0.5-x}Ni_xFe_{0.43}Al_{0.07}O_2$ (x=0-0.5 mol%) compositions. Structural characterizations were performed by SEM for microstructural study, XRD for crystal structure determination, and FTIR analyses for detecting bond types. The lowest BET surface area was observed in the undoped composition among the investigated samples. CR2032 coin cells prepared with $Na_{0.67}Mn_{0.5-x}Ni_xFe_{0.43}Al_{0.07}O_2$/sodium metal were used for electrochemical analyses of the produced cathodes. CV, EIS, and capacity measurements of the cells were performed at room temperature. The highest capacity of the cells was found to be 172 mAh/g and 203 mAh/g at C/3 and C/20 rates, respectively, for the undoped samples. It was observed that with the increase in Ni content in $Na_{0.67}Mn_{0.5}Fe_{0.43}Al_{0.07}O_2$, the distance between Na layers decreased. This can be attributed to the differences in the ionic radii of Mn and Ni ions replacing it in the crystal structure.

Keywords: Next-generation batteries, Sodium-ion batteries, MnFe-based cathodes, Ni doping, $Na_{0.67}Mn_{0.5-x}Ni_xFe_{0.43}Al_{0.07}O_2$

1. GİRİŞ

Karbon salınımının en az indirilmesi için sürdürülebilir kaynaklar kullanılarak yeşil enerji sistemlerinin yaygınlaştırılması kritik bir gerekliliktir. Bu çevreci sistemlerin sürekliliği ve ulaşılabilirliği için şarj edilebilir enerji depolama teknolojilerinin geliştirilmesi üzerine ciddi çalışmalar yapılmaktadır. Bunlar arasında kuşkusuz en ciddi öneme sahip olanı şarj edilebilen pil teknolojilerinin ARGE çalışmaları gelmektedir. Özellikle de iyon piller (örn., Li-iyon piller; LIB'ler) hacimsel enerji yoğunluğu, güvenlik ve hafiflik gibi ticari gereksinimleri karşılamalarından dolayı çok önemli bir yer teşkil etmektedir. Fakat doğadaki lityum kaynaklarının sınırlı olması ile birlikte artan enerji talebi LIB'lerde kullanılan başta lityum olmak üzere Ni ve Co gibi kaynakların da tükenme problemlerini beraberinde getirmektedir. Yeni pil kimyaları ile Li, Ni ve Co'a olan bağımlılığın en aza indirilmesine yönelik çalışılmalar her geçen gün artmaktadır. Bu doğrultuda yapılan çalışmalar sodyum iyon pillerin (SIB'ler) en önemli alternatif olarak öne çıktığını ortaya koymaktadır. Özellikle Na bileşikleri, lityum tuzlarından çok daha bol bulunduğundan fiyatları lityumdan 10 ila 50 kat daha ucuzdur (Palomares ve ark., 2012). Bu nedenle Na iyon pilleri (SIB'ler) yeni nesil şarj edilebilir piller olarak beklenmektedir. SIB'lerin gelişim süreçlerindeki ilerlemeler bakımından güvenilir katot malzemelerinin incelenmesi üzerine yapılan çalışmalar kritik bir önem taşımaktadır (Ellis ve Nazar, 2012). Gerçekleştirilmiş olan araştırmalarda SIB'ler için en umut vaat eden katot malzemesi tabakalı sodyum manganez oksitleri olarak değerlendirilmektedir (Cao ve ark., 2023; Liu ve ark., 2020; Mortemard de Boisse ve ark., 2014). Çeşitli yapılarda mangan oksitler arasında P2 fazı Na_xMnO_2 ($0 \leq x \leq 1$), 215 mAg/h kapasite ve 2.0–3.5 V voltaj penceresi ile önemli ölçüde daha yüksek bir kapasite sergilemektedir. Ancak, örnekler arasında interkalasyon ve deinterkalasyon sırasında Jahn-Teller bozulmasından kaynaklanan faz dönüşümleri görülmüştür (Caballero ve ark., 2002; Kumakura ve ark., 2016).

Tabakalı P2-$NaMnO_2$ yapılı katot malzemeleri üzerinde gerçekleştirilen mevcut araştırmaların büyük bir çoğunluğu malzemenin döngüsel kullanımı sırasında yapısal bozulma ile ilgili elektrokimyasal davranışları iyileştirmeye odaklanmıştır. Bu amaçla en yaygın kullanılan yöntem ise, Mn bölgelerine farklı oranlarda çeşitli geçiş metallerinin katkılanması ile oluşturulan $Na_xMn_{1-y}M_yO_2$ (M=Geçiş metali, $0 \leq x \leq 1$) yapılarıdır. Mg, Ti, Co, Ni, Cu ve Zn geçiş metallerinin katkılanması ile elde edilen $Na_xMn_{1-}yMyO_2$ yapılarında ana malzemenin bozulma derecesi ve elektrokimyasal özellikleri üzerinde katkılamanın etkileri rapor edilmiştir (Kumakura ve ark., 2017). Yapılan araştırmalarda metal katkılamanın örgü parametresini ve geçiş metali tabakalar arası mesafesini değiştirerek geri dönüşü olmayan faz geçişlerini bastırabileceğini, döngü ve hız performansını iyileştirebileceğini, daha iyi malzemeler için bir referans sağlayabileceğini göstermektedir. Ayrıca geçiş metali katkılama oksijen redoks reaksiyonlarını tetikler ve yüksek enerji yoğunluğuna katkıda bulunur. Hatta farklı elementler seçilerek yapılan çok elementli katkılamanın, tek element katkılamadan daha iyi elektrokimyasal özelliklerin elde edilmesinde oldukça etkili olduğu literatürde rapor edilmiştir (Jiangh ve ark., 2023; Zhou ve ark., 2022). Çoklu katkılama sarj/deşarj sırasında meydana gelen P2-OP4 ve P2-P2’ faz geçişlerini büyük ölçüde azalttığı bilinmektedir (Huang ve ark., 2021). Benzer sonuçlar $Cu^{2+}/Ni^{2+}/Ti^{4+}$, Mg^{2+}/Ni^{2+} çoklu katkılamalarda da görülmüştür (Ma ve ark., 2020; Zhang ve ark., 2020). Fe^{3+} ve Ni^{2+} çoklu katkılama P2–OP4 ve P2–P2′ faz geçişlerini kısmen baskılamış, Mn^{3+} içeriğini azaltmış, Jahn–Teller etkisini bastırmış ve malzemenin kararlılığını artırmıştır (Hwang ve ark., 2019).

Genel olarak geçiş metalleri ile katkılamanın elektrokimyasal davranışları iyileştirip, örgü bozulma derecesini azalttığı ortaya konulmuştur. Al katkılamanın $Na_{0.67}Mn_{0.5}Fe_{0.5}O_2$'nin yapısı ve elektrokimyasal özellikleri üzerindeki etkileri incelendiğinde, Al'un Mn veya Fe yerine geçmesinin “a” ve “c” örgü parametrelerini azalttığı ancak, “d” aralığını büyütüp, Na-O bağlarını uzatarak özellikle $Na_{0.67}Mn_{0.5}Fe_{0.47}Al_{0.03}O_2$ için Na^+ difüzyonunu ve hız kapasitesini artırdığı görülmüştür (Altın ve ark., 2020). Ayrıca Al katkılamanın Mn^{3+} ve Jahn−Teller distorsiyonunu azalttığı ve katmanlı yapının stabilitesini artırarak döngü performansını yükselttiği raporlanmıştır (Wang ve ark., 2018). Yapılan çalışmalarda dörtlü sistemli katkılamanın üçlü katkılamadan daha kararlı olduğu ve çevrim sırasında oluşan geçiş metali çözünmesini önleyerek pil performansını arttırdığı da görülmüştür (Hwang ve ark., 2018; Mullaliu ve ark., 2020). Mevcut literatür incelendiğinde, Ni^{2+} ve Al^{3+}/Fe^{3+} katkılamanın zayıf ve istenmeyen P2′–P2 faz geçişini bastırdığı ve yapısal kararlılığı artırdığı görülmektedir. Ancak yine de şarj sırasında P2′–OP4 faz geçişinin gerçekleştiği belirtilmektedir (Choi ve ark., 2019; Liu ve ark., 2020). P2-$Na_{0.67}Ni_{0.33}Mn_{0.67}O_2$ yüksek enerji yoğunluğu, yüksek çalışma voltajı (3.8 V), yüksek spesifik kapasite, kolay sentez ve iyi hava stabilitesi nedeniyle pratik SIB uygulamaları için umut verici bir katot malzemesi olarak değerlendirilmektedir (Zhang ve ark., 2019). Ancak yüksek voltajda (Na^+/Na karşısında 4.2 V) P2–O2 faz geçişi, geri dönüşü olmayan oksijen kaybı meydana gelmesi ile metal oksit tabakasının kaymasına ve çevrim sırasında hızlı kapasite bozulmasına neden olması gibi bazı dezavantajlara sahiptir (Wu ve ark., 2016; Feng ve ark., 2022). Yapılan yoğun çalışmalar sonucunda önemli ilerlemeler kaydedilmesine rağmen Mn tabanlı katot malzemelerin pil performansları hala ideal seviyede değildir. Performansı arttırmaya yönelik olarak gerçekleştirilen birbirinden farklı birçok çalışmalardan rapor edilen olumlu sonuçlara rağmen henüz ticarileşme aşamasına geçilememiştir.

Bu çalışmada, P2-$Na_{0.67}Mn_{0.5}$-$Fe_{0.43}Al_{0.07}O_2$ yapısında Mn latis pozisyonlarına Ni katkılama yapılarak tabakalı yapıların örgü bozulmalarına çözüm sunulması ve performansın arttırılması amaçlanmıştır. SIB’ler için katot malzemesi olarak kullanılmak üzere $Na_{0.67}Mn_{0.5-x}Ni_xFe_{0.43}Al_{0.07}O_2$ (x=0-0.5) kompozisyonunda tozların katı hal sentezi tekniği ile yüksek sıcaklıklarda üretimi gerçekleştirilmiştir. Tozların yapısal özelliklerinin karakterizasyonu için XRD, FTIR, Raman, SEM ve BET analizleri yapılmıştır. Elektrokimyasal analizler için anot malzemesi olarak saf sodyum metali kullanılarak CV, EIS ve kapasite ölçümleri oda sıcaklığında gerçekleştirilerek pil hücreleri incelenmiştir. Çalışma kapsamında elde edilen sonuçların yakın gelecekte Li-iyon pillere alternatif olarak Na-iyon pillerin ticarileşmesi ve yaygınlaşması sürecine olumlu katkılar yapması beklenmektedir.

2. MATERYAL VE YÖNTEM

Çalışma kapsamında SIB hücrelerinde kullanılacak $Na_{0.67}Mn_{0.5-x}Ni_xFe_{0.43}Al_{0.07}O_2$ katot tozları x=0-0.5 olarak yüksek saflıkta Na_2O_2 (%99.9, Alfa Aesar), Mn_2O_3 (%99.9, Sigma Aldrich), Fe_2O_3 (%99.8, Alfa Aesar), Al_2O_3 (%99.9, Sigma Aldrich) ve NiO (%99 Alfa Aesar) başlangıç toz bileşenleri kullanılarak üretilmiştir. Bu çalışmada Ni^{+2} katkısı ve oranlarının seçimi, literatürde bulunan önceki araştırmalar ışığında gerçekleştirilmiştir (Zhao ve ark., 2021; Li ve ark., 2022). Başlangıç toz bileşenleri hassas terazi yardımıyla stokiyometrik reçeteye göre tartılarak bir agat havanda yaklaşık 1 saat boyunca karıştırılmıştır. Sentezlenen tozlardan hidrolik pres yardımı ile 5 ton altında peletler oluşturulduktan sonra 900°C'de 6 saat boyunca ısıl işlem uygulanmıştır. Ardından yapısal karakterizasyonlar için hazırlanan örneklerin XRD, SEM ve BET ölçümleri gerçekleştirilmiştir. Farklı kompozisyonlarda (x=0-0.5) Ni içeriğine sahip numunelerde faz oluşumları ve kristal yapı incelemeleri X-ışınları kırınımı (XRD) yöntemiyle CuKα ($\lambda K\alpha$=1.5405 Å) kullanılarak Bruker D 8 Advance model cihaz ile gerçekleştirilmiştir. Örneklerin FTIR spektrumları, Perkin Elmer Spectrum One spektrofotometre ile ölçülmüştür. Mikroyapı görüntüleri LEO 1430 VP model SEM cihazı ile elde edilmiştir. Üretilen tozların yüzey alanları, Gemini VII 2390t model cihaz kullanılarak Brunauer-Elmet-Teller (BET) tekniği ile araştırılmıştır. Farklı kompozisyonlardan seçilen örneklerin Raman spektrumları, 532 nm lazer kullanılarak Konfokal Raman Mikroskobu (JASCO, NRS-4500 NMDS) ile elde edilmiştir.

Elektrokimyasal ölçümler için CR2032 düğme pil hücreleri kullanıldı. Hücrelerin katotlarını hazırlamak için sırasıyla 70:15:15 ağırlık oranlarında aktif katot tozu, süper karbon ve PVDF karıştırılarak *N*-methylpyrrolidone (NMP) içinde bir manyetik karıştırıcıda bir gece boyunca karıştırılmış ve bir doktor bıçağı kullanılarak 100 µm kalınlığında alüminyum folyo üzerine serilmiştir. Ardından vakumlu etüvde 110°C'de 24 saat boyunca kurutma yapılmış ve silindirik hadde cihazıyla haddeleme işlemi uygulanmıştır. CR2032 pil hücrelerine uygun 15 mm çapında bir diskler halinde kesildikten sonra yüksek saflıkta Ar gazı içeren koruyucu atmosfere alınmıştır. Pil hücrelerinin birleştirme işleminde katot olarak hazırlanan $Na_{0.67}Mn_{0.5-x}Ni_xFe_{0.43}Al_{0.07}O_2$ (x=0-0.5) diskleri, anot olarak saf sodyum metali, elektrolit olarak 1M NaClO4 (PC/EC=50/50) ve membran olarak Whatman GF/B kullanılmıştır. Redoks reaksiyonların belirlenmesi 1.5 V – 4.3 V aralığında 0.1 mVs^{-1} tarama hızıyla Döngüsel Voltametri (CV) tekniği ile gerçekleştirilmiştir. CV ölçümleri Ivium Octostat30 potansiyostat/galvanostat cihazında oda sıcaklığında gerçekleştirilmiştir. Galvanostatik şarj/deşarj ölçümleri ise Neware BTS4000 ile, elektrokimyasal empedans spektroskopi (EIS) çalışmaları ise 0.1 mHz'den 200 kHz'e kadar 10mV AC gerilim kullanılarak ZIVE SP1 potansiyostat/galvanostat ile yapılmıştır.

3. BULGULAR VE TARTIŞMA

3.1 Yapısal Özellikler

Sentezlenen $Na_{0.67}Mn_{0.5-x}Ni_xFe_{0.43}Al_{0.07}O_2$ (x=0-0.5) örneklerine ait örneklerin 10 kX büyütmedeki SEM görüntüleri Şekil 1'de verilmiştir. Mikroyapı görüntülerinde farklı Ni içeriğine sahip örneklerde benzer morfoloji ve boyutlarda tane oluşumları gözlemlenmiştir. Ayrıca tanelerin tabakalı yapı oluşumlarını işaret eden plakacık formunda olduğu dikkat çekmektedir. Yine tüm örneklerde belirli oranda bir porozite görülmekle beraber x=0.3 Ni içeren kompozisyonda görece daha yoğun ve homojen yapı oluşumu görülmektedir. Sonuç olarak SEM ile gerçekleştirilen mikroyapı incelemeleri farklı oranlarda Ni katkısının tane oluşumuna boyut ve morfoloji olarak belirgin bir etkisinin olmadığını ortaya koymaktadır. Mevcut literatür incelendiğinde P2 tipi katotlar için bu çalışmadaki sonuçlara benzer tane oluşumlarının gözlemlendiği görülmektedir (Yabuuchi ve ark., 2014; Ramasamy ve ark., 2017; Kanwade ve ark., 2022).

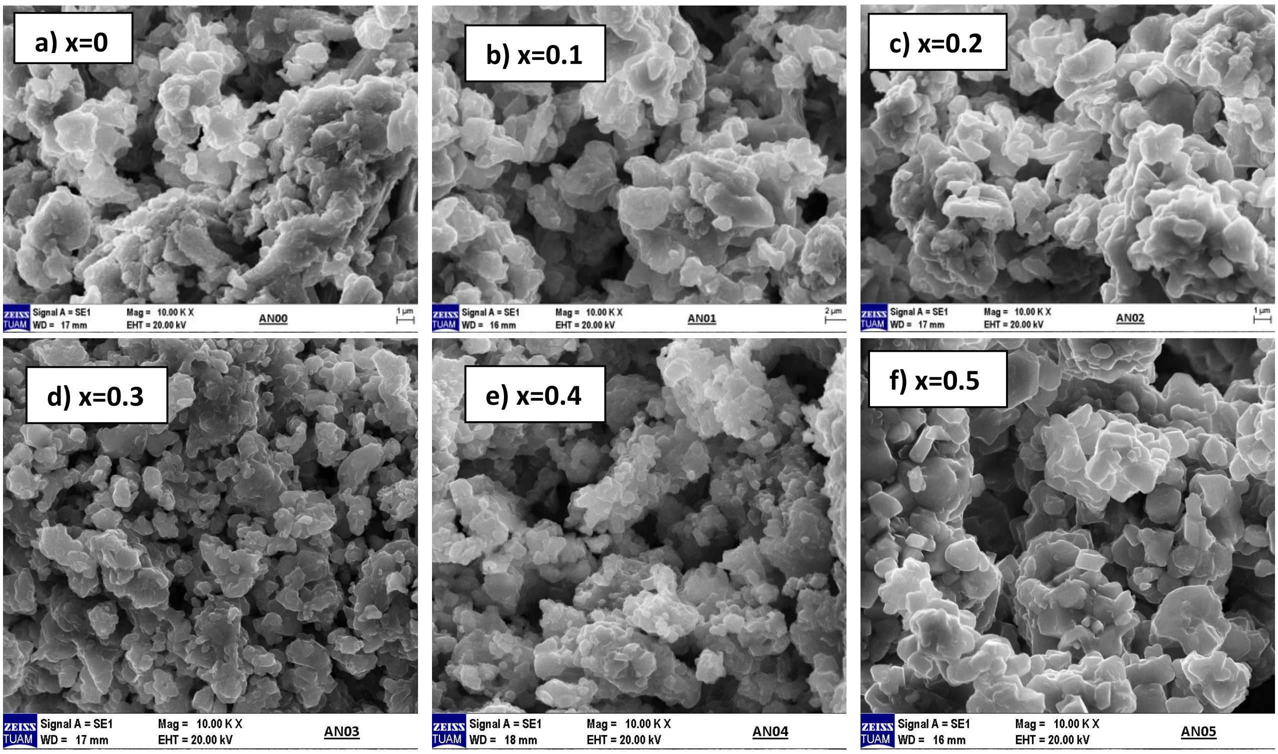

Şekil 1. 900˚C'de 6 saat ısıl işlem görmüş $Na_{0.67}Mn_{0.5-x}Ni_xFe_{0.43}Al_{0.07}O_2$ (x= 0-0,5) numunelerine ait 10000x büyütmede SEM görüntüleri

Katkısız ve değişen oranlarda Ni katkısı içeren örneklerden elde edilen XRD desenleri indekslenerek Şekil 2'de verilmiştir. XRD desenlerinde değişen Ni içeriğine bağlı olarak farklı pik oluşumları ve/veya pik şiddeti değişimleri gözlemlenmektedir. Bu durum farklı faz oluşumlarını işaret etmekle birlikte tüm kompozisyonlarda kristal yapının P2-tipi ve P63/mmc simetrisi (No. 194) ile uyumlu olduğu belirlenmiştir (Yuan ve ark., 2014). Katkı olarak kullanılan Ni iyonlarının kristal yapıda çözündüğü ve Ni'in Mn iyon bölgelerine başarılı bir şekilde yerleştiği ve oluşması beklenen fazın oluştuğunu görülmektedir. P63/mmc simetrisine sahip kristallerin 0,0,0 pozisyonunda iki farklı Na iyon bölgesi bulunduğu ve geçiş metallerinin kristal örgü içinde 0,0,0 pozisyonuna yerleşmekte olduğu, dolayısıyla bu çalışmada üretilen kompozisyonlarda Ni iyonlarının Mn iyonları ile başarılı bir şekilde yer değiştirdiği mevcut literatür ışığında söylenebilir (Wang ve ark, 2018).

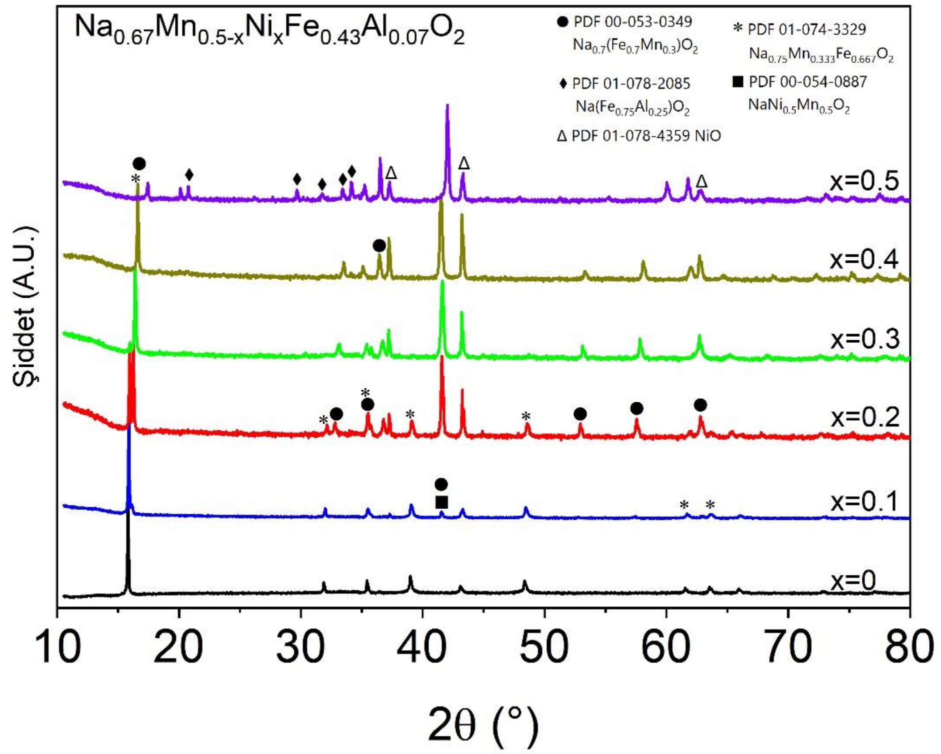

Şekil 2. 900˚C'de 6 saat ısıl işlem görmüş $Na_{0.67}Mn_{0.5-x}Ni_xFe_{0.43}Al_{0.07}O_2$ numunelerine ait XRD desenleri

Bu çalışmada, katkı olarak seçilen Ni iyonlarının yapı içerisinde Mn iyonları ile yer değiştirmesi amaçlanmıştır. Kristal yapıda bulunan mangan katyonlarının Mn^{+3}, Mn^{+4} gibi farklı değerliklerde bulunabildiği ve atomik olarak Ni elementinin elektron konfigürasyonunun [Ar] $3d^8$ $4s^2$ olarak yazıldığı bilinmektedir. Ni^{+2} iyonları, [Ar]$3d^8$ ile kararlı bir yapıya sahip olsa da yapı içinde Ni^{+2} ve Ni^{+3}'ün varlığına dair rapor edilen çalışmalar bulunmaktadır. Bu durumda, Ni iyonlarının Ni^{+2} ve Ni^{+3} olarak Mn^{+3} veya Mn^{+4} ile değerlik durumları ve yarı çaplarına göre yer değiştirmesi mümkün olabilir. Bu iyonların yarıçapları dikkate alındığında, Ni^{+3} ile Mn^{+3} yer değişiminin kristal kafes hacminde bir azalmaya neden olduğu ancak Ni^{+2} ile Mn^{+3} ve Mn^{+4} yer değişiminin kristal yapının hacminde tam tersine bir artışa neden olduğu gözlemlenmiştir. Bu durum, Mn iyonlarının değerlik durumunun Ni^{+2} ile yapı içinde yer değiştirmesiyle Mn^{+3}'ten Mn^{+4}'e dönüşmesi ile açıklanabilir (Wang ve ark., 2019; Kalyoncuoglu ve ark., 2024).

Şekil 3.a'da üretilen katkısız ve Ni katkılı $Na_{0.67}Mn_{0.5}Fe_{0.43}Al_{0.07}O_2$ tozlarının FTIR spektrumları verilmiştir. Elde edilen FTIR bantları yapıda beklendiği gibi Fe-O, Mn-O, Na-O ve Ni-O piklerinin bulunduğunu ortaya koymuştur. 481 cm^{-1}'de görülen (P1) karakteristik Fe-O, Ni-O bağları ile ilişkilidir (Yuliantika ve ark., 2019). 541 cm^{-1}'deki ve 615 cm^{-1}'deki bantlar (P2 ve P3), Mn-O ve Mn-O-Mn Fe-O-Fe'den kaynaklanırken 868 'deki P4 Na-O kaynaklıdır (Zheng ve ark., 2013; Rahmawati ve ark., 2020). 1019 ve 1450 cm^{-1}'de görülen P5 piklerinin, Ni-O ve 1450'deki pikinin de Fe-O ve Ni-O'dan kaynaklanmakta olduğunu belirtmişlerdir (Adekunle ve ark., 2014; Yuan ve ark., 2009). Son olarak FTIR spektrumlarındaki 1559 cm^{-1}'deki bantlar, havadan gelen nemden kaynaklanan su molekülleri ile ilişkilendirilmektedir (Adekunle ve ark., 2014).

Şekli 3.b'de verilen örneklerde 5 farklı Raman kayması gözlemlenmiştir. Literatürde rapor edilen çalışmalarda da benzer sonuçlar gözlemlemiş olup 200 cm^{-1} ile 700 cm^{-1} arasındaki Raman kaymalarının P2-tipi yapıların A1g, E1g ve E2g modları ile açıklanabileceği ifade edilmiştir (Zhao ve ark., 2014). 1094 cm^{-1}'deki pikin de yapıdaki Na_2CO_3'e ait olduğu belirtilmektedir (You ve ark.,

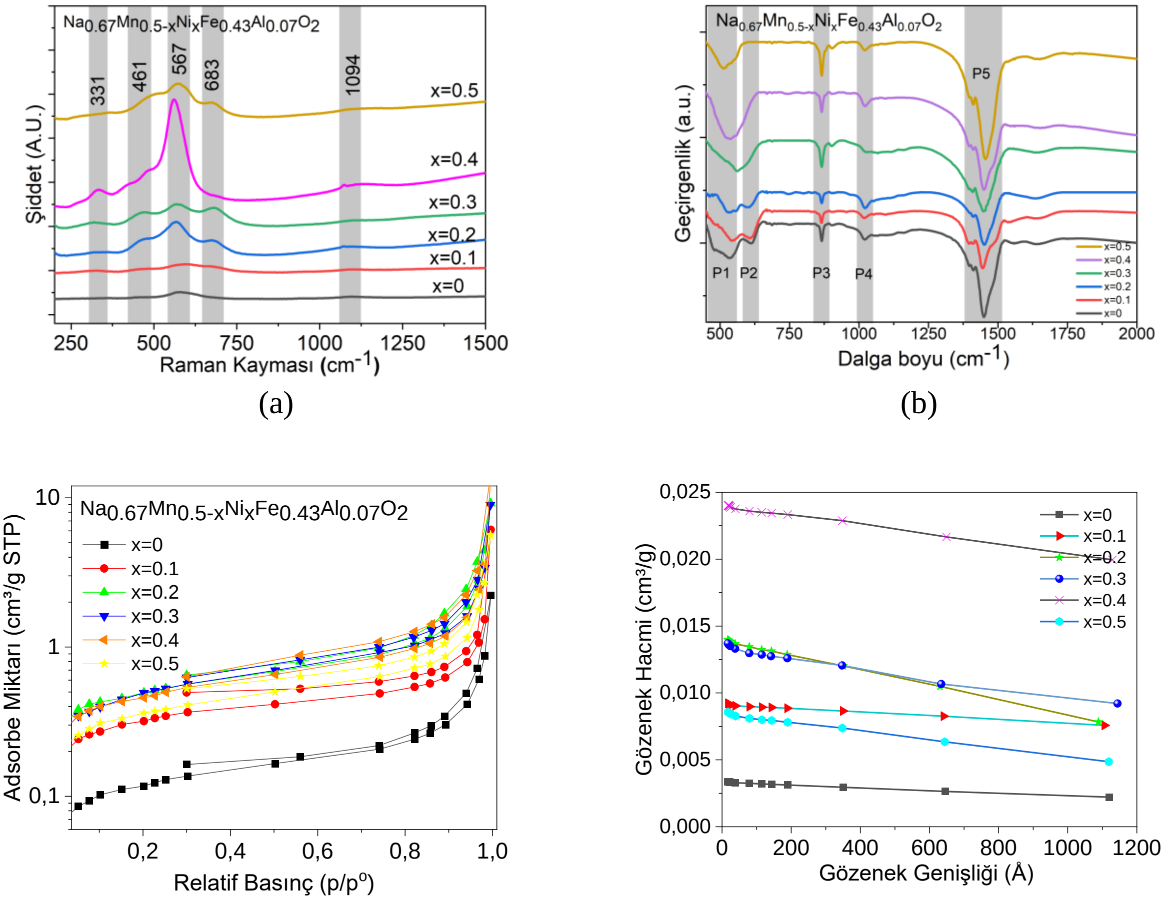

(a) (b)

(c) (d)

Şekil 3. 900˚C'de 6 saat ısıl işlem görmüş $Na_{0.67}Mn_{0.5-x}Ni_xFe_{0.43}Al_{0.07}O_2$ numunelerine ait a) FTIR spektrumları, b) RAMAN spektrumları, c) Azot adsorpsiyon-desorpsiyon izotermal eğrileri, d) BJH gözenek boyutu dağılım eğrileri

Çizelge 1. 900˚C'de 6 saat ısıl işlem görmüş $Na_{0.67}Mn_{0.5-x}Ni_xFe_{0.43}Al_{0.07}O_2$ tozlarına ait yüzey alanları

Katkı oranı	NaMnNiFeAlO$_2$ Yüzey Alanı (m^2/g)
x=0.0	0.4216
x=0.1	1.1536
x=0.2	1.7543
x=0.3	1.8020
x=0.4	1.6480
x=0.5	1.2950

2018). MnO_x Raman spektrumu genellikle 450–550 cm^{-1} ve 550–750 cm^{-1} arasında iki farklı belirgin marker moduyla karakterize edilebilmektedir (Xia ve ark., 2013).

900 °C'de ısıl işlem görmüş örneklerin yüzey ve gözenek boyutu analizleri azot adsorpsiyon-desorpsiyon tekniği ile gerçekleştirilmiş olup Şekil 3.c ve 3.d'de izotermal eğrileri ve Barrett-Joyner-Halenda (BJH) gözenek boyutu dağılımı eğrileri gösterilmektedir. Belirgin bir histerezis döngüsü olmayan azot adsorpsiyon-desorpsiyon izotermal eğrileri, örneklerin gözeneksiz doğasını göstermektedir. BJH gözenek boyutu dağılım eğrilerinden hesaplanan gözenek hacmi ihmal edilebilir düzeydedir. $Na_{0.67}Mn_{0.5-x}Ni_xFe_{0.43}Al_{0.07}O_2$ tozlarına ait BET yöntemine dayalı izoterm tabanlı

hesaplanan özgül yüzey alanları Çizelge 1'de verilmiştir. Sonuçlar irdelendiğinde azot adsorpsiyon-desorpsiyon izotermal eğrileri, BJH gözenek boyutu dağılım eğrileri ve BET özgül yüzey alanı değerlerinin Ni katkılama ile önemli ölçüde arttığı ve özellikle x=0.3 ve 0.4 oranlarında en yüksek değerlere ulaşıldığı söylenebilir.

3.2 Elektrokimyasal Ölçümler

Elektrokimyasal özellikleri test etmek için CR2032 düğme pil hücreleri ile örnek elektrotların sodyum metale karşı galvanostatik şarj/deşarj ölçümleri gerçekleştirildi. C/3 akım hızında 100 çevrim gerçekleştirilen ölçümlerin voltaj-kapasite grafikleri Şekil 4'te verilmiştir. Deşarj kapasiteleri ve kapasite kaybı değerleri Çizelge 2'de, kapasite eğrileri ise Şekil 5.a'da verilmektedir. Ni katkısız örnek, 172 mAh/g ile en yüksek başlangıç deşarj kapasitesini göstermiştir ancak 100 döngü sonrasında sadece %54'lük bir kapasite tutma oranı ile bu değerin 92 mAh/g'a düştüğü gözlemlenmiştir. Öte yandan Ni katkılamanın kapasite değerlerinde ciddi düşmelere yol açtığı ancak kapasite tutma performansının x=0.3 katkı oranına kadar çok büyük ölçüde düşüş göstermediği tespit edilmiştir. En iyi kapasite tutma oranı yaklaşık %57 değeri ile x=0.2 katkı oranında elde edilmiştir. Kapasite kayıp oranlarını gösteren grafik Şekli 5.b'de verilmiştir. C/20 akım hızında 50 çevrim gerçekleştirilen galvanostatik şarj/deşarj ölçüm grafiği de Şekil 5.c'de görülmektedir. Bu koşullarda ölçülen en yüksek deşarj kapasitesi yine 203 mAh/g başlangıç ve 50 çevrim sonrasında 131 mAh/g ve %64 kapasite tutma oranı ile katkısız örneğe aittir. Artan Ni içeriğinin hücre kapasitesinde sistematik olarak azalmaya neden olduğu da belirgin olarak görülmüştür. Benzer çalışmalar incelendiğinde, farklı oranlara sahip yapılarda da belirli oranların üzerinde katkı elementinin artışı tersinir olmayan faz geçişleri sergileyerek yapısal kararsızlığa ve bununda kapasite kayıplarına neden olduğu görülmüştür (Wang ve ark., 2016; Luo ve ark., 2017, Liang ve ark., 2024).

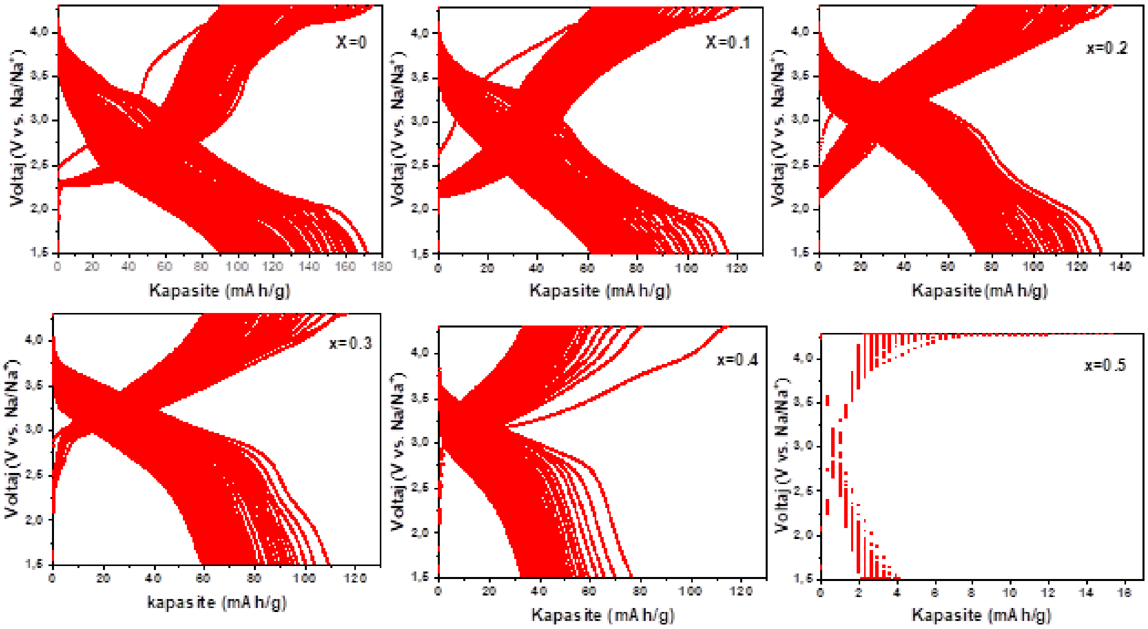

Şekil 4. C/3 akım hızlarında 100 çevrim gerçekleştirilen x= 0–0.5 aralığında $Na_{0.67}Mn_{0.5-x}Ni_xFe_{0.43}Al_{0.07}O_2$ örneklerine ait galvanostatik deşarj grafikleri

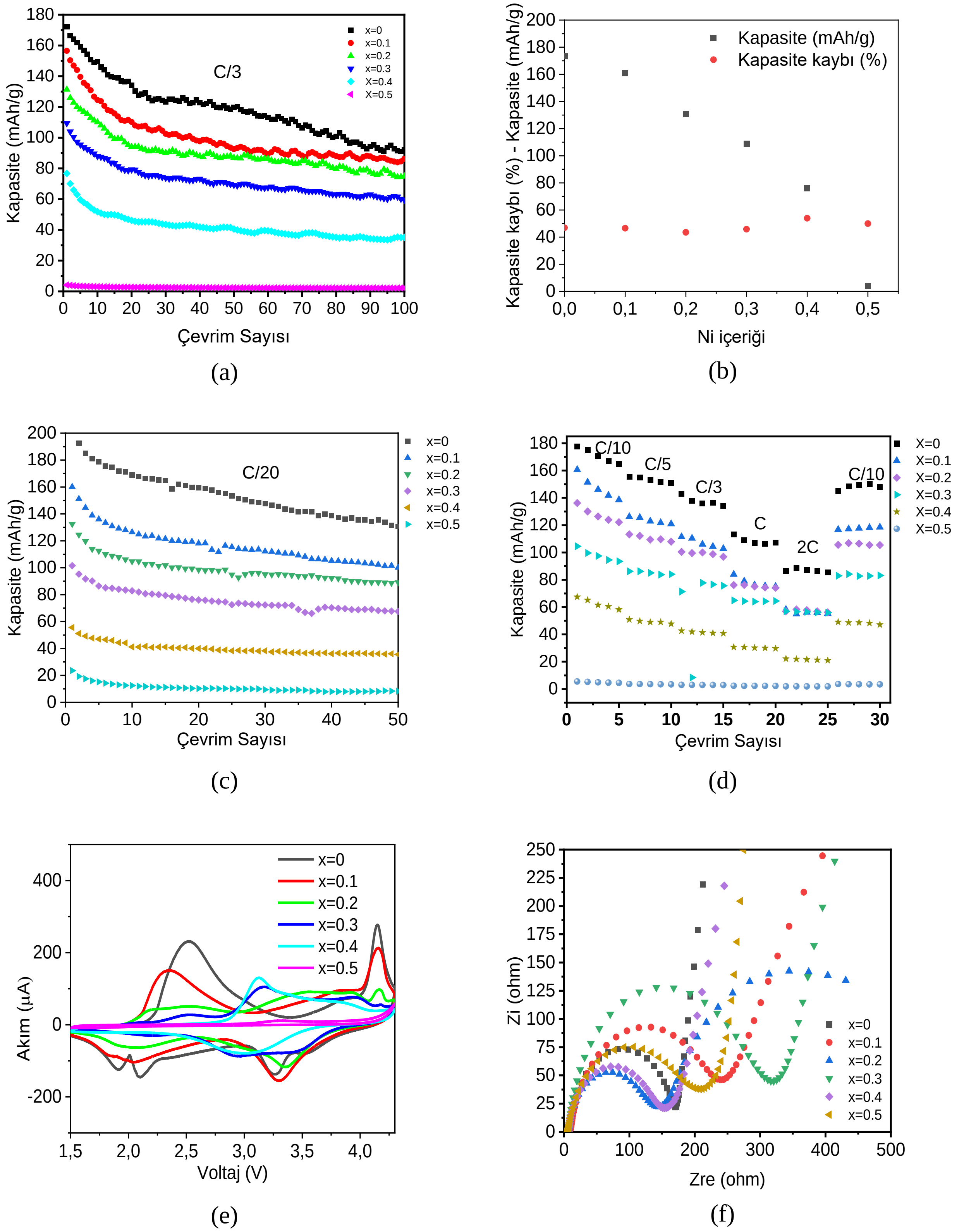

(a) (b)

(c) (d)

(e) (f)

Şekil 5. $Na_{0.67}Mn_{0.5-x}Ni_xFe_{0.43}Al_{0.07}O_2$ (x= 0-0.5) numunelerine ait a) C/3 akım hızında galvanostatik deşarj çevirim sayısına bağlı kapasite, b) Ni oranı ile kapasite kaybı ilişkisi, c) C/20 akım hızında galvanostatik deşarj çevirim sayısına bağlı kapasite, d) farklı akım hızlarında deşarj çevirim sayısına bağlı kapasite, e) 1.5-4.3 V aralığında akım-voltaj (CV) ve f) EIS eğrileri

Çizelge 2. 900˚C'de 6 saat ısıl işlem görmüş $Na_{0.67}Mn_{0.5-x}Ni_xFe_{0.43}Al_{0.07}O_2$ (x= 0-0.5) Ni katkılı numunelere ait C/3'de farklı çevrim sayılarında ölçülen mAh/g olarak kapasite değerleri ve 100 çevrim sonunda kapasite kayıp/tutma oranları

Ni (%mol)	1. Çevrim	10. Çevrim	25. Çevrim	50. Çevrim	75. Çevrim	100. Çevrim	Kapasite Tutma Oranı (%)
x=0.0	172	149	125	119	102	92	54
x=0.1	156	124	105	92	88	86	55
x=0.2	131	110	91	86	82	74	57
x=0.3	109	87	75	69	65	59	54
x=0.4	76	51	54	40	37	35	46
x=0.5	4	3	2	2	2	2	50

Şekil 5.d'de 5 çevrim olarak gerçekleştirilen örneklere ait C/10, C/5, C/3, C ve 2C akım hızlarına ait farklı akım hızlarında deşarj çevirim sayısına bağlı kapasite değişimleri görülmektedir. Artan Ni içeriğinin hücre kapasitesinde azalmaya neden olduğu görülmektedir. Ni katkısız örneğin farklı akım oranları için yüksek kapasite değerlerini gösterdiği gözlemlenmiştir. Bu durum $Na_{0.67}Mn_{0.5}Fe_{0.43}Al_{0.07}O2$ katoduna 0.1-0.5 oranlarında Ni katkılamanın katman içine Na yerleştirme/çıkarma mekanizmasını olumsuz etkilediğini göstermektedir. 0.1≤x gibi yüksek oranlarda Ni katkılamanın sonucu olarak farklı C hızlarında da düşük kapasiteler elde edilmiştir. Yüksek akım yoğunluklarına çıkıldığında belirli oranda tersinir kapasitenin korunduğu görülmüştür. Meydana gelen kapasite kayıpları Mn^{3+} kaynaklı Jahn-Teller distorsiyonu ve büyük Na iyonlarının interkalasyon/deinterkalasyon nedeniyle meydana gelen hacim değişikliklerinden kaynaklı olduğu düşünülmektedir (Li ve ark., 2017).

Örneklerin CV (Döngüsel Volltametri) ölçümleri 0.1 mV/s taramada hızında ve 1.5–4.3V aralığında Ivium marka Octostat30 potansiyostat-galvanostat cihazında gerçekleştirilmiştir. Örneklerin geniş bir elektrokimyasal pencereyi desteklediği görülmüştür. Hem Ni hem de Fe elektrokimyasal olarak aktif olduğu ve şarj voltaj aralığında (4.0-4.3V) mevcut olduğu yapılan benzer çalışmalarla da benzerlik gösterdiği görülmüştür (Xie ve ark., 2016; Jeong ve ark., 2019). Şekil 5.e'de görüldüğü üzere en yüksek redoks pikleri katkısız örneğe aittir. $Mn^{3+/}Mn^{4+}$ piki olan ilk pik yaklaşık 2.5 V, ikinci pik $Fe^{3+/}Fe^{4+}$ redoks piki yaklaşık 4.2 V dolaylarında örneklere ait CV grafiklerinde görüldüğü üzere 0.2 ve sonrasında Mn yerine konulan Ni'in pik şiddetlerini değiştirdiği ve yapıda bozulmaların olduğu görülmektedir. 3.5 V civarında görülen bu bozulmaların hücrelerdeki John Teller distorsiyon (JTD) etkileri ile ilişkili olduğu bilinmektedir (Zhang ve ark., 2021). Ni katkı oranının arttırılmasının Na giriş-çıkışının olumsuz etkilediği, bunun da kapasitelere yansıdığı galvanostatik şarj-deşarj sonuçlarıyla desteklenmiştir.

Örnek elektrotlarının Nyquist grafiklerindeki EIS (Elektrokimyasal İmpedans Spektroskopisi) Şekil 5.f'de gösterilmiştir. Örneklerin yüksek frekansta bir yarı çemberle ile birleşen doğrusal bir çizgi gösterdiği görülmektedir. Tipik olarak, yarı çember bölgesi elektrot/elektrolit arayüzündeki şarj taşıma direncini temsil etmektedir (Choi ve ark., 2020). Örneklerden x=0.2 elektrodunun, en küçük yarı çaplı yarı çemberi göstererek en küçük şarj taşıma direncine sahip olduğu belirlenmiştir. Yapı içerisinde farklı faz/faz geçişlerinin meydana gelmesi Nyquist eğrilerinin oluşumuyla bilinmektedir (Chaali ve ark., 2023). Bu çalışmada elde edilen bulgular yapı içerisinde faz geçişlerinin olduğunu destekler niteliktedir.

4. SONUÇ

Bu çalışmada, doğadaki lityum kaynaklarının sınırlı olması ile birlikte artan enerji talebi ve maliyet nedeniyle Li-iyon pillere (LIB) alternatif olarak son yıllarda yeni nesil şarj edilebilir piller olarak üzerine yoğun araştırmaların yürütülmekte olduğu Na iyon piller (SIB) için en umut vaat eden katot malzemesi olarak öne çıkan tabakalı sodyum manganez oksitleri arasında P2 faz yapılı $Na_{0.67}Mn_{0.5-x}Ni_xFe_{0.43}Al_{0.07}O_2$ (x=0-0.5) elektrotları, yüksek sıcaklıklarda hızlı soğutma ile katı hal reaksiyon yöntemi kullanılarak başarıyla sentezlenmiştir. Çalışma kapsamında elde edilen başlıca sonuçlar şöyle özetlenebilir:

- XRD analizleri, tüm örneklerin P2 tipi bir kristal yapı sergilediğini ortaya koymaktadır.
- FTIR ve Raman ölçümleri, XRD sonuçları ile uyumludur ve Ni, Fe ve Mn iyonlarının çoklu değerlik durumlarının varlığını kanıtlamaktadır.
- BET ölçümleri de x=0.2 kompozisyonunun 1.7543 m^2/g değeriyle katkısıza (0.4216 m^2/g) oranla yaklaşık dört katı daha fazla spesifik yüzey alanına sahip olduğunu göstermiştir.
- Elektrokimyasal özellikler kapsamında en iyi kapasite tutma oranı yaklaşık %57 değeri ile x=0.2 Ni katkı oranında elde edilmiştir.
- Örneklerden x=0.2 elektrodunun, en küçük yarı çaplı yarı çemberi göstererek en küçük şarj taşıma direncine sahip olduğu belirlenmiştir.
- CV profillerinde Mn/Ni ve Fe iyonlarından kaynaklanan iki belirgin redoks piki tespit edilmiştir.
- CV ölçümleri Ni katkı oranının x=0.2 ve sonrasında piki şiddetlerinde belirgin olarak değişime akım-voltaj karakteristiklerinde bozulmaların olduğunu ortaya koymuştur. Görülen bu bozulmaların hücrelerdeki John Teller distorsiyon (JTD) etkileri ile ilişkili olduğu literatürde rapor edilmiştir.
- $Na_{0.67}Mn_{0.5-x}Ni_xFe_{0.43}Al_{0.07}O_2$ için x=0 ile 0.5 aralığında Ni katkılamanın Na iyonlarının interkalasyon/deinterkalasyon sürecinde kısıtlamalara yol açtığı görülmüştür.
- Na iyonunun stokiyometrisi değişen Ni-katkılı örneklerde difüzyon davranışının yapı ve elektrokimyasal özellikleri arasındaki korelasyonlara ilişkin ipuçlarının elde edilmiş olduğu görülen bu çalışmanın bulguları, Na-iyon piller için yeni katot malzemesi geliştirilmesi çalışmalarına ışık tutucu niteliktedir. Gelecek çalışmalar kapsamında katkısız ve Ni katkılı numunelerde iyonik iletkenlik ölçümlerinin sonuçları bu çalışmada elde edilen bulguların teyidi açısından değerli olacaktır.

5. TEŞEKKÜR

Bu çalışma, TÜBİTAK tarafından 220N335 başvuru numaralı proje ve Afyon Kocatepe Üniversitesi Bilimsel Araştırma Projeleri Koordinasyon Birimi tarafından “21.FEN. BİL.40” kodlu proje ile desteklenmiştir.

6. ÇIKAR ÇATIŞMASI

Yazarlar, bilinen herhangi bir çıkar çatışması veya herhangi bir kurum/kuruluş ya da kişi ile ortak çıkar bulunmadığını onaylamaktadırlar.

7. YAZAR KATKISI

Burcu Kalyoncuoğlu veri toplama ve veri analizi, Metin Özgül denetim ve doğrulama, Serdar Altın sonuçların irdelenmesi ve bilimsel literatür ışığında değerlendirilmesi süreçlerinde katkıda bulunmuşlardır.

8. KAYNAKLAR

Adekunle A. S., Oyekunle J. A. O., Oluwafemi O. S., Joshua A. O., Makinde W. O., Ogunfowokan A. O., Eleruja M. A., Ebenso E. E., Comparative Catalytic Properties of Ni(OH)2 and NiO Nanoparticles Towards the Degradation of Nitrite (NO2 -) and Nitric Oxide (NO), International Journal of Electrochemical Science 9(6), 3008-3021, 2014.

Altin S. E., Altundağ S., Altin E. M., Harfouche M., Bayri A., An investigation of the improvement in energy storage performance of Na 2/3 Mn 1/2 Fe 1/2 O 2 by systematic Al-substitution. Journal of Materials Science: Materials in Electronics 31, 14784-14794, 2020.

Chaali Y., Dahbi M., Sabbar E., Zakaria D., Comparative study of Na0. 67Ni0. 25Co0. 17Mn0. 58O2 P-Type cathode materials for sodium-ion batteries: Combustion synthesis and combined analysis of structural, electrical, and dielectric properties. Ceramics International 49(21), 33607-33617, 2023.

Caballero A., Hernan L., Morales J., Sanchez L., Pena J. S., Aranda M. A., Synthesis and characterization of high-temperature hexagonal P2-Na 0.6 MnO 2 and its electrochemical behaviour as cathode in sodium cells. Journal of Materials Chemistry 12(4),1142-1147, 2002.

Calzaferri G., Gallagher S. H., Bruehwiler D., Multiple equilibria describe the complete adsorption isotherms of nonporous, microporous, and mesoporous adsorbents. Microporous and Mesoporous Materials 330, 111563, 2022.

Cao Y., Xiao M., Sun X., Dong W., Huang F., Recent Advances on High-Capacity Sodium Manganese-Based Oxide Cathodes for Sodium-ion Batteries. Chemistry–A European Journal. 29(12), e202202997, 2023.

Choi J. U., Yoon C. S., Zhang Q., Kaghazchi P., Jung Y. H., Lee K. S., Ahn D. C., Sun Y. K. Myung S. T., Understanding on the structural and electrochemical performance of orthorhombic sodium manganese oxides. Journal of Materials Chemistry A 7(1), 202-211, 2019.

Choi W, Shin H. C., Kim J. M., Choi J.Y., Yoon W. S., Modeling and applications of electrochemical impedance spectroscopy (EIS) for lithium-ion batteries. Journal of Electrochemical Science and Technology 11(1), 1-13, 2020.

Ellis B. L, Nazar L. F, Sodium and sodium-ion energy storage batteries, Current Opinion in Solid State and Materials Science 16(4), 168-177, 2012.

Feng J., Luo S., Cai K., Yan S., Wang Q., Zhang Y., Liu X., Research progress of tunnel-type sodium manganese oxide cathodes for SIBs. Chinese Chemical Letters 33(5), 2316-2326, 2022.

Huang X., Li D., Huang H., Jiang X., Yang Z., Zhang W., Fast and highly reversible Na+ intercalation/extraction in Zn/Mg dual-doped P2-Na 0.67 MnO 2 cathode material for high-performance Na-ion batteries. Nano Research 14, 3531-3537, 2021.

Hwang J. Y., Myung S. T., Sun Y. K., Quaternary transition metal oxide layered framework: O3-type Na [Ni0. 32Fe0. 13Co0. 15Mn0. 40] O2 cathode material for high-performance sodium-ion batteries. Journal of Physical Chemistry C 122(25), 13500-13507, 2018.

Hwang J. Y., Du H. L., Yun B. N., Jeong M. G., Kim J. S., Kim H., Jung H. G., Sun Y. K., Carbon-free TiO2 microspheres as anode materials for sodium ion batteries. ACS Energy Letters 4(2), 494-501, 2019.

Jeong M., Lee, H., Yoon, J. and Yoon, W.S., O3-type NaNi1/3Fe1/3Mn1/3O2 layered cathode for Na-ion batteries: Structural evolution and redox mechanism upon Na (de) intercalation. Journal of Power Sources 439, 227064, 2019.

Jiang H., Qian G., Liu R., Liu W. D., Chen Y., Hu W., Effects of elemental doping on phase transitions of manganese-based layered oxides for sodium-ion batteries. Science China Materials 66(12), 4542-4549, 2023.

Kalyoncuoglu B., Ozgul M., Altundag S., Bulut F., Oz E., Sahinbay S., Altin S., High-performance Na-ion full-cells with P2-type Na0. 67Mn0. 5-xNixFe0. 43Al0. 07O2 cathodes: Cost analysis for stationary battery storage systems. Journal of Energy Storage 79, 110203, 2024.

Kanwade A., Gupta S., Kankane A., Tiwari M. K., Srivastava A., Satrughna J. A., Yadav S. C., Shirage P. M., Transition metal oxides as a cathode for indispensable Na-ion batteries. RSC advances 12(36), 23284-23310, 2022.

Kumakura S, Tahara Y, Kubota K, Chihara K, Komaba S. Sodium and manganese stoichiometry of P2-type Na2/3MnO2. Angewandte Chemie International Edition. 4;55(41):12760-3, 2016.

Kumakura S., Tahara Y., Sato S., Kubota K., Komaba S., P′2-Na2/3Mn0. 9Me0. 1O2 (Me= Mg, Ti, Co, Ni, Cu, and Zn): correlation between orthorhombic distortion and electrochemical property. Chemistry of Materials 29(21), 8958-8962, 2017.

Li J. Y., Lü H. Y., Zhang X. H., Xing Y. M., Wang G., Guan H. Y., Wu X. L., P2-type Na0. 53MnO2 nanorods with superior rate capabilities as advanced cathode material for sodium ion batteries. Chemical Engineering Journal 316, 499-505, 2017.

Li S., Sun Y., Pang Y., Xia S., Chen T., Sun H., Zheng S., Yuan T., Recent developments of layered transition metal oxide cathodes for sodium-ion batteries toward desired high performance. Asia-Pacific Journal of Chemical Engineering 17(4), e2762, 2022.

Liang Y., Liu W., Wu H., Tang Z., Xu L., Developing high-performance sodium-ion battery cathode materials through regulating the Ni/Fe ratio in Na0. 67NixFe0. 52-xMn0. 48O2. Journal of Power Sources 617, 235159, 2024.

Liu Z., Xu X., Ji S., Zeng L., Zhang D., Liu J., Recent progress of P2-type layered transition-metal oxide cathodes for sodium-ion batteries. Chemistry–A European Journal, 26(35), 7747-7766, 2020.

Liu X., Zhong G., Xiao Z., Zheng B., Zuo W., Zhou K., Liu H., Liang Z., Xiang Y., Chen Z., Ortiz G. F., Al and Fe-containing Mn-based layered cathode with controlled vacancies for high-rate sodium ion batteries. Nano Energy 76, 104997, 2020.

Luo C., Langrock A., Fan X., Liang Y., Wang C., P2-type transition metal oxides for high performance Na-ion battery cathodes. Journal of Materials Chemistry A 5(34), 18214-18220, 2017.

Ma P., Kang W., Wang Y., Cao D., Fan L., Sun D., Binary metal co-substituted P2-type Na0. 67Mn0. 7Cu0. 15Ni0. 15O2 microspheres as robust cathode for high-power sodium ion battery. Applied Surface Science, 529, 147105, 2020.

Mortemard de Boisse B., Carlier D., Guignard M., Bourgeois L., Delmas C., P2-Na x Mn1/2Fe1/2O2 phase used as positive electrode in Na batteries: Structural changes induced by the electrochemical (de) intercalation process. Inorganic chemistry 53(20), 11197-11205, 2014.

Mullaliu A., Kuroki K., Keller M., Kubota K., Buchholz D., Komaba S., Passerini S., Structural investigation of quaternary layered oxides upon Na-ion deinsertion. Inorganic Chemistry. 59(11), 7408-7414, 2020.

Palomares V., Serras P., Villaluenga I., Hueso K. B., Carretero-González J., Rojo T., Na-ion batteries, recent advances and present challenges to become low cost energy storage systems. Energy & Environmental Science 5(3), 5884-5901, 2012.

Rahmawati F., Kusumaningtyas A. A., Saraswati T. E., Prasetyo A., Suendo V., Mn-doped NaFeO2 from a low purity-Fe precursor and its performance as cathode for Sodium-Ion Battery. Inorganic and Nano-Metal Chemistry 51(3), 383-390, 2020.

Ramasamy H.V., Kaliyappan K., Thangavel R., Seong W. M., Kang K., Chen Z., Lee Y. S., Efficient method of designing stable layered cathode material for sodium ion batteries using aluminum doping. Journal of Physical Chemistry Letters 8(20), 5021-5030, 2017.

Wang H., Liao X. Z., Yang Y., Yan X., He Y. S., Ma Z. F., Large-scale synthesis of NaNi1/3Fe1/3Mn1/3O2 as high performance cathode materials for sodium ion batteries. Journal of The Electrochemical Society 163(3), A565, 2016.

Wang H., Gao R., Li Z., Sun L., Hu Z., Liu X., Different effects of Al substitution for Mn or Fe on the structure and electrochemical properties of Na0. 67Mn0. 5Fe0. 5O2 as a sodium ion battery cathode material. Inorganic chemistry 57(9), 5249-5257, 2018.

Wang Y., Wang X., Li X., Yu R., Chen M., Tang K., Zhang X., The novel P3-type layered Na0. 65Mn0. 75Ni0. 25O2 oxides doped by non-metallic elements for high performance sodium-ion batteries. Chemical Engineering Journal 360, 139-147, 2019.

Wu X., Xu G. L., Zhong G., Gong Z., McDonald M. J., Zheng S., Fu R., Chen Z., Amine K., Yang Y., Insights into the effects of zinc doping on structural phase transition of P2-type sodium nickel manganese oxide cathodes for high-energy sodium ion batteries. ACS applied materials & interfaces 8(34), 22227-22237, 2016.

Xie Y., Wang H., Xu G., Wang J., Sheng H., Chen Z., Ren Y., Sun C. J., Wen J., Wang J., Miller D. J., In operando XRD and TXM study on the metastable structure change of NaNi1/3Fe1/3Mn1/3O2 under electrochemical sodium-ion intercalation. Advanced Energy Materials 6(24), 1601306, 2016.

Yabuuchi N., Kubota K., Dahbi M., Komaba S., Research development on sodium-ion batteries. Chemical reviews 114(23), 11636-11682, 2014.

You Y., Dolocan A., Li W., Manthiram A., Understanding the air-exposure degradation chemistry at a nanoscale of layered oxide cathodes for sodium-ion batteries. Nano letters 19(1), 182-188, 2018.

Yuan D., Hu X., Qian J., Pei F., Wu F., Mao R., Ai X., Yang H., Cao Y., P2-type Na0. 67Mn0. 65Fe0. 2Ni0. 15O2 cathode material with high-capacity for sodium-ion battery. Electrochimica Acta 116, 300-305, 2014.

Zhang L., Wang C., Liu Y., Ren M., Du J., Chen A., Li F., Suppressing interlayer-gliding and Jahn-Teller effect in P2-type layered manganese oxide cathode via Mo doping for sodium-ion batteries. Chemical Engineering Journal, 426, 130813, 2021.

Zhao W., Kirie H., Tanaka A., Unno M., Yamamoto S., Noguchi H., Synthesis of metal ion substituted P2-Na2/3Ni1/3Mn2/3O2 cathode material with enhanced performance for Na ion batteries. Materials Letters 135, 131-134, 2014.

Zhao Y., Li L., Wu Y., Fang Y., Xie, H., Progress of the Elements Doped NaFeO2 Cathode Materials for High Performance Sodium-ion Batteries. Chemistry Select 6(36), 9701-9708, 2021.

Zhang X., Qiu F., Jiang K., He P., Han M., Guo S., Zhou H., Improving the structural and cyclic stabilities of P2-type Na 0.67 MnO 2 cathode material via Cu and Ti co-substitution for sodium ion batteries. Chemical Communications 56(46), 6293-6296, 2020.

Zheng M., Zhang H., Gong X., Xu R., Xiao Y., Dong H., Liu X., Liu Y., A simple additive-free approach for the synthesis of uniform manganese monoxide nanorods with large specific surface area, Nanoscale Research Letters 8, 1-7, 2013.

Zhou D., Zeng C., Xiang J., Wang T., Gao Z., An C., Huang W., Review on Mn-based and Fe-based layered cathode materials for sodium-ion batteries. Ionics 28(5), 2029-2040, 2022.